TECHNISCHE UNIVERSITÄT MÜNCHEN

Department Chemie

Lehrstuhl für Biotechnologie

Substrate recognition determinants of the small heat shock protein αB-crystallin and its role in cataractogenesis

Katrin Christiane Back

Vollständiger Abdruck der von der Fakultät für Chemie der Technischen Universität München zur Erlangung des akademischen Grades eines Doktors der Naturwissenschaften (Dr. rer. nat.) genehmigten Dissertation.

Vorsitzender:	Univ.-Prof. Dr. Bernd Reif
Prüfer der Dissertation:	1. Univ.-Prof. Dr. Johannes Buchner
	2. Univ.-Prof. Dr. Sevil Weinkauf

Die Dissertation wurde am 16.02.2016 bei der Technischen Universität München eingereicht und durch die Fakultät für Chemie am 30.03.2016 angenommen.

Contents

Summary

Crystallins constitute about 90% of the protein content in the vertebrate eye lens. They are responsible for the refractive index gradient in the lens and for maintaining lens transparency which is indispensable for vision. The crystallin gene family can be divided into two subfamilies. The β/γ-crystallins are, to current knowledge, structural proteins that exist as monomers (γ-crystallins) or as multimers ranging from dimers to hexamers (β-crystallins). α-crystallin, however, belongs to the family of small Heat shock proteins (sHsps) and forms large oligomeric assemblies. sHsps are molecular chaperones and can interact with destabilized proteins to prevent formation of light-scattering and cytotoxic protein aggregates.

To elucidate the mechanism of substrate interaction of αB-crystallin, different mutants were analyzed in this work concerning structure, dynamics and function. It was found that the N-terminal regions (NTRs) contain several equivalent binding sites and that subunit exchange might be the bottle neck of substrate interaction. In peptide array experiments, five different model substrates were analyzed for binding motifs of αB-crystallin. The amino acid composition of the best hits resembled the composition of the NTRs of αB-crystallin. From the combination of all results it was derived that that the NTRs of αB-crystallin form binding sites in the oligomeric assembly and act as pseudo-substrates at the same time.

To complement the performed *in vitro* studies on substrate interaction, α-crystallin isolated from murine eye lenses was analyzed. For lens α-crystallin larger oligomer sizes and increased heterogeneity was observed compared to recombinant α-crystallin. 2-dimensional gel electrophoresis revealed that post-translational modifications such as phosphorylation and truncation were the main reasons for the observed differences. Unexpectedly, the only lens protein that could be found in complex with α-crystallin in minor amounts was βB2-crystallin. In different mouse models of cataract bearing mutations in either α-, β- or γ-crystallin genes, truncated α-crystallin was found to constitute a large proportion of the aggregated protein fraction. The observed increase in α-crystallin truncation and subsequent aggregation correlated with post-translational modification of βB2-crystallin, which seems to play a key role in cataract formation. The prevailing theory of cataract prevention by α-crystallin through formation of stable substrate complexes could not be confirmed.

A model of substrate interaction with α-crystallin was developed suggesting reversible interactions of α-crystallin with unfolding intermediates. “Irreversible” formation of substrate complexes was found to be unfavorable due to the high aggregation propensity of these macromolecular assemblies.

1. Introduction

1.1 The importance of Heat shock proteins for proteostasis

Cells have developed a potent quality control system to maintain proteome integrity and thereby to assure survival. Although the natively folded state of proteins is energetically favored, protein misfolding and aggregation can occur immediately during protein synthesis or at later time points and lead to formation of toxic aggregates in the cell (Brockwell and Radford, 2007). This is of special importance under conditions that challenge the proteostasis system like environmental stress conditions (e.g. oxidative stress, UV- and heat stress), during metabolic stress, in the presence of destabilizing mutations or in diseases like cancer (fig. 1) (Chen et al., 2011; Dobson, 2003; Hartl and Hayer-Hartl, 2009).

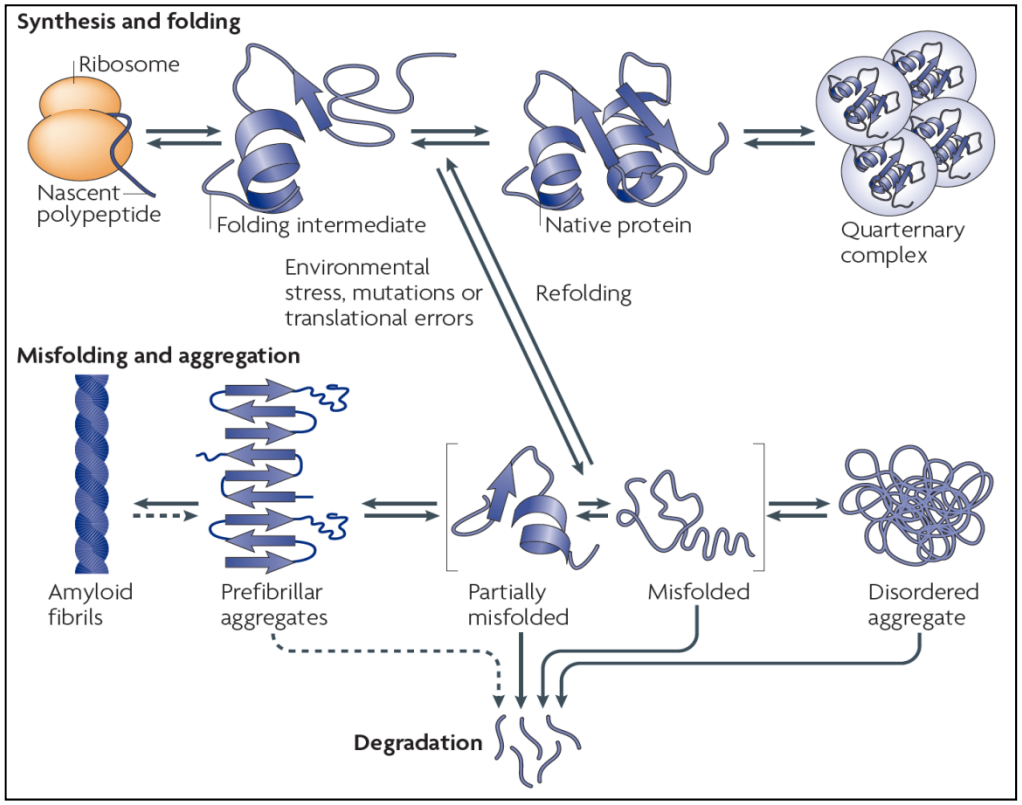

Fig. 1: A protein folds through different intermediates to its native, three-dimensional structure. Proteotoxic stresses, mutations in the synthesized protein or translational errors can cause protein misfolding. Once present, misfolded intermediates can be refolded to the native state or be degraded by different cellular proteolysis systems to prevent the accumulation of misfolded proteins. Once the quality-control network is overwhelmed - for example, through persisting stress conditions - aggregates can form. Aggregates can have varying degrees of structure, ranging from mostly unstructured to highly ordered β-sheet-rich amyloid fibrils. Disordered aggregates and intermediates during amyloid formation may be degraded. Arrows indicate a process that can include several single steps; dashed arrows indicate a process of minor significance Adopted from Tyedmers et al. (2010).

There are three different ways to deal with misfolded proteins and all of these are assisted by molecular chaperones (fig. 2).

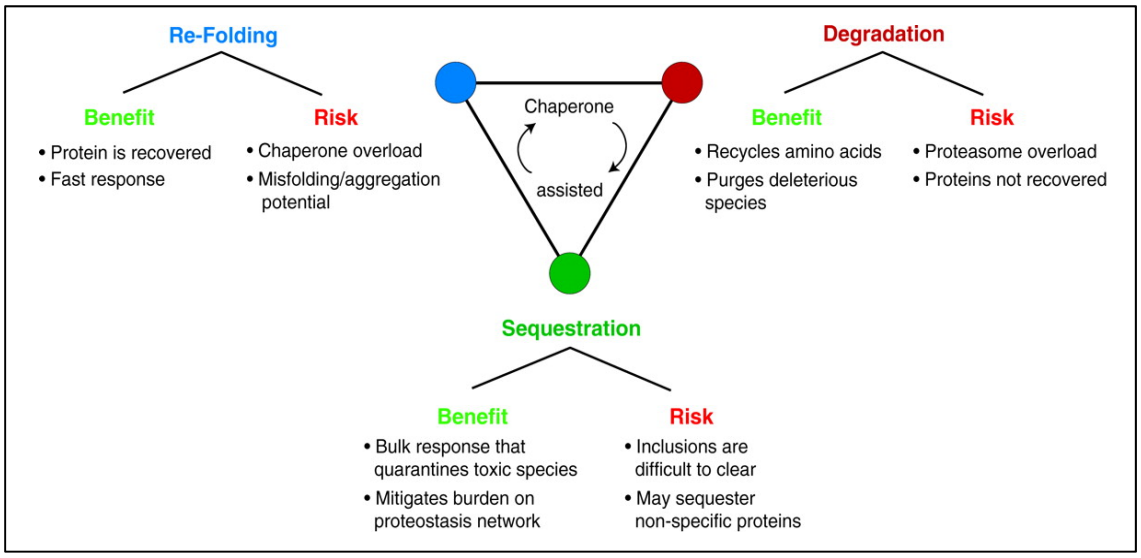

Fig. 2: Cellular strategies to maintain protein homeostasis. Cells have evolved distinct yet interconnected cellular strategies to maintain protein homeostasis. Each strategy presents advantages and drawbacks. Misfolded proteins can either be refolded, degraded, or delivered to distinct quality control compartments that sequester potentially deleterious species. These strategies are all assisted by molecular chaperones that ensure the system remains balanced. Failure of the cellular strategies can tip the protein homeostasis balance and lead to a decrease in cell viability. Adopted from Chen et al. (2011), ©2011 by Cold Spring Harbor Laboratory Press.

Molecular chaperones are members of a large class of proteins that is called 'Heat shock proteins' (Hsp). This name originates from their discovery in the 1960s, when their upregulation upon heat stress was first observed in *Drosophila melanogaster* (Ritossa, 1962; Ritossa, 1964). Hsps have been classified into six families according to their molecular masses: Hsp100s, Hsp90s, Hsp70s, Hsp60s, Hsp40s and small Heat shock proteins (Bakthisaran et al., 2015). The different families fulfill diverse functions from assistance of *de novo* protein folding, to prevention of protein aggregation, refolding and inclusion body disaggregation (Richter et al., 2010).

Molecular chaperones have to interact promiscuously with a large number of different substrate proteins to carry out their task. It is proposed that early unfolding intermediates are recognized and bound by their exposed hydrophobic patches independently of their exact amino acid composition and structure (Walter and Buchner, 2002). The purpose of this interaction is to avoid unspecific intermolecular interaction between unfolding proteins mediated by these hydrophobic regions. The different chaperone families use different approaches to fulfill their function and can be divided into two classes by their mechanism of action: 'Foldases' exhibit different affinities towards their substrates dependent on different

conformational states that are induced by ATP binding and hydrolysis. This leads to binding and release of substrate proteins which promotes the folding process and is performed by most of the molecular chaperones except the so called small Heat shock proteins (sHsps). These so called 'holdases' bind unfolding substrates and prevent aggregation in an ATP-independent manner (Eyles and Gierasch, 2010; Horwitz, 1992; Jakob et al., 1993).

1.2 Characteristics of small Heat shock proteins

sHsps are a family of molecular chaperones that are found in all kingdoms of life (fig. 3) and are named according to their low monomeric molecular mass of 12 - 43 kDa (Haslbeck et al., 2005). In their native state, most sHsps form large, dynamic oligomeric assemblies. (Narberhaus, 2002) Although sHsps are ubiquitously found, they are the least conserved heat-shock proteins. A comparison of 8700 sHsp sequences with an average length of 161 amino acids, and an average molecular mass of about 18 kDa showed no conserved amino acid in the whole sequence (Kriehuber et al., 2010). However, they all share a common domain organization, but only a low sequence homology (de Jong et al., 1993). The characteristic feature of sHsps is the conserved central α-crystallin domain (ACD) which has a length of about 90 - 100 residues and displays a sequence homology of 20 - 60 % depending on the phylogenetic relationship (de Jong et al., 1993; Kappe et al., 2010). This central domain is flanked by an N-terminal region (NTR) with highly variable amino acid sequence and a shorter C-terminal extension (CTR) that is moderately conserved in amino acid sequence and length (de Jong et al., 1998; Kriehuber et al., 2010). The NTR has an average length of 56 amino acids, but it varies from 25 residues in Hsp12 proteins from *C. elegans* to 247 in yeast Hsp42 (Haslbeck et al., 2005). In yeast Hsp26, a region of the NTR next to the ACD was defined as an additional domain called middle domain (Haslbeck et al., 2004). The CTR has an average length of only 10 residues and contains the highly conserved IXI motif, which is supposed to be important for inter-dimer connections (Basha et al., 2012; Haslbeck et al., 2005; Hilton et al., 2012).

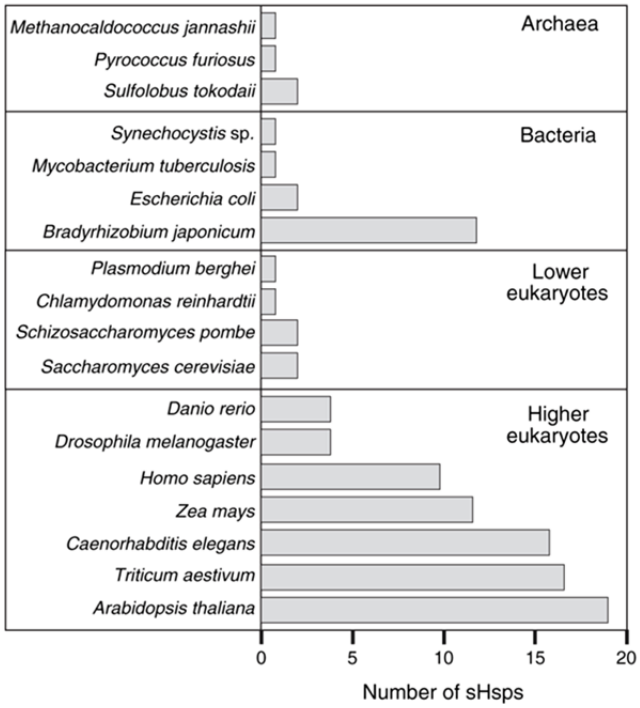

Fig. 3: Schematic overview of the number of representatives of the sHsp family in different organisms. In general, from bacteria to higher eukaroytes, a substantial increase in number of sHsps per organism is observed. Rhizobia are notable exception to these trends. Adopted from Haslbeck et al. (2005).

In mammals, at least ten sHsps have been identified and divided into two groups: Class I sHsps are characterized by ubiquitous expression and play a role in cell survival under several stress conditions, while Class II sHsp expression patterns are tissue-restricted. Therefore, Class II-sHsps are supposed to fulfill specific tasks for example in tissue development and cell differentiation (tab. 1).

Tab. 1: Nomenclature, distribution and functions of small heat shock proteins (see Taylor and Benjamin (2005) and references therein for details); adapted from Bakthisaran et al. (2015).

Name	Subunit MW (kDa)	pI	Tissue distribution	Stress-inducibility	Class	Function
Hsp27 (HspB1)	22.8	6.4	Ubiquitous, high levels in heart, striated and smooth muscles	+	I	Chaperone activity, stabilization of cytoskeleton, anti-apoptotic and anti-oxidant function
HspB2 (MKBP)	20.2	4.8	Heart, skeletal and smooth muscle	-	II	Chaperones DMPK and enhances its kinase activity. Target protein-dependent chaperone activity, myofibrillar integrity, anti-apoptotic function, mitochondrial energetic, anti-apoptotic

Name	Subunit MW (kDa)	pI	Tissue distribution	Stress-inducibility	Class	Function
HspB3	17.0	5.9	Heart, brain, skeletal and smooth muscle	-	II	Target protein-dependent chaperone activity, Maintaining myofibrillar integrity
αA-crystallin (HspB4)	19.9	6.2	Abundant in eye lens. skeletal muscle, liver, spleen, adipose tissue (low level)	-	II	Chaperone activity, genomic stability, eye lens refractive index
αB-crystallin (HspB5)	20.2	7.4	Ubiquitous, abundant in eye lens. High levels in heart and muscle	+	I	Chaperone activity, stabilization of cytoskeletal and nucleoskeletal matrix, cell cycle, cardioprotection, eye lens refractive index, regulation of muscle differentiation, anti-apoptoticfunction
Hsp20 (HspB6)	16.8	6.4	Ubiquitous, abundant in muscle -	-	I	Smooth muscle relaxation, cardioprotection, chaperone activity, anti-apoptotic
HspB7	18.6	6.5	Heart and skeletal muscle. Adipose tissue (low level)	-	II	Chaperone activity, maintaining myofibrillar integrity,
Hsp22 (HspB8)	21.6	4.7	ubiquitous	+ (cell type dependent)	I	Chaperone activity, induction of autophagy
HspB9	17.5	9.0	Testis	-	II	Role in cancer/testis antigen
HspB10	28.3	8.4	Testis	-	II	Elastic cytoskeletal structure

1.3 sHsp functions in the cell - more than just sponges

As mentioned above, sHsps are known to be a first line of stress defense by binding unfolding proteins promiscuously und thereby preventing there accumulation in cytotoxic protein aggregates. The complexes of sHps and diverse substrate proteins are putatively stable and keep the substrate in a refolding-competent state. However, to refold the substrate proteins, ATP-dependent foldases are necessary that cooperate with the sHsp-machinery and clear the occupied sHsps so they can resume their task (fig. 4) (Ehrnsperger et al., 1997; Haslbeck and Vierling, 2015; Lee et al., 1997).

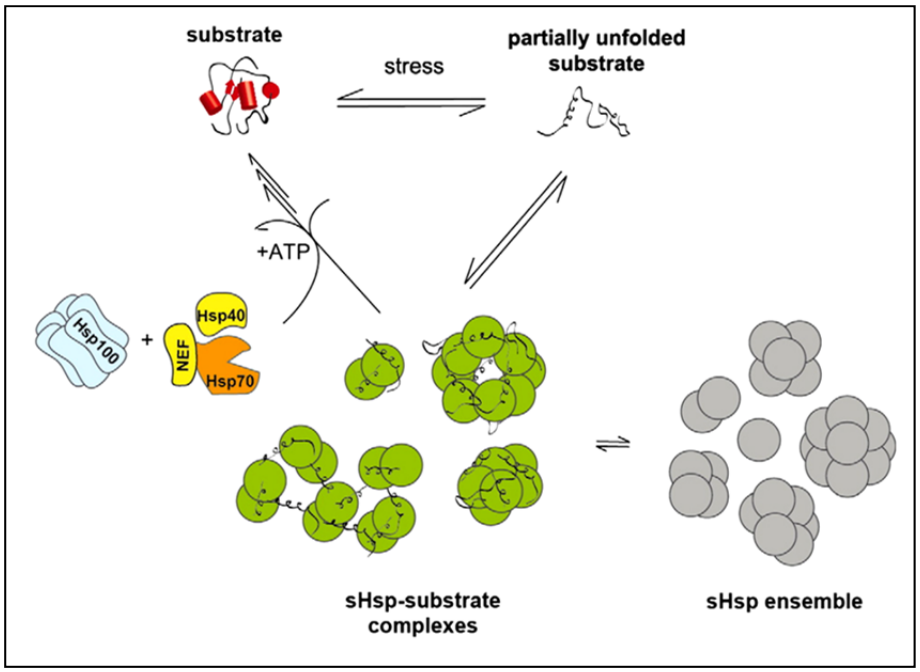

Fig. 4: Model for the chaperone function of sHsps. Under stress conditions when substrate proteins are destabilized and begin to unfold, sHsps bind these partially unfolded substrates in an energy-independent manner and keep them in a folding-competent state. The physiologic ensemble of sHsp oligomers (gray) are activated (green) by a shift to a higher content of smaller species (often dimers). The substrate is stabilized by this activated ensemble of sHsps (green) and may reactivate spontaneously or is captured in stable sHsp/substrate complexes (of still enigmatic organization). Bound substrates are subsequently refolded by the ATP-dependent Hsp70 chaperone system (composed of Hsp70, Hsp40 and a nucleotide exchange factor, NEF) and may involve the Hsp100/ClpB chaperone system in cells and cellular compartments where it is found; adopted from Haslbeck and Vierling (2015) with permission of Elsevier.

Yet, refolding is not the only possible fate of damaged proteins. The ubiquitin-proteasome system is also an important player in the cell protection system being responsible for degradation of misfolded proteins. Coordination between refolding and degradation is essential for a functional proteostasis system, although it is still not clear how it is regulated in detail. This role is supposed to be taken over by sHsps that are known to directly and indirectly interact with the proteasome or were found to be part of ubiquitin ligase complexes (Lanneau et al., 2010). To describe the interactions of sHsps and all other proteins in the cell under normal and under stress conditions, a model called ‘Dynamic partitioning hypothesis’ was suggested. It describes two types of interactions: Type I interactions are reversible low affinity interactions with all proteins in the cell to prevent further unfolding of early-unfolding intermediates or to fine-tune activity of specific proteins. Type II-interactions with higher affinity result in the substrate complexes described above (fig. 5) (Bakthisaran et al., 2015).

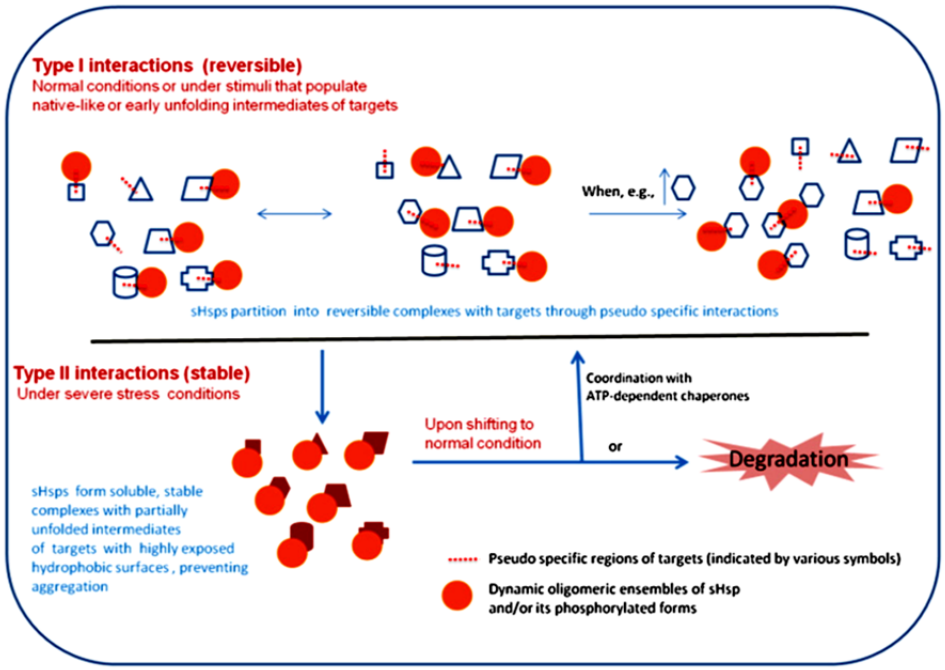

Fig. 5: Schematic representation of the 'Dynamic partitioning hypothesis' from the promiscuous interactions and pleiotropic functions of sHsps; adopted from Bakthisaran et al. (2015).

Besides prevention of aggregation and assistance of degradation of damaged proteins, sHsps in human cells interact with all three main components of the cytoskeleton. Hsp27, αB-crystallin and Hsp20 interact with actin. Hsp20 interacts with the actin-crosslinking protein actinin (Tessier et al., 2003), Hsp27 interacts with Keratin (Kayser et al., 2013) αB-crystallin associates with intermediate filaments like vimentin and desmin (Nicholl and Quinlan, 1994; Song et al., 2008). Through these interactions, sHsps regulate cytoskeleton assembly and disassembly, can prevent depolymerisation or the aggregation of cytoskeleton components under stress conditions. Furthermore, sHsps assist filament-filament interaction (Garrido et al., 2012; Perng et al., 1999a). To fulfill these functions, phosphorylation seems to be essential. Selective phosphorylation at Ser59 through the p38MAPKAP2-pathway triggers αB-crystallin to prevent microtubules and actin microfilaments from depolymerisation in the presence of disorganizing substances (Launay et al., 2006). Mutations in αB-crystallin that impair protection of intermediate filaments lead to desmin-related cardio- and neuro-myopathies such as Alexander's disease (Hagemann et al., 2009; Vicart et al., 1998).

Furthermore, sHsps were found to play an important role in cell differentiation and can prevent apoptosis-induced cell death, autophagy and necrosis. Due to the diverse essential functions of sHsp, malfunctions often lead to severe diseases like neurodegenerative diseases, myopathies and cataracts (Acunzo et al., 2012; Balch et al., 2008). sHsps are reported to be

strongly upregulated in some forms of cancer, making it an interesting therapeutic target. In these fields extensive research is performed and the findings are too broad to be summarized here sufficiently. Hence, in the following sections, some examples of the role of α-crystallin are described in more detail.

1.4 α-crystallin - one of the best characterized sHsps and still puzzling

α-crystallin was extensively studied during the last 35 years and plenty of literature exists about its structural organization and function *in vitro* and *in vivo*. Yet, its mechanism of function is still not even close to being elucidated.

The two α-crystallin isoforms αA- and αB- crystallin share about 60 % sequence identity. (Bloemendal and de Jong, 1991) While αA-crystallin is almost exclusively found in the eye lens with only minor traces in other tissues (Srinivasan et al., 1992), αB-crystallin is ubiquitously expressed in all tissues with the highest abundance in brain, heart and skeleton muscles (Iwaki et al., 1990). In rodents and some other mammals but not in humans, an alternative splicing product of αA-crystallin can be found named αA_{ins}-crystallin that exhibits an insertion of 23 amino acids at the end of the NTR (van Dijk et al., 2001).

1.4.1 Domain architecture of α-crystallin

α-crystallin as one of the most prominent members of the sHsp family shows the typical domain organization (fig. 6) described in 1.2. The monomeric subunit form large, polydisperse assemblies that show a hiercharchical architecture (Braun et al., 2011; Jehle et al., 2011). The structures of the ACDs of both isoforms are well characterized by NMR and X-ray crystallography and consist of β-sheets arranged in an immunoglobulin-like fold (Bork et al., 1994). The ACDs are only able to form dimers and are the basic building block for higher order oligomers (Bagneris et al., 2009; Jehle et al., 2009; Laganowsky et al., 2010). The intra-dimer connection is mediated by the β6- and β7-strands like is all mammalian ACDs and in contrast to metazoan ACD, where the β6-stands are swapped between the neighboring monomeric subunits (Haslbeck et al., 2016).

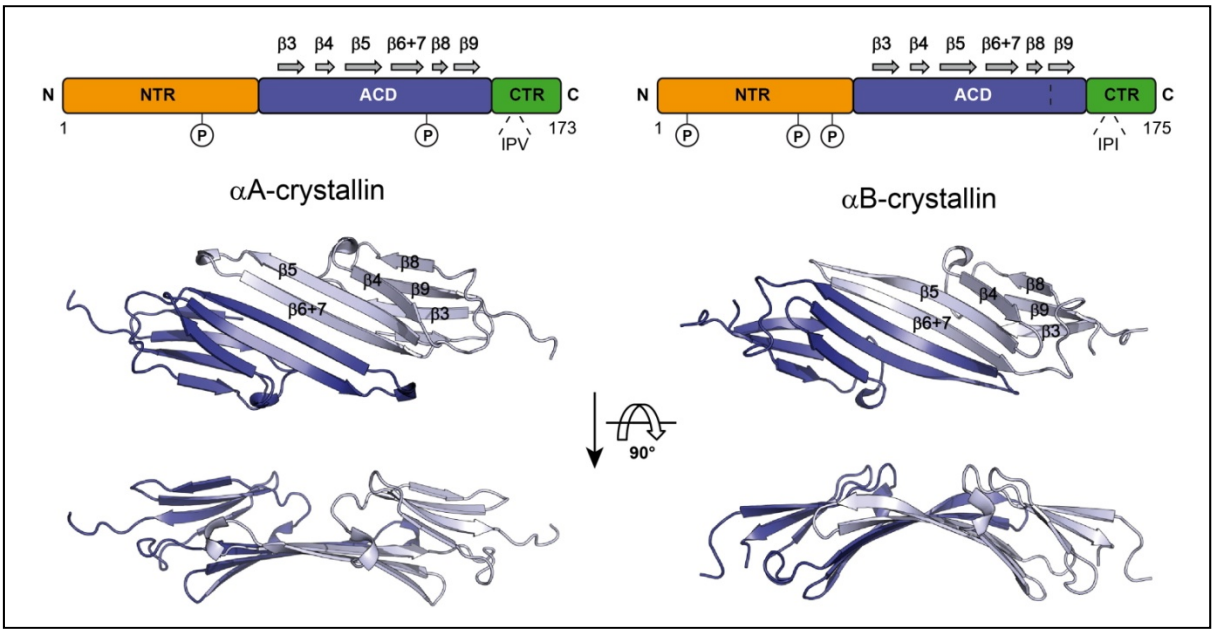

Fig. 6: Domain organization of α-crystallins. Upper panels: domain organization of αA (left panel) and αB (right panel). N-terminal region (NTR) (orange), α-crystallin domain (ACD) (blue), C-terminal region (CTR) (green).The conserved IXI motifs and the major phosphorylation sites (Ser19, Ser45, and Ser59 for αB and Ser45 and S122 for αA) are indicated. Lower panels, structures of the respective ACD-dimers (αB; solid state NMR, PDB ID: 2KLR and αA; X-ray, PDB ID: 3L1F) Adopted from Haslbeck et al. (2016) with permission of Elsevier.

The rather short C-terminal region contains the conserved IXI-motif at position 159-161 in both cases and is responsible for inter-dimer connections to build up lower-order oligomeric assemblies, but is at the same time supposed to be responsible for its polydispersity (Delbecq and Klevit, 2013). NMR-studies showed that the polar CTR is solvent-exposed and mainly unstructured like synthesized peptides of the same sequence (Carver et al., 1999; Treweek et al., 2010). These properties render the CTR especially important for the extraordinarily high solubility of α-crystallin, but at the same time susceptible to proteolytic cleavage (Ghosh et al., 2006; Siezen and Hoenders, 1979).

The N-terminal region is about 65 residues long and besides some predicted secondary structure motifs also highly flexible and unstructured. In contrast to the CTR, it is very hydrophobic and is essential for formation of higher-order oligomers. It has a large influence on subunit exchange dynamics and oligomer ensembles (Haslbeck et al., 2016). Studies on N-terminal deletion variants of α-crystallin showed that formation of higher order oligomers is inhibited without the NTR (Kundu et al., 2007).

Exchanging NTR of different sHsps completely changes their quaternary structure and chaperone activity (Eifert et al., 2005). Already short insertions have a big influence on sHsp

behavior as shown for a 14 amino acid peptide that was inserted between NTR and ACD of Hsp16.5 from *Methanocaldococcus jannaschii* (McHaourab et al., 2012).

This and the fact, that NTRs are highly variable between different sHsps qualifies this domain as an ideal point for regulation of activity and selectivity. In the case of αB-crystallin, regulation is accomplished by phosphorylation in the NTR (Peschek et al., 2013). One of the two major phosphorylation sites of αA-crystallin is also found within this region (Lund et al., 1996; Miesbauer et al., 1994).

1.4.2 The pseudo-atomic model of human αB-crystallin

Although studied for a long time, no high-resolution structure could be solved for αA-crystallin so far. This is presumably due to the even higher polydispersity of homo-oligomer distributions compared to αB. Studies on truncated versions of αA-crystallin of different organisms and negative stain EM-data on full-length homo-oligomers of αA suggest the NTR as the necessary link within the multimeric subunits. In contrast to αB-crystallin, tetrameric building blocks were reported (Laganowsky and Eisenberg, 2010). The presence of one or two cysteine residues is assumed to play an important role for structural heterogeneity and for potential functions in the eye lens, but this is subject of ongoing studies (Haslbeck et al., 2016).

For αB-crystallin, the existing 3D-models could be greatly improved in 2011, when two high-resolution models of a 24-mer were published. Based on the 24-mer-architecture, models of oligomers with a different numbers of subunits could be obtained as well. In fig. 7 the evolution of the 3D-models is shown. Starting from first negative stain electron micrographs of bovine lens α-crystallin (Koretz and Augusteyn, 1988), data from X-ray crystallography, cryo-EM, solution and solid state NMR, and SAXS were combined resulting in the two currently existing pseudo-atomic models, that were also supported by crosslinking - mass spectrometry experiments (Braun et al., 2011; Jehle et al., 2011).

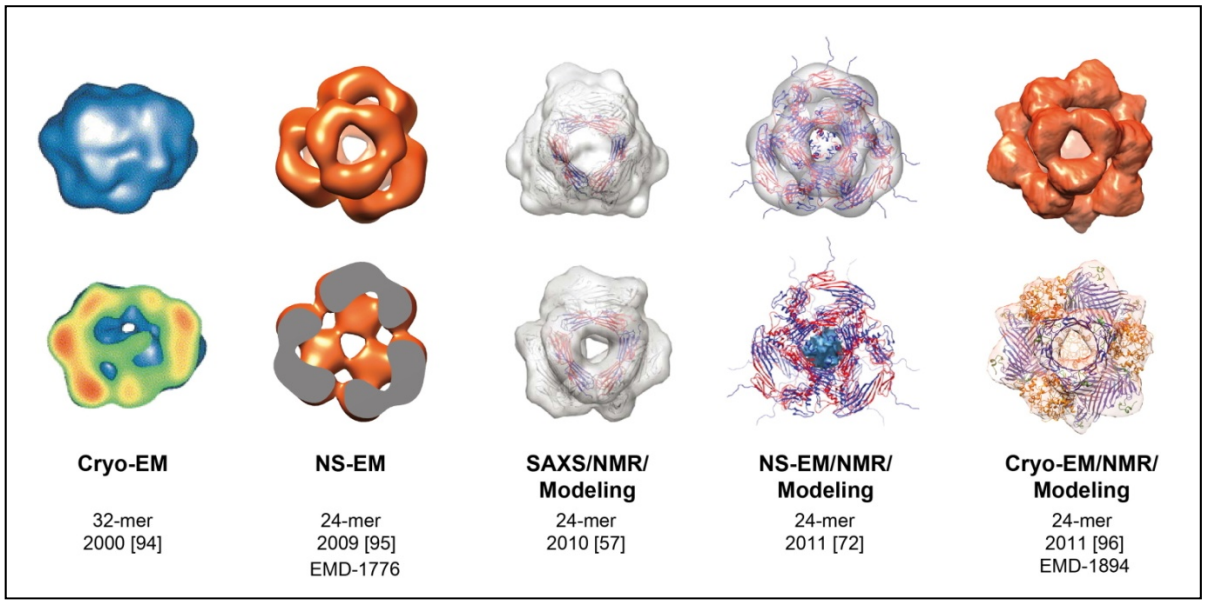

Fig. 7: Evolution of structural models of αB. αB oligomer models shown according to their publication date from left to right. Earlier studies by cryo-EM recognizing the structural variability αB oligomers were complemented throughout the last decade by hybrid approaches that combined structural data from SAXS, NS- and cryo-EM, NMR, X-ray crystallography and structural modeling which finally led to a pseudo-atomic, 3D-model of αB. The main methods employed, number of subunits within the 3D reconstruction, references and EMDataBank deposition IDs (if available) are given below the respective 3D model. Adopted from Haslbeck et al. (2016) with permission of Elsevier.

Although in both models the NTR is supposed to be the key feature for higher oligomer formation, the striking difference between the two models is the arrangement of the NTR. While in the Jehle model the NTRs are located in the center of the oligomer (Jehle et al., 2011), in the Braun model the NTRs are surface-exposed and located at the three-fold symmetry axes. In both models, the NTRs are spatially close. This was confirmed by crosslinking-ms experiments and by the fact that cysteine residues introduced in this region are able to form disulfide bonds with neighbouring NTRs (Peschek, 2012). A fact that supports the Braun model is the susceptibility of the NTRs for posttranslational modifications. The three major phosphorylation sites in αB-crystallin are the N-terminal serine residues at position 19, 45 and 59 (Peschek et al., 2013). Furthermore, the NTRs represent putative substrate binding sites that are protected from proteolysis after substrate binding *in vitro* (Aquilina and Watt, 2007). For the mentioned reasons, the Braun model will be used as basis for discussion in this work (Braun et al., 2011).

As mentioned before, the first level of interaction within the 24-mer is the formation of dimers at the β7-interface of the ACD. Two types of dimer conformations were assumed that differ in the orientations of their N- and C-terminal regions. Three of these primary building blocks form hexamers as a second level of hierarchy via binding of the C-terminal I-P-I motif

of one subunit to the hydrophobic groove formed by the β4- and β8-strands of a different dimer.

The third level of hierarchy is the assembly of 24-mers by the hexameric building blocks. These intra-hexamer connections are established by interactions of six NTRs at each of the four three-fold symmetry axes on the surface (Braun et al., 2011).

1.4.3 Mutations in α-crystallin and their impact on structure and function

A number of mutations in α-crystallin were characterized concerning structural and functional impact *in vitro*. Some of these variants were found to be related to different diseases *in vivo* such as neurodegenerative, associated to cataract, myopathies and neuropathies, others were created to investigate the role of distinct amino acids in α-crystallin. An overview of the major variants of αA- and αB-crystallin is shown in tab. 2.

Tab. 2: Overview of variants of α-crystallin analyzed *in vitro* and *in vivo*.

mutation	observed effects	reference
αB R11H	nearly WT-like molecular mass and thermal stability, decreased surface hydrophobicity, enhanced chaperone-like activity, induction of apoptosis, autosomal dominant nuclear congenital cataract	(Chen et al., 2009; Chen et al., 2010)
αB P20S	WT-like molecular mass, impaired chaperone function, decreased subunit exchange kinetics, autosomal dominant posterior polar congenital cataract, abnormal nuclear localization, unusual ability to trigger apoptosis	(Li et al., 2008)
αA R21Q	autosomal dominant congenital cataract	(Laurie et al., 2013)
αA R49C	autosomal dominant hereditary cataracts, small eye phenotype and severe cataracts at birth in homozygosity, increased apoptosis rates	(Xi et al., 2008)
αA R54C	recessive whole cataracts, loss of characteristic cellular features, disruption of subcellular structures (actin filaments, mitochondria)	(Xia et al., 2006)
αB R56W	recessive, variable lens opacities	(Khan et al., 2010)
αA F71L	no significant changes in molecular mass, secondary and tertiary structure as well as hydrophobicity at moderate temperatures; exhibits decreased thermal stability, structural changes after pre-heating; partial loss of chaperone function (substrate dependent)	(Bhagyalaxmi et al., 2009; Validandi et al., 2011)
αA G98R	decreased thermal and chemical stability, folding defects, bacterial expression as inclusion bodies, aggregation-prone after refolding leading to formation of large oligomers lacking chaperone function; cortical cataract in teenage-age progressing to total opacity (presenile autosomal dominant cataract)	(Clark et al., 2012; Raju et al., 2011; Santhiya et al., 2006; Singh et al., 2006)

mutation	observed effects	reference
αA N101D, N123D αB N78D, N146D	deamination-mimicking mutants; reduced levels of chaperone activity, alterations in secondary and tertiary structures, altered surface hydrophobicity, formation of larger homo- and hetero- aggregates	(Asomugha et al., 2011; Gupta and Srivastava, 2004)
αA R116H	increased surface hydrophobicity, impaired chaperone function, autosomal dominant inherited congenital cataract	(Gu et al., 2008; Pang et al., 2010)
αA R116C	increased oligomeric size, secondary and tertiary structural changes, decreased surface hydrophobicity, decreased chaperone function, impaired binding to actin autosomal dominant congenital cataract	(Brown et al., 2007; Shroff et al., 2000)
αA Y118D	higher molecular mass, changes in the secondary structures, increased chaperone activity, reduction of Y118D mutant protein levels in heterozygous mutant lenses, decreased αA and αB transcripts in the homozygous mutant lenses increased dominant nuclear cataract	(Huang et al., 2009; Xia et al., 2006)
R120G	reduction or loss of chaperone activity, co-aggregation with unfolding proteins, decreased beta-sheet content, closure of a groove at dimer interface, increased molecular weight, desmin-related myopathy, cataract; inhibition of autophagy reversal of cataract through stabilization of the closed groove by sterol compounds	(Bova et al., 1999; Clark et al., 2011; Makley et al., 2015; Pattison et al., 2011)

Despite the thorough analyses of the numerous described modifications in tab. 2, the detailed mechanism of α-crystallin function could not be elucidated sufficiently, so far.

1.4.4 Substrate recognition sites - the molecular basis for chaperone function

The amino acids or the respective sequence patches in α-crystallins as well as in the diverse substrate proteins which are involved in sHsp - substrate interactions are still largely unknown. To elucidate binding motifs, peptide arrays were performed to screen binding of *Bradyrhizobium japonicum* sHsps HspB and HspH to peptides derived from their own sequences and to peptides derived from the sequence of model substrate Citrate synthase (CS) (Lentze and Narberhaus, 2004). Single peptides could be determined as binding sites in the substrates. Another approach using crosslinking/ms techniques resulted in a different binding site in CS for Hsp21 (Ahrman et al., 2007b). Unfortunately, no universal binding motif could

be discovered to elucidate the determinants of substrate binding so far, neither in α-crystallin nor in the corresponding substrates.

According to several studies summarized below, all three sequence parts of αA and αB seem to be involved in substrate recognition and binding (Haslbeck et al., 2016).

Although it was shown that the isolated ACD is not able to prevent aggregation of some model substrates (Kundu et al., 2007), it was demonstrated that it is able to interact with certain model substrates like the amyloid forming Aβ-peptide (Mainz et al., 2015). Even substrate binding sequences within the ACD were assigned and synthesized peptides consisting of these amino acid sequences were shown to exhibit chaperone activity comparable to full-length proteins *in vitro* (Banerjee et al., 2015; Bhattacharyya et al., 2006; Sharma et al., 1997; Sharma et al., 2000).

Both terminal regions in α-crystallin are also promising candidates for substrate interaction sites: Deletion of either of them diminishes chaperone function. Exchanging the termini between different sHsps completely changes their behavior. Especially the rather unstructured NTR has a high content of hydrophobic amino acids that could be involved in binding of hydrophobic substrate patches. Some of these residues are highly conserved which could hint to important roles as e.g. the Phe-residues in the conserved stretch SRLFDQFF between position 20 and 30 (Ghosh et al., 2006).

The NTR as binding site for substrates is also supported by protection of this region from proteolytic digestion by bound substrate (Aquilina and Watt, 2007). Insertion of the photoactivatable crosslinker Bpa in 32 positions in PsHsp18.1, a well characterized plant sHsp, showed highest cross-linking rates in the NTR, but not a universal binding site for different substrates (Jaya et al., 2009).

The counter-parts in potential interaction partners are also not understood sufficiently although several studies were performed to determine the characteristic features in substrate proteins that mark them for binding to sHsps using mass spectrometry, cross-linking and peptide arrays (Cheng et al., 2008; Lentze and Narberhaus, 2004; Santhoshkumar and Sharma, 2002).

The mentioned studies were only a few examples of the numerous studies that were conducted to contribute to the understanding of α-crystallin. Yet, the mechanism of function that is important to elucidate the contribution of α-crystallin to the huge cellular quality control system could not be clarified and is still an important topic of ongoing research.

1.5 Crystallins and the vertebrate eye lens

Many studies were published investigating the behavior of α-crystallin in a non-native environment *in vitro* (Haslbeck et al., 2016). Since the structures and the function of these 'polydisperse all-rounders' are highly sensitive to any changes of the experimental, it is of great interest to have a closer look at α-crystallin under physiological conditions. A special tissue, where - in contrast to other tissues - both isoforms αA and αB are main actors and can be analyzed under physiological conditions is the vertebrate eye lens, which is described in more detail in the following sections.

1.5.1 The vertebrate eye lens and its development

The eye lens is essential to focus incoming light on the retina. The unique morphology of the lens is optimized to fulfill this task. It consists of epithelial cells, which originate from the anterior lens vesicle, of primary fiber cells, that develop from the posterior lens vesicle cells and of secondary fiber cells that evolve later in lens development from epithelial cells (fig. 8). Secondary fiber cells continue to be formed throughout life.

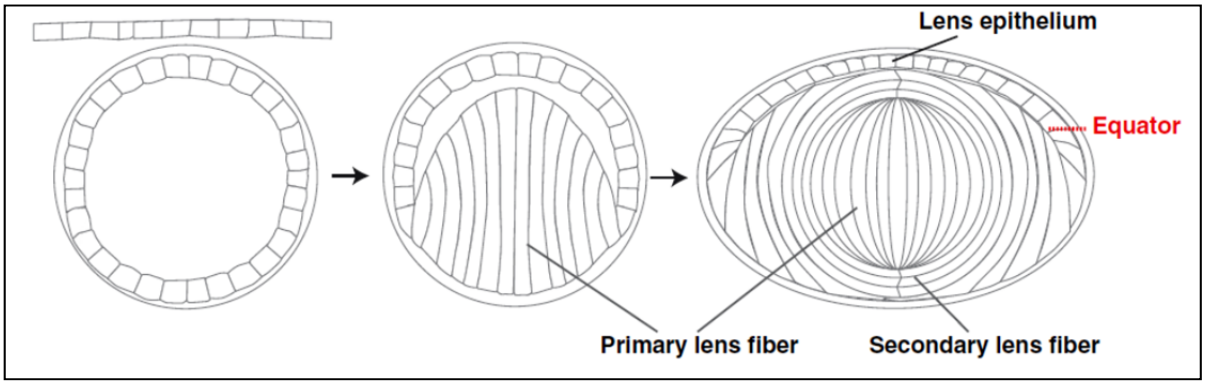

Fig. 8: Lens development in mammals. (Left) The lens placode detaches from surface ectoderm and forms the lens vesicle. (Middle) Cells in the posterior half of the lens vesicle elongate and differentiate into primary fiber cells, which form the lens fiber core. On the other hand, cells in the anterior half maintain a proliferative state and form mono-layered lens epithelium. (Right) Lens epithelial cells differentiate into lens fiber cells at the peripheral margin of the lens epithelium, which is called the equator. Newly differentiating lens fiber cells elongate to become secondary lens fibers and cover the old lens fiber core. Adopted from Mochizuki and Masai (2014) with permission of Wiley and Sons.

In the mature lens, an avascular cellular structure of hexagonally packed, highly elongated fiber cells is arranged in concentric circles, with the oldest cells in the center and the youngest on the outside (Bloemendal et al., 2004). The characteristic shape of the terminally

differentiated fiber cells is determined and maintained by an extensive, lens-specific cytoskeleton. Besides known cytoskeleton components like actin and vimentin, it is built up from the so called beaded filaments 1 and 2 that consist of the intermediate filament-like proteins Phakinin and Filensin as well as α-crystallin. It is formed during fiber cell differentiation.

Besides cell elongation and cytoskeleton rearrangements, another important concomitant of fiber cell differentiation is the elimination of all scattering cell organelles like nuclei, mitochondria, ribosomes and proteasomes. This results in a gradient of decreasing metabolism like protein synthesis and degradation rates from the outer cortex to the core of the lens resulting in an organelle free zone in the center of the mature lens (fig. 9). The very limited remaining proteostasis options require exceptionally high protein stabilities to guarantee a proper lens refractive index. (Bassnett, 2009; Clark et al., 2012)

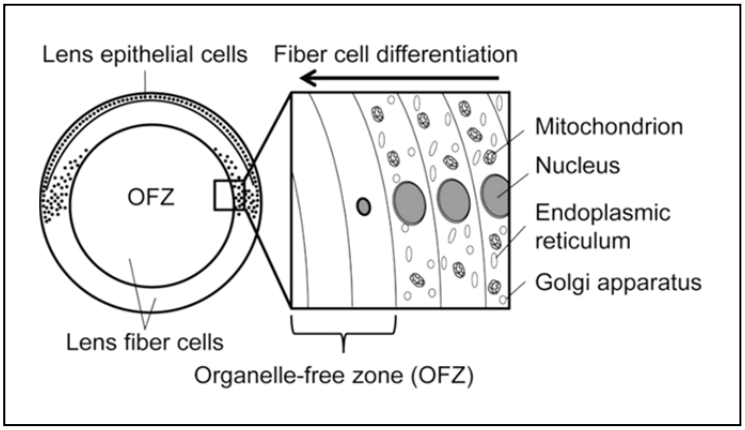

Fig. 9: The lens and programmed organelle degradation. A model of lens epithelial to fiber cell differentiation and organelle degradation. Differentiating secondary fiber cells around the organelle-free zone (OFZ) are shown (right panel). The nucleus, mitochondrion, endoplasmic reticulum, and Golgi apparatus are degraded almost simultaneously. Taken from (Morishita and Mizushima, 2015) with permission of Wiley and Sons.

1.5.2 The lens cytoplasm and its proteins – the crystallin family

To assure good vision, a gradient of increasing refractive index from cortex to core is required in the lens. In addition to the regular alignment of fiber cells, this is realized by different mixtures of the three members of the crystallin family at exceptionally high protein concentrations ranging from 150 mg/mL up to 1 g/mL with short-range spatial orders, but at the same time avoiding absorbance or light scattering properties (Bloemendal et al., 2004; Delaye and Tardieu, 1983). Besides α-crystallin, that was described in detail above, the

β/γ-crystallin family plays an important role in the lens. These proteins do not exhibit chaperone activity and is supposed to mainly contribute as structural proteins in the lens.

Together, the crystallins constitute about 90 % of the water soluble proteins (Horwitz, 2003). In mammals, α-crystallin constitutes 20% (rodents) - 40 % (humans) of the total lens proteins. There are six genes that express β-crystallins (β A1/A3 β A2, βA4, β B1, β B2, β B3 and seven different γ-crystallin genes (γA-F and γS, former βS which was reclassified) (Bloemendal et al., 2004). Originally thought to be lens specific, later studies showed expression of β- and γ-crystallin in other tissues outside the lens, but there is little information on their function. (Graw, 2009a; Wang et al., 2004)

Although all of the crystallins have similar monomeric molecular masses, the structural characteristics of β/γ-crystallins differ significantly from α-crystallin. While the latter shows a sHsp-domain architecture and forms high molecular mass oligomers as described above, β- and γ-crystallins are built up of four Greek key motifs that are organized in two domains (Richardson, 1977). β-crystallins form homo- and hetero-dimers as well as low-order oligomers with up to six subunits, whereas γ-crystallins only exist in their monomeric form. In contrast to α-crystallin, several high-resolution X-ray structures of β- and γ-crystallins exist that provided detailed insights into their molecular constitution (Slingsby and Clout, 1999; Smith et al., 2007). Representative crystal structures of βA4- and γD-crystallin are shown in fig. 10.

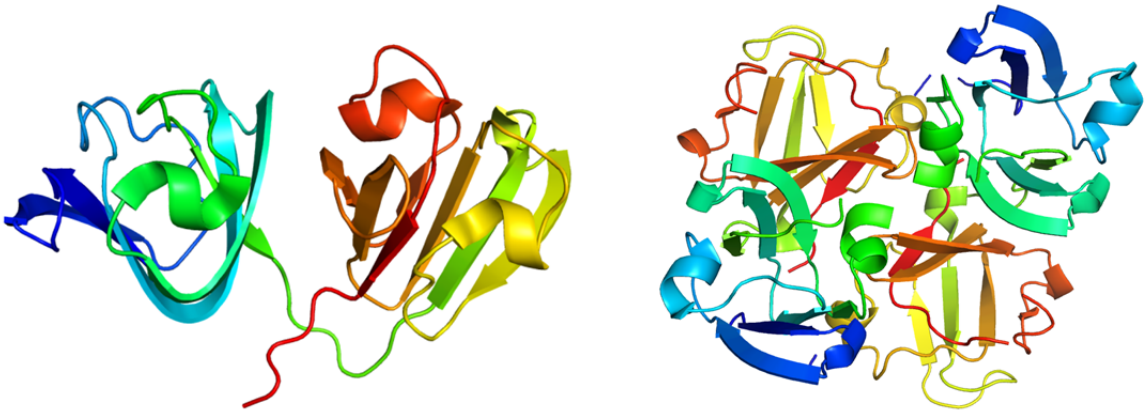

Fig. 10: Crystal structures of monomeric human γD-crystallin (pdb 1HK0) (left) and dimeric βA4-crystallin (pdb 3LWK) (right). Monomeric subunits are rainbow-colored from N- (blue) to C-terminus (red); **left:** γD-crystallin structure is built up of 4 greek key motifs organized in two domains that are connected by a liker region. **Right:** In βA4, two monomeric subunits form a dimeric assembly.

1.5.3 Functions of α-crystallin in the lens

In 1992 Horwitz showed that α-crystallin, being a member of the sHsp family, can act as a molecular chaperone *in vitro* using model substrates like Alcohol dehydrogenase, but also purified lens β- and γ-crystallins as well as whole lens lysates. He showed decreased light scattering in the presence of α-crystallin under heat stress conditions up to 60°C or using chemically denatured substrate proteins. Although these experimental conditions didn't exactly reflect physiological stress conditions, α-crystallin was and still is assumed to be the main reason for the life-long lens transparency (Horwitz, 1992). In the last 25 years, extensive studies were conducted investigating the chaperone function *in vitro* using different model substrate, but also lens proteins. It was shown, that α-crystallin prevents aggregation of substrates that were exposed to variety of stress conditions like heat, UV-light or oxidative stress (Carver et al., 2002; Haslbeck et al., 2016; Santhoshkumar and Sharma, 2001). The chaperone activity of αB-crystallin was shown to be increased by post-translational modifications, especially phosphorylation. This was confirmed by many *in vitro* studies that mimicked phosphorlyation by introduction of Asp or Glu residues (Ahmad et al., 2008; Ecroyd et al., 2007). It was even possible to create a detailed model of the activated αB-crystallin species (Peschek et al., 2013).

In the recent years, many more functions have emerged for α-crystallin in the lens.

It was found to interact with different components of the cytoskeleton. It was shown, that αB-crystallin can prevent aggregation of tubulin and desmin (Arai and Atomi, 1997; Perng et al., 1999b), but it also binds and stabilizes F-actin, intermediate filaments and microtubules and prevents depolymerization (Fujita et al., 2004; Perng et al., 1999a; Singh et al., 2007). The participation of α-crystallin in the fiber cell-specific beaded filaments was already mentioned. This fact renders α-crystallin highly important for fiber cell development since these elongated cells are dependent on a functional cytoskeleton for cell stabilization and cell arrangement in the lens.

Anti-apoptotic functions were also discussed for αB-crystallin and other sHsps (Acunzo et al., 2012; Arrigo et al., 2002; Kamradt et al., 2001) It was found that overexpression of αB-crystallin in stressed cells impedes maturation of caspase-3, a central protease involved in apoptosis (Kamradt et al., 2001; Kamradt et al., 2005). Studies in lens epithelial cells support these findings (Andley et al., 2000). Another possible mechanism to prevent apoptosis was proposed through binding to proapoptotic proteins like BAX or p53, which was demonstrated in several studies (Mao et al., 2004; Watanabe et al., 2009). Prevention of UVA-induced

apoptosis by both α-crystallin isoforms was also shown, demonstrating other mechanisms of αA and αB to prevent stress-induced cell death except the classical chaperone function (Liu et al., 2004).

The role in programmed cell death and its prevention is assumed to be highly relevant in lens development and maintenance. In the context of lens development, autophagy is discussed and is also topic of the latest research (Kannan et al., 2012; Morishita and Mizushima, 2015).

Regulation of proteasomal degradation (Boelens et al., 2001), anti-inflammatory effects (Masilamoni et al., 2005) and neuroprotective functions (Ousman et al., 2007) are further examples for the diverse tasks in the context of cell protection.

1.5.4 Cataract and crystallins

Estimated ~20 million cases of blindness worldwide are caused by opacities in the eye lens, that are known as cataract (Graw, 2009b). Cataracts are classified according to the time-point of appearance. Congenital cataracts are present at birth and are mostly a result of pathological changes that occur already during lens development (Graw, 2004). This type of cataract is mostly caused by mutation either in a member of the crystallins or in other lens proteins that are essential for proper lens development. Often it is accompanied by smaller lens sizes in adults or incomplete fiber cell differentiation or other abnormalities in lens morphology. In contrast to that, early onset cataracts usually appear in young individuals and are also often caused by mutations or by environmental influences. Age-related cataract is the most common type of cataract, which constitutes 90% of all cataract cases and is subdivided by the areas that are affected into nuclear, cortical and posterior subcortical cataract (Lang, 2014; Truscott and Friedrich, 2016). It is a consequence of changes in the lens that affect morphology or protein biochemistry. Increasing lens thickness and hardening of the nucleus complicate diffusion from the lens epithelial cell and the cortex to the OFZ to supply this region that lacks any kind of metabolism. Post-translational modifications like deamination, glycosylation, oxidation and phosphorylation as well as degradation leads to either loss-of-function of essential lens components or even aggregation of proteins that directly leads to opacification (Abdelkader et al., 2015).

All these described modifications affect α-, β- and γ-crystallins as well as other lens proteins and were studied intensively during the last years in animal models and in human lenses

(Lampi et al., 1998; Su et al., 2011). However, the complex interplay of all lens components in this very crowded environment is rather sensitive and still not completely understood.

The role of α-crystallin as a chaperone in the eye lens is also not sufficiently investigated. *In vitro* experiments using β- and γ-crystallins as substrates always lead to large, aggregation-prone substrate complexes and are usually performed under conditions far from physiological like at temperatures of 60°C. At room temperature no interactions were observed so far. Refolding of bound substrates by the Hsp70/40-machinery would only be possible in the outer metabolic-active regions, since in the inner fiber cell ATP-levels are decreased due to lack of mitochondria (Clark et al., 2012). Moreover, chaperoning β- and γ-crystallin during aging cannot be the only function in the lens since studies with knock-out mice demonstrated that double knock-out mice have significantly smaller lenses than wild type mice and fiber cell differentiation is severely disturbed (Boyle et al., 2003). The single αB-crystallin knock-out does not show a lens phenotype (Brady et al., 2001), but it has a decreased lifespan, which makes it impossible to study age-related cataract in these mice. The αA-crystallin knock-out mouse shows a cataract phenotype. It is characterized by proteins aggregates in the lens containing mainly αB-crystallin (Brady et al., 1997).

Recent studies showed a beneficial influence of sterol compounds on cataract development. Lens opacifications could be prevented or even reversed by application of sterol containing eye drops. This effect is limited to a certain number of sterols. Lanosterol - a precursor in the synthesis of cholesterol that is enriched in the eye lens - has been shown to prevent cataract formation while cholesterol does not have any impact on formation of light scattering aggregates (Zhao et al., 2015). In a different study, a high-throughput screening for sterol compounds that exhibit stabilizing effects on α-crystallin was performed. The resulting hits including lanosterol partially restored transparency in cataract models (Makley et al., 2015).

All in all, further studies need to clarify the underlying mechanisms of crystallin solubility in the lens. This is also the case for hereditary cataracts caused by destabilizing mutations since the underlying mechanisms are far less characterized and often affect lens development. Revealing the molecular basis would contribute a lot to the understanding of the exact mechanisms of lens development and support therapeutic approaches to cure crystallin-associated blindness.

1.6 Objectives

In this work three main aspects were addressed concerning the role of α-crystallin as a chaperone *in vitro* and its role in lens development and proteostasis.

In the first part, the determinants of the oligmeric architecture of α-crystallin, its dynamics and the correlation to its ability to prevent aggregation of thermo-sensitive model substrates were analyzed. As mentioned above, the molecular basis of the chaperone properties of α-crystallin could not be assigned to single amino acids or short stretches. Different functions were assigned to each of the three domains, but even this allocation of tasks is still under discussion. Therefore, a set of mutations within the NTR of αB-crystallin was created to be analyzed according to size, dynamics and activity.

In the second part of this thesis, the focus was on the bound model substrates. In the cell, a huge amount of proteins has to be protected by sHsps under different stress conditions, but without disturbing their function under normal conditions. Therefore, recognition motif is essential consisting either of distinct amino acid combinations or secondary structure motifs that are uniquely accessible during substrate unfolding. To shed light on these special recognition motifs in substrate proteins, peptide arrays were designed consisting of the sequences of the commonly used model substrates ADH, CS, insulin, MDH, lysozyme and p53. Binding of αB-crystallin to distinct sets of peptides was analyzed.

In the third part, the substrate interaction was analyzed in the context of the murine eye lens. In this context, murine αA- and αB-crystallin were purified and analyzed in *in vitro*-assays. To address the *in vivo*-function, the age-related changes in the composition of murine WT eye lens lysates were characterized and purified α-crystallin from these lenses was analyzed for bound substrates. Furthermore, lens lysates of mice bearing mutations in all three types of crystallins (α, β, and γ) were compared to WT lysates to contribute to the understanding of the role(s) of α-crystallin in the very special environment of the eye lens and its connection to cataract formation.

2. Material

2.1 Chemicals

2-Mercaptoethanol	Sigma
8-Anilino-1-naphthalenesulfonic acid (ANS)	Sigma
Acetic acid	Roth
Acrylamid/Bis solution 38:2 (40% w:v)	Serva
Agar Agar	Serva
Agarose	Serva
Ammonium persulfate (APS)	Roth
Alexa Fluor® 350 maleimide	Life technologies
Alexa Fluor® 488 maleimide	Life technologies
ATTO 488 NHS-Ester	Atto-tec
Bio-Rad Protein Assay (Bradford)	Bio-Rad
Coomassie Brilliant Blue R-250	Serva
Deoxynucleoside triphosphates (dNTPs)	Roche
Dimethyl sulfoxide (DMSO)	Sigma
Dithiothreitol (DTT)	Roth
Ethylenediaminetetraacetic acid disodium salt (EDTA)	Merck
Galactose	Merck
Glucose	Merck
Glycerol	Roth
Guanidinium chloride (GdnCl)	Sigma
Isopropyl β-D-1-thiogalaktopyranoside (IPTG)	Serva
Kanamycin sulfate	Roth
LB medium	Serva
Milk powder	Roth
Phenylmethanesulfonyl fluoride (PMSF)	Sigma
Protease inhibitor Mix G, HP	Serva
Sodium dodecylsulfate (SDS)	Serva
Stain G	Sigma
SYPRO® Orange	Thermo Fisher Scientific
TCEP	Pierce
TEMED	Roth
Tris	Roth

Tween-20	Merck
Urea	Merck
WesternBright ECL-Spray™	Advansta

2.2 Consumables

Amicon Ultra-15 Centrifugal Filter Units	EMDMillipore
Amicon Ultra-4 Centrifugal Filter Units	EMDMillipore
Ultracel Ultrafiltration disc 10 kDa NMWL ,76 mm and 44.5 mm	EMDMillipore
Dialysis membranes Spectra/Por (various MWCOs)	Spectrum Laboratories
Semi-micro cuvette, PS	Brand
UV-Cuvette micro, center heights: 8.5 mm	Brand
PCR tubes	BioRad Laboratories
Cellstar®, 15 and 50 mL	Greiner Bio One
Petri dishes, PS, 94 mm	Greiner Bio One
pH indicator	Merck
Reaction tubes, 0.5, 1.5 mL and 2 mL	Sarstedt

2.3 Oligonucleotides

α-crystallin primers:	
Maus_aA_fwd	CGATCCCATGGACGTCACCATTCAGCATCC
Maus_aA_rev	GATCGCGGCCGCCTAGGACGAGGGTGCAGAG
maA_V124E_fwd	CCGTCTGCCTTCCAATGAAGACCAGTCC
maA_V124E_rev	GGAGAGGGCGGACTGGTCTTCATTGGAAGG
Maus_aB_fwd	CGATCCCATGGACATCGCCATCCACCAC
Maus_aB_rev	GATCGCGGCCGCCTACTACTTCTTAGGGGCTG
aB_Δ20_fwd	GATCCCATGGCAAGCCGCCTCTTCGAC
aB_Δ26_fwd	GATCCCATGGCATTCTTCGGAGAGCACC

aB_Δ28_fwd	GATCCCATGGGAGAGCACCTGTTGG
aB_Δ40_fwd	GATCCCATGGCATCTACTTCCCTGAGTCC
aB_Δ51_fwd	GATCCCATGGCACCCTCCTTCCTGCG
aB_C-term_rev	GATCGCGGCCGCCTATTTCTTGGGGGCTG
aB_W9C_fwd	CATCGCCATCCACCACCCCTGCATCCGC
aB_W9C_rev	GAAAGGAAAGAAGGGGCGGCGGATGCAGGGGTG
aB_R11A_fwd	CCCCTGGATCGCCCGCCCCTTCTTTC
aB_R11A_rev	GAAAGAAGGGGCGGGCGATCCAGGGG
aB_R22Q_fwd	CACTCCCCCAGCCAGCTCTTCGACCAGTTC
aB_R22Q_rev	GAACTGGTCGAAGAGCTGGCTGGGGGAGTG
aB_F24A_fwd	CAGCCGCCTCGCCGACCAGTTCTTC
aB_F24A_rev	GAAGAACTGGTCGGCGAGGCGGCTG
aB_F24E_fwd	CCAGCCGCCTCGAGGACCAGTTCTTC
aB_F24E_rev	GAAGAACTGGTCCTCGAGGCGGCTGG
aB_F24P_fwd	CAGCCGCCTCCCTGACCAGTTCTTC
aB_F24P_rev	GAAGAACTGGTCAGGGAGGCGGCTG
aB_Q26A_fwd	CGCCTCTTCGACGCATTCTTCGGAGAGC
aB_Q26A_rev	GCTCTCCGAAGAATGCGTCGAAGAGGCG
aB_Q26P_fwd	CCGCCTCTTCGACCCTTTCTTCGGAGAGC
aB_Q26P_rev	GCTCTCCGAAGAAAGGGTCGAAGAGGCGG
aB_F27A_fwd	CCTCTTCGACCAGGCATTCGGAGAGCACC
aB_F27A_rev	GGTGCTCTCCGAATGCCTGGTCGAAGAGG
aB_F27E_fwd	CCTCTTCGACCAGGAGTTCGGAGAGCACC
aB_F27E_fwd	GGTGCTCTCCGAACTCCTGGTCGAAGAGG
aB_F27R_fwd	CTCTTCGACCAGCGTTTCGGAGAGCACCTG
aB_F27R_fwd	CAGGTGCTCTCCGAAACGCTGGTCGAAGAG
aB_F28A_fwd	CTCTTCGACCAGTTCGCAGGAGAGCACCTGTTG
aB_F28A_rev	CAACAGGTGCTCTCCTGCGAACTGGTCGAAGAG
aB_F28E_fwd	CTCTTCGACCAGTTCGAGGGAGAGCACCTGTTG

aB_F28E_rev	CAACAGGTGCTCTCCCTCGAACTGGTCGAAGAG
aB_F27,28A_fwd	CTCTTCGACCAGGCAGCAGGAGAGCACCTGTTG
aB_F27,28A_rev	CAACAGGTGCTCTCCTGCTGCCTGGTCGAAGAG
aB_F27,28E_fwd	CTCTTCGACCAGGAGGAAGGAGAGCACCTGTTG
aB_F27,28E_rev	CAACAGGTGCTCTCCTTCCTCCTGGTCGAAGAG
aB_E34Q_fwd	GGAGAGCACCTGTTGCAGTCTGATCTTTTCC
aB_E34Q_rev	GGAAAAGATCAGACTGCAACAGGTGCTCTCC
aB_P39Q_fwd	GGAGTCTGATCTTTTCCAGACGTCTACTTCCC
aB_P39Q_rev	GGGAAGTAGACGTCTGGAAAAGATCAGACTCC
aB_W60C_fwd	CGGGCACCCAGCTGCTTTGACACTGG
aB_W60C_rev	GAGAGTCCAGTGTCAAAGCAGCTGGG
aB_S135Q_fwd	CCTCTCACCATTACTCAATCCCTGTCATCTGATGG
aB_S135Q_rev	CCATCAGATGACAGGGATTGAGTAATGGTGAGAGG
aB_R163A_fwd	CCATTCCCATCACCGCTGAAGAGAAGCC
aB_R163A_rev	GGCTTCTCTTCAGCGGTGATGGGAATGG
aB_N-term_fwd	GATCCCATGGACATCGCCATCCACCAC
T7 prom	TAATACGACTCACTATAGGG
T7 term	GCTAGTTATTGCTCAGCGG
γD-crystallin primers:	
gD_I4F_ fwd	CCATGGGTAAGTTCACCCTGTATGAAGATCG
gD_I4F_ rev	CGATCTTCATACAGGGTGAACTTACCCATGG
gD_W43R_ fwd	GTTGATAGCGGTTGTCGTATGCTGTATGAACAG
gD_W43R_ rev	CTGTTCATACAGCATACGACAACCGCTATCAAC
gD_R59H_ fwd	GCAGTATTTCCTGCATCGTGGTGATTATGC
gD_R59H_ rev	GCATAATCACCACGATGCAGGAAATACTGC
gD_V76D_ fwd	GTCTGAGCGATAGCGATCGTAGCTGTCGTC
gD_V76D_ rev	GACGACAGCTACGATCGCTATCGCTCAGAC

2.4 Substrate proteins and antibodies

The following proteins were used as model substrates in aggregation assays and were purchased from the listed companies.

Malate dehydrogenase (MDH), from pig heart mitochondria	Roche
Citrate synthase (CS)	Roche
Lysozyme, from chicken egg white	Roth

In the final peptide array protocol, a HRP conjugated monoclonal anti αB-crystallin-antibody was used (Biomol) to detect αB-crystallin binding to the peptide spots. (Anti-alphaB Crystallin, clone 3A10.H4, HRP conjugated, original supplier: StressMarq Biosciences)

2.5 Enzymes, standards and Kits

Phusion® High-Fidelity DNA Polymerase	NEB
*Nco*I-HF®	NEB
*Not*I-HF®	NEB
*Dpn*I®	NEB
T4 ligase	Promega
Go*Taq*® DNA polymerase	Promega
peqGOLD 1 kb DNA ladder	Peqlab
Wizard® *Plus* SV Minipreps DNA Purification System	Promega
Wizard® SV Gel and PCR Clean-Up System	Promega
Pyruvate kinase (PK)	Roche
Unstained SDS-PAGE Standards, low range	Bio-Rad

2.6 *E.coli* strains and plasmids

strain	genotype	Origin
Mach 1	ΔrecA1398 endA1 tonA Φ80ΔlacM15 ΔlacX74 hsdR(rK^- mK^+)	Invitrogen
BL21-CodonPlus® (DE3)RIL	F^- *ompT* hsdS(rB^- mB^-) *dcm*$^+$ *Tetr gal* l (DE3) *end*A *I* [*arg*U *ile*Y *leu*W *Cam*R]	Stratagene

All constructs were cloned in pET28b (Novagen) containing a kanamycin resistance gene.

2.7 Media, buffers and stock solutions

All *E. coli* cultures were grown in LB_0-medium (Serva). The powder was dissolved resulting in a final concentration of 20g/L according to the manufacturer's recommendation.

Phosphate-buffered saline (PBS) buffer was used for the majority of experiments that were performed during this thesis. Buffers used for molecular biology, protein purification, electrophoresis or other experiments are listed in the according method section.

Phosphate-buffered saline (PBS)	$Na_2HPO_4 \cdot H_2O$ pH 7.4	10 mM
	KH_2PO_4	2.0 mM
	NaCl	137 mM
	KCl	2.7 mM

Stock solutions used in experiments performed during this thesis are shown below.

Kanamycin	35 mg/mL in dest. H_2O
IPTG	1 M in dest. H_2O
PMSF	0.2 M in 2-Propanol
TCEP	0.5 M in dest. H_2O
DTT	1M in dest. H_2O
TCA	72% (w/v) in dest. H_2O
APS	10 % in H_2O

2.8 Chromatography Materials and Columns

Resource-Q, 6 mL	GE Healthcare
Superdex 200 26/60	GE Healthcare
Superdex 75 26/60	GE Healthcare
Q Sepharose Fast Flow	GE Healthcare
SP Sepharose Fast Flow	GE Healthcare
Superdex200 10/300 GL	GE Healthcare

2.9 Devices

2D Gel electrophoresis: Ettan DALT II System	Amersham Biosciences (GE Healthcare)
Autoclave Varioclav EP-Z	H+P
Cell Disruption: TS Series Bench Top	Constant Systems
Centrifuges	
Avanti J-25 and J-26 XP	Beckman Coulter
Optima XL-A (equipped with FDS)	Beckman Coulter (Aviv)
Optima XL-I	Beckman Coulter
Rotina 46R	Hettich
Tabletop centrifuge 5415	Eppendorf
Tabletop centrifuge 5418 R	Eppendorf
Chromatography systems	
ÄKTA FPLC P-920	GE Healthcare
Equipped with:	
UPC-900 UV-detector	GE Healthcare
Frac-900/950 fraction collectors	GE Healthcare
Superloops (various volumes)	GE Healthcare
Circular dichroism spectropolarimeter:	
J715 (with PTC 348 WI Peltier device)	Jasco
Thermomixer comfort	Eppendorf
Thermomixer 5436	Eppendorf
Fluorescence spectrophotometers:	
FluoroMax-2	Spex
FP-8500	Jasco

SDS PAGE electrophoresis and blotting devices	Hoefer
Homogenizer Silent Crusher M	Heidolph
HPLC system:	Shimadzu
LC-20AC pump	
DGU 20A3 degasser	
SIL-20AC autosampling system	
SPD-20A UV detector	
RF-10AXL fluorescence detector	
FRC- 10 fraction collector	
Incubator	MYTRON
ImageQuant 300 Imager	GE Healthcare
ImageQuant LAS 4000	GE Healthcare
Magnetic stirrer Heidolph MR2000	Heidolph
Mass spectrometers:	
LTQ Orbitrap XL	Thermo Scientific
Ultraflex II MALDI ToF/ToF	Bruker Daltonics
PCR:	
T100 Thermal Cycler	Bio-Rad
MJ Mini Personal Thermal Cycler	Bio-Rad
pH meter	WTW
Power amplifiers EPS 3500, 3501 and 1001	GE Healthcare
Scales	
SI-4002	Denver Instruments
Isocal AC 211S	Sartorius
1409 M	Sartorius
Scanner: ImageScanner III	GE Healthcare
Shaker	
Centromat S	B. Braun
GFL 3005	GFL
POLYMAX 2040	Heidolph
Ultrafiltration cell (stirred), model 8400 or 8050	Amicon
UV-Vis spectrophotometers	
Varian Cary50 Bio	Agilent
Ultrospec 1100 Pro	GE Healthcare
Nanodrop1000	Peqlab
Vortex MS2	IKA
Water bath F6-K	Haake

2.10 Software

Adobe Photoshop CS4	Adobe Inc.	
DCDT+ 2.1.4	John Philo	Philo (2006), Stafford (1992)
EndNote X7	Thomson Reuters	
ImageQuantTL	GE Healthcare	
LabScan 6.0	GE Healthcare	
Microsoft Office 2010	Microsoft	
MMass 2.4	Martin Strohalm	
Origin 8.6G	OriginLab Corp.	
PyMOL 0.99rc6	Schrödinger, LLC	
SedFit 14.1	Peter Schuck	Schuck (2000)
Sednterp	David B. Hayes , Tom Laue, John Philo	Laue et al. (1992)
SedView 1.1	David B. Hayes, Walter F. Stafford	Hayes and Stafford (2010)

2.11 Online-tools

ClustalW/Omega	http://www.ebi.ac.uk/Tools/msa/clustalo/
NCBI Blast	http://blast.ncbi.nlm.nih.gov/
PeptideCutter	http://web.expasy.org/peptide_cutter/
ProtParam	http://web.expasy.org/protparam/
PEP-FOLD peptide structure prediction	http://bioserv.rpbs.univ-paris-diderot.fr/services/PEP-FOLD/
Translate tool	http://web.expasy.org/translate/
WebLogo	http://weblogo.berkeley.edu/logo.cgi

3. Methods

3.1 Molecular Biology

To obtain plasmids containing the encoding DNA sequence to produce the proteins of interest, the following methods were applied.

3.1.1 Polymerase chain reaction

Polymerase chain reaction (PCR) was used to amplify DNA-fragments for analytical or preparative use or for site directed mutagenesis. All PCRs were performed under conditions shown below.

PCR-reaction composition:

H_2O	31.5 µL
5x HF-Phusion Puffer	10 µL
dNTP-Mix (each 10 mM)	1 µL
5'-Primer (10 pmol/ µL)	2.5 µL
3'-Primer (10 pmol/ µL)	2.5 µL
Template DNA	2 µL
Phusion-Polymerase (2U/ µL)	0.5 µL

PCR-reaction conditions:

Cylces	Temperature	Time
1x	98°C	1 min
35X	98°C	30 s
	65-55°C	30 s
	72°C	30 s/ kb
1x	72°C	10 min

Point mutations were introduced using an adapted QuikChange® Mutagenesis-Protocol. PCRs were performed under conditions shown above. After the PCR reaction 5.7 µL NEB cut smart buffer and 1 µL *Dpn*I were added and incubated for 2 h at 37°C and subsequently used for *E.coli* Mach1 transformation.

For cloning of deletion variants of αA- and αB-crystallin, the inserts were amplified under standard PCR conditions using forward primers containing a 5' *Nco*I- and reverse primers containing 3' *Not*I restriction site. PCR-products were purified using the Wizard® SV Gel and PCR Clean-Up System (Promega). Purified PCR products were digested with 1µL of *Nco*I-HF and 1 µL of *Not*I-HF for 4 h under the reaction conditions recommended by the manufacturer and subsequently purified again using the Wizard® SV Gel and PCR Clean-Up System (Promega).

For ligation 3 µL of inserts and 1 µL of digested pET28b and 1 µL T4 Ligase were incubated in QL-buffer for 12 min at room temperature and used for transformation of *E. coli* Mach1 cells. False positive colonies were excluded by applying colony PCR using the GoTag® polymerase (Promega) T7 promotor and T7term primers and screening for insertion of approximately the right size of 550 bp.

3.1.2 Agarose gel electrophoresis

Agarose gel electrophoresis was conducted with DNA samples for analytical or preparative reasons. 1 g Agarose was dissolved in 100 mL TAE buffer and 4 µL of StainG solution was added. Electrophoresis was performed for 20 min at 120 V. The StainG-treated DNA bands were detected under UV-light in an ImageQuant 300 Imager (GE Healthcare).

TAE (50x)	Tris/Acetate pH 8.0	2 M
	EDTA	50 mM
DNA loading dye (5x)	Glycerol	50% (v/v)
	EDTA (pH 8.0)	10 mM
	Bromphenolblue	0.2% (w/v)
	Xylencyanol	0.2% (w/v)

3.1.3 DNA purification

Purification of PCR fragments and preparation of plasmids from *E. coli* Mach1 cultures were performed according to the manufacturer's protocol using Promega Wizard® SV Gel and PCR Clean-Up System or Wizard® *Plus* SV Minipreps DNA Purification System.

3.2 Transformation of *E. coli*

200 µL of chemically competent *E. coli* Mach1 cells and 20 µL of PCR or ligation product or 100 µL of chemically competent *E. coli* Bl 21 cells and 0.5 µL of Plasmid solution were incubated for 20 min on ice. The mixtures were heat-shocked for 1 min at 42 °C in a table top incubator, cooled down for 1 min on ice and then diluted with 1 mL LB_0. The transformed

cells were incubated for 1 h at 37°C and 200 rpm and subsequently plated on LB_0-Agar-kanamycine plates.

3.3 Protein production and cell disruption

For protein production, transformed *E. coli* BL21 (DE3)-CodonPlus cells were transformed with the respective plasmids and incubated over night in 50 mL of LB_0-medium with 35 µg/mL kanamycin at 37°C and 180 rpm. 2 L LB_0-medium were inoculated with 30 mL of the prepared over night culture and incubated at 37°C until an OD_{600} of ~0.9 was reached. Expression was induced by adding 1 mM IPTG followed by incubation over night at 30°C.

Cells were harvested in a Beckman Avanti at 8500 x g and 10°C, resuspended in TE buffer containing Protease Inhibitor Mix G (Serva) and disrupted at 2 kbar using the high pressure cell disruption system. Lysate was cleared or inclusion bodies were separated by centrifugation at 40000 x g at 10°C for 35 min.

3.4 Purification of native αB WT and variants from *E. coli* lysate

After cell disruption, all soluble αB-crystallin variants were purified using anion exchange chromatography followed by size exclusion chromatography. In some cases a second AEX or SEC was performed for further purification.

3.4.1 Ion exchange chromatography (IEX)

As a first purification step the supernatant was applied to a Q-Sepharose-column equilibrated with TE buffer. Subsequently, the column was washed with 5 CVs buffer A. Elution was carried out by applying a linear salt gradient from 0 to 500 mM NaCl. All proteins eluted at 100 mM - 150 mM NaCl. Fractions were analyzed using SDS-PAGE.

TE buffer A	Tris/HCl, pH 8.3	50 mM
	EDTA	2 mM
TNE buffer B	Tris/HCl, pH 8.3	50 mM
	EDTA	2 mM
	NaCl	1 M

3.4.2 Size exclusion chromatography (SEC)

Pooled fractions from AEX were concentrated using an Amicon stirred ultrafiltration cell model 8400 or 8050 and applied to a Superdex 200 26/60 column in TE-size exclusion buffer. 3 mL fractions were collected and analysed by SDS-PAGE. If an adequate purity was achieved, the fractions containing the pure protein were dialyzed in PBS-buffer and aliquots were frozen in liquid nitrogen and stored at -80°C.

TNE size exclusion buffer	Tris/HCl, pH 8.3	50 mM
	NaCl	400 mM
	EDTA	2 mM
Phosphate-buffered saline (PBS)	Na_2HPO_4, pH 7.4	10 mM
	KH_2PO_4	2.0 mM
	pH 7.4NaCl	137 mM
	KCl	2.7 mM

If purity was not sufficient, the pooled factions from SEC were diluted with TE buffer to a maximum salt concentration of 20 mM NaCl and either applied to a ResQ-Column or to a Q-Sepharose for a second time.

In some cases e.g. for purification of multiple Glu-mutations into αB-crystallin it was necessary to continue with a hydrophobic interaction chromatography.

3.5 Inclusion body purification and refolding of αB Δ20, mαA V124E and γD-crystallin variants

αB-crystallin Δ20, mαA V124E and all γD-crystallin modifications could not be obtained in their soluble form but as inclusion bodies. After expression and cell disruption, inclusion bodies were separated from the cell lysate by centrifugation. Inclusion bodies were purified by re-suspending it in IB preparation buffer containing 2 % Triton X-100. After stirring for 1 h the inclusion bodies were centrifuged for 15 min at 10 °C at 18000 x g and washed three times with IB preparation buffer without Triton X-100.

The purified inclusion bodies were dissolved in Urea buffer A. The dissolved denatured proteins were purified using the protocol described before (Marcinowski, 2011). After ion exchange chromatography, the denatured proteins were refolded by dialysis at 0.1-0.5 mg/ mL with refolding buffer.

The refolded proteins were further purified by size exclusion chromatography in PBS using a Superdex75-column.

IB preparation buffer	Tris/HCl, pH 7.5	100 mM
	NaCl	100 mM
	EDTA	10 mM
Urea buffer A	Tris/HCl, pH 7.5	50 mM
	EDTA	10 mM
	Urea	5 M
Urea buffer B	Tris/HCl, pH 7.5	50 mM
	EDTA	10 mM
	Urea	5 M
	NaCl	1 M
Refolding buffer	Tris/HCl, pH 8.0	250 mM
	EDTA	10 mM
	L-Arginine	100 mM
Phosphate-buffered saline (PBS)	Na_2HPO_4, pH 7.4	10 mM
	KH_2PO_4	2.0 mM
	NaCl	137 mM
	KCl	2.7 mM

3.6 SDS-Polyacrylamide gel electrophoresis

SDS-PAGE was performed using a modified protocol of Laemmli (Laemmli, 1970). Due to their similar molecular mass, all proteins were separated on 15% polyacrylamide gels. Samples were mixed with 5X Laemmli sample loading buffer and heated to 95°C for 5 min. Electrophoresis was carried out at 35 mA for 35 min. Gels were stained with Coomassie R250 (Fairbanks et al., 1971).

Laemmli sample loading buffer (5x)	Tris/HCl, pH 6.8	300 mM
	SDS	10% (w/v)
	Glycerol	50% (v/v)
	2-Mercaptoethanol	5% (v/v)
	Bromophenol blue	0.05% (w/v)
Laemmli running buffer (10x)	Tris/HCl, pH 8.3	250 mM
	Glycine	2M
	SDS	1% (w/v)
Separation gel buffer (2x)	Tris/HCl, pH8.8	1.5 M
	SDS	0.8% (w/v)
Stacking gel buffer (4x)	Tris/HCl, pH 6.8	250 mM
	SDS	0.4% (w/v)
Fairbanks A	2-Propanol	25% (v/v)
	Acetic acid	10% (v/v)
	Coomassie Blue R250	0.05% (w/v)
Fairbanks D	Acetic acid	10% (v/v)

3.7 Protein labeling

For fluorescence spectroscopy and aUC using the Aviv Fluorescence detections system, proteins were labeled with fluorescent labels amine or thiol reactive probes. All labeling reactions were carried out according to the Molecular Probes® Handbook (Johnson, 2010) for 2 h at room temperature and protected from light. Labeling of cysteine residues was carried out in PBS buffer. Protein samples were reduced with 1 mM TCEP 30 min before the reactive probe was added to the solution. The reaction was stopped by adding 30 mM β-mercaptoethanol. Unbound label was removed using a PD-10 column followed by dialysis over night at 4°C.

3.8 UV/Vis spectroscopy

3.8.1 Determination of protein concentration

The molar concentration of purified recombinant proteins was determined by their specific absorbance at 280 nm. The aromatic amino acids Trp and Tyr as well as disulfide bonds are mainly responsible for UV-absorbance of proteins at 280 nm. Dependent on the amino acid composition, molar extinction coefficients ε can be calculated. These can be used for determination of concentration applying the Beer-Lambert law (equation 1). (Atkins, 2004)

$$c = \frac{A}{\varepsilon \cdot d} \tag{1}$$

(c = concentration (mol/L), A = absorbance, ε = molar extinction coefficient (M^{-1} cm^{-1}), d = path length (cm).

The extinction coefficients (see appendix) were calculated using the protparam tool (Wilkins et al., 1999). The absorbance was determined in a NanoDrop1000 or Cary 50 spectro-photometer.

For determination of lens lysate protein concentration the Bradford-Assays reagent was used (Bradford, 1976). In this assay, coomassie G250-dye in binds to proteins an acidic environment. Thereby a spectral shift from brown/red to blue can be observed. 100 µL of different dilutions of the protein solution was added to 1 mL of pre-diluted Bradford reagent (1:5 in H_2O). After incubation for 10 min at RT, the absorbance at 595 nm is determined. After calibration the actual concentration of the samples can be calculated.

3.8.2 Chaperone activity assay

To assess the *in vitro* chaperone activities of different α-crystallin variants, different substrates were used. To determine the chaperone activity the amount of aggregated substrate protein was measured by monitoring the increase of pseudo-absorbance at 350 nm in a Cary 50 spectrophotometer. The reaction conditions for each substrate are described below.

L-Malate dehydrogenase

MDH is a heat-sensitive protein that aggregates at 42°C (Hartman et al., 1993). It was used to analyze chaperone activity in PBS. 4 µM MDH was incubated at 42°C in filtered and degassed PBS-buffer with different α-crystallin concentrations (0.5 µM - 4 µM) for 60 min.

Citrate Synthase

CS is a heat-sensitive protein that aggregates at 42 °C (Buchner et al., 1998). It was used to analyze chaperone activity of more active mutants. 1 µM CS was incubated with with different α-crystallin concentrations (1-10 µM) at 42°C for 60 min in CS-Assay buffer.

CS Assay buffer	$Na_2HPO_4 \cdot H_2O$ pH 7.4	5 mM
	KH_2PO_4	1 mM
	NaCl	70 mM
	KCl	1.4 mM

Lysozyme

Lysozyme is a less sensitive to heat than MDH and CS. However, under reducing conditions it aggregates easily (Hamaguchi, 1964). In chaperone assays 5 µM Lysozyme were pre-incubated with different α-crystallin concentrations (0.5 - 5 µM) at 37°C for 15 minutes. Subsequently, aggregation was induced by addition of 1 mM TCEP.

γD-crystallin

The highly thermostable substrate γD-crystallin (see section 4.3) was denatured in PBS + 5M GdnCl for at least 3 hours or overnight. The protein was diluted 1:50 into the pre-diluted and pre-incubated α-crystallin in PBS at 37°C to yield a final concentration of 2 µM γD and varying concentrations of αB-crystallin. The solution was mixed immediately.

3.9 CD spectroscopy

CD spectroscopy is used to obtain information on the secondary structure composition and the thermal stability of proteins (Kelly and Price, 2000). This is based on their ability to absorb left and right hand circular polarized light to different degrees depending mainly on the chiral structure elements. After passing through the sample, the light is elliptically polarized. Far-UV-spectra can give information about the secondary structure of a protein. Spectra of β-sheet-rich proteins exhibit a specific minimum around 218 nm, whereas minima and maxima of unstructured or mainly α-helical proteins clearly differ from that. The concentration dependent measured ellipticity can be converted to mean residue ellipticity using equation 2.

$$\Theta_{MRW} = \frac{\Theta \cdot 100}{d \cdot c \cdot N_{aa}} \quad (2)$$

Θ_{MRW} = mean residue ellipticity (deg cm^2 $dmol^{-1}$), Θ = ellipticity (deg), d = path length (cm), c = concentration (M), Naa = number of amino acids.

The ellipticity was measured in a Jasco J-715 Circular Dichroism (CD) spectropolarimeter. All measurements were conducted in 1 mm quartz cuvettes (Hellma) with protein concentrations of 0.2 mg / mL. The experimental parameters used for CD-spectra and thermal transitions are shown below.

Parameters of CD- spectra-measurements

wavelength	260 - 203 nm
data pitch	0.2 nm
scanning mode	continuous
speed	20 nm/ min
response	4 s
bandwidth	1 nm
accumulations	7

Parameters of thermal transitions

temperature	20 - 95 °C
data pitch	0.5 °C
delay time	0 s
heating rate	15 °C/ h

3.10 Fluorescence spectroscopy

When molecules absorb light, they are transformed from their electronic ground state to an excited state. Due to their much higher mass compared to electrons, they react delayed to this change in the surrounding electron density and are therefore accompanied by vibrations. From a quantum mechanical view this means that intensities of electronic transitions are always dependent on the overlap of their wave functions with wave functions of the possible vibrational levels (Franck-Condon principle). Hence, electronic transitions are most likely accompanied by vibrational transitions resulting in an excited electronic and vibrational state (= vibronic transition). The excited molecule can immediately return to its ground state by emission of a photon. More frequently the molecule first undergoes radiation-less transitions to the vibrational ground state within the excited electronic state by e.g. collisions with surrounding molecules. Returning to the electronic ground state is accomplished following the Franck-Condon principle by spontaneous emission of a photon of less energy than the absorbed photon. Hence, longer wavelengths can be observed. This process is called fluorescence. The difference in wavelength between absorbed and emitted light is called stokes shift and differs for each fluorophore (Atkins, 2004). The detailed experimental settings for each method based on fluorescence spectroscopy are described in the following sections.

3.10.1 Thermal shift assay (TSA)

The thermal stability of proteins was determined by using the fluorescent dye SYPRO®Orange (ThermoFisher Scientific). Upon binding to hydrophobic patches of unfolding proteins, its fluorescence at 488 nm increases, which can be monitored in a Mx3000P qPCR machine (Ericsson et al., 2006).

For thermal transitions a 1 : 1000 dilution of Sypro Orange mix with αB variants at a final concentration of 10 µM was used. Fluorescence was monitored in a Mx3000P qPCR machine. Heating rate was set to 1 °C/min. Measurements were performed in triplicates.

3.10.2 ANS binding

1-anilinonaphthalene-8-sulfonic acid (ANS, Sigma-Aldrich) is sensitive to changes in hydrophobic environment similar to the later discovered SYPRO®Orange (Stryer, 1965).

This property can be used to investigate relative overall hydrophobicities of different α-crystallin variants. Increasing fluorescence at 370 nm as a consequence of binding to hydrophobic protein patches was monitored in a Fluoromax-2 fluorescence spectrometer 10 µM of α-crystallin was mixed with 100 µM of a freshly prepared ANS-solution in PBS and incubated for 2 h at rt protected from light. Fluorescence spectra of the pre-incubated samples were recorded using the experimental settings shown below.

Emission	400 - 600 nm
excitation	370 nm
increment	1 nm
Integration time	0.5 s
accumulations	3
temperature	25°C

3.10.3 Subunit exchange kinetics using FRET

Fluorescence resonance energy transfer (FRET) can take place between two fluorophores in spatial proximity with approximately parallel dipole orientations. If emission spectra of donor and excitation spectra of acceptor molecules overlap, a direct energy transmission from donor to acceptor occurs. If so, the observed fluorescence of donor molecules decreases while the acceptor fluorescence increases at the same time. The FRET efficiency decreases with the inverse 6th power of intermolecular distance (equation 3). Due to this correlation, FRET can be used to monitor intermolecular interaction like binding and dissociation.

$$E = \frac{1}{1+(\frac{r}{R_0})^6} \quad (3)$$

E = FRET efficiency, r = donor-acceptor-distance, R_0 = Förster distance.

To investigate subunit exchange kinetics, αB-crystallin S153C was labeled with two different labels, Alexa Fluor® 350 and Alexa Fluor® 488. The separately labeled αB batches were mixed in a 1:1 ratio at 1 µM final concentration of each labeled component and incubated for 4 h at 37°C to reach equilibrium in oligomer distribution. The reaction was monitored by recording fluorescence spectra in a Jasco FP-8500 under the conditions shown below.

Ex wavelength	375.0 nm
Measurement range	380 - 600 nm
Data interval	1 nm
Scan speed	200 nm/min
Sensitivity	Medium
Ex bandwidth	2.5 nm
Em bandwidth	5.0 nm
Response	1 s
Intensity normalization	Off
Auto gain	Off
Shutter control	Open only for measurement

The different subunit exchange kinetics of different mutants was measured indirectly by adding 40 µM of unlabeled αB mutants to the preformed FRET-complex formed with 1 µM αB S153C Alexa Fluor® 350 and 1µM αB Alexa Fluor® 488. The subsequent increase in donor fluorescence upon replacement of labeled by unlabeled mutant subunits at 37°C was monitored using the experimental settings shown below. All samples were incubated separately for 3h at 37°C before measurements for temperature equilibration.

Measurement range	0 - 180 min
Data interval	1 min
Ex wavelength	375.0 nm
Em wavelength	440.0 nm
Sensitivity	Medium
Ex bandwidth	2.5 nm
Em bandwidth	5 nm
Response	2 sec
Intensity normalization	Off
Blank correction	Off
Auto gain	Off
Shutter control	Open only for measurement

3.11 Quaternary structure analysis techniques

To assess changes in oligomeric assemblies of the analyzed proteins, three methods were used: Analytical size exclusion chromatography, analytical ultracentrifugation and negative stain transmission electron microscopy. These methods are described below.

3.11.1 Analytical size exclusion chromatography

To assess changes in oligomeric size, analytical size exclusion chromatography was used. The separation is dependent on the pore size of the chromatography material. Separation is achieved by diffusion of smaller molecules into the pores while larger particles pass through the column. This results in different elution times of particles in solution (Porath and Flodin, 1959). Experiments were carried out on the Shimadzu HPLC system equipped with an SPD-20A detector and a fluorescence detection system RF-10A XL. HPLC runs were performed in PBS using a Superdex200™ 30/100 GL-column at a flow rate of 0.5 mL/min. The used sample compositions and concentrations varied dependent on the performed experiments. The exact conditions are shown in section 4 for each experiment.

3.11.2 Analytical ultracentrifugation

Analytical ultracentrifugation (aUC) is a powerful method to analyze different hydrodynamic parameters of macromolecules in solution without disturbing matrix interactions. In aUC experiments a centrifugal force is applied to the sample solutions while sedimentation of the analytes monitored in 'real-time' by using absorbance, interference or fluorescence detection systems. The process of sedimentation is governed by three forces: gravitation, buoyancy and hydrodynamic friction. The balance of these three forces is the basis of the Svedberg equation (equation 4).

$$s = \frac{v}{\omega^2 r} = \frac{MD(1-\bar{V}\rho)}{RT} \quad (4)$$

s = sedimentation coefficient (s), v = observed radial velocity (m/s), ω = angular velocity of the rotor (m/s^2), $\omega^2 r$ = centrifugal field, M = molar weight (g/mol), $\bar{V}$ = partial specific volume (cm^3/g), ρ = density of the solvent (g/cm^3), D = diffusion coefficient (m^2/s), R = gas constant (8.314472 J/K mol), T = absolute temperature (K)

There are two types of experiments that can be performed: Sedimentation velocity experiments (SV) using a high centrifugal force and sedimentation equilibrium experiments (SE) at lower centrifugal force. The application of a lower centrifugal speed results in an equilibrium of two forces: sedimentation on the one hand and the inversely directed back diffusion of the analytes depending on the emerging concentration gradient on the other hand. The concentration distribution across the cell is only dependent on the molecular mass. A disadvantage of SE experiments is, that only average sedimentation coefficients and molecular masses of all analytes present in the sample can be determined which impedes analysis of sample compositions. To obtain more information about the latter, SV experiments have to be performed. As a consequence of the high applied centrifugal force, all analytes in the sample sediment to the bottom of the aUC-cell. This process contains additional information on analyte shape and sample heterogeneity (Scott and Schuck, 2006).

Sedimentation velocity (SV) experiments were carried out using a ProteomeLab XL-I (Beckman, Krefeld, Germany) supplied with absorbance optics. All experiments were performed in PBS at 20°C at 34 000 rpm in an eight-hole Beckman-Coulter AN-50 Ti rotor. Sedimentation was monitored at 230 or 280 nm dependent on the sample concentration.

For binding experiments SV experiments were performed in a ProteomeLab XL-A (Beckman, Krefeld, Germany) supplied with an Aviv AU-FDS. With this method of detection, only species exhibiting fluorescence excitable around 488nm can be observed. Here, atto488 or atto532 fluorescent dyes were coupled to the proteins (s. 3.5 protein labeling).

Data analysis was carried out using different software dependent on the experimental questions.

For lower resolution distributions to analyse binding or change in oligomer size g(s*)-distributions were calculated using dc/dt+ version 2.4.1 by John Philo (Philo, 2006; Stafford, 1992).

For higher resolution or determination of molecular mass, Sedfit (P. Schuck) was used. Data analysis was performed using a non-model based continuous Svedberg distribution method (c(s)), fitting f/f_0 and time (TI) and radial (RI) invariant noise (Schuck, 2000).

3.11.3 Electron Microscopy

All negative stain-EM experiments mentioned in this thesis were performed in collaboration with the group of Prof. Sevil Weinkauf (Technische Universität München, Garching). EM experiments and data analysis were conducted by Dr. Carsten Peters and Dr. Christoph Kaiser. A detailed description of the EM methods is published elsewhere (Braun et al., 2011; Peschek et al., 2009).

3.12 Peptide Arrays

The interaction of αB-crystallin with membrane-bound peptides of substrate proteins was assayed using customized CelluSpots™ peptide arrays (Intavis Bioanalytical Instruments AG). A list of tested peptides used on the chips is shown in the appendix. Before use, arrays were rinsed for 30 sec with EtOH p.A. followed by washing once for 30 sec and 3 times for 5 min with PBS-T. To prevent unspecific binding to the cellulose matrix, arrays were blocked for 1 h using 5 % milk powder in PBS-T. After washing once for 30 sec and three times for 10 min with PBS-T the arrays were incubated for 3 h at 37°C and 65 rpm with 5 ml of 15 µM aB in PBS. As a negative control arrays were incubated with PBS only. The protein solution or PBS was removed and membranes were subsequently washed for 30 sec once and 3 times for 45 min. Binding was detected using a HRP-conjugated monoclonal anti-αB-crystallin antibody (Biomol) in PBS + 1% milk powder at 4°C overnight. Extensive washing was performed on a shaker with PBS once for 1 min, twice for 45 min and once for 60 min at rt. The blots were developed by adding Western bright ECL-Spray (Advansta) according to the manufacturer's instructions in an ImageQuant LAS 4000 (GE Healthcare) equipped with a chemoluminescence detection system. Spot intensities were determined using ImageQuantTL Software (GE Healthcare) and normalized to the most intense spot on each replicate. Mean average values and standard deviations were calculated from the normalized spots. The used buffer and the experimental protocol is summarized below.

PBS-T	Na_2HPO_4,	10 mM
	pH 7.4	2.0 mM
	KH_2PO_4	137 mM
	NaCl	2.7 mM
	KCl	
	Tween	0.1% (w/v)

Activation	1 x 30 sec EtOH p.a.
Washing	1 x 30 sec in PBST, 3 x 5 min in PBS-T
Blocking	1 x 1 h in 5% (w/v) milk powder in PBS-T
Washing	1 x 30 sec , 3 × 10 min in PBS-T
Binding of αB-crystallin	2 h , incubation of 15 µM αB-crystallin in 5 ml PBS at 37°C and 65 rpm
Washing	1 x 30 sec, 3 × 45 min in PBST
Binding of anti-αB-antibody	overnight; anti-αB-crystallin-antibody dilution 1 : 2000 in 5 mL of 1%(w/v) milk powder in PBS-T at 8°C and 40 rpm
Washing	1 x 30 sec, 2 x 45 min. 1 x 60 min in PBS-T
Detection	Addition of Western bright ECL-spray in an ImageQuant LAS 4000

3.13 Preparation of α-crystallin from mouse lenses

Mouse lenses were kindly provided by Dr. Graw (Helmholtz-Center Munich) and stored at -80°C. For lysis, lenses were thawed on ice, 100 µL LE-buffer were added per lens pair and lenses were homogenized by manually crushing (20 times) with a micro tissue homogenizer for 1.5 mL reaction tubes (kindly provided by Prof. Dr. Graw, Helmholtz Zentrum Munich). Afterwards, the homogenizer was washed 2 times with 50 µL LE buffer. The washing solution was added to the lens lysate. After centrifugation for 10 min at 10000 x g and 4°C, the soluble fraction was separated and the pellet was washed 2 times with 100 µL LE buffer. The pellet was dissolved it in 50 - 100 µL Urea buffer dependent on pellet size and solubility.

Overall protein concentrations were determined performing Bradford Assays (s. 3.8.1).

LE buffer	Tris/HCl, pH 7.8	50 mM
	DTT	3 mM
	PMSF	0.1 mM
Urea buffer	Tris/HCl, pH 8.6	50 mM
	NaCl	50 mM
	EDTA	1 mM
	DTT	2 mM
	Urea	6 M

3.14 2D-Gel electrophoresis

Soluble and urea-soluble fractions of lens lysates or purified α-crystallin-fractions from mouse lenses were analyzed by 2-dimensional gel electrophoresis (2-DE). Here, proteins are separated in the first dimension by their isoelectric point using a pH gradient under denaturing conditions (Isoelectric focusing, IEF)). In the second step, proteins are separated by their molecular mass in a SDS-Gel electrophoresis.

For soluble and urea-soluble fraction, 15%-gels were used. For IEF Immobiline DryStrip pH 3-10, 24 cm (GE Healthcare) were used.

For IEF of small sample amounts or purified α-crystallin-fractions Immobiline DryStrip pH 3-10, 7 cm (GE Healthcare) or Immobiline DryStrip pH 4 - 7, 7 cm (GE Healthcare) were used. The second separation was carried out using SERVA*Gel*™ TG PRiME™ 14 % precast gels with one 2D-well.

All gels were stained using colloidal coomassie and destained with acetic acid (10% (v/v)).

Purified α-crystallin-fractions from SEC-HPLC were desalted by TCA-precipitation (s. 3.14).

Electrophoresis was performed under the conditions recommended by the manufacturer (GE Healthcare, 2010) by Bettina Richter.

2-DE sample loading buffer	Urea	7 M
	Thiourea	2 M
	DTT	65 mM
	CHAPS	2% (w/v)
IPG-Strip equilibration buffer	Tris/ HCl pH 8.8	50 mM
	Urea	6 M
	Glycerol	30% (v/v)
	SDS	2% (w/v)
2-DE running buffer	Tris/ HCl 8.8	25 mM
	Glycine	192 mM
	SDS	0.1% (w/v)
2-DE resolving gel buffer	Tris-base/ HCl pH 8.8	1.5M

3.15 TCA precipitation for desalting

A 72% (w/v) TCA solution was diluted into the samples to result in an end concentration of 10% TCA. Samples were incubated 1 h on ice, centrifuged for 30 min at 4°C and 13000 rpm. The supernatant was discarded and the pellet was washed 3 times with 80% aceton cooled to -20°C. The precipitated protein pellet was dissolved in 2DE-buffer.

3.16 Mass spectrometry

3.16.1 Maldi-TOF

For protein identification or determination of correct molecular masses of purified mutants Maldi-TOF was used. Samples were prepared by Bettina Richter. Measurements were performed by Helmut Krause and Gina Feind using an Ultraflex II MALDI ToF/ToF (Bruker). The resulting peptide spectra were compared to the Mascot database (Perkins et al., 1999).

3.16.2 Orbitrap XL

For higher sensitivity measurements an OrbitrapXL (ThermoScientific) was used. Measurements and analyses were performed by Marina Daake.

4. Results and Discussion

4.1 The role of the N-terminal domain of human αB-crystallin

As already described in section 1.4.3, all three parts of αB are supposed to play an important role in substrate interactions. The ACD is the best characterized region of αB. The sequences ^{57}APSWIDTGLSEMR^{69} that marks the end of the NTR and the beginning of the ACD and ^{93}VLGDVIEVHGKHEER^{107} in the ACD were identified by crosslinking and mass spectrometry to be involved in substrate binding (Sharma et al., 1997). A peptide consisting of the sequence of αB residues 73-92 was discovered to suppress formation of light scattering aggregates in chaperone assays and was named 'mini-αB' (Bhattacharyya et al., 2006). The corresponding sequence in αA-crystallin 70-88 revealed the same functionality (Banerjee et al., 2015). The analyzed binding sites are shown in fig. 11.

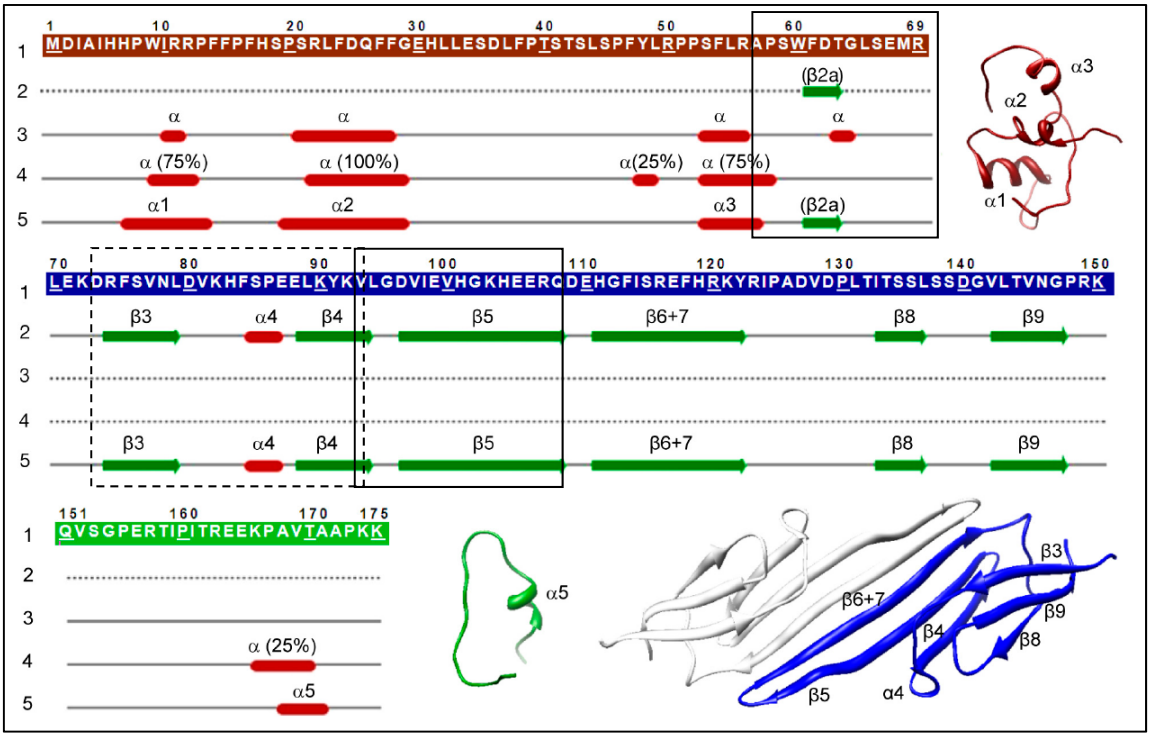

Fig. 11: Amino acid sequence (first line) and secondary structure prediction of the NTR (red), ACD (blue) and CTR (green) of αB-crystallin. Second line: secondary structure elements observed in the NMR structure of α-crystallin domain (pdb 2KLR). Third and fourth lines: secondary structure elements predicted by the servers I-Tasser and Phyre, respectively. The β and α denote β-strands and α-helices, respectively. Fifth line: secondary structure elements included in the pseudo-atomic model of human αB-crystallin. Dashed lines indicate the position of 'mini-αB' (Bhattacharyya et al., 2006), straight lines indicate binding sites identified by crosslinking/ms (Sharma et al., 1997); adapted from Braun et al. (2011).

These short peptide stretches seem to play an important role in α-crystallin for chaperone function, but isolated peptides cannot help to elucidate further the interplay with different other sequence stretches in the full length protein and do not contain information about the impact of the oligomer assembly on the function.

The role of the CTR was analyzed by mutational studies. Deletion of the CTR or introduction of mutations, that decrease flexibility, lead to a decrease of chaperone activity (Andley et al., 1996; Takemoto et al., 1993).

The least characterized region in αB-crystallin concerning structure as well as its involvement in chaperone function is the NTR. The high flexibility of this region complicates structure analysis by methods like X-ray crystallography or NMR-spectroscopy. A fundamental role of the NTR can be assumed from the 24-mer model published in 2011 (pdb-code 2YGD, Braun et al. (2011)). Even if the pseudo-atomic modeling of the NTR is only an approximation or can only represent a snapshot of many different possible conformations, it demonstrates that the NTR is a linker between the different hexameric subunits on a three-fold symmetry axes in the tetrahedral 24-mer assembly (fig. 12).

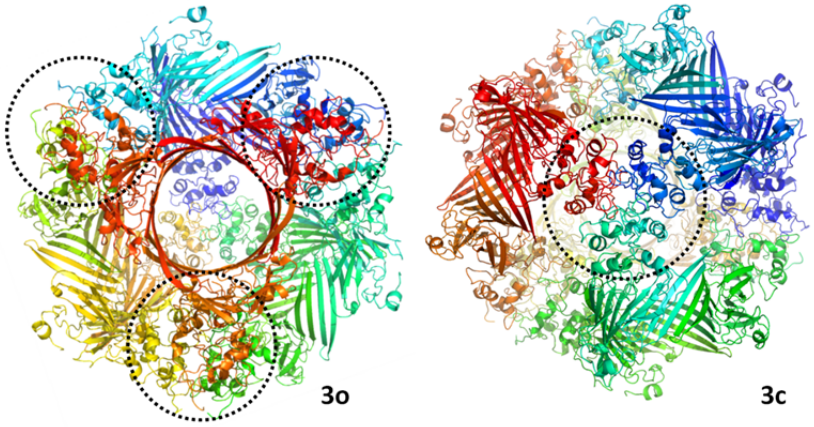

Fig. 12: Three-dimensional model of the αB-crystallin 24-mer (pdb 2YGD). **Left:** View along the three-fold symmetry axis intercepting the 'hole' created by three different ACD-dimers. **Right:** view along the three-fold symmetry axis intercepting the six different N-terminal regions.

To elucidate the impact of the NTR, several mutational studies were conducted analyzing the change of chaperone function. The important role of the NTR for oligomeric assembly and for function was shown for αA-crystallin by deletion of the NTR (Kundu et al., 2007). The same effect could be observed for human αB (fig. 13), although the loss of function is only true for certain substrates, indicating different binding modes for different substrates. Prevention of fibril formation of Aβ could be shown for αB WT as well as for ΔNTR-mutant (fig. 13) (Mainz et al., 2015).

Another hint to the importance of the NTR in αB are the main phosphorylation sites at position 19, 45 and 59 that are all located in the NTR and regulation of αB-crystallin quaternary structure and chaperone function by phosphorylating these serine residues has been shown (Peschek et al., 2013).

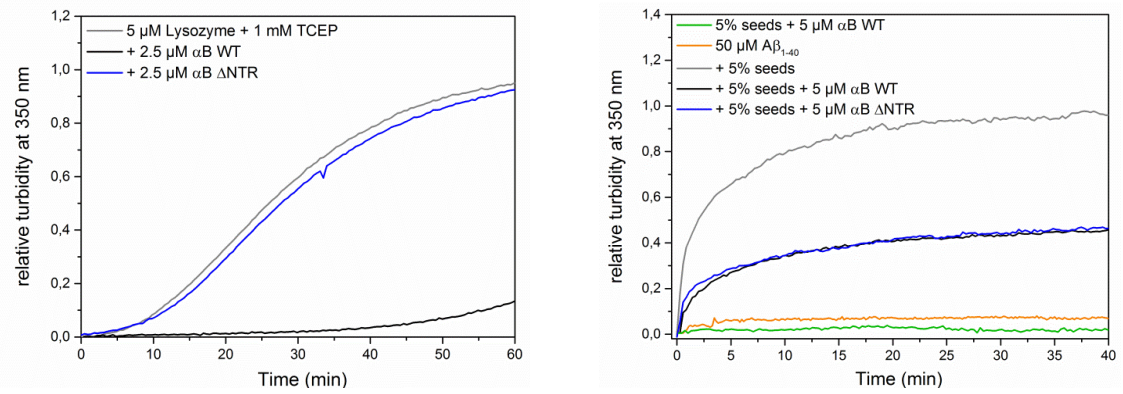

Fig. 13: Comparison of function of αB WT and ΔNTR; **left:** Chaperone assay using lysozyme as a substrate. While WT is still able to prevent aggregation, ΔNTR does not inhibit aggregate formation; **right:** Seeded fibril formation of $A\beta_{1\text{-}40}$ is inhibited partially by WT and ΔNTR to the same extend.

4.1.1 Subdividing the N-terminal region by different deletion variants

To assign the regions in the NTR that are responsible for oligomer formation and chaperone activity, mutations were introduced into human αB-crystallin. As a first rough partitioning of the NTD, deletion mutants were generated. Secondary structure predictions were included in construct design (Braun et al., 2011). In fig. 14 the different structural sections are shown.

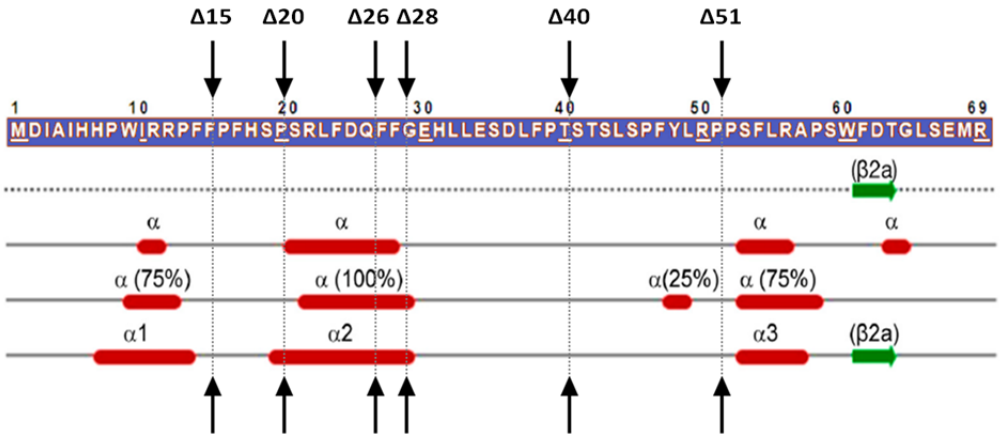

Fig. 14: Amino acid sequence (first line), secondary structure predictions of the NTR of αB-crystallin. Second line: secondary structure elements observed in the NMR structure of α-crystallin domain (pdb 2KLR). Third and fourth lines: secondary structure elements predicted by the servers I-Tasser and Phyre, respectively. The percentages in the brackets relate to the frequency of prediction by different Phyre programs. The β and α denote β-strands and α-helices, respectively. Fifth line: secondary structure elements included in the pseudo-atomic model of human αB-crystallin. The vertical lines indicate the position, where the domain was cut in the characterized deletion variants; adapted from Braun et al. (2011).

The positions of the predicted helices in the pseudo-atomic 3D model of the 24-mer αB-crystallin are shown in fig. 15. The first 20 residues containing helix α1 and one Trp, three Phe-residues and two Arg-residues are shown in red. Region 21-28 is highly conserved in many sHsps and forms helix α2 (shown in green). In this model, the helical structures seem to form a stabilizing framework caging the less structured regions of the NTR.

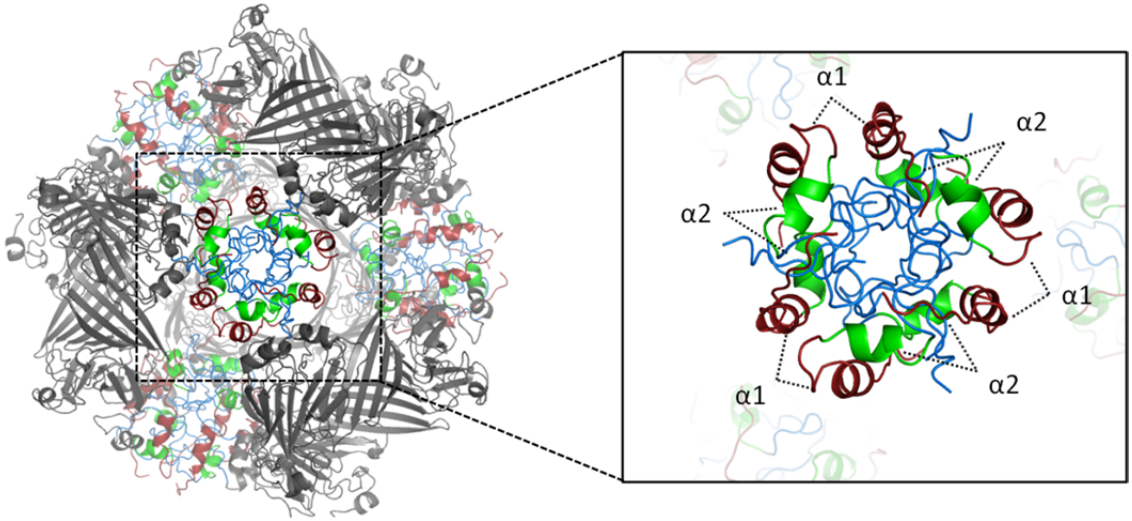

Fig. 15: Three-dimensional model of the αB-crystallin 24-mer (pdb 2YGD), view along the 3c three-fold symmetry axis; **right:** Close-up of the cage-like arrangement of the 6 N-terminal domains connecting hexameric substructures to form large oligomer. Residues 1-20 are shown in red, the highly conserved residues 21-28 are shown in green, the unstructured residues 29-51 are shown in blue.

4.1.1.1 Purification of deletion variants

The mutant αB Δ20 was mainly produced in inclusion bodies, but refolding resulted in good yields of pure soluble protein. The variants αB Δ26, αB Δ28, αB Δ40 and αB Δ51 were produced as soluble proteins in *E. coli*. αB ΔNTR was purified by Dr. Jirka Peschek. All proteins were identified as αB by tryptic digest followed by MALDI-Tof analysis and Mascot database search (Perkins et al., 1999). Additionally all molecular weights were determined by mass spectrometry of the full-length proteins to assure the correct mutation was purified.

4.1.1.2 Structural characterization of αB deletion variants

Secondary structure and thermal stability

Correct folding of the mutants was analyzed by CD-spectroscopy. The secondary structure of all constructs is comparable to αB WT structure. The shape of the spectrum with a minimum at ~217 nm is characteristic for β-sheet rich proteins (fig. 16).

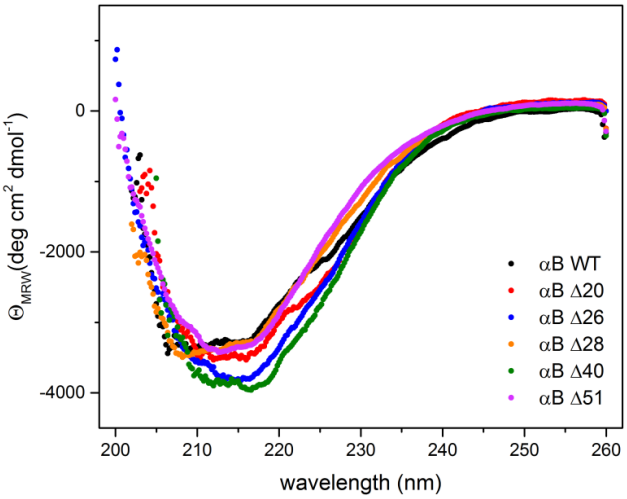

Fig. 16: CD-spectra of αB WT and deletion variants.

The temperature stability was determined by thermal transitions monitored by CD-spectroscopy and by fluorescence spectroscopy (Thermal Shift Assay, TSA). In fig. 17 transitions obtained by CD-spectroscopy are shown. When αB WT is heated up to 95°C, the ellipticity at 218 nm first increases till ~80°C, then a signal jump can be observed that is due to aggregation without unfolding. Formation of fibril-like structures is presumably the result of these transitions as it is known for αB to form fibrillar structures under denaturing conditions (Meehan et al., 2004). αB Δ20 shows a similar signal change until ~50°C, at higher temperatures no signal change could be observed anymore. If these transitions are fitted using a Boltzmann-model, a melting temperature of 62°C can be obtained for WT and 46°C for Δ20, but signal changes in both curves can be observed already at very low temperatures of ~35°C. The detailed secondary structure changes leading to this phenomenon are still unknown. The thermal transitions of all other deletion variants are completely different from the WT curve, but are very similar among themselves. Δ26 shows minor differences between 30°C and 40°C that resemble a biphasic transition, but cannot be fitted with sufficient quality. Oligomer rearrangements that also affect secondary structure probably dominate the behavior of αB WT and Δ20 while all other tested deletion variants

exhibit mono-phasic concerted thermal transitions with melting temperatures T_m of ~ 55°C that represent the unfolding of the β-sandwich structure of the ACD. The NTR obviously enhances thermal stability.

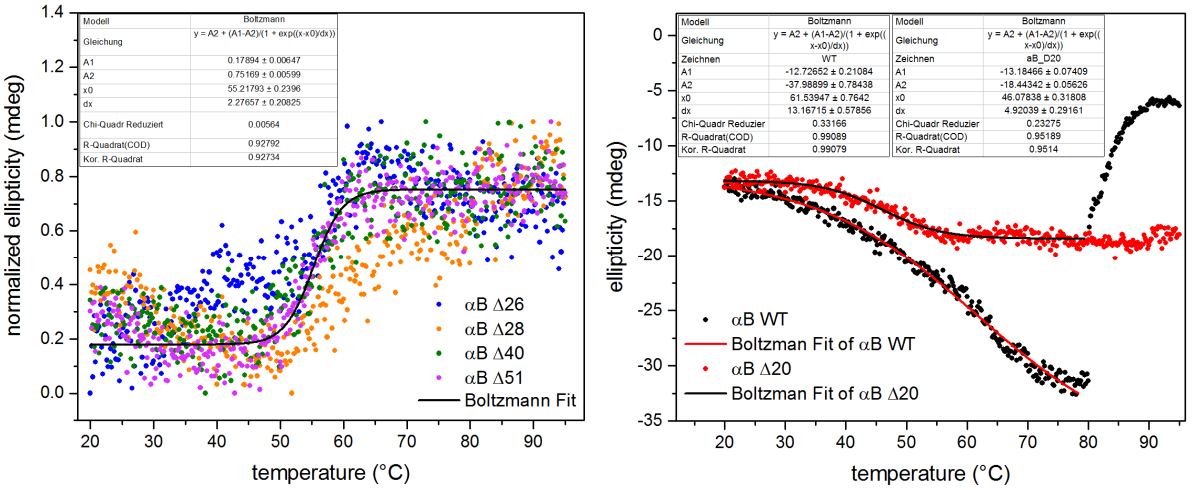

Fig. 17: Thermal transitions of αB WT and deletion variants monitored by CD-spectroscopy. Derived melting temperatures are 61 ± 0.8°C for WT, 46.1 ± 0.3°C for Δ20 and ~55-60°C for Δ28, Δ40 and Δ51. For Δ26 a second transition can be assumed at about 37°C. For WT and Δ20 these temperatures indicate secondary structure rearrangements in the NTR upon temperature increase rather than unfolding.

Thermal transitions using SYPRO Orange (TSA) show changes in protein hydrophobicity that usually correlate with unfolding and exposure of the hydrophobic protein core. Therefore, this method does not only detect changes in secondary structures like CD-spectroscopy. The oligomeric nature of α-crystallin with its hydrophobic, flexible NTRs impedes the determination of mono or biphasic transitions with midpoints from TSA assays. Nevertheless, some information might be derived from the curves (fig. 18).

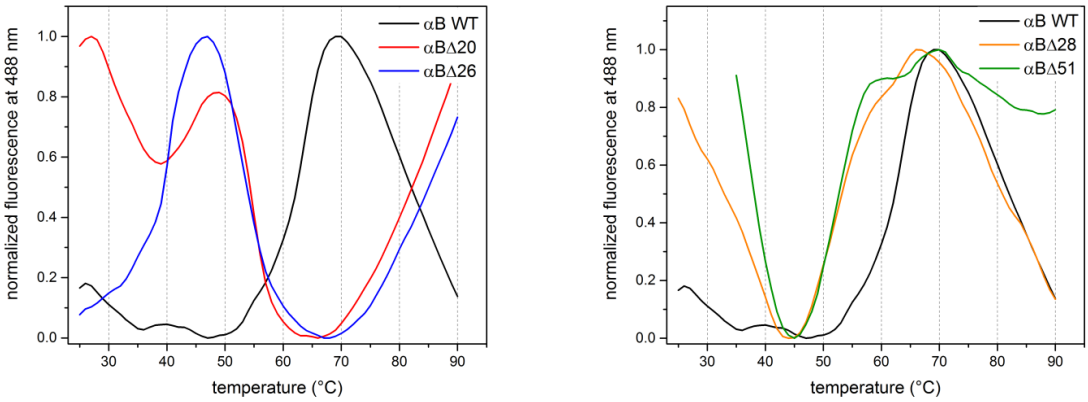

Fig. 18: Temperature-dependent change of SYPRO Orange fluorescence signal at 585 nm in the presence of αB WT and deletion variants (Thermal Shift Assay). Exposure of hydrophobic patches is observed for αB Δ20 and Δ26 around 40°C.

If a transition midpoints could be estimated from the curves, the transition temperatures of αB WT, Δ28 and Δ51 are in agreement with the T_m-values determined by CD-spectroscopy, ~63°C and ~55°C respectively, although the observed transition of αB WT is more defined in the TSA-assay. For Δ20 and Δ26, the TSA results differ significantly from the CD-spectroscopy data. Both deletion variants exhibit similar transitions around 40-45°C. This temperature range overlaps with heat-shock temperatures that are used in chaperone assays. These transitions were not observed in CD spectroscopy which implies that the origins of the observed transitions are presumably rearrangements in ternary or quaternary structure resulting in exposure of hydrophobic patches.

Surface hydrophobicity

The overall hydrophobicity of each mutant at 25°C was assessed by change in ANS fluorescence upon binding to the different αB-variants (fig. 19). Deletion of the first 20 residues already decreases the hydrophobicity drastically. Deleting more of the NTR leads to further signal decrease. Surprisingly, the first 20 residues have a big influence, although in the hydrophobicity plot, the first residues show similar scores than the remaining part of the NTR.

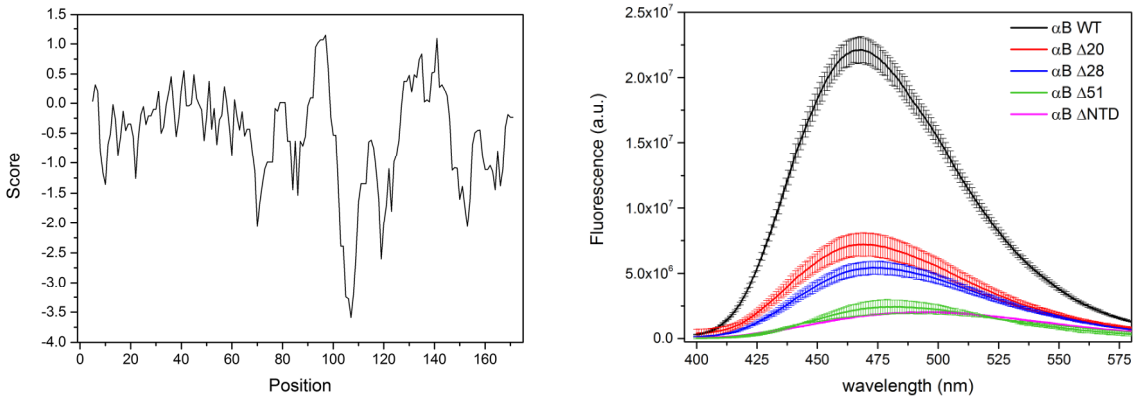

Fig. 19: left: Calculated hydrophobicity score of αB-crystallin (Kyte and Doolittle, 1982); **right:** ANS-fluorescence spectra in the presence of αB WT and deletion variants. The overall hydrophobicity decreases rapidly with increasing length of deletion.

Quaternary structure

To analyze the influence of the deleted part of the NTR on their oligomeric size, the variants were characterized by aUC. To assess the effect of physiological temperature on the molecular structure a temperature screening was first performed using αB WT (fig. 20).

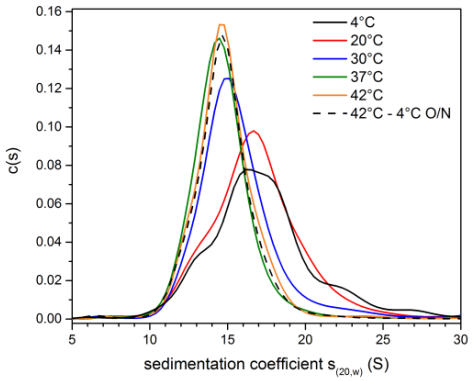

Fig. 20: Temperature dependent normalized c(s)-distributions of αB WT obtained by aUC and analysis with Sedfit after freezing the purified protein in aliquots in $N_{2(l)}$ and storage at -80°C; Artificially induced interactions presumably formed during freezing or storage can be reversed by pre-equilibration at 37°C or higher resulting in a more heterogeneous size distribution.

After storage at -80°C, the oligomer assembly seems to adopt different conformations with sedimentation coefficients of ~ 16 S compared to the physiological temperature range ($s_{(20,w)} \approx 14$ S). The reversibility was tested by first incubating the samples at the respective temperatures followed by a temperature shift to 4°C and overnight incubation. Reversibility to a more heterogeneous distribution could not be detected after subsequent incubation at 4°C over night, indicating artificially induced structural arrangements originating from the freezing process of the purified protein as opposed to a fast temperature-dependent activation mechanism. A possible mechanism could be π-π interactions between the numerous aromatic and arginine side chains at low temperatures in the frozen state.

To analyze if this shifts can also observed for the deletion mutants, aUC analysis was performed after pre-incubation at 4°C and 37°C (fig. 21).

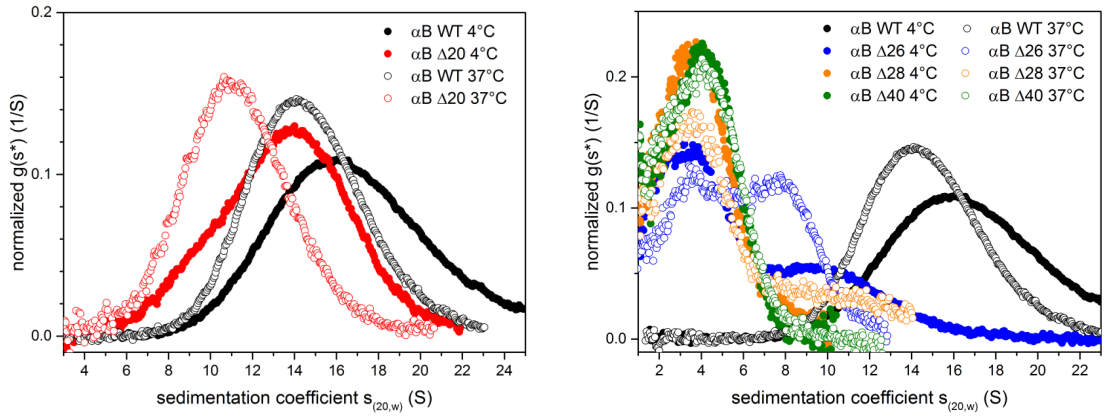

Fig. 21: Temperature dependent normalized g(s*)-distributions obtained by aUC and analyzed with dcdt+; **left:** αB Δ20 in comparison to αB WT, deletion of residue 1-20 does not impair the ability to form large oligomers **right:** αB Δ26, Δ28 and Δ40 in comparison to αB WT after incubation at 4°C and 37°C. Only αB Δ26 is able to form oligomers with sedimentation coefficients of 8-10 S.

αB Δ20 is still able to form large oligomers similar to αB WT with a sedimentation coefficient of ~14 S). After pre-incubation at 37°C, the same shift towards a more homogenous population at a smaller sedimentation coefficient of ~ 10 S could be observed. The molecular weight could not be determined exactly, but analysis using Sedfit (P. Schuck) hints to ~20-mers at 4°C for Δ20, while after incubation at 37°C the resulting molecular weight resembles the molecular weight of dodecamers.

The mutant αB Δ26 seems to consist of a fraction of small oligomers of ~4 S, that do not undergo temperature-dependent rearrangements, and a fraction of higher order oligomeric species that shows a temperature-dependent shift from 10 S to 8 S. In contrast, αB Δ28 forms mainly small oligomeric species with a sedimentation coefficient of ~ 4 S and Δ40 forms small assemblies exclusively. The molecular weight of the small species with a sedimentation coefficient of about 4 S could not be determined exactly from the obtained aUC data, but it can be assigned to species ranging between trimers to maximum hexamers.

4.1.1.3 Functional characterization of all deletion variants

To correlate effects of oligomer size and hydrophobicity to activity, chaperone assays were performed using MDH and CS as model substrates. In experiments with αB WT it turned out that MDH is chaperoned efficiently and its aggregation is also partially suppressed when MDH is present in molar excess (fig. 22).

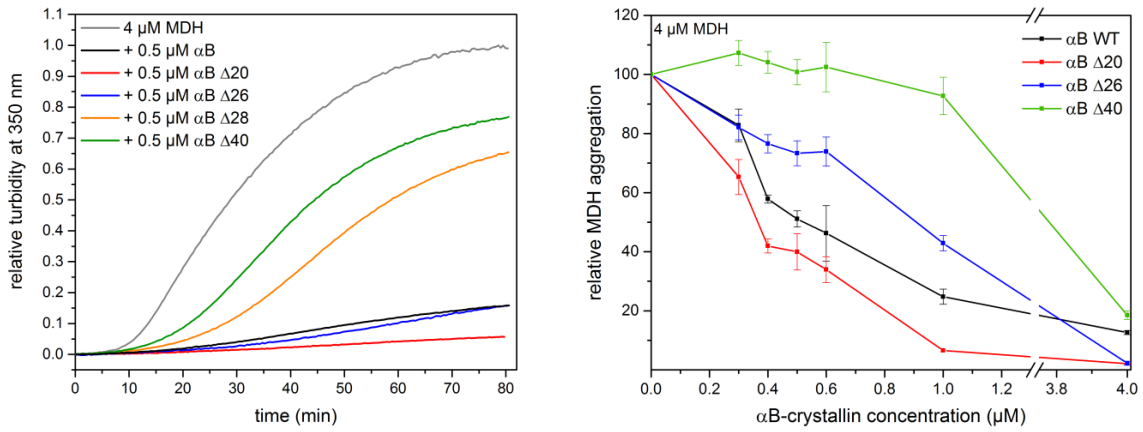

Fig. 22: Chaperone assay of αB WT and the different deletion variants. Thermally induced aggregation of heat sensitive MDH was monitored at 350 nm in a Cary50 spectrometer at 42°C in presence of different αB-crystallin variants. **left:** Representative assay with 4 µM MDH + 1 µM αB-variant showing increasing turbidity of the solution with time; **right:** 4 µM MDH were incubated with different concentrations of αB and maximal aggregation was plotted against αB-concentration.

As shown in fig. 22 no direct correlation between chaperone properties of α-crystallin towards MDH and number of deleted residues could be determined. Surprisingly, deletion of the first 20 aa, containing one Trp and three Phe residues, improves aggregation suppression ability, although the deletion decreases the observed surface hydrophobicity. Deletion of 26 residues does not decrease activity compared to WT whereas deletion of the first 28 residues or more strongly abolishes chaperone function. At higher concentrations of α-crystallin the mutants Δ20 and Δ26 both show a better performance than WT, whereas Δ28 and Δ40 exhibit a significantly lower activity.

In contrast to MDH, CS-aggregation is not suppressed completely at equimolar ratios by WT (fig. 23). Under the used experimental conditions, WT is only capable of preventing maximally 50% of CS-aggregation. Therefore, it is suitable to analyze the effect of mutants on CS aggregation that exhibit a manifold higher activity in MDH assays. Furthermore, substrate preferences can also be studied conveniently.

As shown in fig. 23, the tendencies from MDH-assays are even more pronounced for CS. The mutants Δ20 and Δ26 show a better performance than WT inhibiting ~90% and ~70% of relative turbidity respectively. Δ28 shows comparable activity to WT with inhibition of about ~40% and Δ40 does not inhibit any aggregation at the analyzed concentrations.

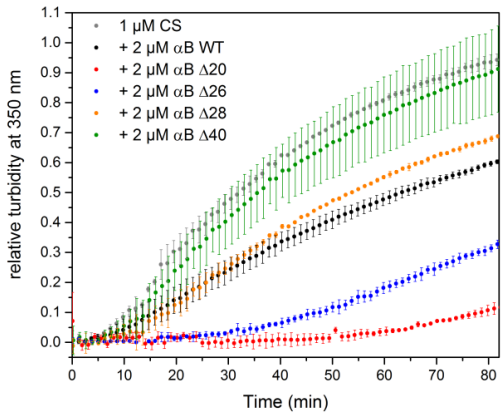

Fig. 23: Chaperone assay of αB WT and the different deletion variants. Thermally induced aggregation of heat sensitive CS (1 µM) was monitored in a Cary50 spectrophotometer at 42°C in the presence of 2 µM of the different αB-crystallin variants.

4.1.1.4 Influence on subunit exchange

To analyze subunit exchange kinetics of αB-crystallin variants, a new FRET-System had to be established due to unavailability of one of the established labels (lucifer yellow). AlexaFluor® 350 and AlexaFluor® 488 were chosen. These labels are relatively small and

hydrophilic and did not disturb αB-crystallin SX-behavior, which is sensitive to large, hydrophobic labels that interfere with correct oligomer assembly. With this label combination a good FRET-signal could be achieved. Complex formation of the AlexaFluor® 350 and AlexaFluor® 488 labeled αB S153C-batches was observed by recording spectra at different time points after mixing the two components at 1 µM concentration of each component at 37°C (fig. 24).

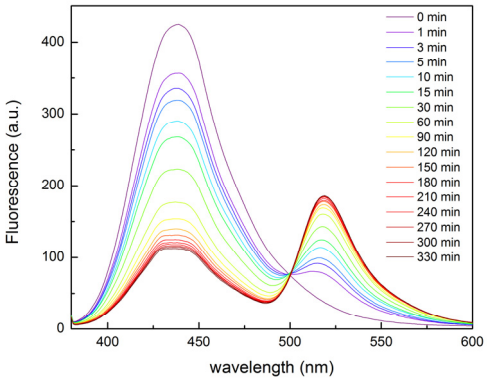

Fig. 24: Subunit exchange of αB WT. Fluorescence spectra at different time points during incubation of 1µM AlexaFluor350® labeled αB S153C with 1µM AlexaFluor488®-labeled αB S153C at 37°C.

SX-kinetics for αB WT and the analyzed mutants were determined by addition of 40 µM unlabeled αB-variants to the preformed complex consisting of the two labeled components as performed in previous studies (Peschek, 2012). The increase of donor fluorescence was fitted with a single exponential model (equation 5) to determine the exchange rate constants (fig. 25) (Bova et al., 1997).

$$Y = A + B \times e^{(-kx)} \tag{5}$$

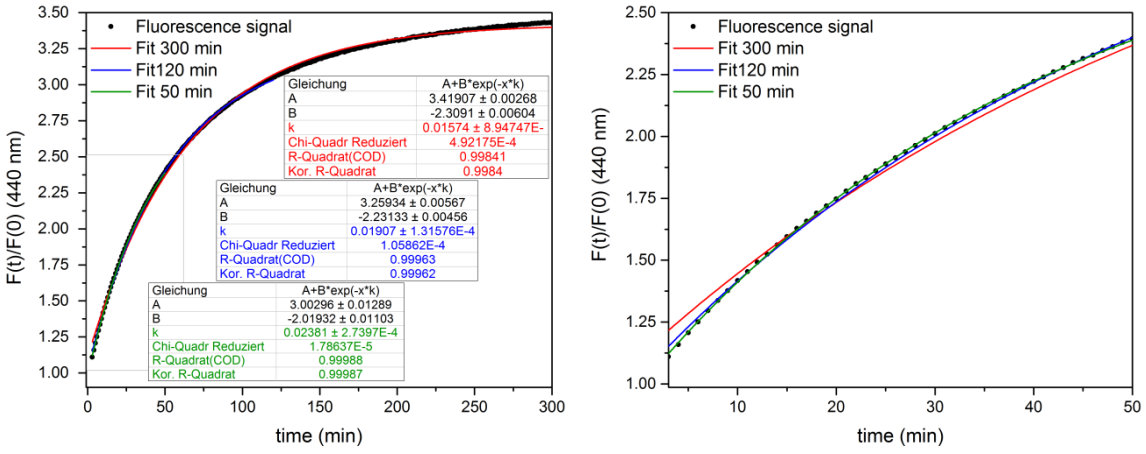

Fig. 25: Subunit exchange kinetics of αB WT. Increase of donor fluorescence during incubation of preformed mixed complexes of 1µM Alexa350®- and 1µM Alexa488®-labeled αB S153C at 37°C with 40 µM unlabeled αB WT. Single exponential fitting was performed for different data ranges (50, 120 and 300 min) to show the improvement of fit quality for smaller time ranges.

Single-exponential fitting of the obtained data did not result in a perfect fit due to a linear increase of the donor signal when equilibrium was reached. In control measurements it could be determined, that addition of unlabeled αB WT to Alexa350®-labeled αB S153C resulted in the same linear signal increase. The change in fluorescence is most presumably due to structural rearrangements in the oligomer after subunit exchange is almost completed. The effect observed for WT was more pronounced for some of the analyzed mutants increasing with faster SX-kinetics and higher structural divergence. This issue has been encountered before in analyses of SX of other macromolecular complexes (Sugiyama et al., 2011). This observation can be explained by the high sensitivity of some fluorescent labels to changes in their molecular environment. To avoid artifacts in the determination of rate constants and to improve fit quality (fig. 25), only the first 50 min after mixing were used for data analysis.

The only deletion mutants analyzed so far concerning SX exchange and compared to αB WT were Δ20 and Δ51. To analyze subunit exchange, a 1:1 mixture of WT and Δ20 was incubated at 37°C over night and analyzed by aUC (fig. 26). The mixture resulted in a sedimentation coefficient distribution that represents a mean of both single components which shows, that the first 20 residues are not essential for subunit exchange. In fig. 26 the subunit exchange kinetics of WT, Δ20 and Δ51 are shown. The rate constant of subunit exchange for αB WT was determined as 0.024 min^{-1} which is in good agreement with the published value (0.02 min^{-1} Peschek (2012)), Δ20 exhibits a 4.5-fold higher rate constant of 0.09 min^{-1} similar to Δ51 with 0.08 min^{-1}, but the increase in donor and decrease in acceptor fluorescence is significantly lower for Δ51 than for WT and Δ20. This indicates a higher affinity of labeled αB S153C to full-length αB than to the N-terminally truncated variant. SX exchange seems to be impaired when a majority of the NTR is missing.

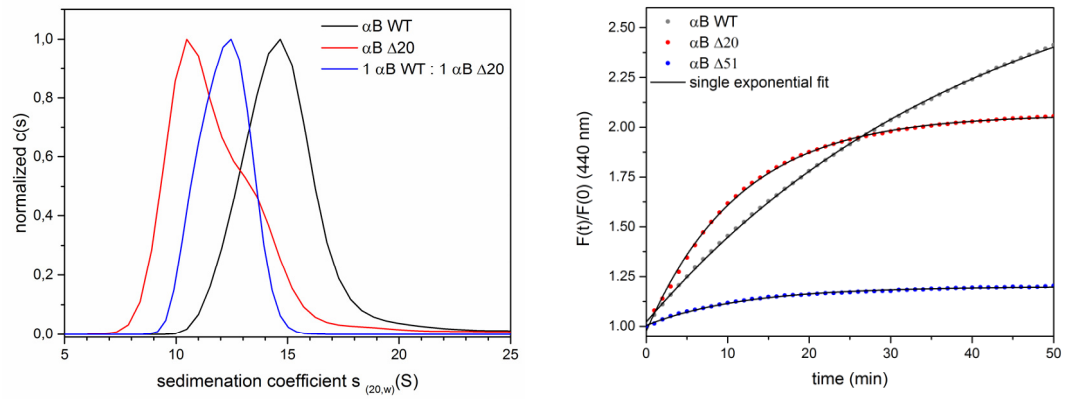

Fig. 26: Subunit exchange of αB WT and Δ20. **Left:** aUC analysis of a 1 : 1 mixture of WT and Δ20 and comparison to the c(s)-distributions of the single components. **Right:** SX-kinetics determined by monitoring the donor fluorescence increase after adding 40-fold excess of unlabeled WT, Δ20 or Δ51 to a preformed complex of 1µM Alexa350®- and 1µM Alexa488®-labeled αB S153C at 37°C.

Taken together, the chaperone assays show increased activity for variants that are still able to form higher order oligomers, which is the case for αB WT, Δ20 and with restrictions for Δ26 as well. Deletion of residues 1-20 including several aromatic, hydrophobic residues even improves chaperone function. In contrast, deletion of residues 1-28 which include the highly conserved sequence ^{21}SRLFDQFF^{28}, diminishes the ability to form larger oligomeric assemblies and chaperone function at the same time. From these data it can be derived, that the putative α-helical region between residue 21 and 28 might be necessary for substrate binding. However, in 2003 the conservation of this sequence in different sHsps was analyzed and the influence of deletion of these residues in αA and αB was published (Pasta et al., 2003). The published data show the same trends as observed for Δ1-20 in this study. Deletion of residues 20-28 leads to formation of smaller oligomers with faster subunit exchange kinetics, lower stability and higher activity in chaperone assays. However, the reported surface hydrophobicity of the published deletion Δ21-28 was higher compared to WT, while the hydrophobicity observed in this study was lowered.

Deletion of the sequence ^{54}FLRAPSWF^{61} also showed the correlation between N-terminal deletion and increased chaperone activity, a shifted oligomer equilibrium to smaller assemblies and higher subunit exchange rates (Santhoshkumar et al., 2009). From these observations several conclusions can be derived: From the increased activity upon deletion of either 1-20 or 21-28, either can be excluded as single main substrate recognition or binding site, although many aromatic residues are located in both of these parts. These residues were assumed to play an important role for chaperone activity in αB as well as in other sHsps (Hanazono et al., 2013; Kelley and Abraham, 2003). However, at least one of the two stretches is necessary for restoring oligomer formation ability and chaperone function. Deletion of either of these regions leads to oligomer destabilization as well as to increased chaperone activity and higher subunit exchange rates at the same time. The underlying molecular mechanism for the observed effects might be the same for deletion of short N-terminal stretches.

After determination of the special role of the very beginning of the NTR, a closer look was taken at the individual amino acids in this region. Different point mutations were introduced mainly in the conserved region 21-28, but also outside of it to examine e.g. the effect of different charges in the NTR.

4.1.2 Impact of point mutations in the NTR on αB-crystallin

To analyze the influence of different physicochemical properties of the amino acid side chains in the NTR in more detail, single and double point mutations were generated and analyzed. The following sets of mutations were chosen:

Aromatic residues could play an important role in substrate binding due to their hydrophobic nature (Heirbraut, 2015). To assess their effect, conserved Phe-residues at position 24, 27 and 28 were exchanged to either apolar Ala- or negatively charged Glu-residues. In other human small heat shock proteins, Phe 27 is least conserved within this amino acid stretch (fig. 27).

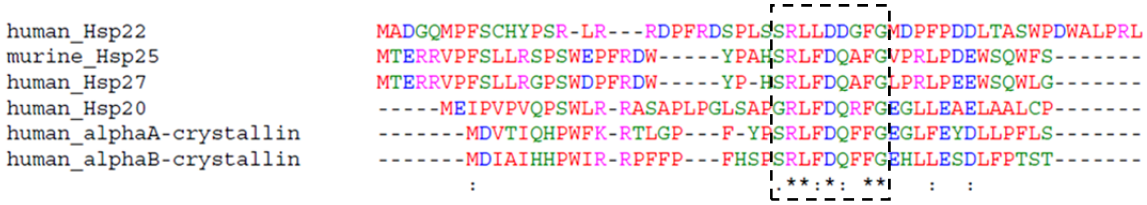

Fig. 27: CLUSTAL O (1.2.1) multiple sequence alignment of partial N-terminal regions of six different sHsps showing the conservation of the SRLFDXF-motif, generated with Clustal Omega (Sievers et al., 2011).

In Hsp27 it is replaced by an alanine and in Hsp20 by an arginine residue. The most outstanding sHsp of the human proteins listed in fig. 27 is sHsp20. When analyzed *in vitro*, Hsp20 forms only dimers and exhibits a poor chaperone activity (van de Klundert et al., 1998). This is of special interest since Hsp20 shares a high sequence homology with α-crystallin. The shortened CTR of Hsp20 is the most obvious difference (fig. 28).

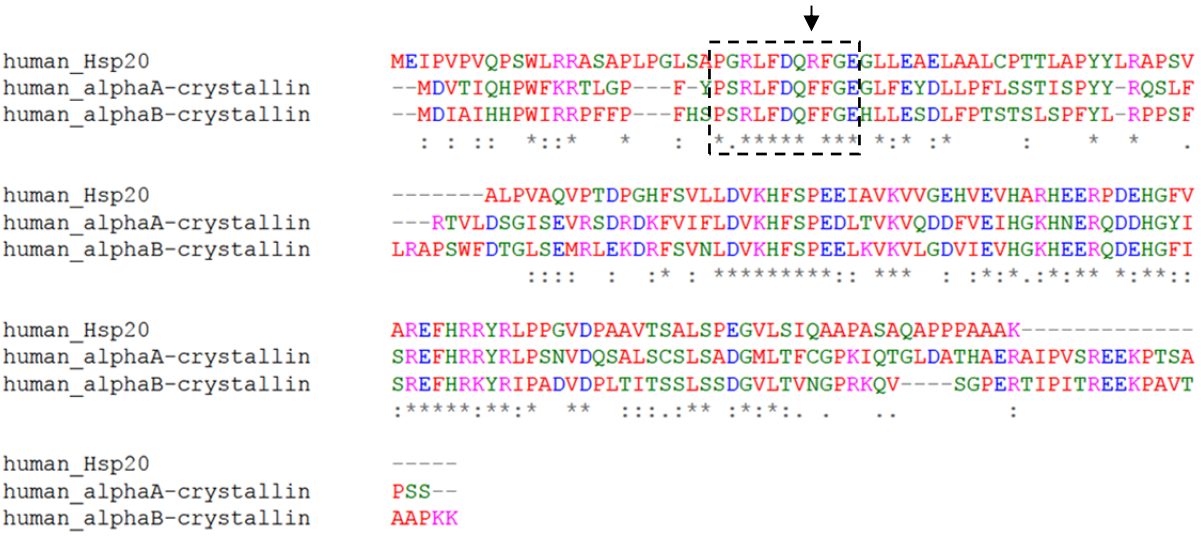

Fig. 28: CLUSTAL O (1.2.1) multiple sequence alignment of dimeric human Hsp20 and oligomeric αA- and αB-crystallin displaying the high sequence similarities; generated by Clustal Omega (Sievers et al., 2011).

Due to the different properties of Hsp20, the effect of Arg at position 27 - the only residue that is not conserved in Hsp20 - was analyzed in αB WT (fig. 28). To avoid potential overruling of the F27R-effect by the Phe-rich region 1-20, that is not present in Hsp20, the mutation was also introduced to the Δ20-deletion mutant (αB Δ20 F27R).

Additionally to the described Phe-residues, Trp9 and Trp60 were mutated to Cys to analyze changes through loss of the two only tryptophan-residues in the whole α-crystallin sequence as well as to analyze the effect of N-terminal crosslinking by disulfide bond formation on its structure and function.

Displacement of charged residues with uncharged amino acids was analyzed with another set of mutations consisting of R11A, R22Q and E34Q. The Arg-residues 11 and 22 were chosen for two reasons: Firstly, arginines are overrepresented in the NTR of sHsps and could therefore play an important role. Secondly, R11- and R22-mutations in αA- and αB-crystallin were found to be involved in cataract-formation (Chen et al., 2010; Laurie et al., 2013). A recent review also emphasizes the role of Arg-residues in α-crystallin (Panda et al., 2016).

In the third group of mutants the helix-breaking amino acid Pro was introduced at positions of F24 and Q26. It was assumed that introduction in the middle of the predicted α-helical region 20-28 could induce significant changes in the system. As a control, F24A and Q26A were also analyzed.

The Pro-content of the NTR of αB-crystallin is relatively high with 13.9% compared to the average proline abundance in proteins (9.7% overall Pro content in full-length αB and 6.3% in bioinformatical studies with 18,666 human proteins (Morgan and Rubenstein, 2013)). To analyze the importance of prolines in αB-crystallin, P39 was exchanged to Q. P39R was already analyzed and found to change size and activity which marks it as a potentially important residue (Numoto et al., 2012).

All three groups of mutations were compared to the WT protein concerning their quaternary structure, chaperone activity and subunit exchange kinetics.

The mutants were purified from *E. coli* lysate in good yields. All proteins were identified as αB by tryptic digest followed by MALDI-Tof analysis and comparison to the Mascot database. Additionally all molecular weights were determined by full-length measurements to assure the correct mutation was purified.

4.1.2.1 Influence of aromatic residues in the NTR

4.1.2.1.1 Role of the conserved phenylalanine residues at position 24, 27 and 28

Quaternary structure

As a first characterization, the purified mutants were analyzed by aUC to determine changes in quaternary structure. The exchange of Phe to either Ala or Glu showed the same effects for Phe 24 and 27. As observed in the study of the N-terminal αB phospho-sites (Peschek, 2012), introduction of Ala does not lead to significant changes in the sedimentation coefficients obtained by SV-aUC. However, mutation to Glu leads to a decrease in sedimentation coefficients of about 2 S compared to WT (14.6 S). This is presumably the result of the introduced negative charges leading to an electrostatic repulsion and thereby to oligomer dissociation like observed before (Peschek et al., 2013). Phe28 shows a slightly different effect. Introduction of Ala leads to a minor increase in sedimentation coefficients of about 1 S, whereas introduction of Glu induces a shift of about 1 S to smaller sedimentation coefficients compared to WT. The influences of replacement of Phe28 by Glu seem to compensate resulting in an overall g(s*)-distribution of F28E very close to the WT distribution. The F28A mutation indicated that - in contrast to F24 and F27 - the presence of a phenylalanine at this position is more important for oligomer integrity. This is also supported by the fact that F28 is the best conserved of these three residues (fig. 29).

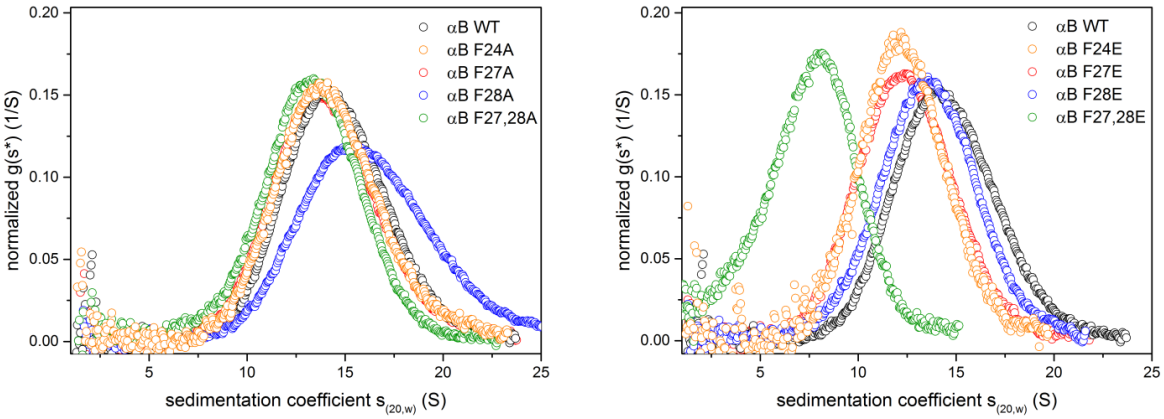

Fig. 29: Normalized g(s*)-distributions obtained from aUC data analyzed with the dcdt+-software package by John Philo; all samples were pre-incubated at 37°C over night; l**eft:** distributions of different Phe to Ala mutations; only F28A shows different sedimentation behavior; **right:** g(s*)-distributions of different Phe to Glu mutations; shifts to smaller sedimentation coefficients can be observed for all samples to different extent.

Double mutations of F27 and F28 to Ala compensate the observed effect for F28A. The double-A mutant shows WT-like sedimentation behavior. In the double E-mutants the effects observed for the single mutants are even amplified leading to an overall shift of the s-value of

about 6 S from WT (14.6 S) to F27, 28E (8 S). This is a larger shift than observed for the published αB-3E (weight average $s_{(20,w)}$ = 12.2 S). A slight 'fronting' of the peak is visible which indicated the presence of even smaller species with a sedimentation coefficient of about 4S. (fig. 29). This could be confirmed using Sedfit (P. Schuck) providing higher resolution analysis (fig. 30). The frictional ratio for all three samples obtained from Sedfit analysis is ~1.2 indicating a mainly globular shape of all analyzed oligomers. The resulting molecular weights correspond to 16 subunits for WT and F27, 28A. For F27, 28E two different species resulted from the fit with ~3 and ~8 subunits. These data were obtained from pre-equilibrated samples (37°C) and therefore the results do not necessarily match older results from not-equilibrated samples since, as shown before, after storage at -80°C a different sedimentation coefficient distribution is obtained (fig. 20). The number of subunits calculated for WT in different aUC analyses ranges between 16 and 20 subunits depending on the best frictional ratio obtained from Sedfit analysis of different WT-samples.

Furthermore, it has to be kept in mind that these molecular weights are only calculated from the obtained sedimentation coefficients and have to be confirmed by other methods. The peak broadening that is always observed for the dynamic oligomer ensembles present in solution further complicates exact determinations of molecular weights by aUC. Nevertheless, it is a good benchmark for further experiments.

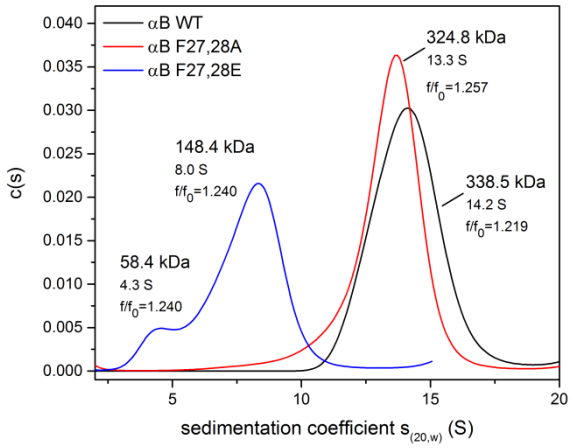

Fig. 30: Normalized c(s)-distributions obtained from aUC data analyzed with Sedfit (P. Schuck); the distribution of αB F27, 28A resembles the observed WT distribution resulting in different calculated average molecular masses of ~ 330 kDa corresponding to 16 subunits. The c(s)-distribution of F27, 28E contains two distinct species with average masses of ~60 and 150 kDa corresponding to an average of 3 and 7.5 subunits.

The Hsp20-like mutation F27R was also analyzed by aUC. With a sedimentation coefficient $s_{(20,w)}$ of about 15 S, F27R sediments WT-like and therefore differs from its 'counter-charge' mutation F27E. Peak-broadening was observed with slight tailing indicating a more

heterogeneous mixture in the F27R-sample, probably consisting of WT-like particles but also a certain number of larger, presumable less defined assemblies (fig. 31). Interestingly, this effect is not observed for Δ20 F27R which exhibits a similar sedimentation behavior as Δ20 ($s_{(20,w)}$ ≈10 S, fig. 31). The obtained subunit-number for the samples obtained from Sedfit analysis is ~12 subunits for Δ20 and Δ20 F27R.

In summary, introduction of a positive charge at position 27 mimicking the dimeric Hsp20 does not have the expected effect of oligomer disruption. If residues 1-20 are present, arginine seems to have a slightly disturbing influence on the oligomer equilibrium rendering the mutant a little aggregation prone. Deletion of residues 1-20 does not induce a significant change in oligomer size. This could either hint to an interaction of Phe 27 with the aromatic residues between position 1 and 20, which is not relevant for Δ20 F27R or this interaction is not relevant in the smaller oligomer assembly formed by αB Δ20 anyway. Furthermore, introduction of positively charged Arg does not result in the same effects as observed for introduction of the negatively charged Glu.

Since Arg is able to participate in π-π or cation-π interactions, it could also interact with the aromatic system possibly created by the large number of Phe-residues in the NTR resulting in different arrangements and destabilization due to the different geometries. More experimental data need to be collected to confirm this hypothesis.

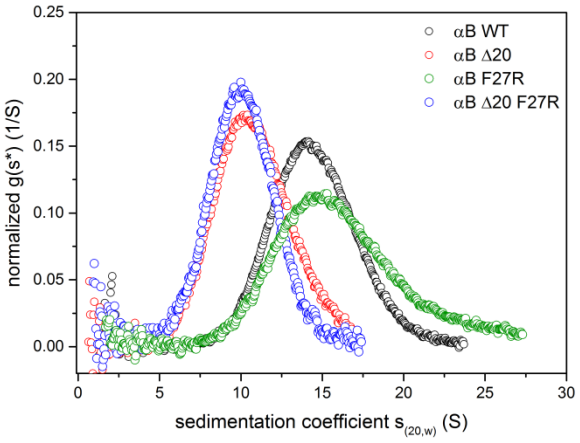

Fig. 31: Normalized g(s*)-distributions obtained from aUC data analyzed with the dcdt+-software; all samples were pre-incubated at 37°C over night. Δ20 and Δ20F27R have similar sedimentation profiles resulting in smaller $s_{(20,w)}$ of ~ 10S. The F27R sedimentation coefficient of 14.8 S resembles the WT sedimentation coefficient of 14.6 S, but the peak shows slight tailing.

Chaperone activity

The ability to prevent substrate aggregation was assessed using MDH and CS as model substrates (fig. 32). For MDH, all Phe to Glu-mutations show an increased ability to prevent

aggregation of MDH compared to WT. Surprisingly, F28A exhibits the same activity, whereas F24A has WT-like chaperone function. F27A could not be analyzed so far.

For CS, exchange of F24 to other amino acids did not improve function, whereas αB F27E prevented aggregation of CS almost completely, while the WT only suppressed slightly.

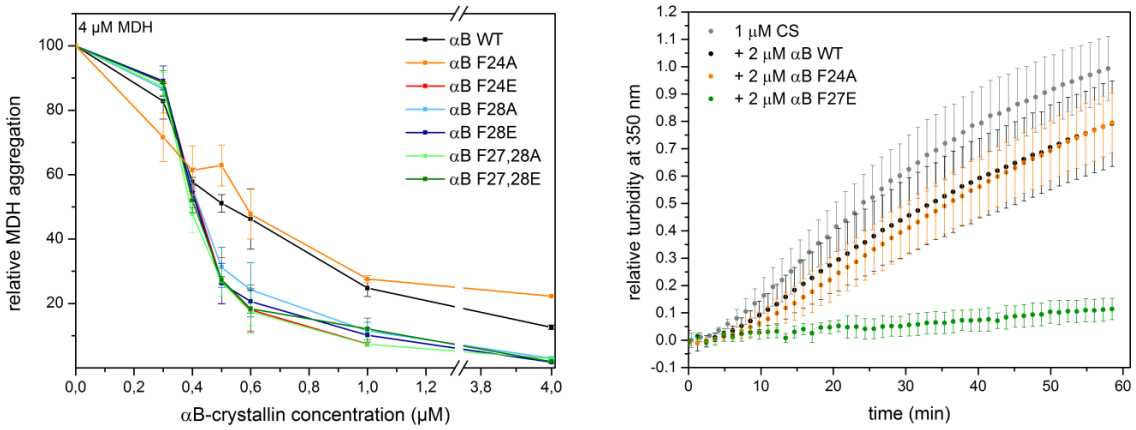

Fig. 32: Chaperone assays of αB WT and the different mutants using thermal denaturation of the used model substrates at 42°C. Solution turbidity was followed at 350 nm in a Cary50 spectrophotometer; **left:** 4 µM MDH were incubated with different concentrations of αB and maximal aggregation was plotted against αB-concentration; **right:** 1 µM CS was incubated with 2 µM αB.

The effect of the F27R mutation on chaperone function was analyzed in the MDH chaperone assays. Δ20 and Δ20 F27R were both able to prevent aggregation better than WT. In fig. 33 the results are shown in comparison to F27, 28A and F27, 28E. All four mutants exhibited a similar improvement in chaperone function. The only variant showing a decreased chaperone activity was F27R with about half the activity in suppression of aggregation.

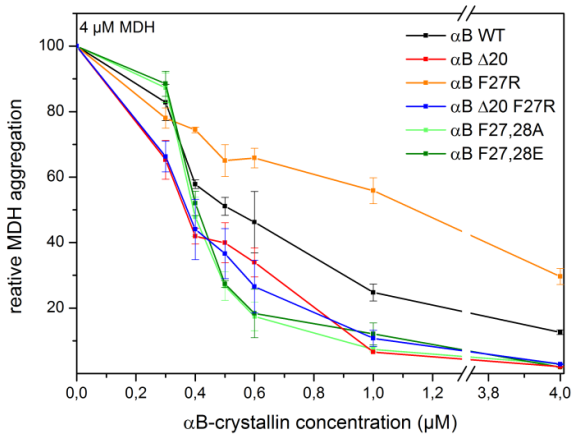

Fig. 33: Chaperone assays of αB WT and the different mutants using thermal denaturation of the used model substrates at 42°C. 4 µM MDH were incubated with different concentrations of αB and solution turbidity was monitored at 350 nm in a Cary50-spectrophotometer. Maximal aggregation was plotted against αB-concentration.

Comparing the results of aUC and activity assays, no clear correlation can be observed. The prevailing opinion of smaller oligomer assemblies leading to an increase in activity could not be confirmed for all mutants. F28A shows a small increase in size according to aUC, but show an equally high activity as the corresponding F28E. F27, 28A has a WT-like size distribution and is more active, as well. Yet, all variants with smaller sedimentation coefficients were more active.

Subunit exchange

SX kinetics were recorded and analyzed as described for WT and Δ20 in section 4.1.1.4. The first 50 min. were fitted with a single exponential function (fig. 34) (Bova et al., 1997).

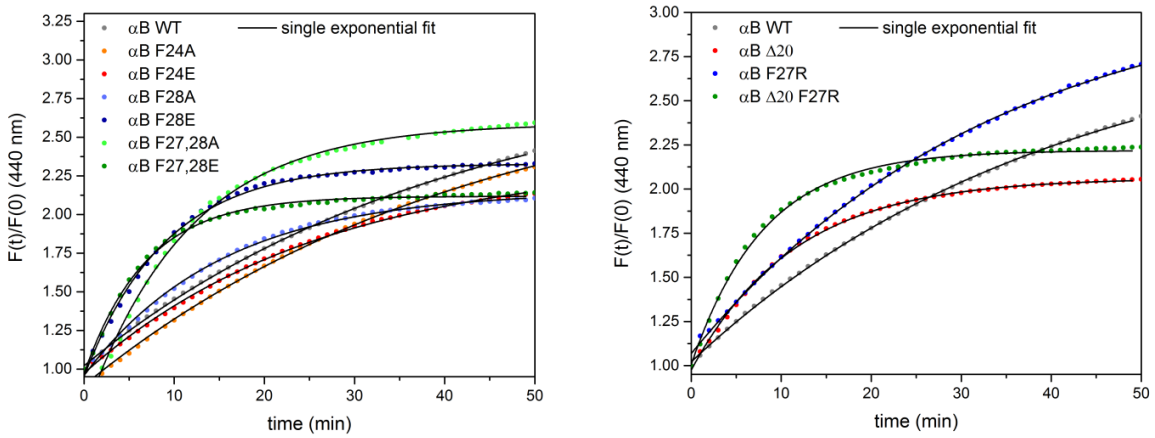

Fig. 34: Subunit exchange of αB-crystallin variants. SX-kinetics were determined indirectly by monitoring the donor fluorescence increase after adding 40 µM unlabeled αB-variants to a preformed complex of 1µM Alexa350®- and 1µM Alexa488®-labeled αB S153C at 37°C. SX rate constants k were derived from single exponential fitting.

Data were recorded for at least five hours to cover the entire exchange progress until the system reaches its equilibrium. After fitting the data, it could be observed that fit quality decreased for variants that exhibited faster subunit exchange kinetics. Therefore, only the first 50 min were used for fitting. It was shown for αB WT, that the fit quality improved, when only the first 50 min of the acquired data range were fitted (see section 4.1.1.4). This was found to be due to a linear signal increase, when the sx-equilibrium is reached. This linear signal contribution is not related to subunit exchange. For faster systems, the used data range and hence the fit quality had a big impact on the results. The rate constants for all mutants are summarized in tab. 3. To summarize F24A and F27R exhibit SX-rate constants similar to αB WT; F24E shows only a slight increase of SX-rate (1.5-fold) whereas the exchange rate of F28A is approx. three-fold higher compared to WT. Δ20 and the double

mutant F27,28A exhibit a four-fold increase and F28E, Δ20 F27R and F27,28E even a five- to six-fold increase in kinetics in the respective order. The rate constant of F27,28E of 0.146 ± 2 $x10^{-3}$ is comparable to 3E SX-rate of 0.142 ± 0.017 min^{-1} (Peschek, 2012).

Tab. 3: Subunit exchange rate constants for αB WT and the characterized Phe-mutants. Exchange of N-terminal Phe-residues to Glu induces an increase in SX-rate constants. Introduction of Ala at the same positions accelerates subunit exchange only at position 28.

αB variant	**SX rate constant (min^{-1})**
WT	0.024 ± 3 $x10^{-4}$
Δ20	0.089 ± 9 $x10^{-4}$
F24A	0.023 ± 9 $x10^{-4}$
F24E	0.037 ± 6 $x10^{-4}$
F27R	0.029 ± 6 $x10^{-4}$
Δ20 F27R	0.120 ± 2 $x10^{-3}$
F28A	0.065 ± 1 $x10^{-3}$
F28E	0.111 ± 2 $x10^{-3}$
F27,28A	0.088 ± 1 $x10^{-3}$
F27,28E	0.146 ± 2 $x10^{-3}$

Comparing subunit exchange kinetics to aUC and activity data, it can be concluded that mutants with WT-like size and WT-like SX kinetics have comparable chaperone abilities (F24A). F27R exhibiting a slightly increased subunit exchange rate and is dominated a more heterogeneous oligomer distribution with a tendency to form larger oligomers leading to a decrease in chaperone activity. The strong increase of the chaperone activity of F28A and F27,28A seems to be a consequence of their high SX-rates.

Size and SX-kinetics seem to influence chaperone function. A shift to smaller sedimentation coefficients is always accompanied with increasing SX-rates, but not vice versa.

The collected data of all mutants are summarized in section 4.1.3 (tab. 4) for a better overview.

4.1.2.1.2 Introduction of cysteine residues at position W9 and W60 of the NTR

αB-crystallin isoforms possess only two Trp-residues in the NTR, one at the beginning at position 9 and one directly at the end at position 60. To analyze if these residues are important for function, cysteine mutants were generated. Introduction of Cys has a second effect: If in close proximity, they can form disulfide bonds and thereby crosslink two neighboring subunits. This connection presumably is formed between 'inter-ACD-dimers'.

aUC was performed under reducing conditions adding DTT followed by 2 h incubation at rt, and without addition of DTT to analyze the state of air oxidation. The differences in monomer-dimer content were analyzed by SDS-PAGE with and without addition of 2-mercaptoethanol (fig. 35). Under non-reducing conditions ~70 % are involved in disulfide bonds.

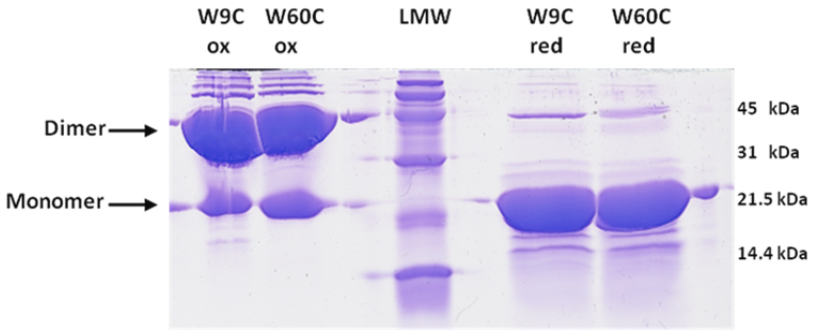

Fig 35: SDS-PAGE of purified αB W9C and W60C. In reduced samples, Laemmli-buffer containing 5% (v/v) 2-mercaptoethanol was used and samples were incubated for 3 min at 95°C. In not reduced 'ox'-samples, Laemmli-buffer without 2-mercaptoethanol was used. In the presence of reducing agent, some minor bands of oxidized dimers and higher order oligomers could be detected. Under non-reduzing conditions, dimers represent the main species with ~70% signal intensity while only and ~20% monomers are present and ~10% higher order multimers.

For aUC analysis, samples were incubated with and without DTT at 25°C and subsequently measured (fig. 36). All mutants show a very similar s-value distribution compared to WT. Only oxidized W9C shows a minor shift to larger sedimentation coefficients.

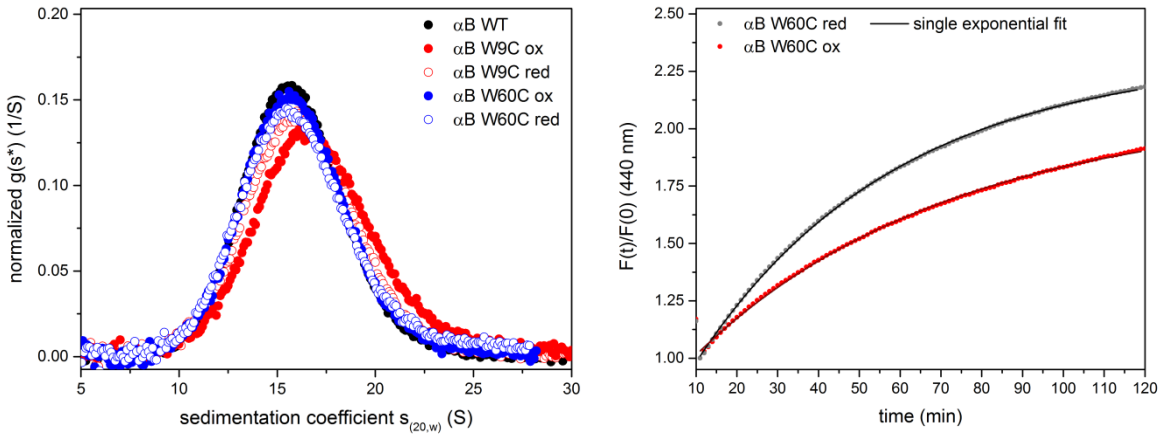

Fig. 36: left: Normalized g(s*)-distributions obtained from aUC data analyzed with the dcdt+-software package; WT and W60C ox were pre-incubated in PBS, W60C red was incubated in PBS + 1 mM DTT for 2 h at rt. **Right:** Subunit exchange of αB-crystallin variants. SX-kinetics were determined indirectly by monitoring the donor fluorescence increase after adding 40 µM unlabeled αB-variants to a preformed complex of 1µM Alexa350®- and 1µM Alexa488®-labeled αB S153C at 37°C. SX rate constants k were derived from single exponential fitting as 0.023 ± $1.7x10^{-4}$ min^{-1} for αB $W60C_{red}$ and 0.015 ± $1.7x10^{-4}$ min^{-1} for αB $W60C_{ox}$.

Like the other analyzed variants, the mutants were assessed in chaperone assays using MDH (fig. 37). In the presence of reducing agents, both mutants have WT-like chaperone properties. In the non-reduced state, the activity is strongly diminished at equimolar concentrations. The reason might be the decreased accessibility of substrate binding sites. There are two possible explanations for this observation. First, covalent linkage of the two positions in the NTR restricts the accessibility to potential binding sites located in the NTR. Another possible reason could be the inhibition of subunit exchange. A decrease of chaperone activity was reported to be connected to decrease subunit exchange rates before (Panda et al., 2016). To address this question, SX-kinetics were analyzed for the W60C mutant under reducing and non-reducing conditions (fig. 37) Subunit exchange is slowed down by introduction of disulfide crosslinks, but it is not completely impaired. Under reducing conditions, αB W60C exchanges subunits with WT-like kinetics (0.023 ± $1.7x10^{-4}$ min^{-1}) while under non-reducing conditions the exchange rate is decreased ~1.5-fold (0.015± $1.7x10^{-4}$ min^{-1}). This can be explained by a small amount of remaining free unlinked monomers and by the fact that also higher multimers could exchange. Too slow subunit exchange rate and decreased accessibility of potential binding sites in the NTR impair the chaperone function of αB-crystallin. This indicates that substrate recognition and binding takes mainly in the NTRs.

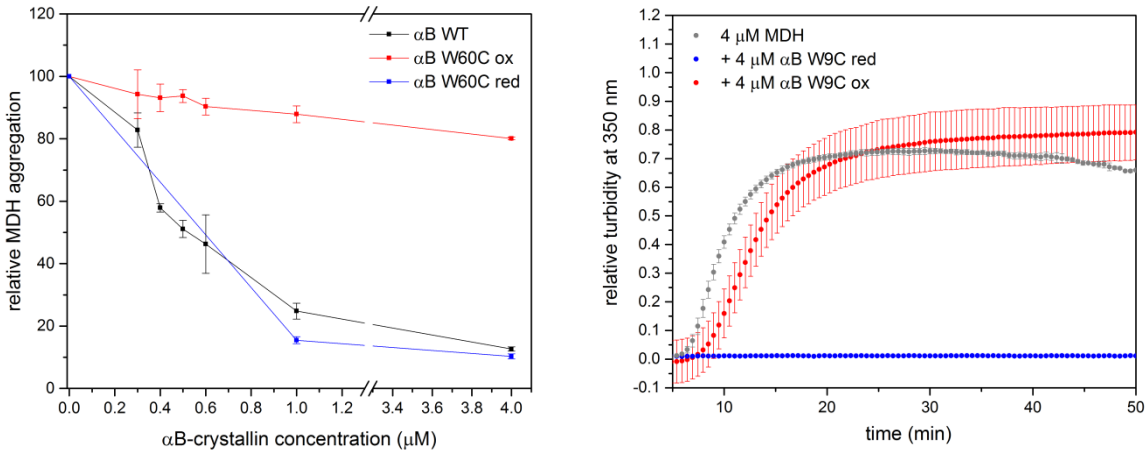

Fig. 37: Chaperone assays of αB WT and the different mutants using thermal denaturation of the used model substrates at 42°C. **left:** 4 µM MDH were incubated with different concentrations of αB W60C and solution turbidity was monitored in a Cary50-spectrophotometer. Maximal aggregation was plotted against αB-concentration. W60C red was preincubated in the presence of 1 mM DTT for 1h at rt. W60C ox was incubated without addition of reducing agent; **right:** 4 µM MDH were incubated with 4 µM αB W9C in the presence of 1 mM DTT or without DTT. Solution turbidity was followed at 350 nm in a Cary50 spectrophotometer.

4.1.2.2 Role of charged amino acids in the NTR

Charged amino acids are known to play an important role in regulation of activity and oligomer assembly (Peschek et al., 2013). Introduction of negative charged Glu-residues enhances activity and SX-kinetics of αB-crystallin and induce a shift in the equilibrium of oligomer distributions to smaller species (see chapter 4.1.2.1). Introduction of the positively charged Arg at Position 27 resulted in the opposite effects. Other studies were performed stating the importance of arginine-residues in the NTR of α-crystallin (Panda et al., 2016). Exchange of Arg11 to His in αB is related to congenital, nuclear cataract (Chen et al., 2009). Surprisingly, the *in vitro*-characterization showed that this mutation leads to an increased chaperone activity without large effects on size distribution (Chen et al., 2010). The mutation R21Q in αA is also related to congenital nuclear cataract (Laurie et al., 2013). To address the impact of Arg, both residues were mutated. For Arg11, Ala was chosen instead of His, since His could also carry a positive charge upon protonation. For Arg22, the corresponding position in αB, Gln was introduced according to the reported mutation found in be cataract associated in αA. Additionally, removal of a negative charged residue close to the conserved stretch 21-28 was assessed with E34Q. This exchange is especially suitable for analysis of the influence of charges since Glu and Gln are almost identical except for the functional group at the end of the side chain.

Quaternary structure

Analysis of these variants using SV-aUC resulted in the s-distributions shown in fig 38. Removal of both Arg-residues caused a slight shift to smaller sedimentation coefficients (~1 S), but the effect was less pronounced compared to the Phe to Glu mutations (~ 2S) at position 24, 27 and 28. E34Q showed the inverse behavior. A shift to bigger s-values was observed, accompanied by slight peak broadening (fig. 38). These mutants were also analyzed by negative stain-EM, revealing the same changes in size distribution. Additionally, a C-terminal mutant (R163A) located within the palindromic sequence ^{156}ERTIPITRE^{164} was analyzed for comparison. This mutant exhibits WT-like structural properties in EM, but increased heterogeneity in aUC analysis resulting in peak broadening (fig. 38).

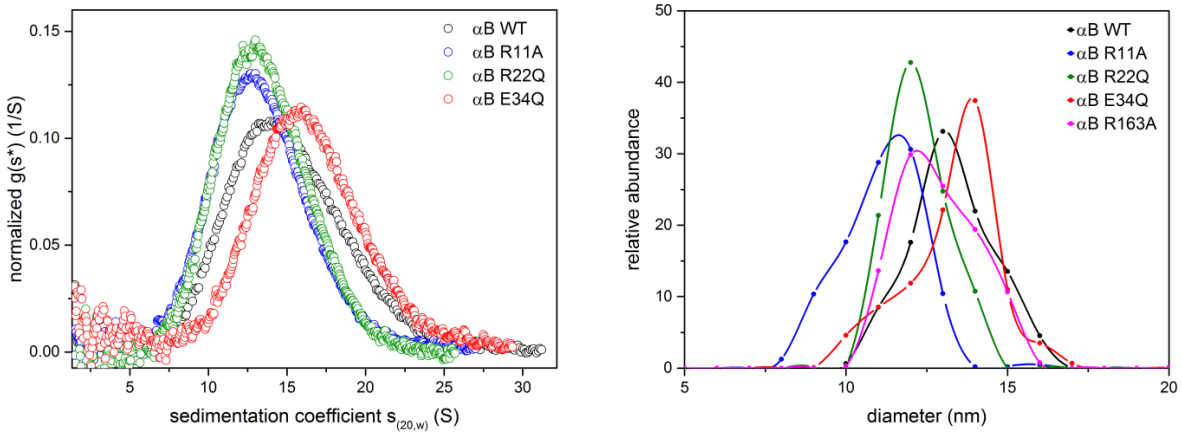

Fig. 38: left: normalized g(s*)-distributions of αB mutants in comparison to αB WT obtained by aUC and analysis with dcdt+. **right:** size distribution obtained by negative stain-TEM experiments performed by Dr. Christoph Kaiser.

Chaperone activity

Activity changes were analyzed using the thermal aggregation assays of MDH and CS in comparison (fig. 39). In MDH-assays, the R11H and R22Q mutants showed an increase in activity of about 40% compared to WT, while for E34Q a decrease in activity (~50%) was observed. R11H and R22Q also exhibit increased activity towards aggregation CS, while the C-terminal mutant R163A did not result in better prevention of substrate protein aggregation. E34Q has a slightly higher activity than WT.

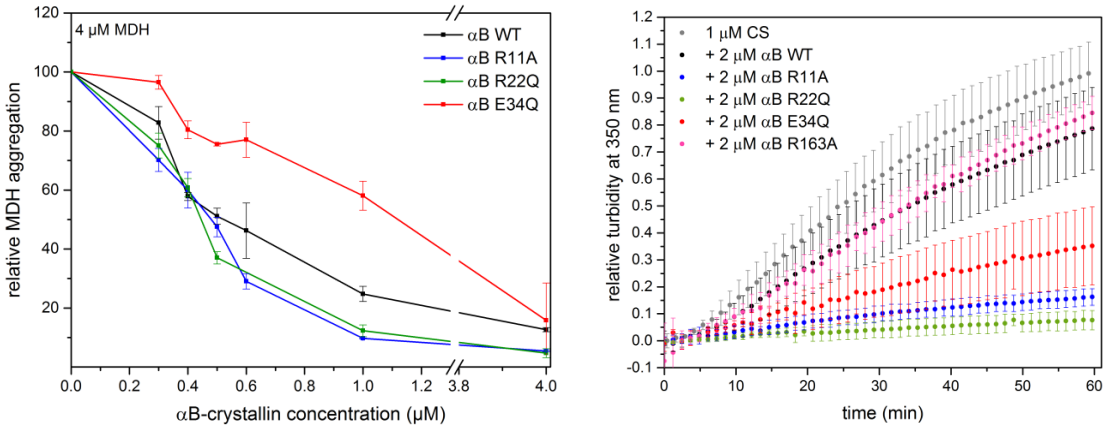

Fig. 39: Chaperone assays of αB WT and the different mutants using thermal denaturation of the used model substrates at 42°C. **left:** 4 µM MDH were incubated with different concentrations of αB and maximal aggregation was plotted against αB-concentration; **right:** 1 µM CS was incubated with 2 µM αB and aggregation was followed at 350 nm in a Cary50-spectrophotometer.

Subunit exchange

SX-kinetics were only analyzed for R22Q (fig. 40). The rate constant obtained from single exponential fitting was 0.038 ± 1 x 10^{-4} min^{-1}, a value which is ~ 1.5-fold increased compared to WT and similar to F24E.

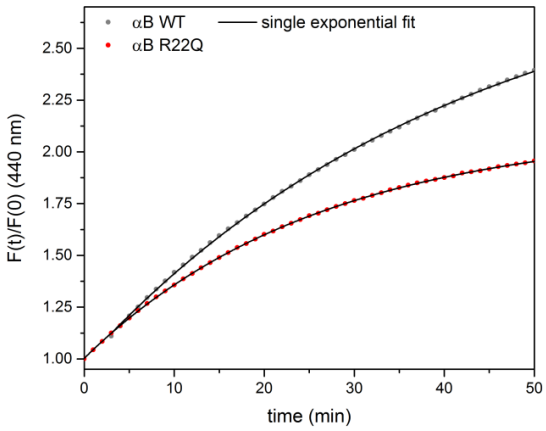

Fig. 40: Subunit exchange of αB-crystallin R22Q compared to WT. SX-kinetics were determined indirectly by monitoring the donor fluorescence increase after adding 40 µM unlabeled αB-variants to a preformed complex of 1µM Alexa350®- and 1µM Alexa488®-labeled αB S153C at 37°C. SX rate constants k were derived from single exponential fitting.

4.1.2.3 Role of Pro-Residues and secondary structure elements in the NTR

Introduction of prolines at positions F24 and Q26 and the corresponding alanine mutations as well as the P39Q mutation were also analyzed for size, activity and SX. The obtained results from all experiments differed significantly between mutations at positions 24 and 26.

Quaternary structure

Introduction of Pro at position 24 had a minor influence on the resulting sedimentation coefficient-distribution, shifting it to smaller s-values, while mutation to Ala resulted in a WT-like distribution. In contrast to this, a drastic change was observed for Q26A as well as for Q26P. Both distributions show a strong shift to larger oligomers with increased heterogeneity and tendencies to form larger aggregates. P39Q showed a WT-like size distribution (fig. 41). The larger oligomer dimensions could also be confirmed by negative stain-EM.

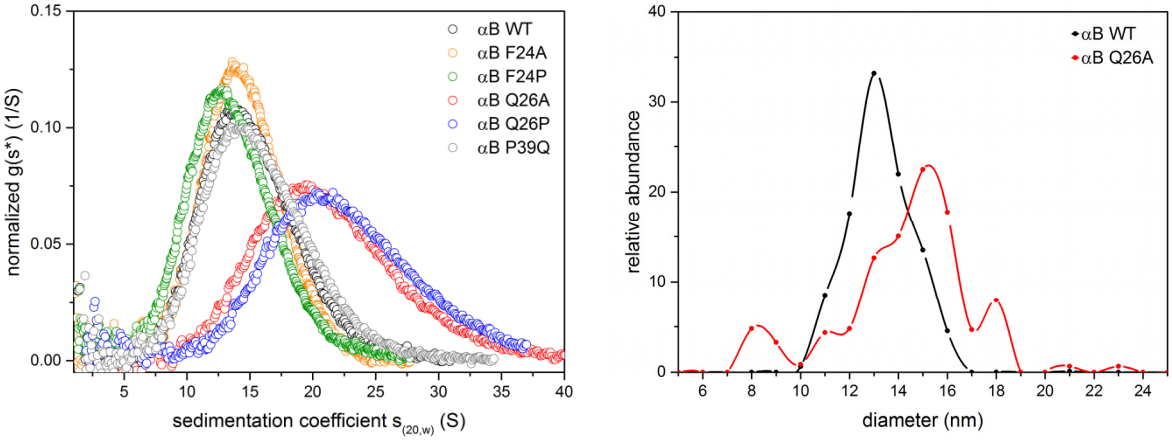

Fig. 41: left: Normalized g(s*)-distributions obtained from aUC data analyzed with the dcdt+-software; samples were pre-incubated at rt 37°C over night. No significant differences in g(s*)-distributions of F24A and P39Q compared to WT could be detected. F24P shows a slight shift to smaller sedimentation coefficients, while Q26A and Q26P sediment significantly faster accompanied by peak-broadening. **Right:** size distribution obtained by negative stain-TEM experiments performed by Dr. Christoph Kaiser.

Chaperone activity

The obtained data on functional differences are dependent on the analyzed model substrate. For MDH, the activity of all four variants resembles the WT. F24P exhibits a slightly decreased ability to protect MDH. Aggregation of CS is not suppressed by F24P. WT and F24A show the same ability of prevent CS-aggregation as well as P39Q with only slightly better efficiencies. A significant effect could be detected for Q26A and Q26P only, which inhibit CS-aggregation almost completely under the given experimental conditions (fig. 42).

The observations for these different Pro-mutants contradict the current picture for the chaperone mechanism of αB-crystallin. While the size distribution of F24P obtained by aUC is shifted to smaller weight-average sedimentation coefficients as observed for R11A, R22Q and other more active mutants, the chaperone activity of F24P is slightly decreased. In

contrast, Q26A and Q26P show strong shifts to larger sedimentation coefficients, but they seem to prevent aggregation of some substrates, like CS, more effective.

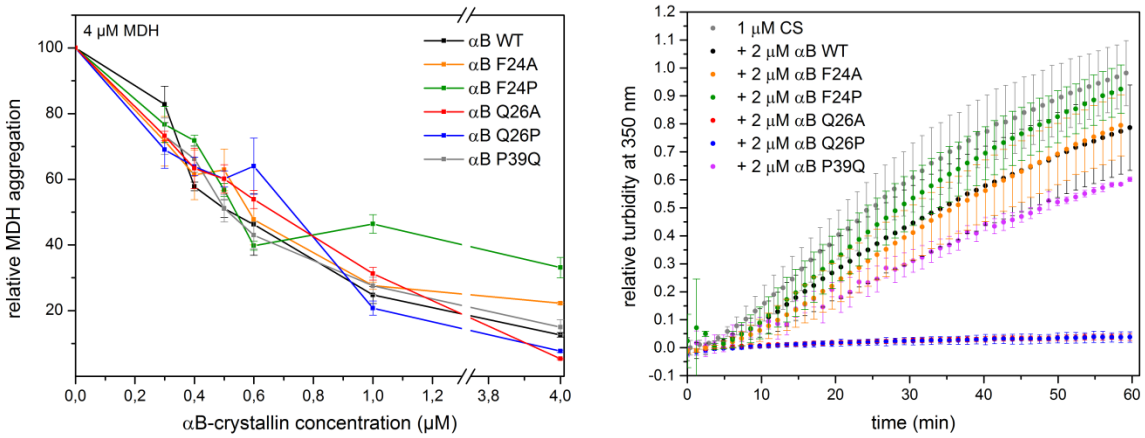

Fig. 42: Chaperone assays of αB WT and the different mutants using thermal denaturation of the used model substrates at 42°C followed at 350 nm in a Cary50 spectrophotometer. **left:** 4 µM MDH were incubated with different concentrations of αB and maximal aggregation was plotted against αB-concentration; **right:** 1 µM CS was incubated with 2 µM αB.

Subunit exchange

For Q26A and Q26P, SX-rates were determined. In fig. 43, donor fluorescence traces of αB WT, Q26A and Q26P are shown. The rate constants determined by single exponential fitting were 0.133± 3.8 x 10^{-3} min^{-1} and 0.132 ± 1.8 x 10^{-3} min^{-1}. This indicates a 5.5-fold increase in exchange kinetics compared to WT (0.024 ± 3 x 10^{-4} min^{-1}) and thereby the strongest increase observed for a single point mutation (tab. 4).

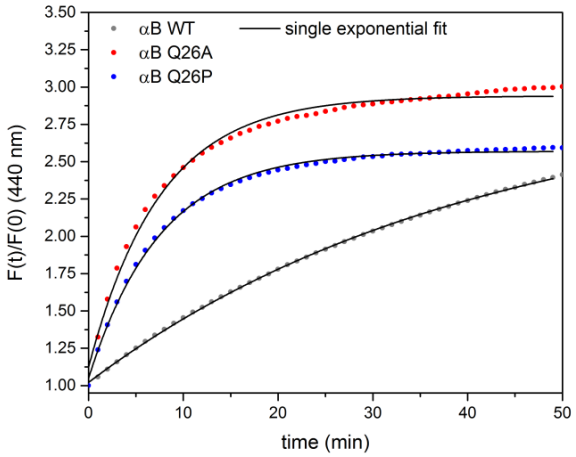

Fig. 43: Subunit exchange of αB-crystallin variants. SX-kinetics were determined indirectly by monitoring the donor fluorescence increase after adding 40-fold excess of unlabeled αB-variants to a preformed complex of 1µM Alexa350®- and 1µM Alexa488®-labeled αB S153C at 37°C. SX rate constants k were derived from single exponential fitting.

4.1.3 Summary and discussion

In tab. 4 all collected data of the analyzed mutants are summarized.

Tab. 4: Overview of the collected data on quaternary structure, chaperone activity, surface hydrophobicity and SX rate constants. For better comparison, WT-like properties are highlighted in yellow, decreased values compared to WT are highlighted in green, and increased values are marked in red except for chaperone activity. Here, an increase in activity is indicated by green color, while a decrease in shown in red. Different color shades indicate different degrees of change. White color indicates parameters that were not determined.

αB variant	Size (aUC)	Activity	Hydrophobicity (ANS)	SX rate constant
WT	14.3 S		22.1 ± 1.0 x10^6 a.u.	0.024 ± 0.3 x 10^{-3} min^{-1}
Δ20	10.4 S	++	7.2 ± 0.9 x10^6 a.u.	0.089 ± 0.9 x 10^{-3} min^{-1}
Δ26	7.7 S, 3.6 S	+	n.d.	n.d.
Δ28	4.5 S	-	5.4 ± 0.5 x10^6 a.u.	n.d.
Δ40	3.7 S	--	n.d.	n.d.
Δ51	3.6 S	--	2.4 ± 0.5 x10^6 a.u.	0.083 ± 2 x 10^{-3} min^{-1}
ΔNTR	n.d.	--	2.0 ± 0.1 x10^6 a.u.	n.d.
R11A	13.1 S	++	20.4 ± 0.6 x10^6 a.u.	n.d.
R22Q	13.2 S	++	19.5 ± 1.2 x10^6 a.u.	0.038 ± 0.1 x 10^{-3} min^{-1}
F24A	14.0 S		n.d.	0.023 ± 0.9 x 10^{-3} min^{-1}
F24E	12.2 S	++	n.d.	0.037 ± 0.6 x 10^{-3} min^{-1}
F24P	13.2 S		n.d.	n.d.
Q26A	20.3 S	MDH ++(CS)	n.d.	0.133 ± 3.8 x 10^{-3} min^{-1}
Q26P	21.7 S	MDH ++(CS)	n.d.	0.132 ± 1.8 x 10^{-3} min^{-1}
F27A	14.0 S	n.d.	n.d.	n.d.
F27E	12.3 S	++	20.5 ± 0.7 x10^6 a.u.	n.d.
F27R	14.8 S	--	n.d.	0.029 ± 6.0 x 10^{-4} min^{-1}
Δ20 F27R	10.1 S	++	n.d.	0.120 ± 2.0 x 10^{-3} min^{-1}
F28A	15.8 S	++	n.d.	0.065 ± 1.0 x 10^{-3} min^{-1}
F28E	13.6 S	++	n.d.	0.111 ± 2.0 x 10^{-3} min^{-1}
F27,28A	13.4 S	++	n.d.	0.088 ± 1.0 x 10^{-3} min^{-1}
F27,28E	8.0 S	++	n.d.	0.146 ± 2.0 x 10^{-3} min^{-1}
E34Q	16.1 S	-(MDH) +(CS)	32.6 ± 2.1 x10^6 a.u.	n.d.
P39Q	15.0 S		24.8 ± 1.2 x10^6 a.u.	n.d.
$WT_{25°C}$	15.8 S	n.d.	n.d.	n.d.
$W9C_{red}$	16.0 S		n.d.	n.d.
$W9C_{ox}$	16.8 S	--	n.d.	n.d.
$W60C_{red}$	15.7 S		n.d.	0.023 ± 1.0 x 10^{-4} min^{-1}
$W60C_{red}$	15.8 S	--	n.d.	0.015 ± 2.0 x 10^{-4} min^{-1}

To elucidate the mechanism of αB-oligomer formation and the determinants of its architecture and their relation to its chaperone function, all collected data were analyzed concerning common tendencies between size, dynamics and activity.

A stringent correlation between smaller oligomeric species and increased chaperone function could not be confirmed for all mutants (Δ28, Δ40, Δ51, F28A, F28E, F27,28A). Oligomers of the WT-like or even higher $s_{(20,w)}$-values were as efficient as smaller particles in preventing substrate protein aggregation. On the other hand, a certain oligomeric size seems to be essential for its function since all deletion variants existing in solution mainly as dimers up to maximally tetra- to hexamers are only able to protect substrate proteins to a low extent compared to WT, or they lost their ability completely. This is in agreement with published data on N-terminal deletions in αA-crystallin (Kundu et al., 2007).

A higher surface hydrophobicity could also not be detected in more active mutants. WT-like ANS-fluorescence intensities or even lower values were observed also for more competent mutants which were analyzed so far.

The most consistent correlation could be found between increased subunit exchange rates and increased activity. This correlation was observed to a certain extent for all mutants. For Q26A and Q26P this correlation could only be shown for CS so far. The effect of substrate specificity has to be analyzed further. F24E was the only analyzed mutant that showed a slight increase in SX-rate (1.5 fold) compared to WT and showed a strong increase in substrate protection. However, this mutant showed a significant shift of its sedimentation coefficient of ~ -2 S compared to WT.

These observations lead to the conclusion that accessibility of the available binding sites is the main factor determining chaperon-substrate interaction. Better accessibility is facilitated by higher subunit exchange rates. Since SX-kinetics are highly dependent on temperature as shown for αA WT and differences can be observed in the physiological temperature range between 35 and 42°C (Bova et al., 1997), this could be an elegant way to activate α-crystallin under heat-stress conditions for short-term regulation, if a quick reaction is required and cannot be accomplished by upregulation of translation.

Subunit exchange could also be a major reason for the higher activity observed for phospho-mimicking mutants of α-crystallin besides the observed shift in equilibrium to smaller oligomer units (Peschek et al., 2013).

The mechanistic relation of subunit exchange kinetics and substrate binding needs to be analyzed in detail. During subunit exchange, parts of αB-crystallin are solvent-exposed which

are usually buried within the oligomer, in the exchanging subunit as well as in the remaining oligomeric assembly. This simplifies access of potential substrate proteins to the burried binding sites. Presumably, faster subunit exchange rates accelerate the possibility of recognition of unfolding proteins leading to substrate binding at an earlier stage of unfolding, which would result in efficient protection of substrate aggregation.

Concerning the role of aromatic residues between position 1 and 28 and Trp60, it can be concluded that no single residue is essential for the chaperone function of αB-crystallin. Exchange to other residues does not alter the activity or even increases the protective action.

The SX-rate and chaperone function is presumably regulated by the ensemble of aromatic residues: By stabilizing the oligomeric 'storage form' of αB-crystallin, the activity is kept at a certain basic level. This stabilization could be realized by temperature-dependent π-π-interactions between aromatic side chains or cation-π-interactions with arginine residues. These types of non-covalent interactions are strongly dependent on temperature, leading to dissociation upon heating. Furthermore, they are highly dependent on geometry of the interacting residues and restricted to residues in a distance of about 3-7 Å with an optimum at 3-4 Å. Contributions of π-π-interactions to protein structures were reported earlier (McGaughey et al., 1998). The vast amount of Phe- and Trp- residues that are putatively in close proximity at the N-terminal connection site within the 24-mer are shown in fig. 44. Additional experimental prove of the spatial proximity are the resulting disulfide bonds forming spontaneously after introduction of cysteine residues at various positions in the NTR. This was shown for Position 9 and 60 in this work (fig. 35) and also for phosphorylation sites 19, 45 and 59 (Peschek et al., 2013).

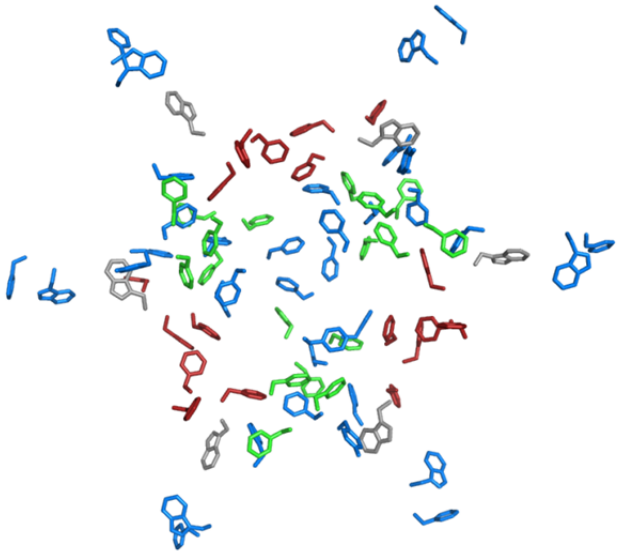

Fig 44: Aromatic residues of the NTR of αB-crystallin in close proximity in the 3D-model (pdb 2YGD).

As a conclusion, replacement of single Phe-residues leads to fewer possible π-π-interactions and thereby to higher subunit exchange rates. This effect resembles the effect of a slight temperature increase. Different phenylalanines seem to be differently important in the system as demonstrated by the different effects observed for F24- and F28- mutations. Deletion of multiple Phe-residues, as in F27,28A and F27,28E or in Δ20 and Δ20,F27R, leads to multiplied effects, which might resemble the effect of a stronger increase in temperature. This mechanism is valid for changing a small number of Phe to other amino acids. Exchange or deletion of too many stabilizing residues, as in Δ28, Δ40 or Δ51, diminishes N-terminal mediated oligomer formation completely and thereby abolishes chaperone activity.

The more pronounced effect of exchange of Phe to Glu is likely to be controlled by electrostatic repulsions following Coulomb's law. These effects might override the remaining weaker aromatic interactions.

This hypothesis is also supported by the comparison of α-crystallin to dimeric Hsp20 lacking all N-terminal Phe-residues except for two (fig. 28). The first Phe-residue, corresponding to F24 in αB, does not seem to contribute significantly to the aromatic interactions as F24A behaves WT-like in all performed experiments. The second corresponds to F28, but a single residue is obviously not enough to set up the aromatic system. In addition, chimeras of αB-NTR and Hsp20 ACD and CTR are able to form large oligomers mediated by the NTR of αB (unpublished data, Mymrikov). However, chaperone activity is not increased to αB WT level at the same time, which confirms the assumption, that N-terminal aromatic residues are not the only substrate binding site, but might exhibit an important regulatory function for substrate interaction.

An exact location of the substrate binding site or of multiple binding sites could not be determined from the data obtained during this work. To draw a conclusion, the experimental results of this work have been complemented with published and unpublished data on other parts of α-crystallin. The N-terminal sequences that were deleted leading to an increase in activity were ^{1}MDIAHHPWIRRPFFPFHAP^{20} (this work), ^{21}SRLFDQFF^{28} (Pasta et al., 2003), and ^{54}FLRAPSWF^{61} (Santhoshkumar et al., 2009). The observation that the deletion of 36 of the 68 N-terminal residues of αB-crystallin does not affect its chaperone function leaves three possible options: Firstly, the binding site is located outside the NTR. However, this does not explain the loss of function upon deletion of the NTR. Secondly, the unstructured region between 29 and 51 is not characterized well and could play an important role. Deletion of the first 40 and 51 residues led to a strong decrease of chaperone function, although truncated crystallins form small oligomeric assemblies of three to six subunits and

Δ51 shows subunit exchange with full length αB-crystallin. This marks the region between 29 and 50 as putatively important. On the other hand Δ1-28 already exhibits a similar activity and size distribution as Δ40. From these facts a single main binding site between position 28 and 40 can be excluded.

The facts discussed above leave only the third possible explanation. The main assumption is that the substrate binding is dependent on a certain oligomer size. This leads to the conclusion that several subunits contribute to the binding site at the same time. This might be realized by several NTRs at the oligomer connection sites. Deletion of small parts of the NTR increases activity which indicates that the NTR interactions regulate access to the binding sites. When small segments are missing, opening of the binding sites is simplified. In this context, the mainly unstructured N-terminal regions with a high content of aromatic amino acids could act as pseudo-substrates also blocking binding sites in other parts of the molecule.

What needs to be investigated is the role of Q26. Exchange to either Ala or Pro leads to a similar increase in oligomer size, chaperone activity towards CS and a striking increase in SX-kinetics. Accordingly, Q26 seems to be a crucial residue for the oligomeric architecture of αB.

4.2 Substrate recognition motifs in model substrate proteins

4.2.1 Establishing a peptide array experiment setup to investigate preferred binding sites in different model substrate proteins

To elucidate the sites in substrate proteins, that interact with αB-crystallin, a CelluSpots™ peptide array (Intavis) of 384 overlapping peptides of the substrates MDH (pdb 1MLD), CS (pdb 3ENJ), Lysozyme (pdb 193L), p53 core domain (pdb 2YBG) and ADH (4W6Z), was designed. To cover the complete protein sequences, peptides of a length of 15 amino acids were chosen with an offset of three amino acids between the different peptides. The peptides were commercially synthesized C-terminally linked to cellulose which subsequently was spotted onto a cellulose membrane fixed to a glass slide. N-termini were acetylated. Each chip contained duplicates of a set of 384 peptides. Two negative control spots were included as well, containing only acetylated cellulose matrix. A complete list of the spotted peptides can be found in the appendix. As first step a binding assay was established. To analyze binding, the membranes carrying the peptide spots were first blocked with milk powder to avoid unspecific binding of αB-crystallin to the cellulose membrane, and subsequently incubated with different αB-crystallin variants at 37°C and 65 rpm. After the incubation and extended washing, the arrays were incubated with a HRP-labeled monoclonal anti-αB-crystallin antibody for detection by chemoluminescence comparable to Western Blot-detection. The gentle shaking emerged to be essential for a sufficiently low background signal as well as extended washing steps after αB-crystallin- and antibody incubation. After the right experimental settings were found, the peptide array-experiments were conducted with three different αB-variants: αB WT, and the activated mutants αB R22Q as well as phospho-mimicking αB 3E (Peschek et al., 2013). Two negative controls were performed following the exact same protocol, while the membranes were incubated for 2 h at 37°C and 65 rpm with PBS instead of protein solution. In fig. 45 overlays of the detected chemoluminescence signals and visible light pictures are shown. The strong background signal in some of the arrays impeded the quantification of one replicate on each chip. For this reason, only triplicates could be analyzed for each variant. Signal intensities of each spot were determined using the ImageQuantTL-software (GE Healthcare). Mean values and standard deviations were determined from the normalized intensities. The given signal intensities were normalized to the spot with maximum signal intensity on each replicate. Subsequently, peptides were divided into four groups: good binders (≥ 60% mean signal intensity), medium binders (< 60% - ≥ 50%), weak binders (< 50 - ≥ 30%) and non-binders

(< 30%). The signal-to-noise ratio for arrays with αB WT was worse than for the more active mutants αB 3E and R22Q. The best hits in the arrays overlap for all three variants, although the signal intensity difference between strong and weak binders is clearly more pronounced for 3E. For further evaluation only good and medium binders were analyzed (tab. 5).

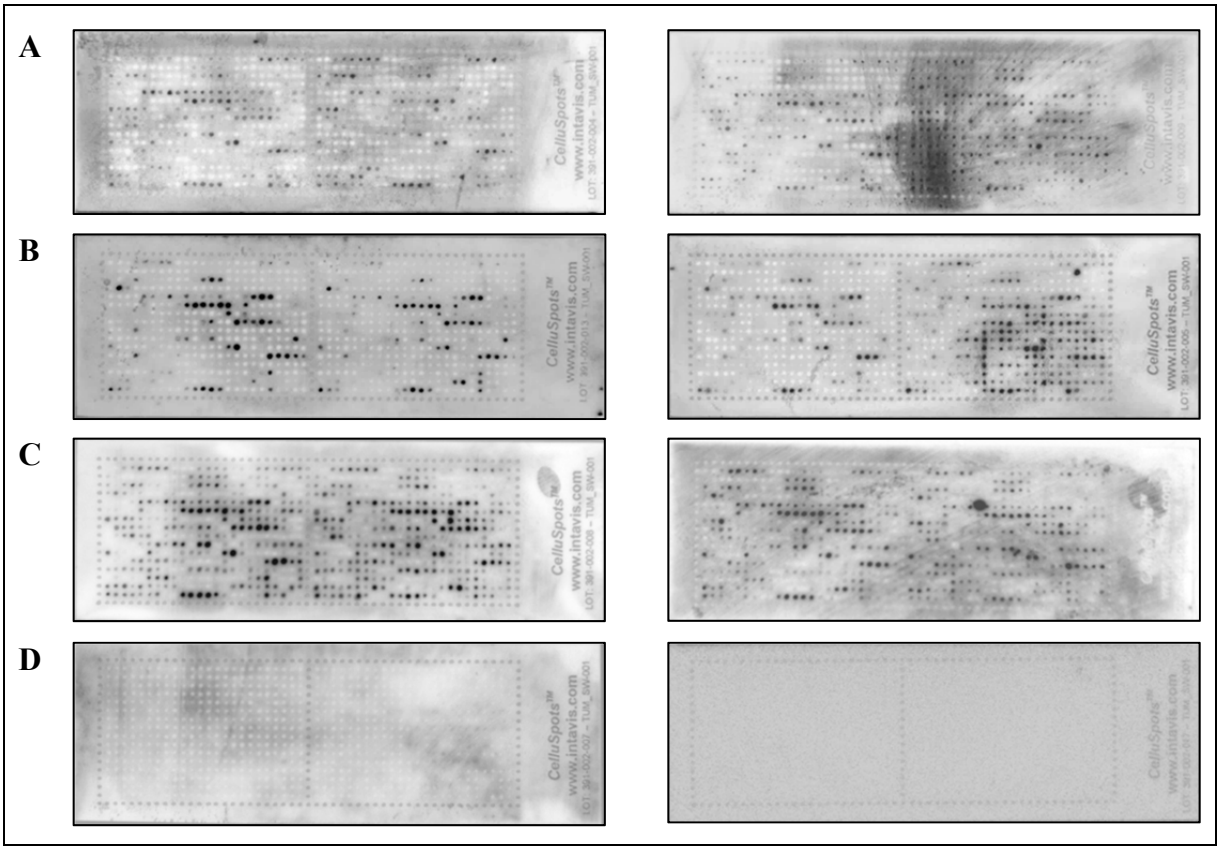

Fig. 45: Overlay of chemoluminescence signal and VIS-picture of the performed peptide arrays **A:** αB WT; **B:** αB 3E; **C:** αB R22Q; **D:** Negative control PBS. On each chip two replicates of a set of 384 peptides was spotted. Left and right half of the chips represent one set of peptides. Top row contains peptides A1 to A24 in the first line and A1 to P1 in the first row on the left. The rightmost replicates in each chip were not included in the quantification due to high background signal.

Tab. 5: List of peptide array hits obtained for αB WT (top), 3E (middle) and R22Q (bottom). Peptides with average signals ≥50% were chosen.

spot	peptide sequence	protein	mean (%)	stand. dev. (%)
L21	Q-K-T-Y-Q-G-S-Y-G-F-R-L-G-F-L	P53 core	86.4	16.5
K16	A-T-L-S-M-A-Y-A-G-A-R-F-V-F-S	MDH	79.9	15.1
F15	L-G-V-L-A-Q-L-I-W-S-R-A-L-G-F	CS	78.2	4.4
F11	N-Y-Y-T-V-L-F-G-V-S-R-A-L-G-V	CS	70.4	27.7
L22	Y-Q-G-S-Y-G-F-R-L-G-F-L-H-S-G	P53 core	65.4	32.0
F14	S-R-A-L-G-V-L-A-Q-L-I-W-S-R-A	CS	59.6	21.6
H19	L-S-L-L-K-N-S-P-L-V-S-R-L-T	MDH	58.6	16.0
P12	A-L-D-F-F-A-R-G-L-V-K-S-P-I-K	ADH	56.8	12.6
E8	N-S-G-R-V-V-P-G-Y-G-H-A-V-L-R	CS	55.9	32.7
E6	Y-I-W-N-T-L-N-S-G-R-V-V-P-G-Y	CS	55.5	12.4
E5	L-R-D-Y-I-W-N-T-L-N-S-G-R-V-V	CS	54.6	11.5
J13	I-F-G-V-T-T-L-D-I-V-R-A-N-A-F	MDH	53.3	9.2
G3	K-R-H-G-L-D-N-Y-R-G-Y-S-L-G-N	Lysozyme	52.9	29.2
K15	A-G-S-A-T-L-S-M-A-Y-A-G-A-R-F	MDH	52.7	5.7
P13	F-F-A-R-G-L-V-K-S-P-I-K-V-V-G	ADH	52.3	15.9
P11	T-R-E-A-L-D-F-F-A-R-G-L-V-K-S	ADH	51.1	13.3
A22	I-R-F-R-G-Y-S-I-P-E-C-Q-K-M-L	CS	50.8	29.5
F12	T-V-L-F-G-V-S-R-A-L-G-V-L-A-Q	CS	49.2	28.9
J23	V-I-G-G-H-A-G-K-T-I-I-P-L-I-S	MDH	48.1	42.9

spot	peptide sequence	protein	mean (%)	stand. dev. (%)
E19	H-D-P-M-F-K-L-V-A-Q-L-Y-K-I-V	CS	81.1	18.8
K16	A-T-L-S-M-A-Y-A-G-A-R-F-V-F-S	MDH	69.4	26.5
F15	L-G-V-L-A-Q-L-I-W-S-R-A-L-G-F	CS	68.0	5.1
F11	N-Y-Y-T-V-L-F-G-V-S-R-A-L-G-V	CS	68.0	1.7
L21	Q-K-T-Y-Q-G-S-Y-G-F-R-L-G-F-L	P53 core	63.8	19.2
F14	S-R-A-L-G-V-L-A-Q-L-I-W-S-R-A	CS	61.0	12.4
E20	M-F-K-L-V-A-Q-L-Y-K-I-V-P-N-V	CS	60.1	10.6
P12	A-L-D-F-F-A-R-G-L-V-K-S-P-I-K	ADH	58.6	13.1
L20	V-P-S-Q-K-T-Y-Q-G-S-Y-G-F-R-L	P53 core	58.3	17.6
H16	G-A-S-G-G-I-G-Q-P-L-S-L-L-L-K	MDH	58.3	10.4
F10	T-E-M-N-Y-Y-T-V-L-F-G-V-S-R-A	CS	56.9	37.4
H19	L-S-L-L-K-N-S-P-L-V-S-R-L-T	MDH	52.4	7.4
F12	T-V-L-F-G-V-S-R-A-L-G-V-L-A-Q	CS	51.3	4.6
D2	T-D-A-Q-F-T-E-L-M-R-L-Y-L-T-I	CS	50.9	7.9
L22	Y-Q-G-S-Y-G-F-R-L-G-F-L-H-S-G	P53 core	49.9	6.9
P13	F-F-A-R-G-L-V-K-S-P-I-K-V-V-G	ADH	49.7	5.6
C13	K-L-P-C-V-A-A-K-I-Y-R-N-L-Y-R	CS	39.7	2.8

spot	peptide sequence	protein	mean (%)	stand. dev. (%)
K16	A-T-L-S-M-A-Y-A-G-A-R-F-V-F-S	MDH	94.3	8.6
L21	Q-K-T-Y-Q-G-S-Y-G-F-R-L-G-F-L	P53 core	85.5	15.1
F15	L-G-V-L-A-Q-L-I-W-S-R-A-L-G-F	CS	78.5	3.7
H19	L-S-L-L-K-N-S-P-L-V-S-R-L-T	MDH	74.7	13.5
J13	I-F-G-V-T-T-L-D-I-V-R-A-N-A-F	MDH	72.6	20.9
L22	Y-Q-G-S-Y-G-F-R-L-G-F-L-H-S-G	P53 core	67.5	14.7
P12	A-L-D-F-F-A-R-G-L-V-K-S-P-I-K	ADH	66.7	8.0
F12	T-V-L-F-G-V-S-R-A-L-G-V-L-A-Q	CS	62.9	9.0
F17	L-I-W-S-R-A-L-G-F-P-L-E-R-P-K	CS	61.5	34.5
F11	N-Y-Y-T-V-L-F-G-V-S-R-A-L-G-V	CS	60.6	5.9
P13	F-F-A-R-G-L-V-K-S-P-I-K-V-V-G	ADH	60.4	9.6
H20	L-L-K-N-S-P-L-V-S-R-L-T-L-Y-D	MDH	57.9	6.9
F13	F-G-V-S-R-A-L-G-V-L-A-Q-L-I-W	CS	55.6	8.0
P11	T-R-E-A-L-D-F-F-A-R-G-L-V-K-S	ADH	53.5	24.2
F14	S-R-A-L-G-V-L-A-Q-L-I-I-W-S-R-A	CS	50.2	12.8
E19	H-D-P-M-F-K-L-V-A-Q-L-Y-K-I-V	CS	49.0	8.7

4.2.2 Analysis of amino acid composition of the binders and non-binders

To compare the sequences of the best hits obtained for each αB-variant, the abundance of each amino acid in all binders and non-binders was calculated. The resulting percentages were normalized to the natural abundance of each amino acid (fig. 46). A value of 0% indicates the same abundance in the analyzed peptides as in the average of all proteins.

A significant overrepresentation of a combination of the aromatic/non-polar residues Leu, Phe, Ala, Val and Tyr, and additionally Arg and Gly in the good binders was striking. In contrast, the negatively charged residues Glu and Asp as well as their amid-derivatives Gln and Asn were only present in low abundances in good binders. His and Met are apparently also not important for substrate recognition. The lack of cysteine residues in binders might be biased since the array buffer did not contain reducing agent. The presence of disulfide bonds between different peptides might impair binding of αB-crystallin to the peptides. In the non-binders the opposite tendency can be observed: Lack of Phe and Arg inhibits binding. The presence of higher amount of Lys does not seem to be favorable for strong binding, but does not lead to non-binding.

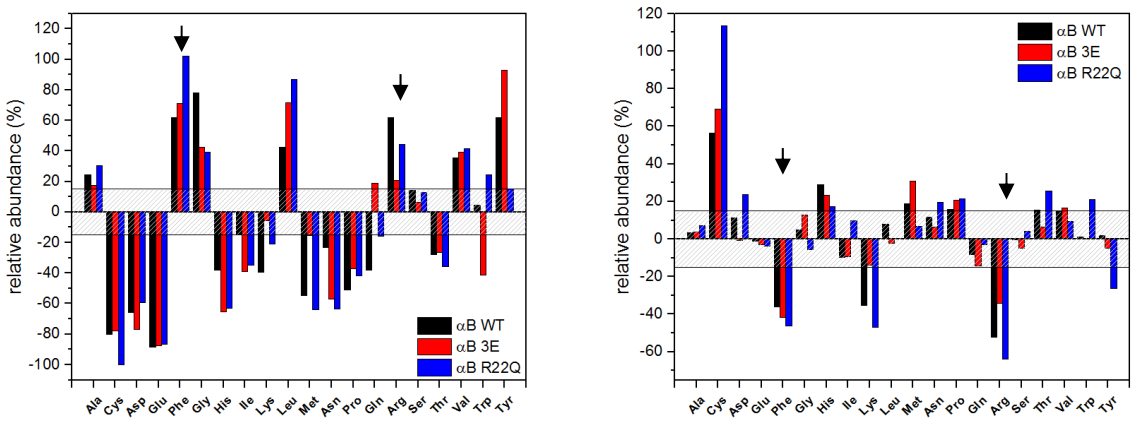

Fig. 46: Relative amino acid abundance in peptide array hits (binders, left) and non-binders (right) obtained for αB WT, 3E and R22Q. Abundances of Phe and Arg are marked with black arrows.

After analysis of amino acid abundance in binders and non-binders, sequence logos were created using WebLogo (Crooks et al., 2004). These graphical representations of the patterns within a multiple sequence alignment facilitate the recognition of essential amino acids at defined positions within the peptide (fig. 47). Comparison of the amino acid sequences of best binders (tab. 5) do not show a conserved sequence motif as expected for highly specific protein interactions. This is not surprising since sHsps are omnipotent binders that protect a lot of different proteins from aggregation that do not share a conserved motif. However,

certain position dependencies of amino acids in the bound peptides seem to exist (fig. 47). Positions 11 and 13 are important for binding to all three variants, while position 7 is more conserved in WT- and R22Q- recognition motifs. The positions 8-10 and 15 do not seem to play an important role. Positions 1, 2 and 7 are not relevant for binding to 3E, position 2 and 5 are not essential for binding to R22Q. This position dependencies need to be confirmed and analyzed further in binding assays with shorter peptides containing the specific amino acids.

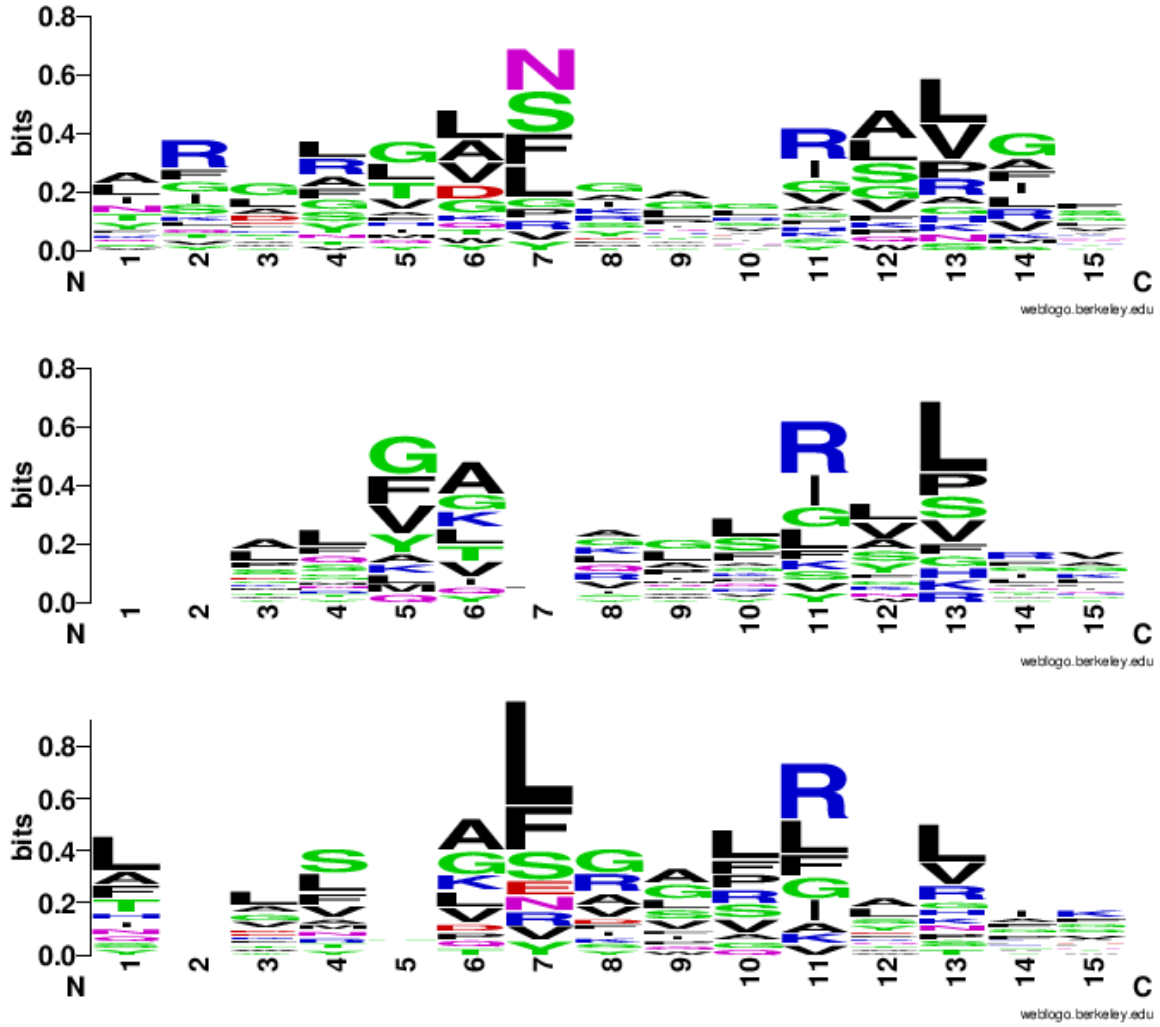

Fig 47: Sequence logo representations of the alignment of the peptide array hits shown in tab. 5 for αB WT (top), 3E (middle) and R22Q (bottom). The Amino acids are colored according to their classification; blue: positively charged; red: negatively charged; black: hydrophobic; green: polar.

Analysis of abundance of amino acids in non-binders (0% signal) resulted in the opposite picture (fig. 48). The position dependencies are even lower for non-binders, but for all three αB-crystallins the representative non-binders show enrichment of negatively charged amino acids mainly in the C-terminal region. αB R22Q shows the most distinct amino acid pattern for non-binders, but the most unspecific pattern for good binders. For αB 3E, the opposite is observed. In the arrays of 3E, less good binders could be detected, but a higher number of

non-binders was observed. This indicates that these two mutants might have a different mechanism of improving their chaperone capacity. While in αB R22Q a positive charge is deleted, the substrate spectrum seems to increase because less ionic repulsion disturbs substrate binding. Introduction of three negative charges in αB 3E increases ionic repulsion in substrate complexes and thereby increasing selectivity for certain binding motifs, but at the same time increasing binding affinity and capacity for selected substrates. This could be a useful mechanism to select the important proteins that are necessary for cell survival under stress conditions. This theory is supported by the fact that the equivalent mutation R22Q in αA leads to cataract although its chaperone activity in *in vitro* assays is increased. By binding more substrates in a more unspecific manner, this mutation could lead to an increased formation of substrate complexes. However, exactly these complexes are condemned to result in mixed proteins aggregates when too much substrate is bound and cannot be refolded.

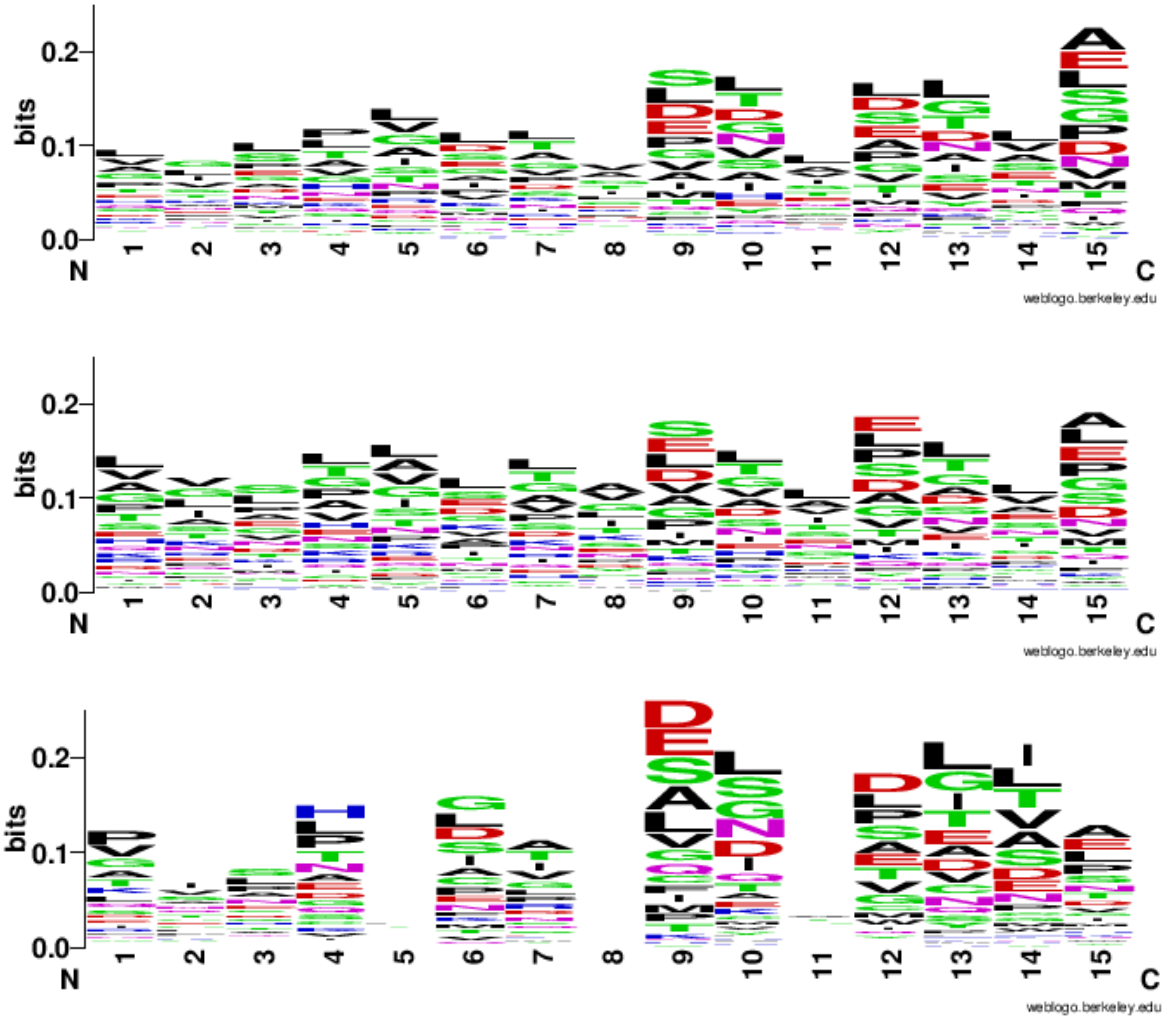

Fig 48: Sequence logo representations of the alignments of the non-binders obtained from the performed peptide array experiments for αB WT (top), 3E (middle) and R22Q (bottom). The Amino acids are colored according to their classification; blue: positively charged; red: negatively charged; black: hydrophobic; green: polar.

4.2.3 Secondary structure prediction of peptides identified as good binders

To assess the effect of potentially important secondary structure elements, peptide structure predictions of the best hits were performed using PEP-FOLD (fig. 49) (Shen et al., 2014).

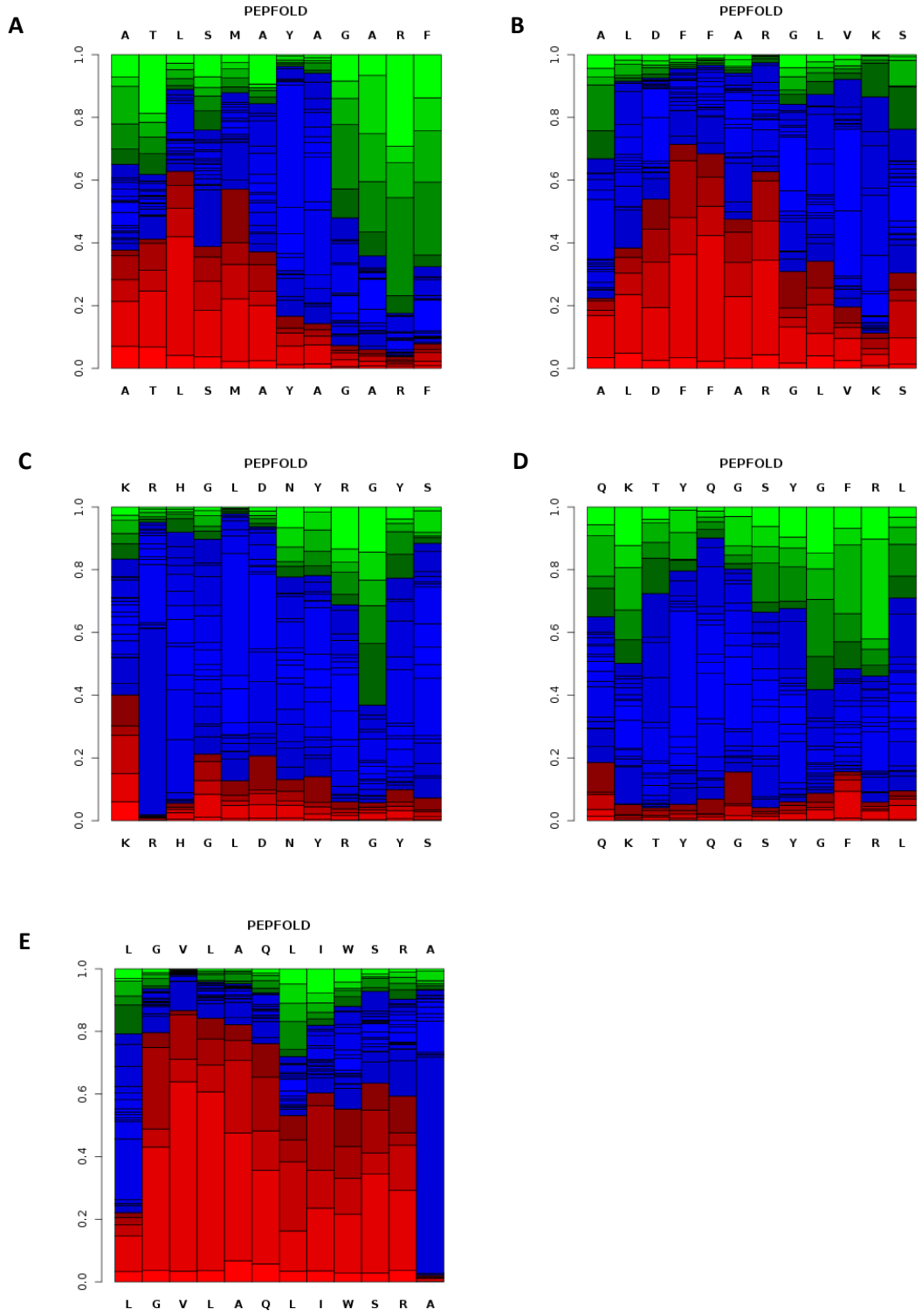

Fig. 49: Structural Alphabet (SA) prediction profiles of the best hits found for each model substrates calculated using the PEP-FOLD server for de-novo secondary structure predictions (Shen et al., 2014). **A:** MDH, **B:** ADH, **C:** lysozyme, **D:** p53, **E:** CS. Predicted probabilities of helical structures are indicated in red, coiled regions are shown in blue and extended structures in green.

The secondary structure prediction of the best hits of the five tested substrates does not show a preferred folding motif. The peptides can be divided into three groups: Group 1 consisting of the best hits for MDH and ADH seem to form N-terminal helical structures, with more coiled structures at the C-terminal end. Group 2 consisting of the best hits for lysozyme and p53 core domain are predicted to form mainly coiled structures whereas Group 3 is presumably mainly α-helical. Secondary structures do not seem to be essential for binding. However, extended regions can be excluded as recognition motif.

4.2.4. Mapping of the best binders on the crystal structures of the analyzed substrate proteins

To analyze the obtained peptide array results further, the best hits were mapped on the structures of all used substrate proteins.

For hen egg white lysozyme luminescence signals show the highest variance between the three tested variants. For αB WT, the best results were achieved for the N-terminal peptide ^{13}KRHGLDNYRGYSLGN^{27}. This peptide was also detected for 3E and R22Q, but with lower signal intensities. In the crystal structure of lysozyme, this sequence is a surface-exposed loop region (fig. 50). This loop is forced in its position by two disulfide bonds shown in fig. 50. For 3E and R22Q the C-terminal ^{112}RNRCKGTDVQAWIRGCRL^{129} region also appears in the list of bound peptides. In the native structure this sequence is located next to the N-terminal binding site determined for WT and it is covalently linked to it by disulfide bonds. However, under the reducing conditions used in the chaperone assays to induce aggregation, the conformational restrictions induced by disulfide bonds are abolished. The peptide is then able to adopt new conformations and side chains pointing to the core of the protein can be exposed and might be recognized by αB-crystallin.

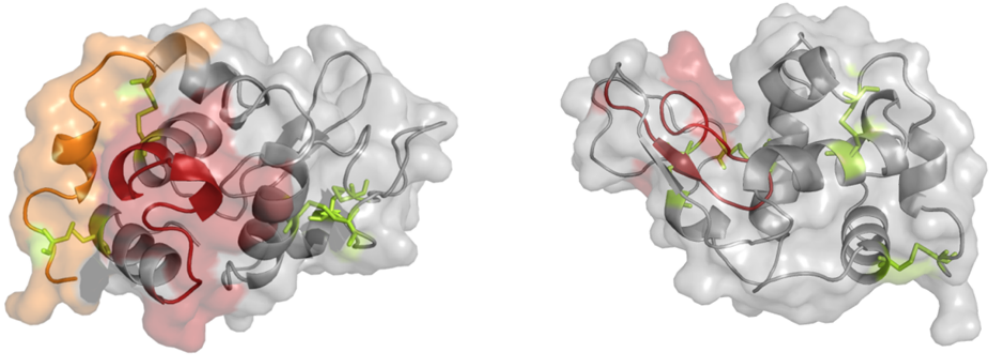

Fig. 50: Crystal structure of hen egg white lysozyme (pdb 193L). The best hits from peptide arrays are shown in red. Potential secondary binding sites are indicated in orange. Disulfide bonds are shown in yellow.

The peptide array hits were also compared to crosslinking/ms results obtained in chaperone assays of αB WT with lysozyme. The published crosslinks (Kriehuber, 2012) surround the mapped binding site (fig. 51) which supports the peptide array data.

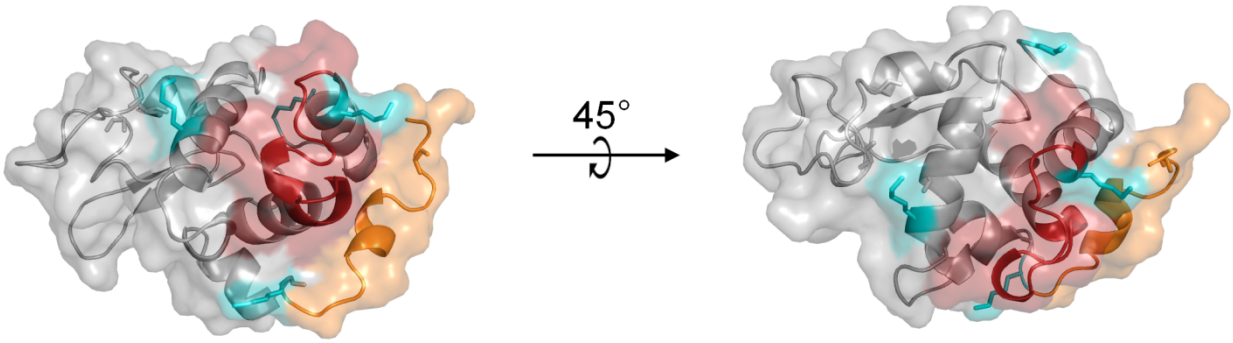

Fig. 51: Crystal structure of hen egg white lysozyme (pdb 193L). The best hits from peptide arrays are shown in red. Potential secondary binding sites are indicated in orange. All residues found in crosslink/ms experiments with αB are shown in cyan.

For both peptides, the 'binding-site-rules' derived from the binders apply. All sequences are composed of arginine residues surrounded by aromatic/hydrophobic and helix breaking residues.

Analysis of binding to ADH peptides resulted in a similar picture. The main binding site ^{301}TREALDFFARGLVKSPIKVVG^{321} for all three variants is located in the middle of the amino acid sequence of ADH. The structure is composed of an α-helical part as well as a surface exposed loop and β-sheet (fig. 52). Like in lysozyme, the sequence is Arg-rich and matches the described pattern. At the C-terminal end of the analyzed ADH sequence and

close to the N-Terminus other binding sites with less signal intensity were found. In the crystal structure these sequences ^{148}VAPILCAGITVYKAL^{162} and ^{328}IYEKMEK GQIVGRYV^{347} are in close proximity to each other as well as close to the main binding site, although they are not adjacent in the amino acid sequence.

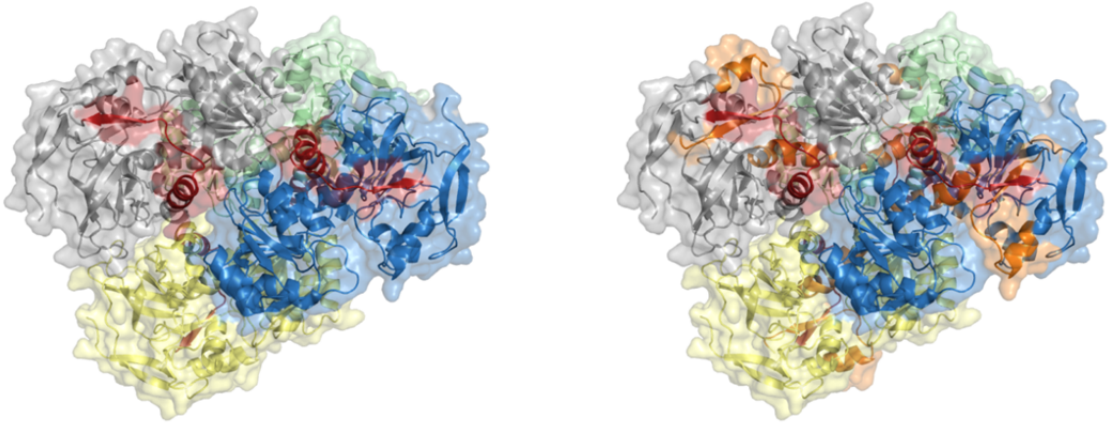

Fig. 52: Crystal structure of yeast alcohol dehydrogenase I tetramer (pdb 4W6Z). The best hits from peptide arrays are shown in red. Potential secondary binding sites are indicated in orange. The four different monomeric subunits are colored in grey, blue, yellow and green.

Moreover, all published crosslinks with αB are located in this region or close to it (fig. 53).

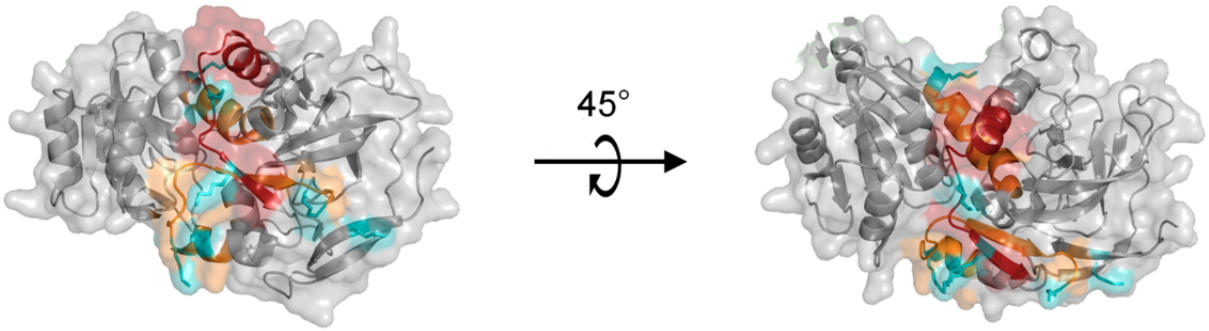

Fig. 53: Crystal structure of alcohol dehydrogenase I monomer (pdb 4W6Z). The best hits from peptide arrays are shown in red. Potential secondary binding sites are indicated in orange. Residues found in crosslink/ms experiments with αB are shown in cyan.

The peptide array hits for the p53 core domain were also mapped to the published crystal structure (fig. 54). The main binding site ^{100}QKTYQGSYGFRLGFL^{117}, that is bound by all tested αB variants, is shown in red. Although these peptides show a high chemoluminescence signal, it is probably not the only binding site, since αB WT does not protect the core domain of p53 as good as 3E. For 3E, the binding seems again more selective than for WT and

R22Q. A second binding site could be detected, that is recognized mainly by 3E, and only weakly by WT (shown in orange in fig. 54). The residues in this peptide are involved in DNA binding. It is possible that the three additional negative charges in 3E support binding to this region and thereby improve interaction of p53 with phosphorylated αB (fig. 55).

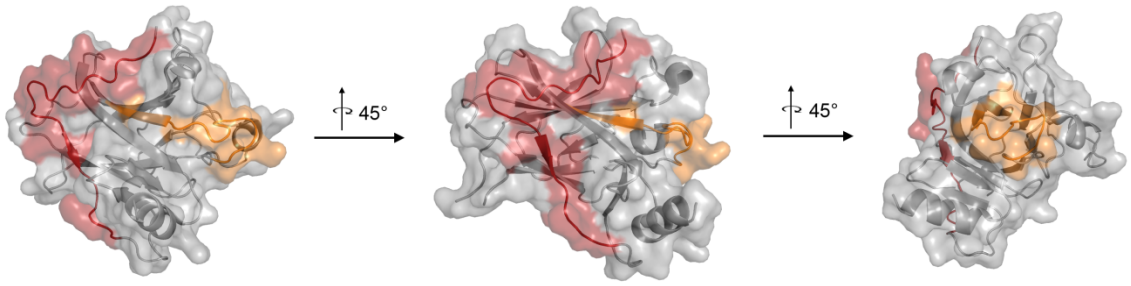

Fig. 54: Crystal structure of p53 core domain (pdb 2YBG). The best hits from peptide arrays are shown in red. Potential secondary binding sites are indicated in orange.

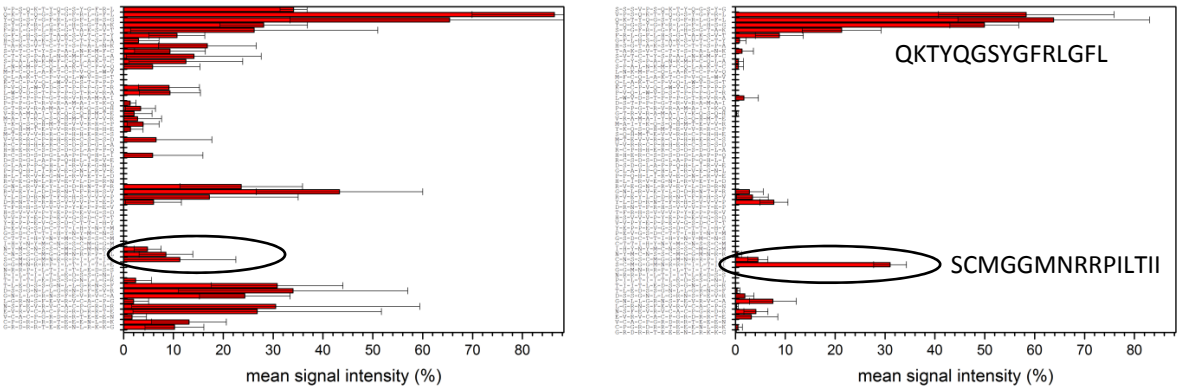

Fig. 55: Normalized average signal intensities in peptide array of the substrate p53 incubated with WT (left) and 3E (right). Selectivity of 3E could be mediated by more selective binding to the peptide marked by a black circle.

In contrast to the secondary binding site in p53 core domain, non of the main binding sites correspond to the active site of the model substrates.

Lysozym, ADH and p53 seem to represent one type of substrate. In these proteins all main binding sites are surface-exposed. Minor structural rearrangements during unfolding are presumably enough to allow recognition of the binding site by α-crystallin. The hydrophobic residues in the binding peptides point towards the protein core and are only exposed during unfolding.

Another type of substrate binding site is present in MDH and CS. In these two proteins the binding sites are completely hidden in the native state and are only exposed after unfolding.

This group needs to be subdivided: The putative major binding sites in MDH ^{16}LSLLLKNSPLVSRLT^{30} and ^{223}ATLSMAYAGARFVFS^{237} are located at different sites in the amino acid sequence, but in the crystal structure they are located close together at the dimer interface (fig. 56). Already upon dissociation into monomers they can be recognized by α-crystallin and bound immediately. Three of the eight published cross-links (N-Terminus, K2 and K217) are located close to the binding site (fig. 56), the five remaining crosslinks are located elsewhere, but the crosslinks found near the detected peptides were the only crosslinks with the NTR of αB. Putative lower affinity binding sites with less signal intensity of the MDH subunits were also detected inside the core of MDH and probably also support complex formation. The results match the published data on MDH obtained from H/D-exchange experiment with MDH and TaHsp16.9 and PsHsp18.1 (Cheng et al., 2008).In this H/D-exchange study, a main binding site was located around residues 228-252 which is overlapping with one of the main binding sites found in this study. Furthermore it was shown, that MDH is bound by sHsps in a very early stage of unfolding which supports the hypothesis that the dimer interface is recognized and the monomeric subunits do not need to unfold further to expose their recogntion motif. This facilitates the prevention of their aggregation by sHsps.

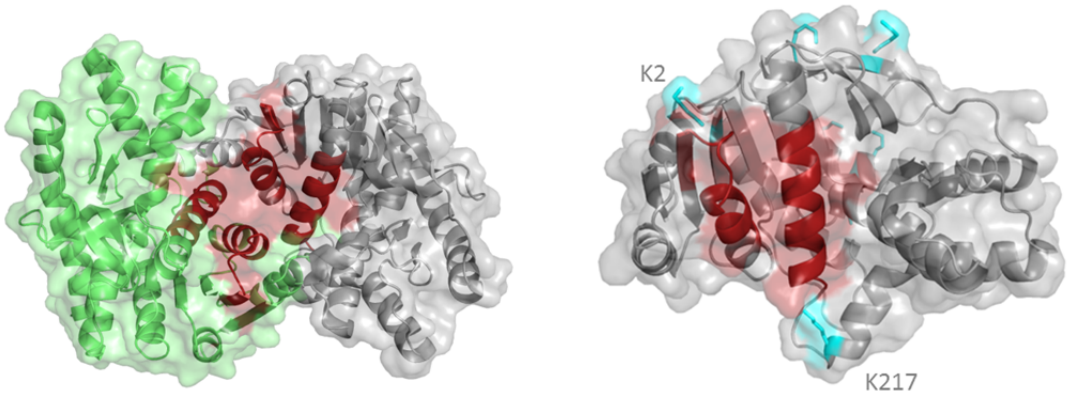

Fig. 56: left: Crystal structure of mitochondrial malate dehydrogenase dimer from porcine heart (pdb 1MLD). The best hits from peptide arrays shown in red are located at the dimer interface. **right:** View of the dimer interface containing the potential binding site in a MDH monomer. Residues found in crosslink/ms experiments with αB are shown in cyan.

In the CS-structure, the best peptide array hit for all three αB variants is an α-helix that is burried in the core of the monomeric subunits. Even after dimer dissociation the binding site is not accessible. Only after unfolding of the monomers, the binding site can interact with the chaperone. A pepide array hit found in R22Q-arrays with medium average signal intensity is

surface-exposed in the structure (fig. 57, blue α-helix). This sequence overlaps with one of only three published crosslinking/ms results (Kriehuber, 2012).

The burried main binding site could explain two observations: Firstly, only three crosslinks were published for CS although the primary sequence contains 438 residues. Secondly, compared to other model substrates like lysozyme and MDH, CS is a poor substrate that is not protected very well by αB WT. To access the binding motif, CS need to be in a late stage of unfolding. At this point, it is increasingly difficult to stabilize a substrate protein.

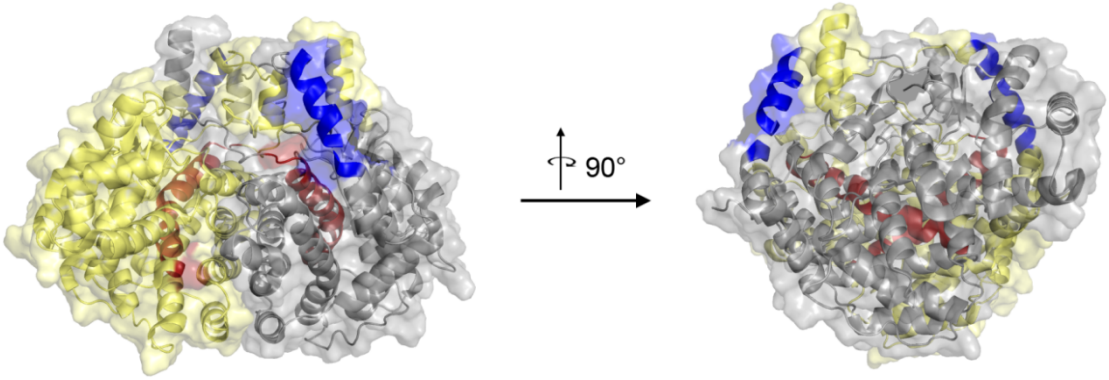

Fig. 57: Crystal structure of pig heart citrate synthase dimer (pdb 3ENJ). The best hit from the peptide arrays shown in red is a α-helical structure burried in the center of the monomeric subunits. A secondary binding site is shown in blue that was only detected in arrays of R22Q with medium signal intensity.

The best hit obtained in this study differs from the published binding motif in CS found for bacterial sHsps (Ahrman et al., 2007a) This peptide that is not present in thermostable forms of CS from thermophilic archaebacteria like *Pyrococcus furiosus* and *Sulfolobus solfatacarium* was found in the peptide array hits, but only among the peptides with lower signal intensities.

4.2.5 Summary and discussion

The main binding sites for all substrate proteins overlap for all three variants. But there are some peptides that are recognized by only one or two of the variants with high signal intensity. As mentioned before, this could imply different affinities towards the different binding sites in proteins as shown for WT and 3E using p53 as a substrate.

From the performed peptide arrays, a set of peptides was derived in good reproducibility that does not exhibit a conserved sequence motif at first glance. This is not surprising since sHsps are universal binders that interact with a large number of proteins that do not necessarily share specific sequence motifs. The analysis of the amino acid composition of the best hits resulted in a predominance of Arg and Gly, the aromatic amino acids Tyr and Phe and other hydrophobic residues like Leu and Val, whereas binders were depleted of Glu/Gln and Asp/Asn. Analysis of the numerous non-binders resulted in increased levels of Cys, His and Met, while a strong depletion of Phe, Arg and Lys could be observed. To further analyze the peptide hits, a secondary structure prediction was performed resulting in mixed structures and no defined preference for certain structural motifs.

The WebLogo-representation of the peptide arrays hits indicated a dependency of peptide recognition on certain positions, especially 11, 13 as well as 5 and 7 for some of the testes variants (fig. 47). These first results need to be analyzed further in binding assays with peptides containing the putatively important residues for binding. Different lengths of peptides should be analyzed as well to investigate the number of amino acids necessary for substrate recognition.

Mapping of the hits on the crystal structures also did not reveal obvious similarities. While for some substrates the best peptide hits were buried in the native structure either in the proteins core (CS) or in the dimer interface (MDH), the detected sequences were also found to be surface exposed as in case of ADH, p53 and lysozyme. For the latter, conformational restrictions by disulfide bonds were proposed as determinant for binding.

The only obvious common property of the hits obtained in the peptide array experiments is the preference in amino acid composition. A defined secondary structure motif could not be found for good binders.

The description of the best hits resembles a description of the properties of the NTR of αB-crystallin, which is also predicted to consist of α-helical regions combined with rather unstructured coil-rich regions. In fig. 58 a comparison of amino acid abundance in binders, non-binders, full-length αB WT and αB-NTR is shown. Several similarities are highlighted in green circles.

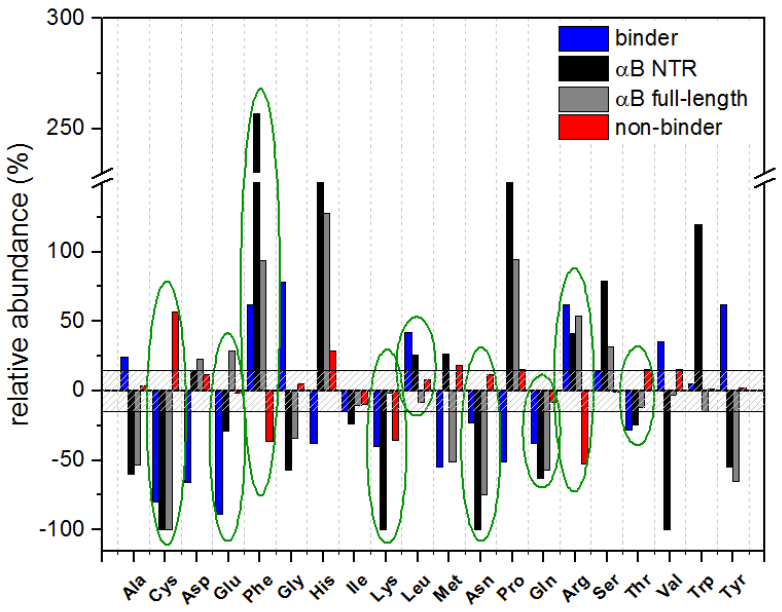

Fig. 58: Relative amino acid abundance in peptide array hits and non-binders as well as αB NTR and αB WT. The same tendencies of amino acid composition between NTR and binders are highlighted in green circles.

This leads to a hypothesis of substrate recognition and binding in which data from the mutational studies on αB-NTR in chapter 4.1 and results from the peptide array analysis are combined: α-crystallin forms large oligomers in which the binding sites are occupied by the substrate-mimicking hydrophobic and flexible NTRs. When parts of these domains are deleted or, during subunit exchange, binding sites are more readily accessible for potential interaction partners. This was shown in this study as well as in other publications. The analyzed regions were ^{1}MDIAHHPWIRRPFFPFHAP^{20} (this work), ^{21}SRLFDQFF^{28} (Pasta et al., 2003), and ^{54}FLRAPSWF^{61} (Santhoshkumar et al., 2009). These sequences match the obtained criteria for substrate recognition very well and resemble the composition of significant hits from peptide array experiments in this work. Some examples are the best hits for p53, MDH, CS and ADH, respectively:

QKTYQGSYGFRLGFL, ATLSMAYAGARFVFS, LGVLAQLIWSRALGF, ALDFFARGL-VKSPIK.

Together with the loss of secondary structures at higher temperatures this model explains the highly promiscuous binding of α-crystallin to its substrates but also selectivity for unfolding proteins under stress conditions without disturbing protein function under normal conditions. The regulation of binding to the substrate could be explained by a concentration dependent binding. The substrate binding sites in αB-oligomer are accessible due to subunit exchange, when subunits leave the oligomer and make room for potential substrate peptides resembling

‘self’-properties. If under normal conditions mainly correctly folded proteins are present, the binding sites are not occupied by other binding partners and the exchanging subunits can return to their previous position in the same or in a different oligomer. When under stress conditions, the amount of accessible competitive binding stretches in substrate proteins increases, these can substitute the NTRs of the exchanging subunits in the oligomeric assembly. Another mechanism of regulation of activity was proposed in section 4.1.3. The SX-rates are increased at elevated temperatures or after phosphorylation which increases activity under stress conditions as well. Stress conditions are recognized by αB through a similar process that occurs in unfolding substrate proteins: hydrophobic interactions are disturbed. As a consequence their stabilizing effects are diminished. Activation by unfolding was proposed for sHsps during pH-shifts before (Foit et al., 2013). These two factors could determine the equilibrium between self-assembly and formation of substrate complexes dependent on the prevailing circumstances. However, these mixed complexes cannot adopt the stable and symmetric assembly formed by αB-homo-oligomers. With increasing amount of substrate within one complex it cannot compensate for the missing αB-subunits and starts to form larger, more undefined complexes that are increasingly prone to aggregate themselves. When only small amounts of substrate proteins need to be protected the system can bypass this stress situation until either ATP-dependent chaperone can refold the bound substrates or the proteasome system can degrade and recycle the damaged proteins.

4.3 The role of α-crystallin in murine eye lens proteostasis

After extensive analysis of αB *in vitro* and its interplay with model substrates, the *in vivo* relevance was investigated. As a first step *in vitro* substrate binding assays were performed with a monomeric, rather stable member of the crystallin family, γD-crystallin. As mentioned in section 1.3, it is proposed that α-crystallin binds unfolding crystallins that become aggregation prone with age (Derham and Harding, 1999; Horwitz, 1992). To analyze this *in vitro*, first chaperone assays were performed with αB- and γD-crystallin. In contrast to the model substrates usually used, γD cannot be unfolded at physiological temperatures. Hence, γD was unfolded by addition of 5 M guanidinium chloride, incubated for several hours at rt and then diluted 1:50 into a αB-solution pre-equilibrated at 37°C as established before. Immediate formation of light scattering aggregates could be prevented when excess of αB was used (Peschek, 2012), but analysis of the formed substrate complexes always resulted in two peaks: An αB-/γD-crystallin complex eluting in the void volume of a TSKgel G4000SW (Tosoh Bioscience LLC) column and remaining αB-crystallin with an elution volume of αB-crystallin homo-oligomers. These observations match the results of published studies on this interaction *in vitr*o (Acosta-Sampson and King, 2010). Analysis by aUC also showed formation of an enormous complex (data not shown). Addition of more αB-crystallin did not change the elution volume of the resulting substrate complexes. The only observed effect was an increase in the αB-crystallin-homo-oligomer peak (fig. 59).

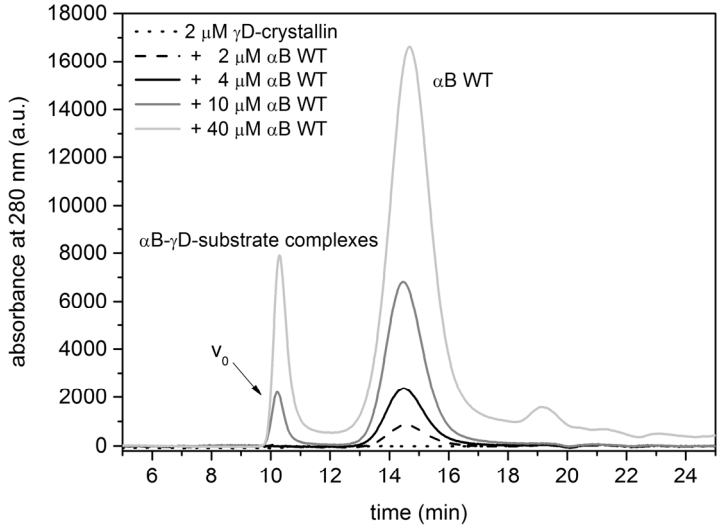

Fig. 59: SEC-HPLC chromatogram. Chaperone assay were performed with γD WT denatured in 5 M urea and binding to αB-crystallin was induced by a 1 : 50 dilution of the denatured γD-crystallin into a pre-equilibrated αB-crystallin-solution at 42°C. The samples were subsequently centrifuged and the supernatant was applied to a Superdex200 column. No monomeric γD-crystallin is present in the supernatant after the chaperone assay. Substrate complexes elute in the void volume, independent of the αB to γD-ratio.

Formation of heterogeneous, huge substrate complexes leads to light scattering. This type of complexes could not be used for further investigation of stable substrate complexes, since they were very heterogeneous and aggregation-prone and did not contain many α-crystallin subunits. In a subsequent step, destabilizing mutations were introduced into γD-crystallin to simplify its thermal denaturation. The mutations were chosen from studies that related cataract formation to these amino acid changes in γD (Graw et al., 2002; Ji et al., 2013; Liu et al., 2005; Messina-Baas et al., 2006; Roshan et al., 2010). Some of these mutations introduce charges into the hydrophobic core of γD promising significant destabilization.

In contrast to γD WT that was purified by Dr. Jirka Peschek according to standard purification protocol, protein production in *E. coli* resulted for in formation of inclusion bodies for all mutants. These were purified according to the protocol in section 3.5 and were refolded in good yields. All purified variants were characterized as natively folded and stability was further characterized in the course of a Bachelor's Thesis (Radmann, 2013). Analysis of thermal stability by TSA-Assay resulted in minor thermal destabilizations (fig. 60). This indicates that folding of γD is the critical step when mutations are present. Once folded, it exhibits a thermal stability above average.

During the course of this work it was published that WT α-crystallins do neither interact with γD WT nor with the destabilized mutants at physiological temperatures. Only the activated phospho-mimicking mutant αB-3D was shown to have a weak affinity (Mishra et al., 2012).

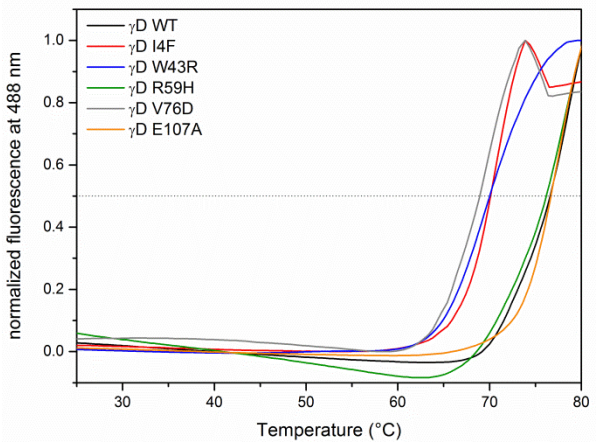

Fig. 60: Temperature-dependent change of SYPRO Orange fluorescence at 585 nm in the presence of γD WT and different cataract associated mutations (Thermal Shift-Assay).

After these experiments showing that γ-crystallins are suboptimal substrates for α-crystallin to analyze complex formation, mouse lens lysates were investigated to screen for authentic substrates of lens α-crystallin.

4.3.1 Establishing the characterization protocol using lenses of two different WT strains

To assess the effect of mutations in different crystallins on α-crystallin substrate complexes, eye lenses of C3HeB/FeJ- and C57BL/6-based mutant mouse lines were investigated using 2D-gel electrophoresis (2-DE) in combination with ms and SEC-HPLC. The analysis procedure was established using lenses of both WT strains. The isolated lenses were kindly provided by Prof. Dr. Joachim Graw (Helmholtz Zentrum Munich). The WT strains are named C3H and BL/6 in the following sections for simplification.

In fig. 61 the final work flow is shown. The ratios of soluble proteins in lens lysates were analyzed by 2-DE of whole lysates and compared to the urea-soluble fraction containing aggregated proteins. Furthermore, lysates were analyzed by SEC-HPLC to analyze changes in the compositions of the three crystallin families and to separate α-crystallin with potentially bound substrates. These purified α-crystallin species were further analyzed by 2-DE, EM and aUC to compare their quaternary structure to recombinantly purified α-crystallins.

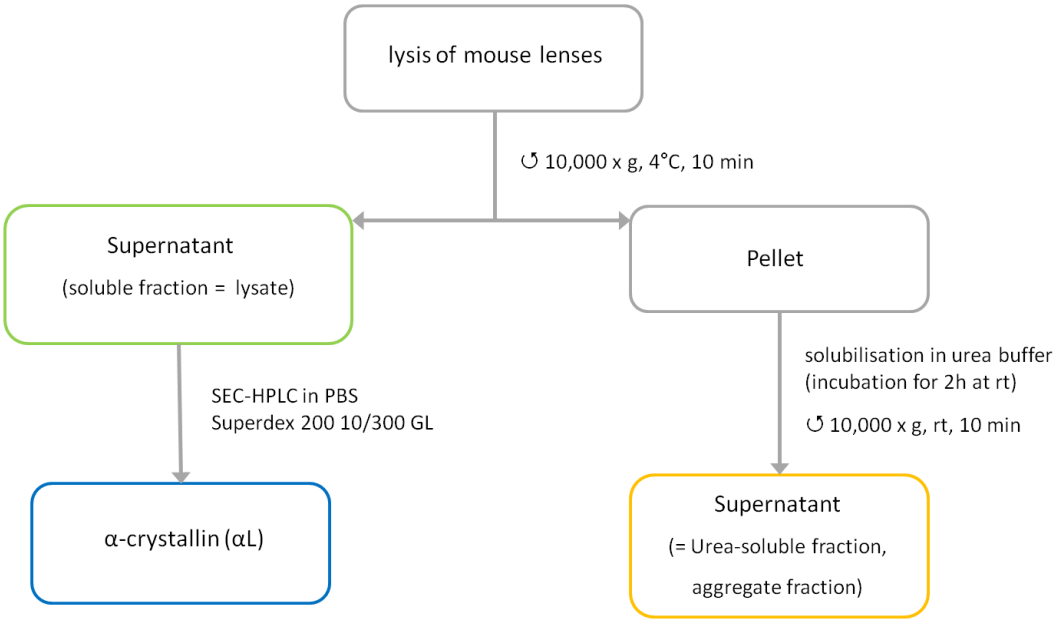

Fig. 61: Flow scheme of mouse lens crystallin separation to obtain different soluble and insoluble fractions.

4.3.1.1 Lens lysate composition of male C3H mice

For analysis of changes in the lysate composition of the soluble fraction after lens lysis compared to the urea-soluble fraction using 2-DE, the parameters first had to be established. Finally, 15%-gels were used with IEF-stripes exhibiting a linear pH-gradient from 3-10 resulting in the best resolution for whole lysate analysis.

Next, the obtained spots were identified by MALDI-TOF-mass spectrometry following tryptic digests. The assignment is shown for a 2-DE gel of a new-born C3H WT sample (fig. 62). The distribution of the crystallins on the gel can be roughly divided into different areas. While the basic γ-crystallins can mainly be found on the right side of the gels (pH 7-8), β-crystallins are, due to their higher molecular weight, detected in the upper area of the gel and divided into an acidic and a basic fraction (βA- and βB-crystallins). Unmodified αA-crystallin can be found bottom left, unmodified αB-crystallin at the borderline between β- and γ-crystallins. Only the spot of the rodent-specific splice-variant αA_{ins}-crystallin is found in between different β-crystallin-spots as its molecular weight is higher due to an inserted amino acids stretch of 23 amino acids between the NTR and ACD. The assignment is in accordance with the published literature (Ueda et al., 2002).

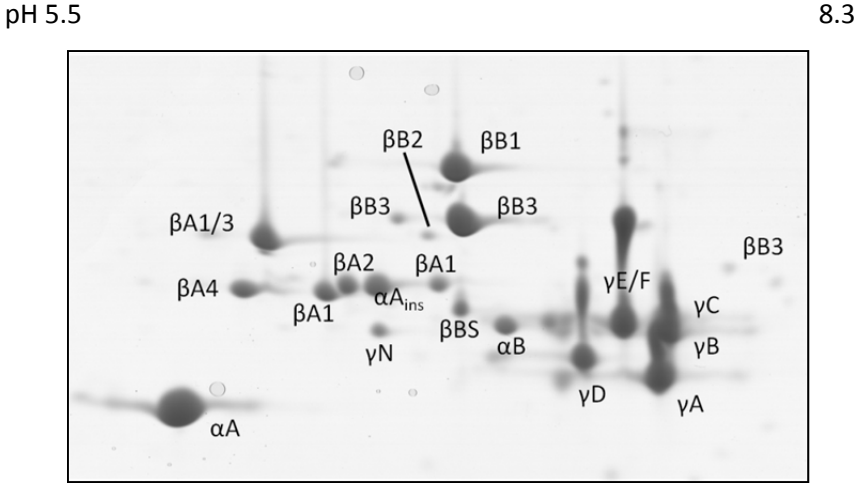

Fig. 62: Assignment of the spots obtained in 2-DE analysis of a new-born C3H WT sample.

After assignment, compositions of lysate and urea-soluble fraction of C3H and BL/6 WT samples of different ages were analyzed by 2-DE and compared. The results were comparable for both WT strains. In this chapter, only the 2-DE analysis of C3H samples are shown, data of BL/6 samples are shown in section 4.3.2.2 in comparison to Aca30-samples, a cataract muse line with BL/6-background.

In lenses of new-born mice, the crystallin spot-pattern on the gel is distinct (fig. 62). All spots could be assigned to the corresponding unmodified full-length crystallin by ms unambiguously.

Already at an age of four weeks the process of crystallin 'aging', which can be seen in increasing modifications of the crystallins, could be observed as reported (Ueda et al., 2002). The biggest differences were observed between new-born and three month old mice. Until an age of twelve weeks an increasing number of spots were observed (fig. 63). These spots originate from different modifications like phosphorylation, deamination and degradation (Ueda et al., 2002). In lenses of new-born mice the urea-soluble fraction is negligible. Therefore, no 2DE-analysis could be performed.

Expression levels of crystallins could also be observed as reported (Ueda et al., 2002), while α- and γ-crystallin are already expressed at birth almost to their final expression level, βB2-crystallin shows the most dramatic change in expression level during the first three month after birth: In new-born lenses, the spot of βB2-crystallin is hardly visible, but in the first weeks after birth, its intensity increases. This is also reflected in SEC-HPLC-chromatograms of lens lysates of different ages (fig. 63). In the first weeks, the peak amplitude of βB2-crystallin increases until it reaches a final level at about four months.

The urea-soluble fraction contained all kinds of crystallins. Especially for αA- and αB-crystallin it is striking that unmodified full-length proteins are mainly found in the soluble fraction, while modified proteins are found in the aggregated fraction. The α-crystallin spots were analyzed by ms-spectrometry and it was found that the observed modifications mainly consisted of phosphorylation and partial degradation. It was reported that α-crystallins are degraded c-terminally with age (Horwitz, 1992; Ueda et al., 2002) and this effect was published to be even more pronounced in cataractous lenses (Takeuchi et al., 2004; Thampi et al., 2002). The C-terminal degradation could be confirmed by tryptic digest followed by Orbitrap ms analysis. Several truncation products of αA-crystallin were detected. Some truncated forms were also phosphorylated. For αB, two main truncation products were found that exhibited either one or two N-terminal phosphorylations. The exact modification sites could not be determined. From about three months on, no significant changes could be observed. The relative composition of supernatant and aggregated proteins was similar for all analyzed samples.

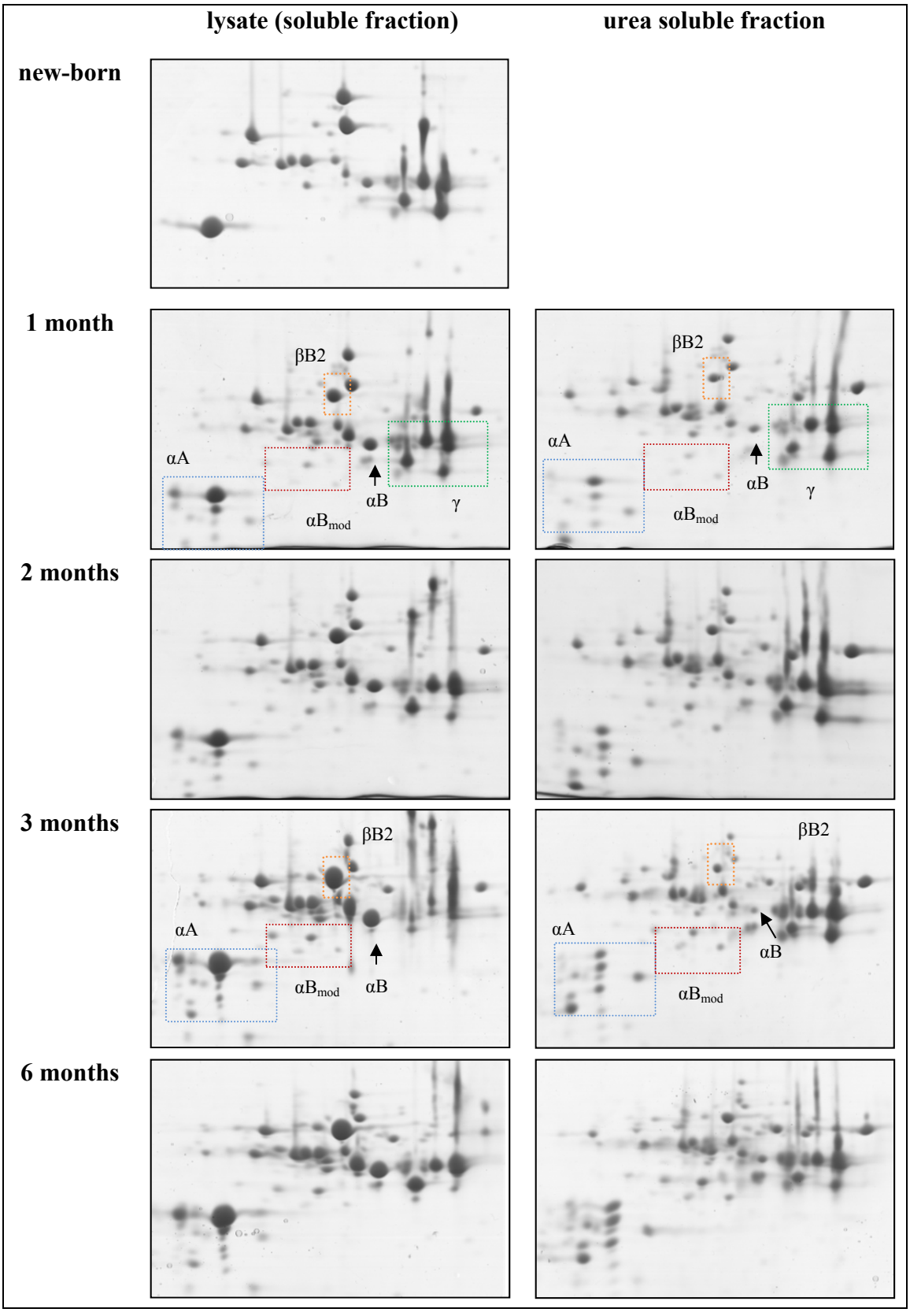
lysate (soluble fraction)
urea soluble fraction
new-born
1 month
βB2
αA
αB
αBmod
γ
2 months
3 months
6 months

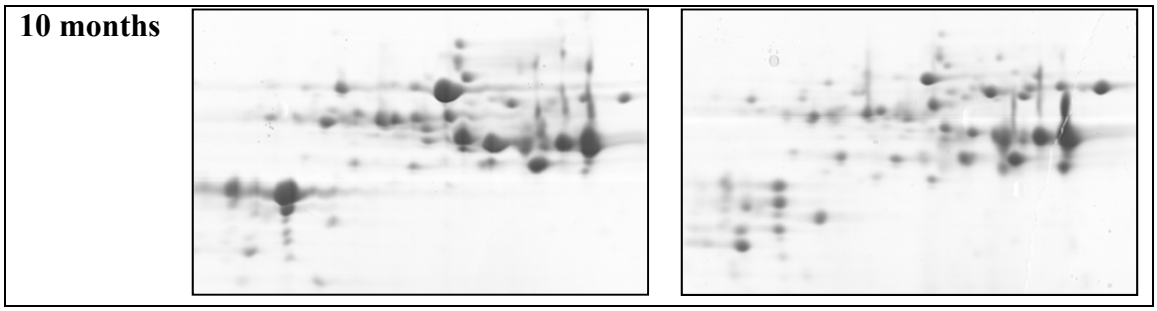

Fig. 63: 2-DE analysis of soluble and insoluble fractions of WT C3H lenses of different ages from new-born to 10 months. The number of spots increases with age. This is a result of progressing modification of all crystallins. Especially the two α-crystallin isoforms, αA- and αB, are affected. The modified variants are found in the aggregate fraction (right) in higher amounts compared to the full-length proteins. The main modifications observed for α-crystallin were truncations and phosphorylations. In the case of αB, these modified variants are marked as αB_{mod} in the gels since they were found separately from the full-length protein in a different region of the gel. βB2 is the only crystallin that is not present in large amounts at birth. However, it is expressed from birth on resulting in the most intense β-crystallin spot in the soluble fraction of adult mice.

In the SEC-HPLC chromatograms of lens lysates, the characteristic peak-order which led to the naming of the different crystallin fraction could be observed. At the void volume of the column, a high molecular weight fraction (HMW) was observed, which increases with age. The nature of this species is discussed below in more detail. α-crystallin forming large oligomers of about 25 subunits eluted subsequently. The dimeric β-crystallins elute at a later time point followed by the monomeric γ-crystallins. The increase of β-crystallins observed by 2-DE is accompanied by the appearance of a peak shoulder (β_h) at slightly higher molecular weights than the β-crystallin-peak (β_L) which is caused by formation of higher order β-crystallin oligomers with more than two subunits.

Furthermore, the oligomer size of α-crystallin increases in the first months. At birth, αL-crystallin from mouse lenses exhibits the same elution volume as recombinantly purified α-crystallin. In lenses of four week old mice, the size is already shifted to a higher molecular weight. From three months on, no differences could be observed in the α-crystallin-peak. The amount of the mentioned high-molecular weight species increases with age (fig. 64).

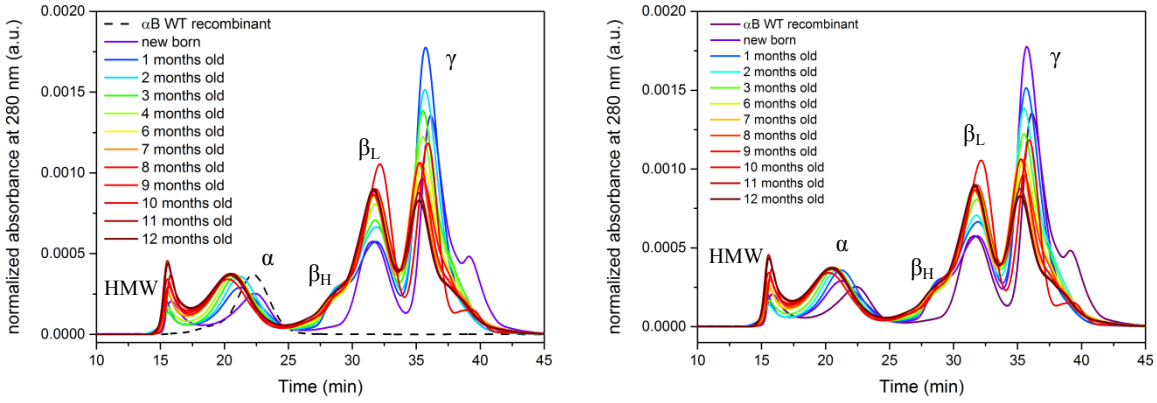

Fig. 64: SEC-HPLC-chromatograms of WT mouse lens lysates of different ages, normalized to the overall signal; high molecular weight-, α-, β- and γ-crystallin-fractions are assigned; **left:** C3H; **right:** BL/6. The peak amplitude of the HMW-fracion increases with age. The elution volume of α-crystallin of new-born samples resembles recombinantly purified α-crystallin. In samples of older mice, the α-crystallin peak is shifted to larger elution volumes. Furthermore, in new-born mice, the peak-shoulder representing the higher order oligomers of β-crystallin is not visible, yet. The ratio of β-crystallin to γ-crystallin changes with age.

4.3.1.2 Characterization of the two different lens α-crystallin fractions HMW and αL-crystallin

Quaternary structure

To obtain more information about formation of potential substrate complexes with increasing age the α-crystallin-fraction was analyzed further using EM and analytical ultracentrifugation. In aUC, the size difference between recombinant α-crystallin and αL-crystallin could be confirmed (fig. 65). Creating hetero-oligomers of recombinant murine αA- and αB-crystallin did not result in a similar oligomer distribution to αL-crystallin.

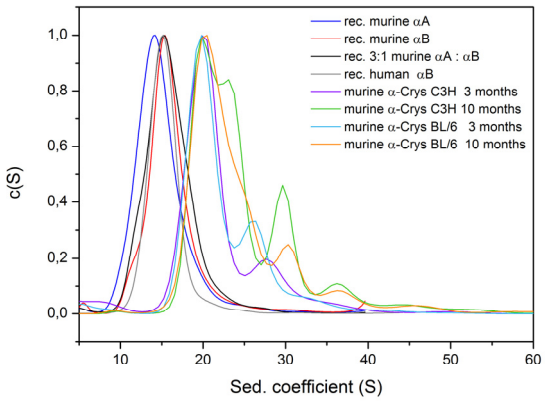

Fig. 65: c(s)-distributions from aUC runs with different mouse α-crystallins from mouse lenses; analysis was performed using Sedfit. All recombinantly expressed and purified proteins exhibit similar c(s)-distributions at smaller sedimentation coefficients. Murine α-crystallin samples form larger complexes that are significantly more heterogeneous.

Furthermore, a slight tendency of αL-crystallin towards increasing heterogeneity and appearance of larger molecular weight oligomers with increasing age was observed (fig. 66).

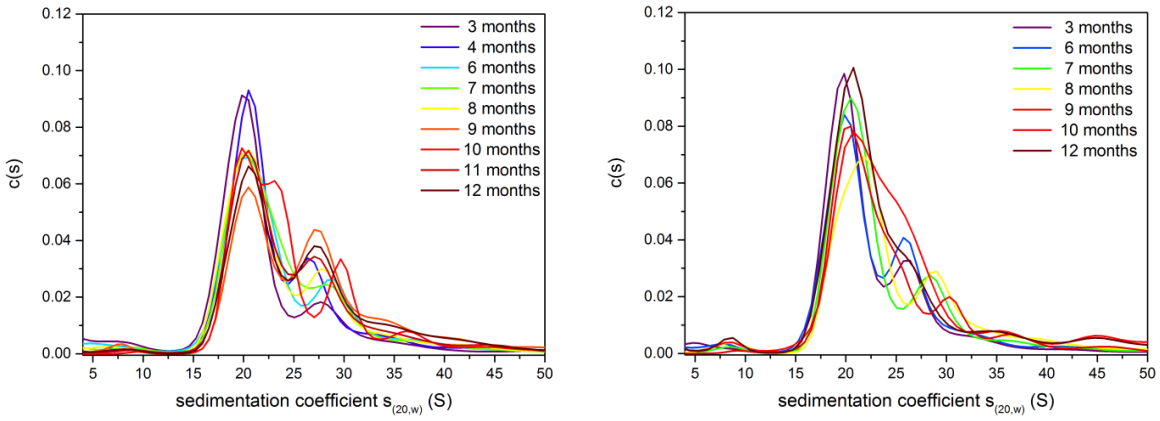

Fig. 66: SV-aUC analysis of purified αL-crystallins of different ages; c(s)-analysis was performed using Sedfit; **left:** C3H samples, **right:** BL/6 samples. The samples do not consist of homogenous oligomers, but contain a mixture of larger and more heterogeneous oligomeric assemblies.

The slight changes of oligomeric assemblies could not be confirmed by negative stain EM. In fig. 67 a Box-plot representation of the obtained size distributions is shown.

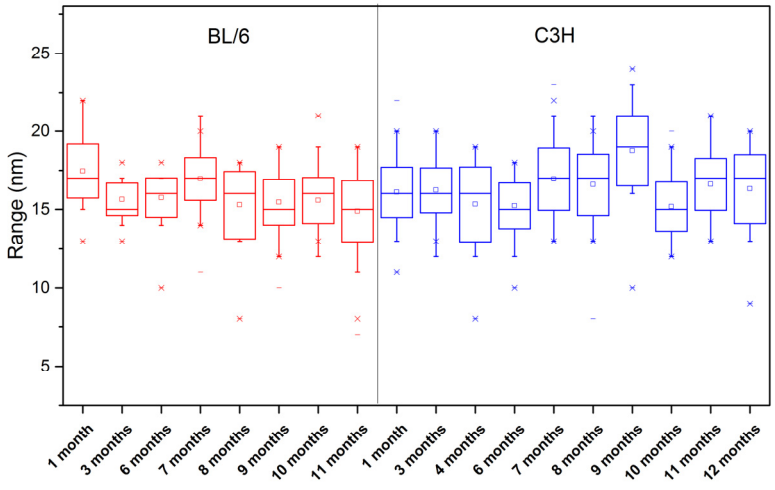

Fig. 67: Box-plot representation of the size distributions of murine lens α-crystallin from WT mice lysates of different ages obtained by NS-TEM. The bottom and the top of the boxes represent the first and third quartile. The horizontal lines mark the second quartile (median). The small squares in the boxes indicate the arithmetic mean. Crosses below and above the boxes show 1% and 99% of the data range, the ends of the whiskers are determined by the most extreme particle diameter found within maximally 1.5 times of the interquartile range. All data particles with sizes above or below the end of the whiskers are defined as outliers. Horizontal lines above and below the boxes indicate the absolute extremes. No significant changes could be detected between the sizes of αL-crystallin of young and old WT mice.

To estimate the variation between different individuals of the same age, two representative ages of C3H WT strain were chosen (three months and eight months) and purified

α-crystallin samples were analyzed by TEM. In fig. 68 the results are shown. Minor variations observed by NS-TEM between different ages are not statistically significant.

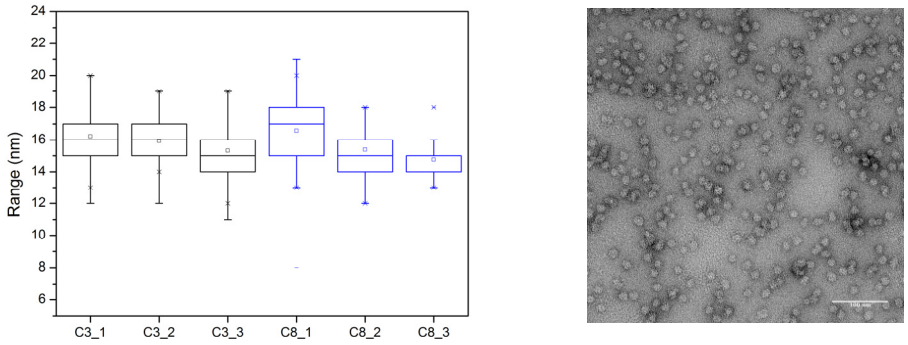

Fig. 68: left: Comparison of αL-crystallin size derived from NS-TEM-data from three different individuals of the same strain and age for C3H, three months old (C3) and eight months old (C8) in a Box-Plot representation; **right:** representative NS-EM picture of a C3H sample. The white scale bar represents 100 nm. Only minor differences could be detected that are not significant.

4.3.1.3 Identification of substrates bound to α-crystallin

Due to its immense heterogeneity, αL-crystallin is even more complicated to analyze by structural methods than recombinant purified WT. From the current data, it cannot be determined whether the minor differences that were observed by aUC are significant.

There are three possible explanations for the increased molecular weight of lens α-crystallin in mice:

Firstly, an additional mRNA-splicing isoform αA exclusively found in rodents and some other mammals could change oligomer assemblies. This isoform of αA named αA_{ins} contains a stretch of 23 amino acids between residue 63 and 64. The ratio of αA : αB : αA_{ins} in the analyzed lenses was determined to be 3 : 1 : 0.45 using ImageQuantTL. The percentage of splice variant is high enough to have an influence on the structural properties of the mixed oligomers formed in the lens. However, in new-born mice, αA_{ins} is already expressed, but the oligomer size is comparable to recombinant protein oligomers. Therefore αA_{ins} cannot explain the observed differences.

A second possible explanation for the higher molecular weight and the increased heterogeneity is the mixture of different modified α-crystallins present in the lens that form hetero complexes and thereby might inhibit formation of symmetric homogenous oligomers

Another possible reason for a peak shift to smaller elution volumes is the formation of substrate complexes with lens proteins. To analyze the behavior of mαA and mαB with

bound substrate, MDH was used as a model substrate *in vitro*. Different amounts of MDH were heated to 42°C in the presence of either rec. mαA, mαB or a preincubated 3:1 mixture of mαA and mαB. After the incubation the mixtures were analyzed by SEC-HPLC (fig. 69).

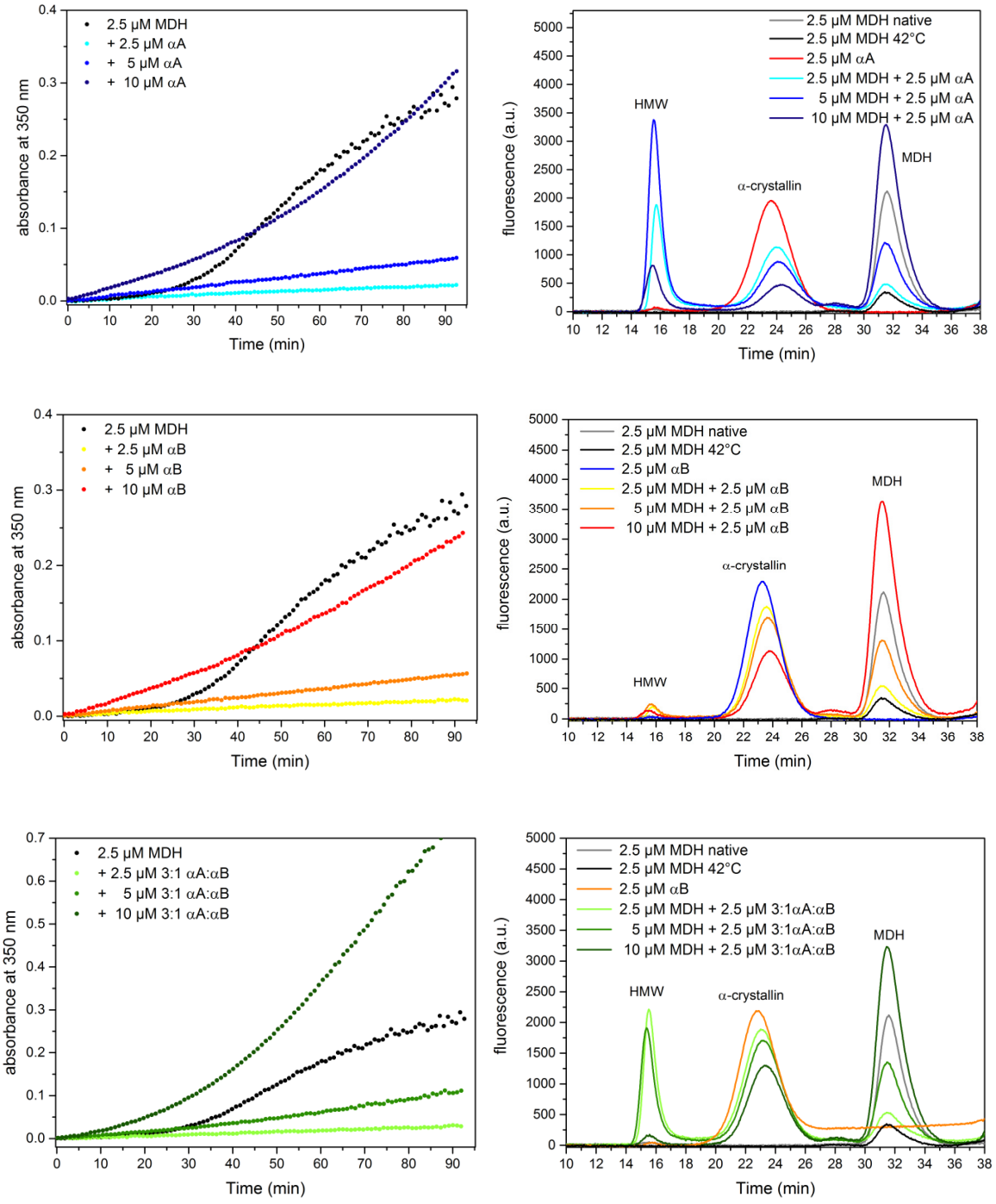

Fig. 69: left: Chaperone assays of mαA-, mαB- crystallin or a 3:1 mixture of mαA:mαB with different concentrations of MDH at 42°C; **right:** after chaperone assays were completed, samples were centrifuged and subsequently analyzed by SEC-HPLC. In the chromatograms, peaks of MDH, α-crystallin oligomers and a HMW-species eluting at the void volume of the Superdex200-column are shown. For αB, the expected HMW-fraction could not be detected in the SEC-HPLC-chromatograms, although a suppression of MDH-aggregation was observed in chaperone assays. The decrease in amplitude of the αB-peak indicates that the formed substrate complexes agregated during sample preparation for SEC-chromatography.

In the chromatograms, three peaks are visible. The peaks with an elution time of ~32 min represent the amount of unbound MDH that is still in solution after heat stress. The peaks at ~22 min belongs to purified α-crystallin. The third peaks, eluting at the void volume of the column after ~15 min, represent the complex of α-crystallin with bound MDH. With increasing amount of substrate, less α-crystallin having the size of the purified homo-oligomer is present. This effect is visible for all three tested α-crystallin variations. A small amount of MDH is still natively folded after heat stress, even if no chaperone is present. The remaining denatured MDH is either aggregated or bound by α-crystallin. When αA is present, a high molecular weight fraction was detected, that consists of large, heterogenous α-crystallin-MDH complexes. In the chromatograms of the samples with the highest amount of MDH and in samples where only αB is present, the HMW-Peak is hardly visible. Nevertheless, the α-crystallin-peak and MDH-peak is decreased as well. This implies the formation of substrate complexes that were too large to stay in solution and either aggregated during the 90 min. incubation, which can be seen in the respective chaperone assays on the left, or the complexes sedimented during sample preparation in the centrifugation step before the SEC-HPLC analysis. In these cases, the chaperone capacity of α-crystallin was exceeded. These findings support the hypothesis, that the HMW-fraction found in mouse lens lysates could consist of α-crystallin-substrate complexes.

To analyze the two different α-crystallin fractions further, samples were analyzed by NS-TEM (fig. 70). In the α-crystallin samples, a heterogeneous mixture of particles can be found in the size range of 15-20 nm. This is slightly larger than what was observed for recombinant α-crystallin oligomers. In contrast, the few particles that could be analyzed in the HMW-samples were huge protein assemblies with diameters up to 50 nm. In earliers studies, it was reported that these particles consist mainly of α-crystallin (Carver et al., 1996). Due to the low particle number and big heterogeneity, no size distribution could be obtained. The low particle number of the latter is due to the aggregation propensity of these samples that complicates their analysis and the low amount obtained from mouse lenses.

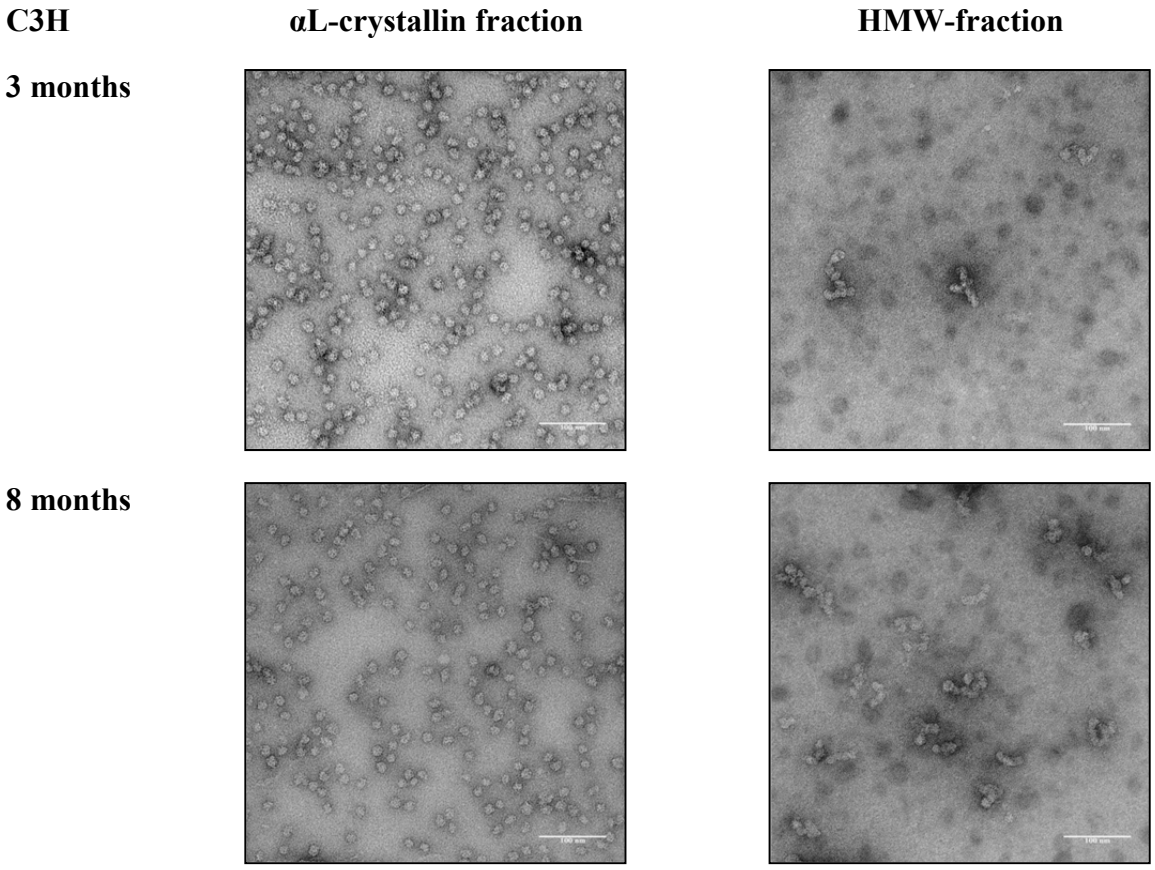

Fig. 70: NS-TEM analysis of three and eigth months old αL- and HMW-samples purified from C3H WT lenses. In the α-crystallin fraction a large number of distinct particles can be seen while in the HMW-sample large, undefined aggregate-like particles were found. The white scale bar represents 100 nm.

Studies on these high molecular weight complexes were conducted earlier (Roy and Spector, 1976). It was found out, that the chaperone activity of these larger α-crystallin complexes is reduced and that αL-crystallin with lower molecular weight disappears in the older cells in the center of the lens, until only the HMW-crystallin remains. In a different study, the NMR-spectra of HMW-crystallin were compared to spectra of substrate complexes formed *in vitro*. The loss of C-terminal flexibility led to the conclusion that HMW-crystallin most probably consists of substrate complexes (Carver et al., 1996).

To determine, whether the observed higher molecular weight and increased heterogeneity of α-crystallin from adult mouse lenses compared to recombinant α-crystallin is only due to degradation and post-translational modifications, or if bound substrates result in larger complexes, both sample types (α-crystallin and HMW) were analyzed by 2-DE. A representative comparison of HMW- and α-crystallin-fractions of nine months old C3H-samples is shown in fig. 71. The spots were assigned after tryptic digest by Orbitrap ms analysis. The gels show that the samples consist of the same main components αA, αA_{ins} and αB. The only non-α-crystallin component found was βB2. The ratios of full length proteins to

modified variants are different. The HMW fraction contains more truncated αA_{ins} and more phosporylated and truncated αB-crystallin. The extent of these signal differences is hard to see, due to the fact that these gels were run close to the maximal recommended protein amount to faciliate assignment by ms and to enable visualization of potential minor components. In another comparison of six month old BL/6 samples with less overall protein amount on the gel to obtain better peak resolution, it can be seen clearly that the most strinking difference is the higher amount of modified α-crystallin.

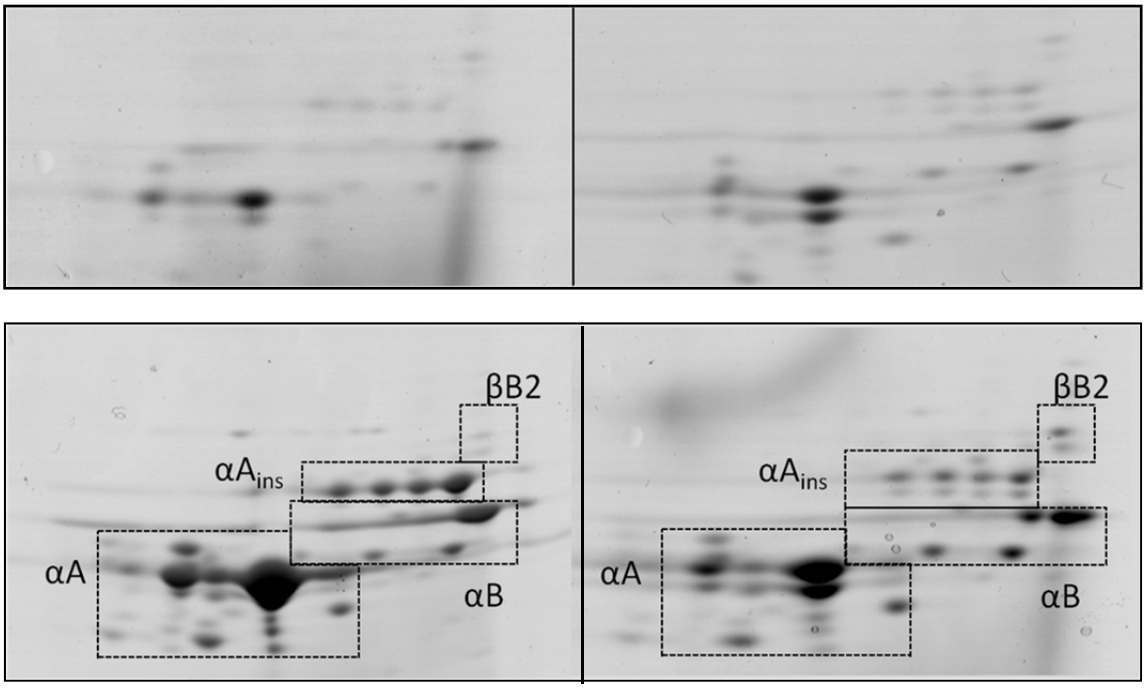

Fig. 71: 2-DE analysis of purified HMW- and α-crystallin-fractions from WT lenses; different modifications of αB- and both αA-crystallin isoforms could be assigned. More modified α-crystallin compared to unmodified full-length protein could be detected in HMW-samples; furthermore, two spots that were found in all samples contained small amounts of βB2 crystallin; **left:** α-crystallin-peak; **right:** HMW-peak. top line: C3H, six months old, bottom line: C3H, nine months old.

Taken together, the results of the α-crystallin characterization using 2-DE analysis confirmed the previous assumptions to some extent. In both α-crystallin sample types, a certain amount of post-translational modifications was found. These result in perturbating effects on the oligomeric architecture of α-crystallin, which is sensitive to changes in amino acid composition as seen in section 4.1.2. Modifications, especially C-terminal truncations lead to a loss of oligomer stabilizing interactions and thereby to the formation of large, less defined assemblies that are prone to aggregation.

On the other hand, βB2 was found bound to α-crystallins in both fractions. Several studies on HMW- α-crystallin were performed in the 1990s and earlier with human and bovine lenses reporting bound β- and γ-crystallins in the center of large undefined particles as well

(Takemoto and Boyle, 1994). EM-studies reported large, asymmetrical particles consistent with the results derived in this study (Kramps et al., 1975). As seen from the substrate complexes formed *in vitro*, large and less defined particles result from binding to subsrtate proteins.

If bound to α-crystallin, the presence of β-crystallin is also a probable explanation for the larger oligomeric size of αL-crystallin compared to recombinant α-crystallin. Binding of β- to α-crystallin in lens lysates under physiological conditions needs to be examined by further experiments. Nevertheless, the presence of these proteins can not be the only reason for the increasing amount of the HMW-fraction, because they were found in both sample types, α-crystallin and HMW. The main difference that can be observed on 2-DE-Gels is the different amount of unmodified full-length α-crystallin.

To examine the role of α-crystallin in cataractous lenses, mutations in all three crystallin-subfamilies were analyzed according to the protocol established with WT-lenses.

4.3.2 Effect of mutations in different crystallins on α-crystallin in the murine eye lenses

Next, the effect of cataract-causing mutations in different crystallins was investigated. Three different homozygous cataract mouse lines were chosen and lenses of different ages were analyzed according to the protocol described above. The phenotypes of the analyzed mutations are described at the beginning of the respective chapters.

4.3.2.1 Aey7 – αA V124E

Aey7 has a C3HeB/FeJ background and carries a mutation in the αA-crystallin encoding gene *Cryaa* which leads to the substitution of Val124 to Glu. A progressive opacification of the lens was observed starting in the embryonic nucleus and posterior suture at eye opening (postnatal day 12) and terminating as nuclear and zonular opacity at approximately the age of 2 months. It was reported that the lenses were reduced in size (Graw et al., 2001).

The mutation V124E is located in the highly conserved ACD, which is the basic building block of α-crystallin and forms a stable β-sandwich structure. In the crystal structure, the side chain of the mutated valine is located in a loop region pointing into the hydrophobic core of

the domain. Introduction of the large negatively charged amino acid glutamate leads to steric and electrostatic repulsion causing perturbations (fig. 72).

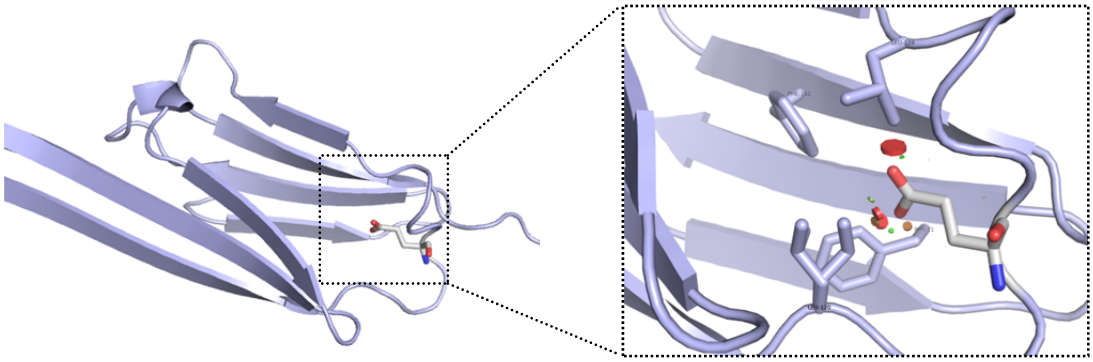

Fig. 72: *In silico*-mutation of V124 to E in the crystal structure of bovine αA-crystallin ACD (pdb 3L1E). The steric repulsion is indicated by red disks displaying overlapping van der Waals-radii.

4.3.2.1.1 *In vitro* characterization of recombinant αA V124E

To analyze this mutation the protein was first purified recombinantly and analyzed *in vitro*.

The protein was expressed as inclusion bodies in *E. coli*. After refolding according to the standard inclusion body protocol, soluble, folded protein was obtained. The secondary structure analyzed by CD-spectroscopy is comparable to WT protein, but it shows a different thermal transition (fig. 73). The ellipticity signal of αA WT increases with temperature until about 80°C, then a signal jump is visible. This type of thermal transition is known from αB WT (see section 4.1.1). The signal increase is probably due to structural rearrangements in the oligomer and, as seen from deletion mutants, depends on the NTR. The signal jump at 80°C is most probably due to aggregation without unfolding. The transition observed for V124E shows a similar decrease in signal, but already at lower temperatures and at 80°C a further signal decrease is observed. No large aggregates were visible in the cuvette. This implies a different underlying mechanism of thermal denaturation. From the early signal decrease it can be assumed that the thermal stability of the mutant is decreased.

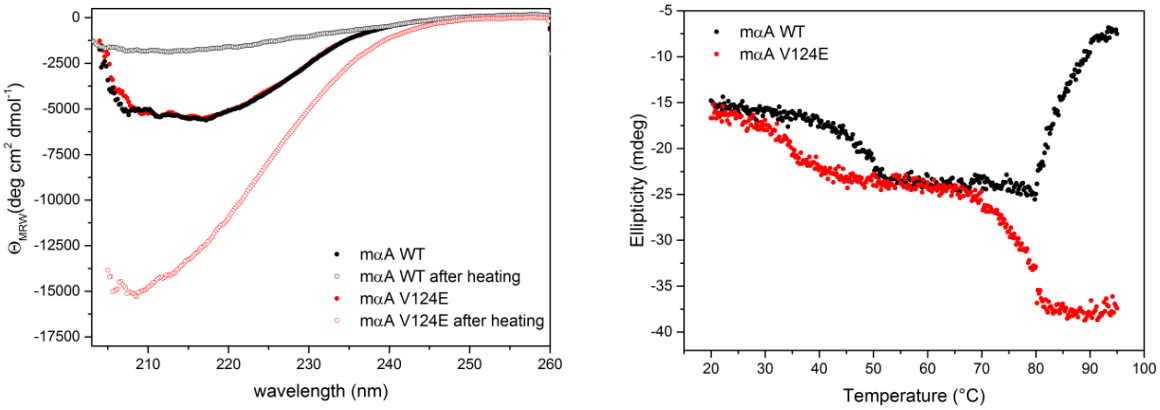

Fig. 73: left: CD-spectra of recombinantly purified murine αA WT and V124E before and after thermal transitions were recorded; **right:** thermal transitions obtained by CD-spectroscopy; αA WT shows a signal increase with temperature resulting in a signal jump at 80°C due to aggregation without loss of the β-sheet structure similar to αB WT, V124E αA does not show a signal jump at 80°C, the β-sheet unfolds upon heating.

The size distributions obtained by EM are dependent on the pre-incubation of the sample at 37°C, as it was observed for different purified α-crystallin samples after storage at -80°C (section 4.1.1). For most variants after incubation at 37°C, the observed average oligomer size decreases. In the case of αA V124E, the size distribution shifts to significantly larger particles. Comparison of WT and V124E by aUC after pre-incubation confirms the large oligomeric assemblies at physiological temperatures (fig. 74). This is presumably correlated to the early transition observed in CD-spectroscopy.

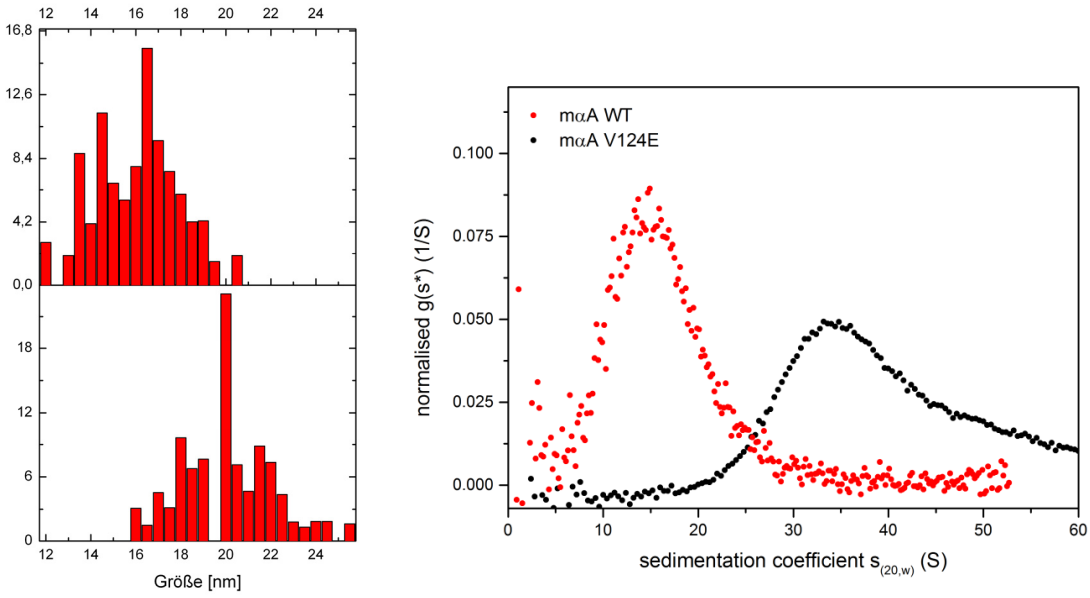

Fig. 74: left: Temperature-dependent shift of the size distribution of αA V124E to larger particle diameters with increasing temperature obtained by NS-EM, Top: pre-incubation at 4°C, bottom pre-incubation at 37°C; figure kindly provided by Dr. Carsten Peters; **right:** normalized g(s*)-distributions of αA WT and αA V124E after pre-incubation at 37°C obtained by aUC and analysis with dcdt+. Physiological temperatures lead to a more heterogeneous mixture of significantly larger particles for αA V124E.

To analyze the mutant further, the overall hydrophobicity was assessed by ANS-binding and chaperone activity was investigated using MDH as a substrate (fig. 75). The hydrophobicity of V124E is increased about 1.5-fold compared to WT without pre-incubation at 37°C. After pre-incubation a stronger increase in hydrophobicity (2-fold) is observed as for WT. Taken together, the data collected on structural properties of the mutant, it seems plausible that destabilization of the ACD by the introduced mutation leads to a less compact β-sandwich structure especially at higher temperatures. The hydrophobic core is exposed to a higher extent and the oligomeric scaffold cannot be sustained.

In fig. 75 it can also be seen, that chaperone function of the mutant is almost diminished completely at 42 °C, correlating with the destabilization of the oligomeric structure.

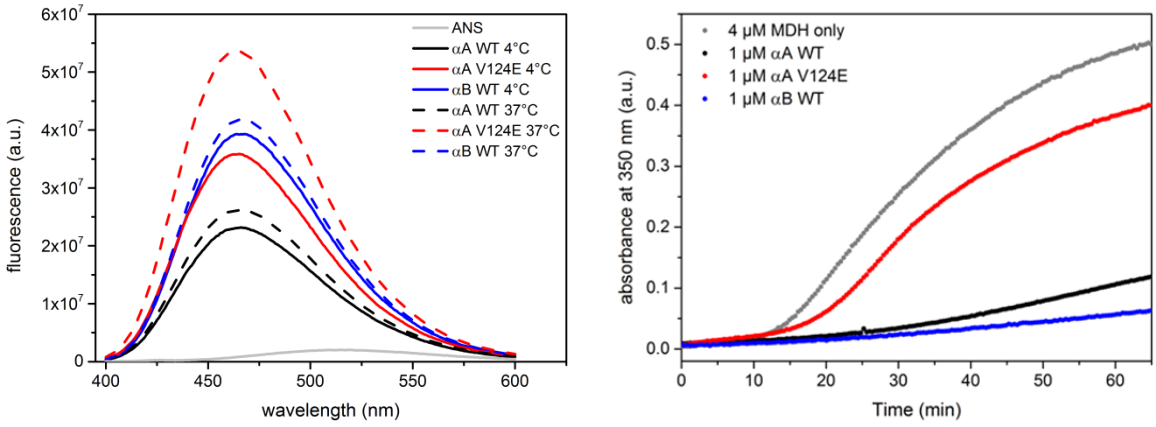

Fig. 75: left: ANS-fluorescence spectra in the presence of αA WT, V124E and αB WT. The surface hydrophobicity of αA V124E is higher than that of WT after pre-incubation at 4°C. Pre-incubation at 37°C leads to an increase in hydrophobicity of all analyzed samples, but the strongest effect could be observed for V124E. right: Chaperone activity of αA WT, V124E and αB WT using thermally denatured MDH as a substrate at 42°C. αA WT exhibits a lower chaperone efficiency than αB WT; αA V124E exhibits a further decrease in activity.

From the collected *in vitro*-data it is assumed that in Aey7 mice a higher extent of aggregation can be observed and that the aggregates mainly contain αA V124E itself as well as potential substrate proteins due to the lost chaperone function of αA. To confirm this assumption, the lens crystallin composition of soluble and insoluble fraction of Aey7-lenses was analyzed.

4.3.2.1.2 *In vivo*-effects of αA V124E mutation – characterization of Aey7 mice

To investigate crystallins in cataractous lenses, 2-DE analysis of lens lysates was performed. It could be observed that the αA-spot exhibited lower signal intensity and was slightly shifted to lower pH-values due to the mutation and the αA_{ins}-spot was missing in 2DE-gels of new-born mice. The overall spot intensities of αA-variants found in the soluble fraction was lower in the case of αA V124E compared to WT (fig. 76).

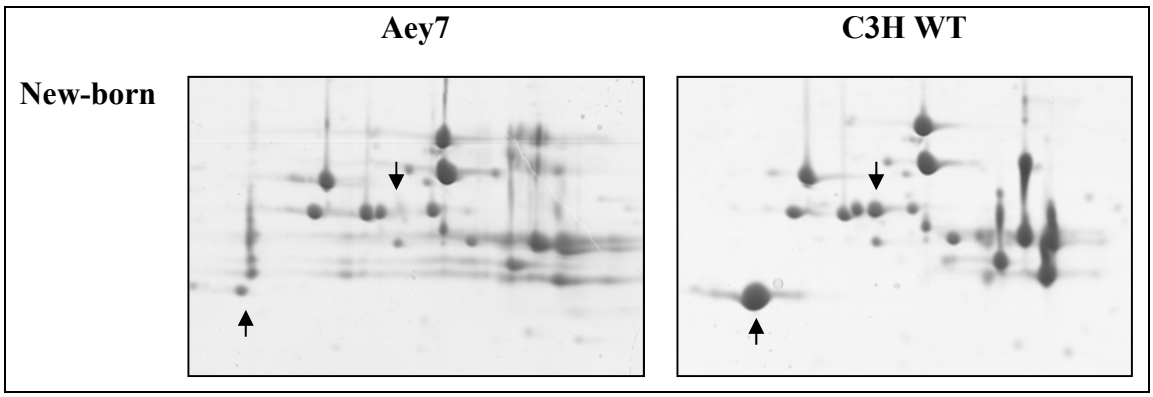

Fig. 76: Comparison of 2-DE analysis of lens lysates of new-born C3H- and Aey7-mice; positions of αA-spots are marked with black arrows. In the left gel αA-spot is shifted to lower pH-values and exhibits lower signal intensity. The αA_{ins}-spot was not detectable.

When comparing the soluble and urea-soluble fractions over time, it can be observed that a large number of spots of low intensity appear in the urea-soluble fraction below the spot of unmodified αA (fig. 77-79). These originate from increased truncation of αA V124E. While mainly full-length and singly phosphorylated V124E can be found in the soluble fraction, all modified variants can only be found in the aggregate-fraction. In C3H WT samples, unmodified full-length αA is the predominant species in the soluble fraction. Additionally, a spot identified as a variation of βB2 appears in Aey7 samples, which was not observed in comparable intensity in WT samples.

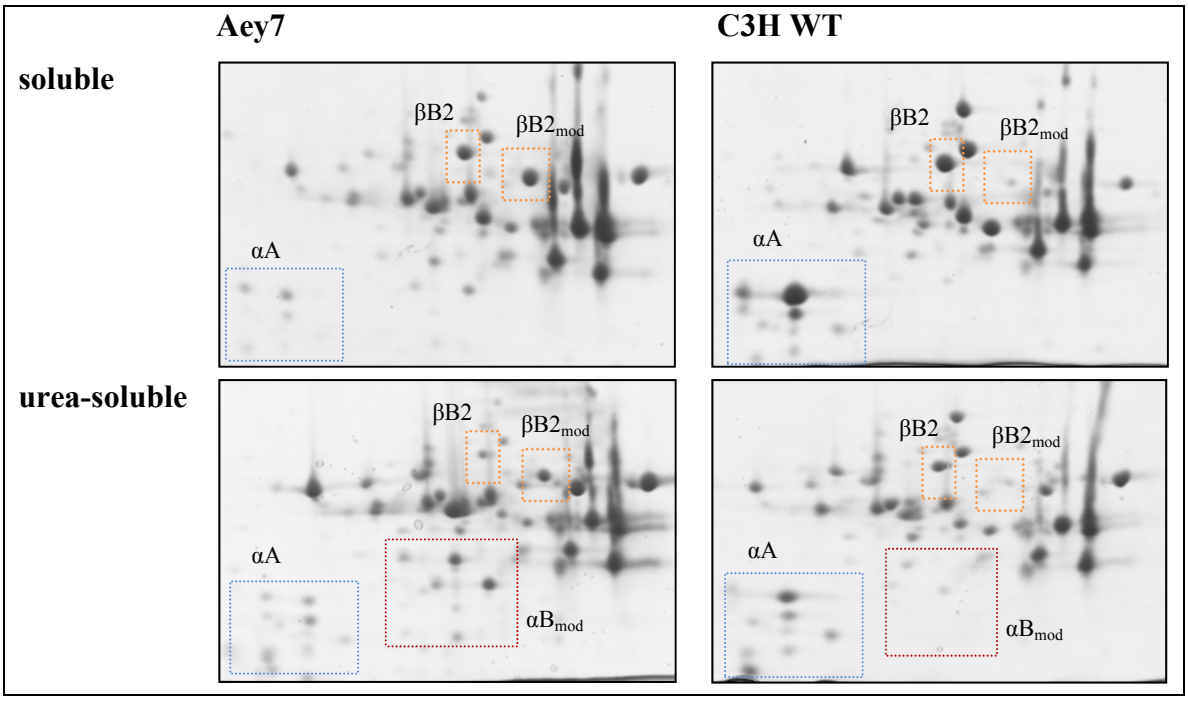

Fig. 77: Comparison of 2-DE analysis of soluble and urea-soluble aggregate fraction of one month old C3H- and Aey7-mice. Less αA-crystallin can be found in the soluble fraction. In the insoluble fraction a higher amount of truncated and phosphorylated αB could be detected. βB2 is increasingly modified in Aey7 mice compared to C3H WT animals.

Mutation of αA-crystallin also led to a decreased level of soluble αB-crystallin (fig. 78). A significantly higher amount of modified αB-crystallin was found in the aggregate fraction. With ageing this tendency continues. Apparently, αB-crystallin is one of the major substrates of αA-crystallin in need for stabilization. This is in accordance with the performed studies on αA-crystallin-knockout, where mainly αB-crystallin was found in the insoluble fraction (Brady et al., 1997). The reason might be the higher overall surface hydrophobicity of αB WT compared to αA WT shown in fig. 75. When αA is not able to mask the exposed hydrophobic patches of αB WT in the formed hetero-oligomers, this might lead to an increase in interaction with other lens proteins and subsequent aggregation. For αA V124E a higher surface hydrophobicity compared to αB was shown. Consequential, this and other αA mutants (Panda et al., 2016; Pang et al., 2010)exhibiting higher hydrophobicity than αA WT, are incapable of compensating the high surface hydrophobicity of αB. Differential expression of αA and αB was reported in different regions of the lens with αA being found predominantly in fiber cells while αB is preferentially expressed in epithelial cells (Robinson and Overbeek, 1996). This could be a mechanism of regulation, with αB probably interacting stronger with other proteins, like for example beaded filaments, to build up a gradient of αA to αB ratio from the center to the outer region of the lens.

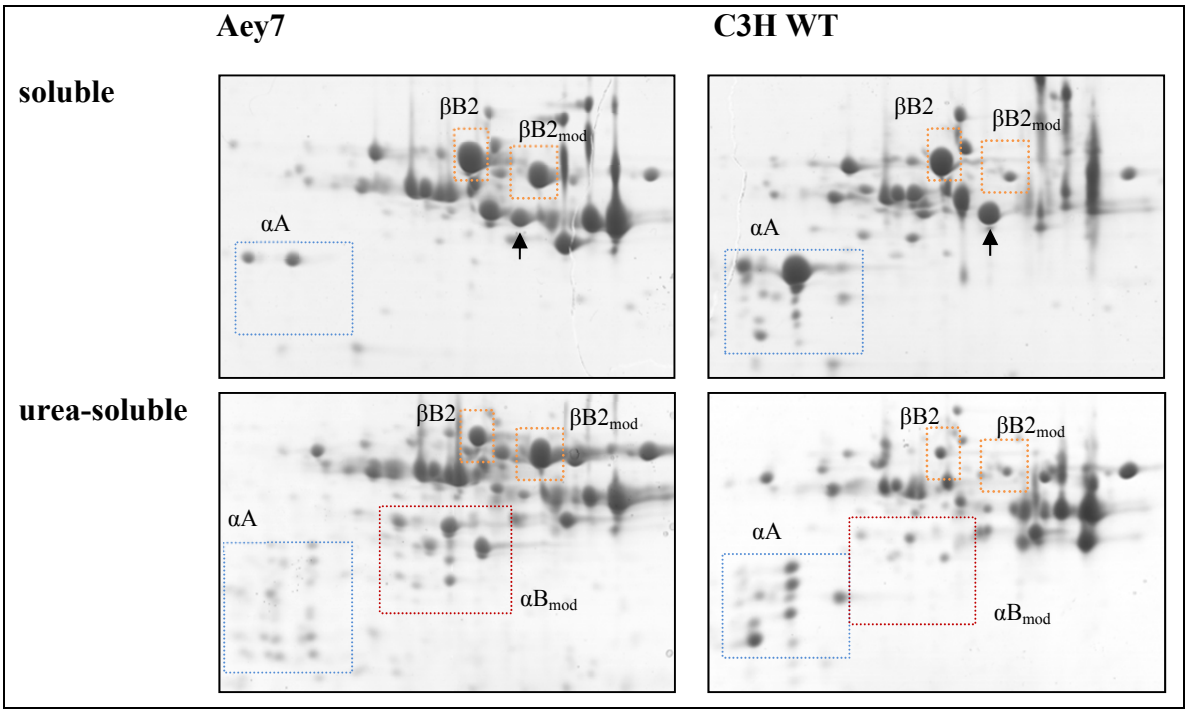

Fig. 78: Comparison of 2-DE analysis of soluble and urea-soluble aggregate fraction of three months old C3H- and Aey7-mice. Less αA-crystallin can be found in the soluble fraction. In the insoluble fraction a higher amount of truncated and phosphorylated αB could be detected. βB2 is increasingly modified in Aey7 mice compared to C3H WT animals.

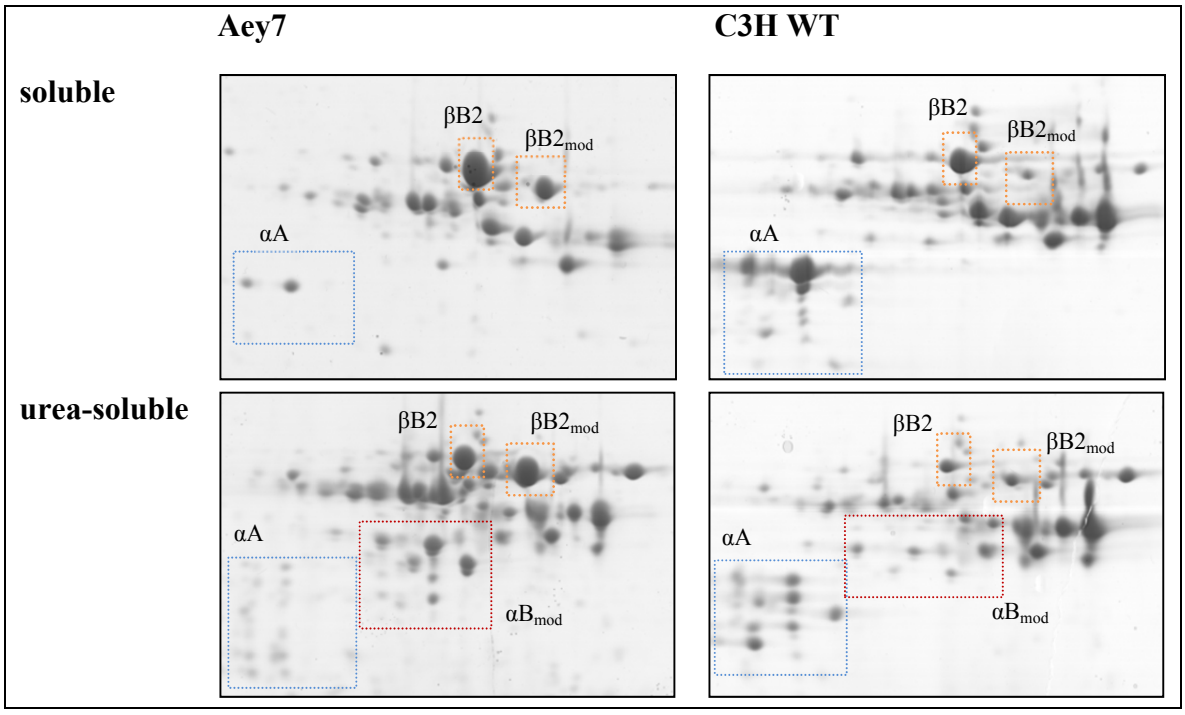

Fig. 79: Comparison of 2-DE analysis of soluble and urea-soluble aggregate fraction of 10-months old C3H- and Aey7-mice. Less αA-crystallin can be found in the soluble fraction. In the insoluble fraction a higher amount of truncated and phosphorylated αB could be detected. βB2 is increasingly modified in Aey7 mice compared to C3H WT animals.

The lens lysates from Aey7 mice were also analyzed by SEC-HPLC. In fig. 80 a comparison of the chromatogram to the WT-chromatogram is shown. While in the WT samples the characteristic peaks for HMW, α-, β-, and γ-crystallin can be observed, the α-peak is missing for V124E. In four week old mice a HMW-Peak is present with higher intensity, but in samples from twelve weeks of age on, no oligomeric α-crystallin peak can be detected anymore. The ratio of β- to γ-crystallin is similar for WT and Aey7 in the sample of one month old mice, but the peak-shoulder originating from higher order β-crystallin assemblies is missing. At three month of age, the β-crystallin content relative to γ-crystallin is significantly higher fitting to the overrepresented βB2-spot observed in 2-DE. The chromatograms shown below are normalized to the overall signal. The amount of soluble protein was strongly decreased with age in Aey7 mice.

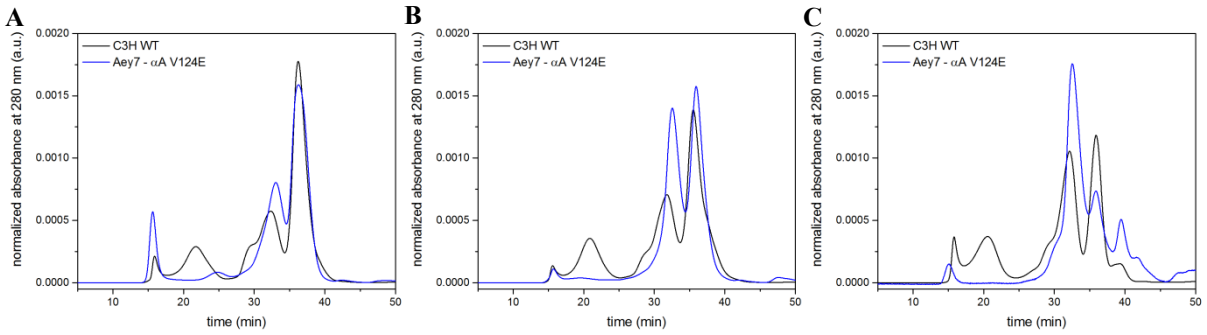

Fig. 80: Comparison of SEC-HPLC chromatograms of C3H and Aey7-lysate samples of different ages; **A:** 1 month, **B:** 3 months; **C:** 10 months. In samples of young animals, a large HMW-peak was detected. This is not present anymore in samples of older individuals. With increasing age, the γ-crystallin peak-intensity decreases. An additional peak at higher elution volumes could be detected, which might originate from γ-crystallin degradation. The β_h-peak is not visible in all Aey7 samples.

4.3.2.2 Aca 30 – βA2 S47P

The mutant Aca30 is based on the C57BL/6 strain and shows a mutation in βA2-crystallin encoding gene *Cryba2*, which leads to an exchange of Ser47 to Pro. The lenses of the *Aca30* mutants are smaller than WT lenses and clear at the time of birth, no significant differences can be observed compared to WT-lenses. At about three weeks of age, clefts in the cornea are described. At 15 weeks a progressive opacification was observed, leading to complete opacification of the whole lens in homozygous mutants at 25 weeks of age, while heterozygous individuals only developed a subcapsular cortical cataract (Puk et al., 2011). The Scheimpflug images (fig. 81) of WT- and the Aca30 mutant-lenses of two different ages demonstrate the degree of opacification in mutant lens.

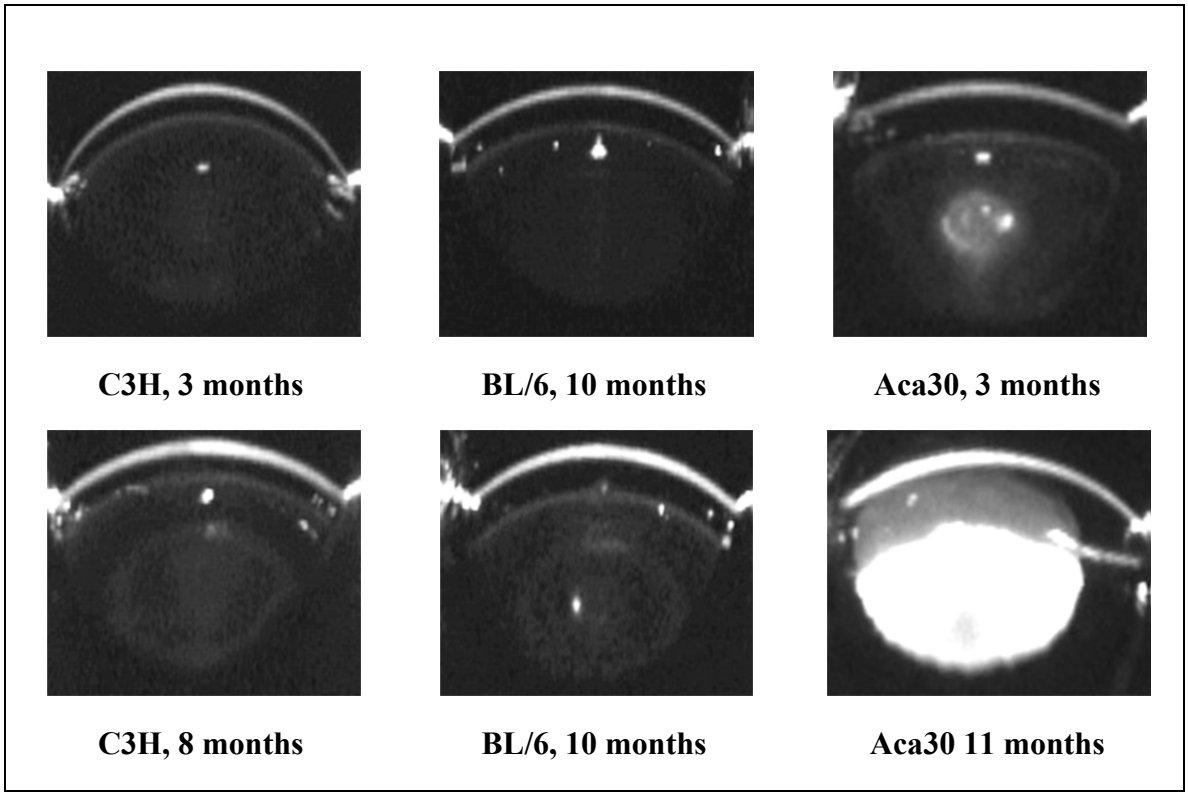

Fig. 81: Scheimpflug images of WT- (C3H and BL/6) and Aca30-lenses at different ages, kindly provided by Prof. Dr. Graw (Helmholtz Zentrum Munich). In Aca30 lenses a nuclear cataract can be observed at 3 months of age leading to complete opacification at the age of 11 months.

2-DE analysis of Aca30 lens crystallin composition

To compare the effect of mutations in β-crystallin, lens lysates of Aca30-mice were analyzed by 2-DE. Similar to samples of Aey7 the βA2- spot of the protein bearing the mutation could not be detected in 2-DE analysis of new-born Aca30 mice (fig. 82). Exchange of Ser to Pro should neither result in large difference in pI nor in molecular weight. Therefore, the spot was expected at a position at the WT position in the gel. The reason for this could either be a down-regulation of the expression or degradation. Aggregation can be excluded due to the fact, that it was not found in any analyzed insoluble fraction of Aca30-samples (fig. 83-85).

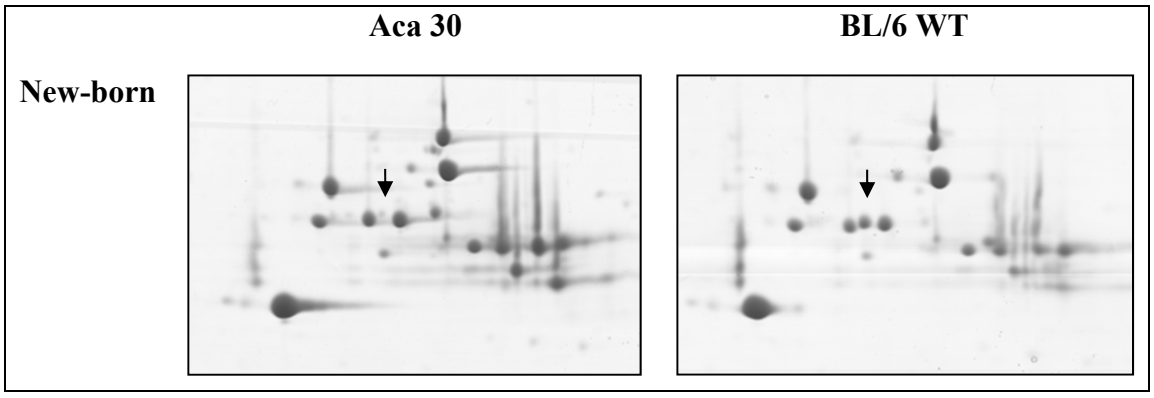

Fig. 82: Comparison of 2-DE analysis of lens lysates of new-born BL/6- and Aca30-mice; the position of βA2-spots are marked with black arrows. The βA2-spot is not visible on the gel. No other crystallins are affected in new-born mice.

At an age of three months, the composition of the urea-soluble fraction of Aca30-samples still resembles the WT composition of the aggregated fraction (fig. 83). These samples correlate to the time point in mouse development, shortly before first opacifications usually are observed. In the lysate a slightly higher spot intensity of modified αA- and αB-crystallin can be observed for Aca30-samples. In comparison to WT samples, less full-length βB2 is present, while a presumably truncated form of βB2 is represented to a higher extent than in WT samples. Interestingly, βB2 was found to interact with α-crystallin in WT lenses. Another difference is the lack of two βB3 spots and one βA1 spot present in the WT sample and in the lenses of new-born mice (marked in orange). The missing proteins are also not found in higher amounts in the aggregates. Degradation is the only plausible explanation.

At six months of age, the lens opacification progress almost reached its final extent. Soluble and aggregate fractions of WT and Aca30 lenses show similar spot patterns except for the higher amount of modified α-crystallin (fig. 84).

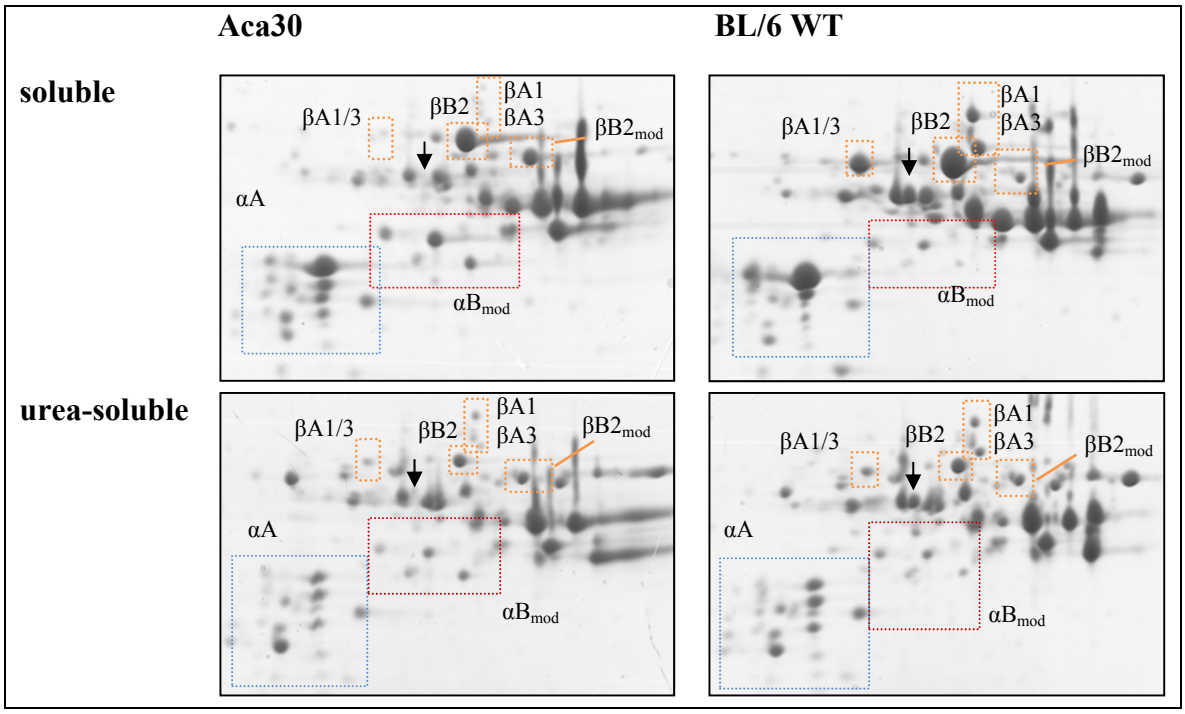

Fig. 83: Comparison of 2-DE analysis of soluble and urea-soluble aggregate fraction of 3 months old BL/6- and Aca30-mice. More modified αA- and αB-crystallin could be found in the soluble fraction. The insoluble fractions of 3 months of Aca30 samples resemble BL/6 WT samples. βB2 is increasingly modified in Aca30 samples compared to WT animals as observed in Aey7-samples already. Members of the βA1/3-family are present in lower concentrations in Aca30 samples. The positions of βA2-spots are marked with black arrows.

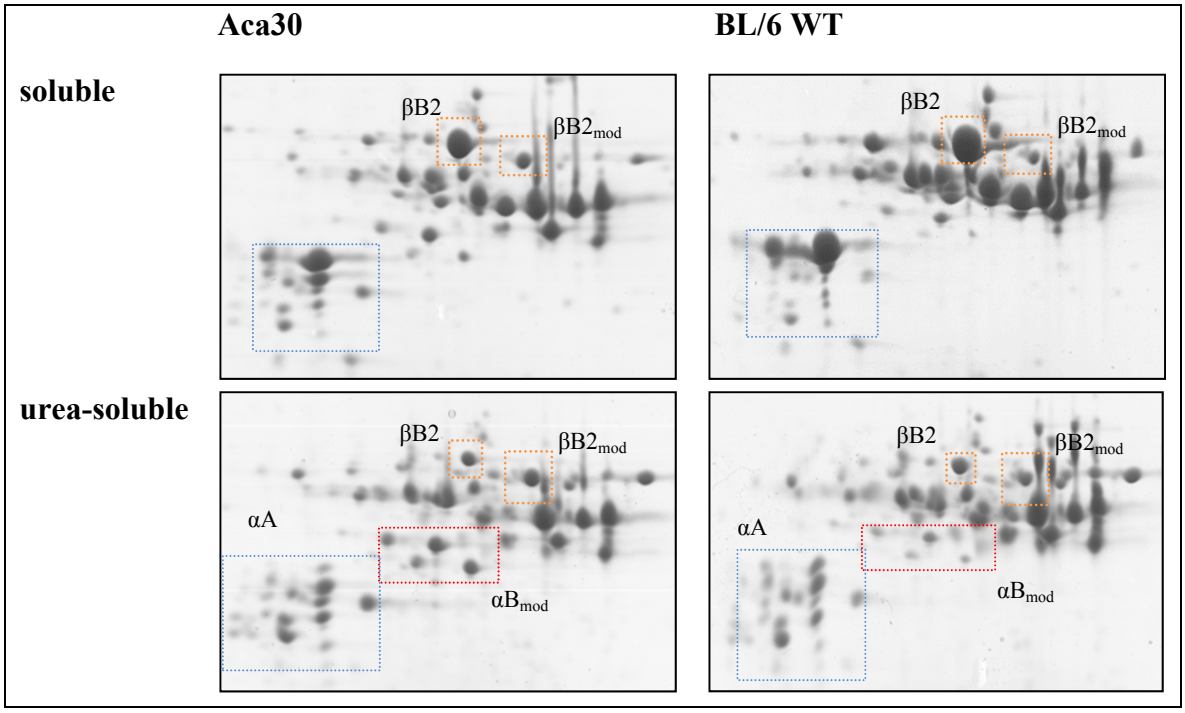

Fig. 84: Comparison of 2-DE analysis of soluble and urea-soluble aggregate fraction of 6-months old BL/6- and Aca30-mice. More modified αA- and αB-crystallin compared to WT samples could be found in the soluble and in the urea-soluble aggregate fraction. βB2 is increasingly modified in Aca30 samples compared to WT animals as observed in Aey7-samples already.

Only four weeks later, when maximum opacification is reached, a decrease of γ-crystallin spot intensities in both fractions was detected. This effect is even more pronounced for eight months old lenses. Apparently, the major contribution to the insoluble fraction is made by α-crystallin (fig. 85).

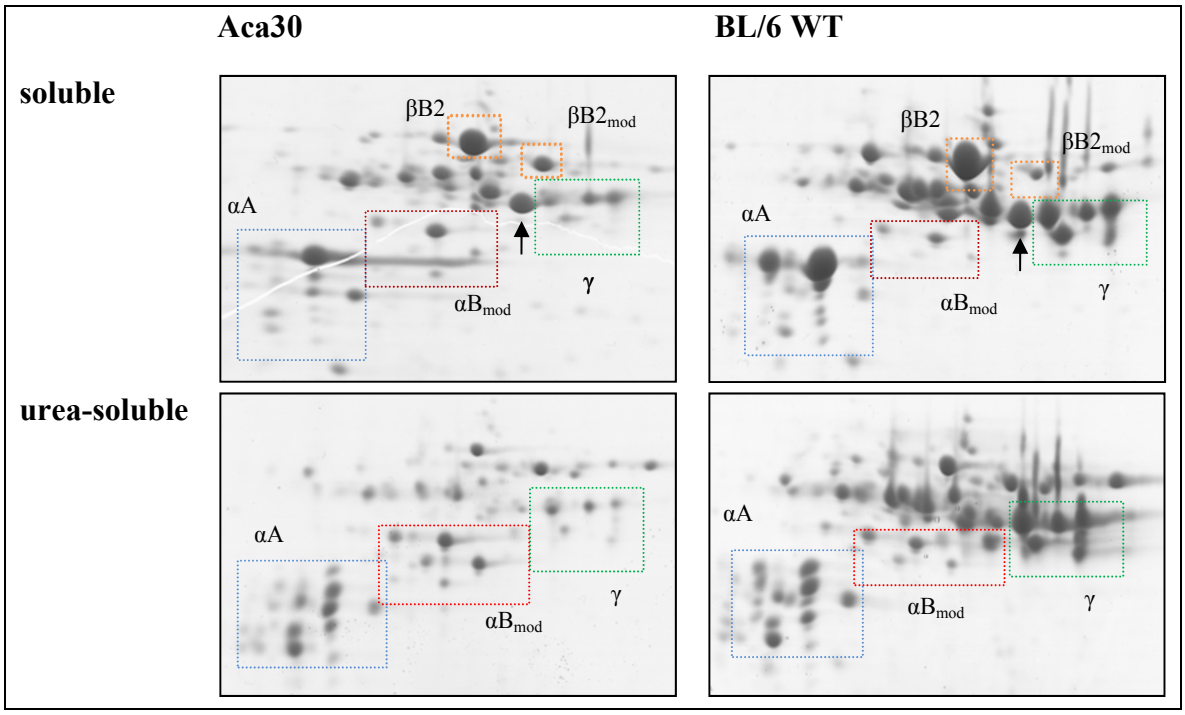

Fig. 85: Comparison of 2-DE analysis of soluble and urea-soluble aggregate fraction of 8-months old BL/6- and Aca30-mice. The urea-soluble aggregate fraction consists mainly of modified αA- and αB-crystallin. Higher amounts of modified βB2-crytstallin were detected in Aca30 samples as observed before in Aey7 samples.

The soluble fraction was analyzed by SEC-HPLC as well (fig. 86). The changes observed in 2-DE could also be seen in SEC-HPLC. A shifted ratio of HMW- to α-crystallin-peaks towards HMW could be correlated with the presence of a higher concentration of modified α-crystallin. As for chromatograms of the Aey7 (αA V124E) samples, the peak shoulder belonging to the β_h-fraction is not visible. This implies the lack of higher order β-crystallin oligomers. From three months on a peak appears at higher elution volumes than the γ-crystallin peak. This implies the formation of increasing amounts of UV-absorbing molecules < 20 kDa. These could be nucleic acids as reported earlier (Graw, unpublished data) or protein fragments due to degradation. An increase of the amplitude of the 'degradation-peak' is accompanied by a decrease in γ-crystallin-peak amplitude. Together with the observed 'loss' of crystallins from seven months of age on, it is possible that γ-crystallins are degraded.

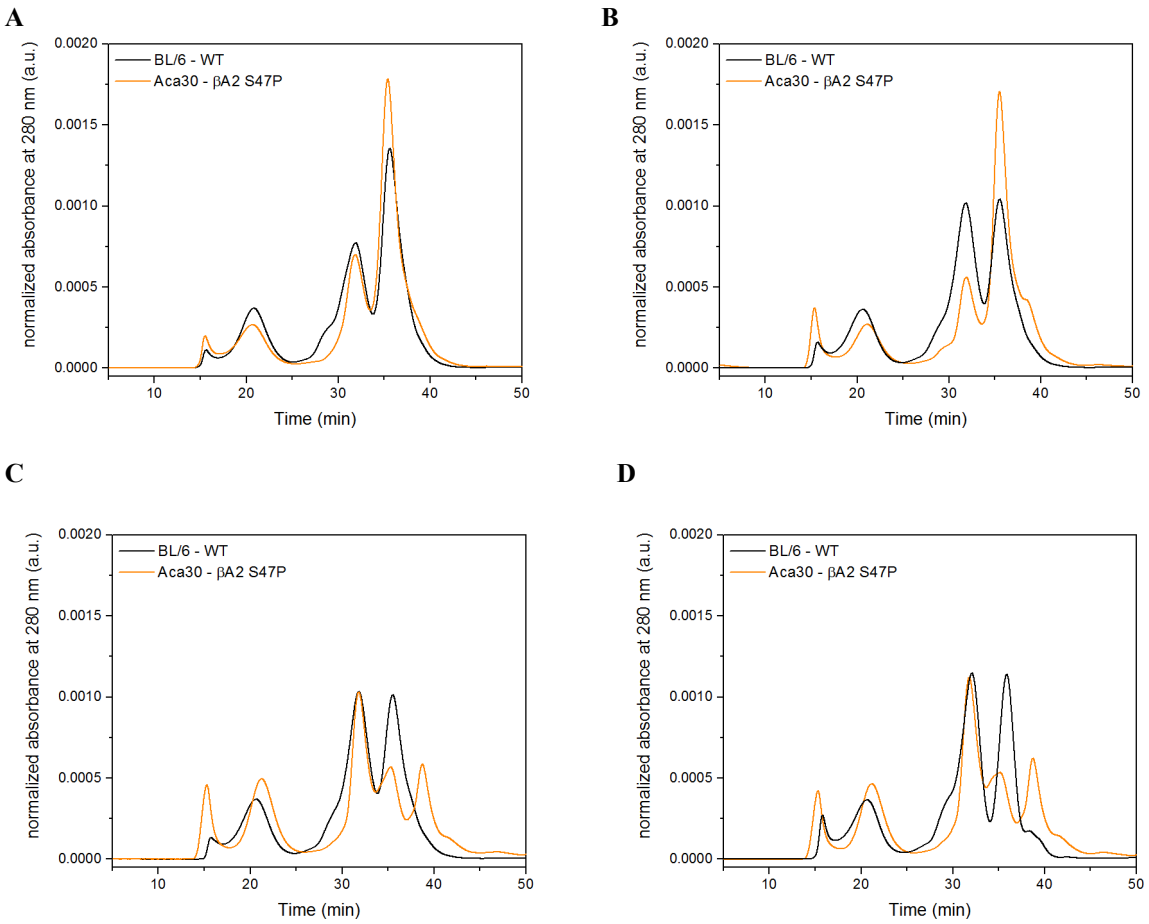

Fig. 86: Comparison of SEC-HPLC chromatograms of BL/6 and Aca30-lysate samples of different ages; **A:** 3 month, **B:** 6 months, **C:** 7 months, **D:** 8 months. In Aca30 samples, the β_h-peak is not visible. With increasing age, the HMW-peak intensity increases. The γ-crystallin peak-intensity decreases from 7 months on. At the same time, an additional peak at higher elution volumes could be detected, which might originate from γ-crystallin degradation.

Surprisingly, a mutation in the βA2-gene that is usually expressed already in new-born mice, leads to a phenotype that can be observed earliest at the age of three months and that is accompanied by increased α-crystallin modification and the loss of several β-crystallin spots. With increasing age, the relative amounts of γ-crystallins decreases. Apparently, more complex relationships exist between the different crystallins than expected.

4.3.2.3 Aey4 - γD V76D

The third mutant mouse line, Aey4, is based on the C3HeB/FeJ WT strain and carries a mutation in the γD-crystallin encoding gene *Crygd* which leads to exchange of Val76 to Asp. The lenses of Aey4 mice show a strong nuclear cataract accompanied by a milky opacity of the surrounding region. Lenses of homozygotes are smaller and show remnants of cell nuclei

throughout the whole lens. Vacuoles and clefts in the anterior part of the lens may indicate reduced fiber cell adhesion (Graw et al., 2002).

A closer look at the crystal structure of γD-crystallin gives rise to assumptions on the origins of the observed defect in protein structure. The side chain of the exchanged Val is part of the hydrophobic core of the N-terminal domain. Introduction of the large and negatively charged Glu can disturb the essential interactions in the β-sheet structure (fig. 87).

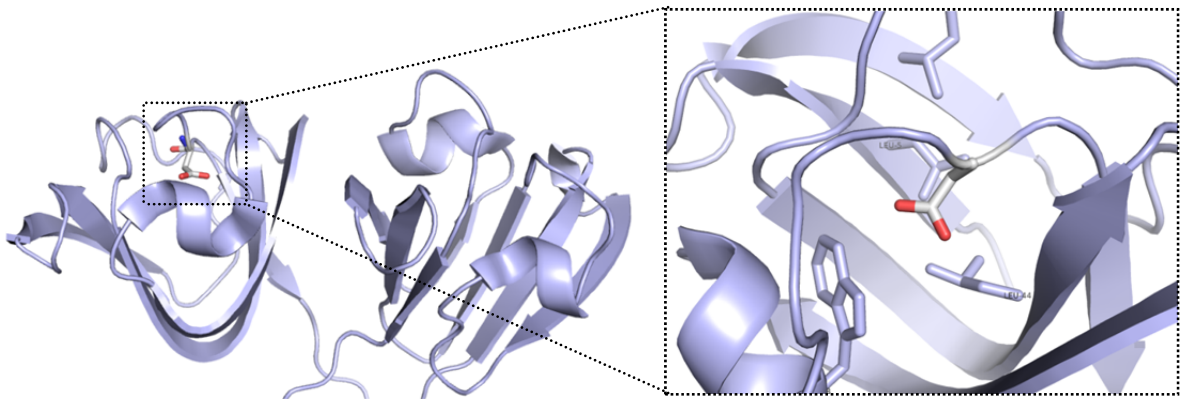

Fig. 87: *In silico*-mutation of V76 to D in the crystal structure of human γD-crystallin (pdb 1HK0). The mutated side chain points into the hydrophobic center of the N-terminal domain causing electrostatic and steric repulsions.

The biophysical properties of this mutant were analyzed and resulted in a destabilizing effect for the N-terminal domain which contains the mutation. This leads to a partial unfolding. The affinity to α-crystallin was also addressed as mentioned before and was found to be low at physiological conditions. It was reported that γD-crystallin can escape the protective mechanism of α-crystallin in the lens (Mishra et al., 2012).

Another *in vivo*-study reported incomplete fiber cell denucleation and reduced connexin levels induced by aggregated γD-crystallin V76D (Wang et al., 2007).

This well-characterized mutation was also analyzed according to the established protocol and compared to the data obtained on αA- and βA2 mutations.

2-DE analysis of Aey4 lens crystallin composition

As for the new-born lenses of Aey7 and Aca30, the protein of interest bearing the mutation is not detectable (fig. 88). A slight shift in pH is expected due to the introduced Glu, but no spot could be assigned. Besides the affected γD, it is noteworthy that no γ-crystallin-spots could be detected except for one spot that was identified as γE/F. This indicates that expression of the whole γ-crystallin gene cluster is down-regulated at birth. Expression of γE/F could be regulated separately, so it would not be affected.

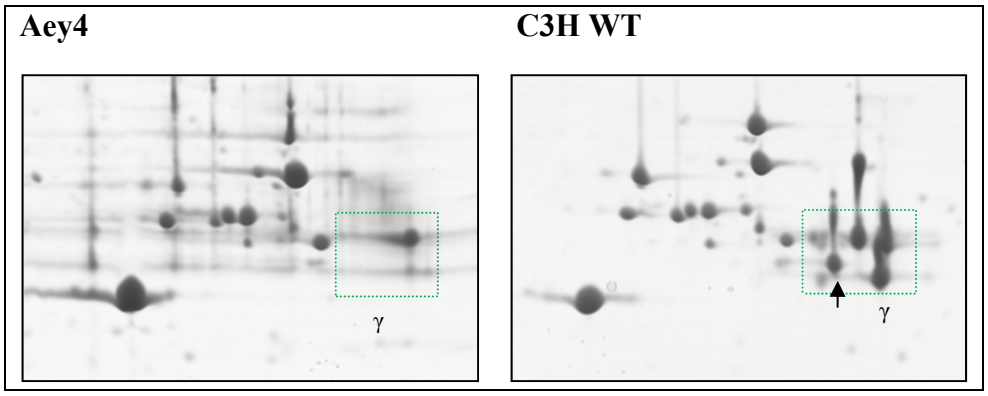

Fig. 88: Comparison of 2-DE analysis of lens lysates of new-born C3H- and Aey4-mice; the γD-spot is marked with a black arrow in the WT-sample. It is missing in new-born Aey4-samples. The only γ-crystallin-spot that could be detected was assigned as γE/F. The expression of γA- and γC-crystallin seems to be down-regulated, too.

After four weeks, striking differences could be observed between WT and γD V76D-lens samples (fig. 89). The number and intensity of spots of modified/degraded αA- and αB-crystallin is significantly higher in the mutant, especially in the aggregate fraction. At that time, all γ-crystallins are present in the sample. The presence of γD V76D could not be confirmed yet. A spot shifted to lower pH-values as expected for the mutation V76D was identified as γ-crystallin. This spot is present in soluble and aggregate fraction in Aey4-samples. It is marked with black arrows in fig. 89. However, it could at least partially consist of otherwise modified γ-crystallin, since in the soluble fraction of WT lenses a spot at about the same position is visible that was assigned as member of the γD/E/F-section, too.

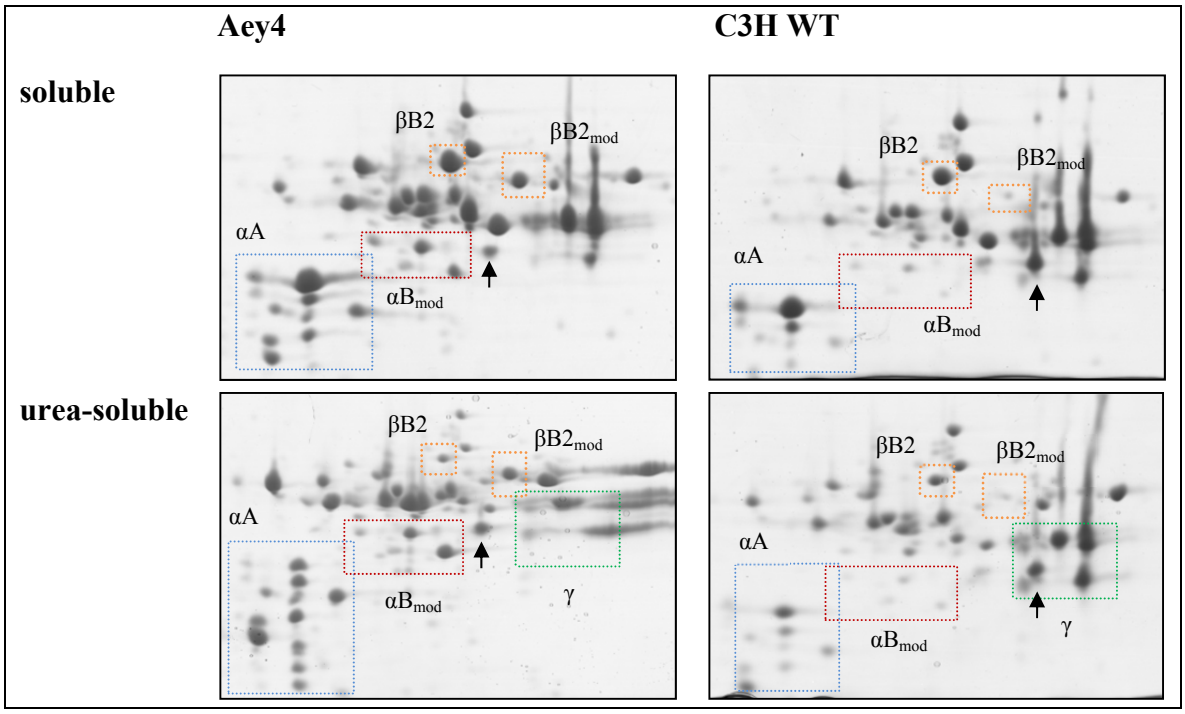

Fig. 89: Comparison of 2-DE analysis of soluble and urea-soluble fractions of 1 months old C3H- and Aey4-mice; putative γD-spots are marked with black arrows. A significant increase of modified αA- and αB-crystallin could be found in the soluble and especially in the urea-soluble fraction. βB2 is increasingly modified in Aey4 mice compared to C3H WT animals as observed for Aey7 and Aca30-samples before. The positions of γD WT and the putative spot of γD-V76D are marked with black arrows.

A surprising observation also made in both mouse mutant lines described before is the higher intensity of the spot identified as modified βB2-crystallin in the soluble fraction as well as in the aggregate fraction (fig. 89). As mentioned before, βB2-crystallin is the only interaction partner of α-crystallin identified in WT samples in this study. However, the mutation in Aey4-mice is located in a γ-crystallin-gene and does not affect any α- or β-crystallin gene.

The higher degradation rate of α-crystallin detected in samples of one month old mice can also be observed in older animals (fig. 90).

With increasing age, the γ-crystallins diminish again in both fractions. The last remaining trace of γ-crystallins is the γB/C spot (fig. 91).

From seven months on, only the most basic γB/C spots can be found in all fractions (fig. 92).

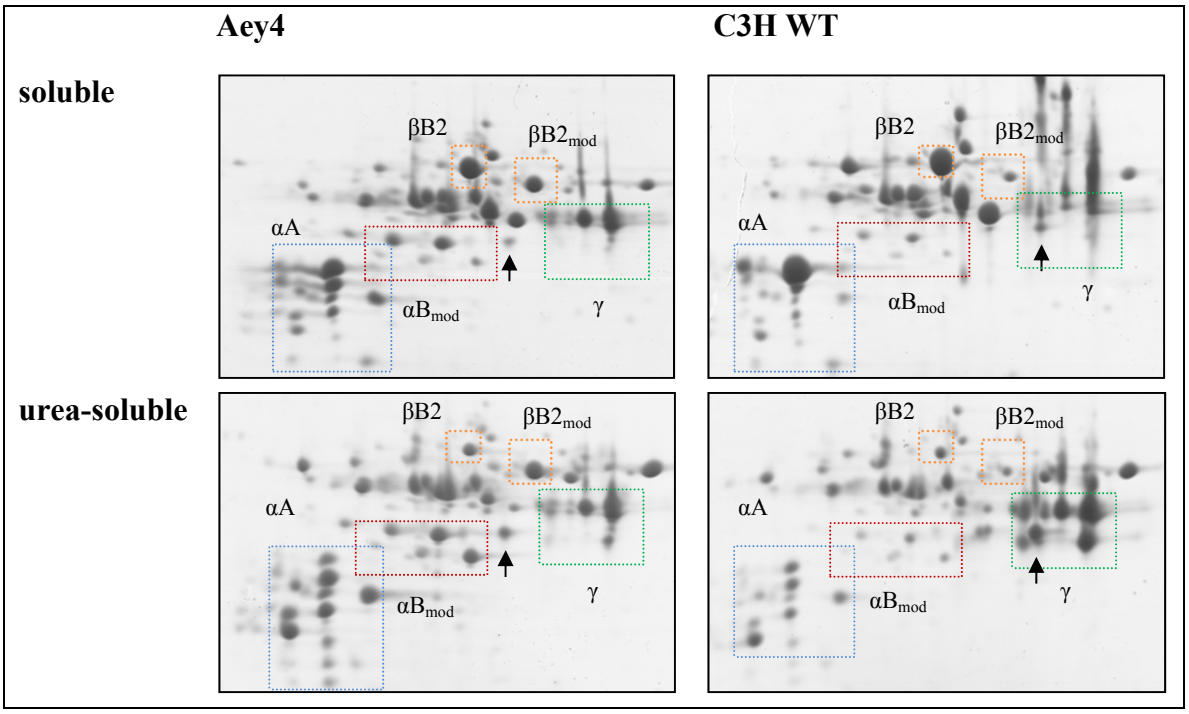

Fig. 90: Comparison of 2-DE analysis of soluble and urea-soluble fractions of 3 months old C3H- and Aey4-mice; putative γD-spots are marked with black arrows. A significant increase of modified αA- and αB-crystallin could be found in the soluble and especially in the urea-soluble fraction. βB2 is increasingly modified in Aey4 mice compared to C3H WT animals as observed for Aey7 and Aca30-samples before. The positions of γD WT and the putative spot of γD-V76D are marked with black arrows.

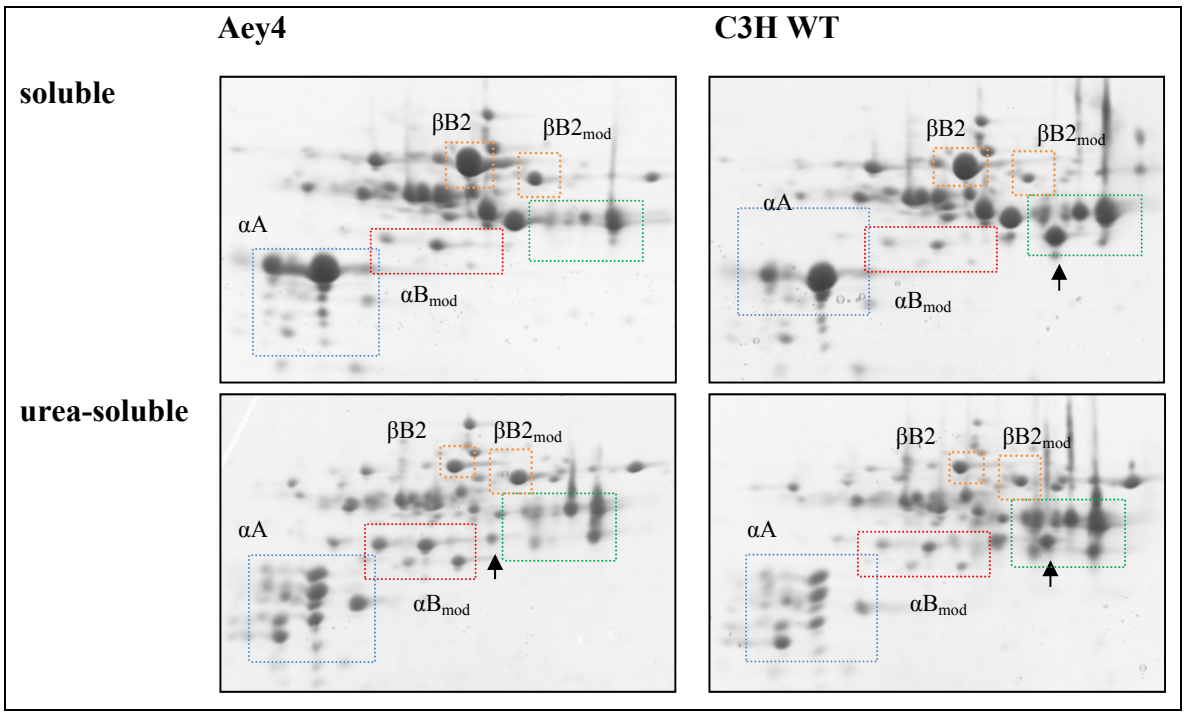

Fig. 91: Comparison of 2-DE analysis of soluble and urea-soluble fractions of 6 months old C3H- and Aey4-mice; putative γD-spots are marked with black arrows. At at age of about 6 months WT and Aey4-sample compositions are almost comparable concerning α-crystallin levels. Slightly higher amounts of α-crystallin can be found in the aggregate fraction. The γ-crystallin-levels start to decrease soluble and urea-soluble fraction.

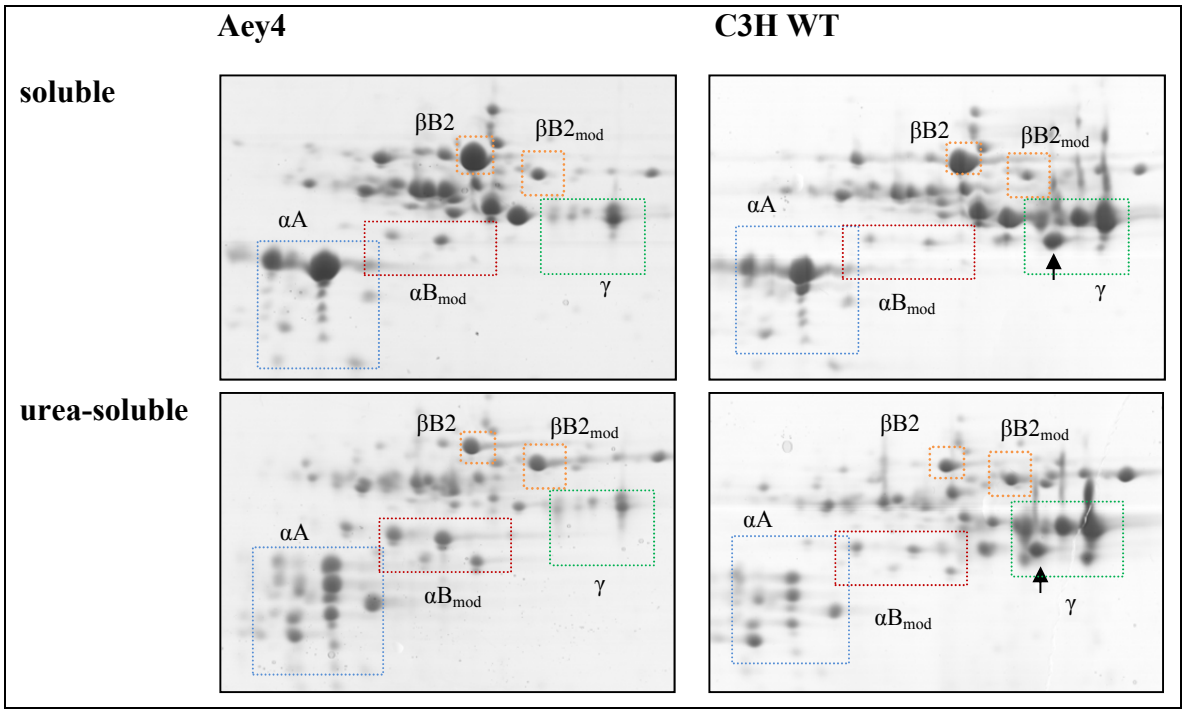

Fig. 92: Comparison of 2-DE analysis of soluble and urea-soluble fractions of 10 months old C3H- and Aey4-mice; γD-spots are marked with black arrows. At at age of about 10 months relative compositions of soluble fractions of WT and Aey4-samples are almost comparable concerning α-crystallin levels. Slightly higher amounts of α-crystallin can be found in the aggregate fraction. The γ-crystallin-levels decreased dramatically in soluble and urea-soluble fraction.

With increasing age, the expression of all γ-crystallin genes is stopped. In rats, the mRNA transcripts of γA, E and F disappear after three months after birth, followed by γC and D. Only the γB-transcript is still detectable at the age of eight months. This matches the observation in 2-DE the crystallins. The only γ-crystallin-spot detectable from seven months of age on was assigned as γB- or γC-crystallin. The amount of α-crystallin transcripts remains high until six months of age (van Leen et al., 1987). Apparently, the end of γ-crystallin expression seems to be correlated with the end of the increased modification of α-crystallin. In samples of ten month old mice, the αA-spots in the soluble fraction of Aey4 samples resemble the αA-spots in the soluble fraction of WT samples (fig. 92).

The observed effects are also reflected in the SEC-HPLC-data. The increased α-crystallin modifications lead to more HMW-species what can be seen in fig. 93. The lower amount of γ-crystallins is represented by the smaller peak area. Again the higher-order β-crystallin-peak is missing like for all characterized mutants. With age, the γ-crystallin peak intensity decreases further (fig. 93).

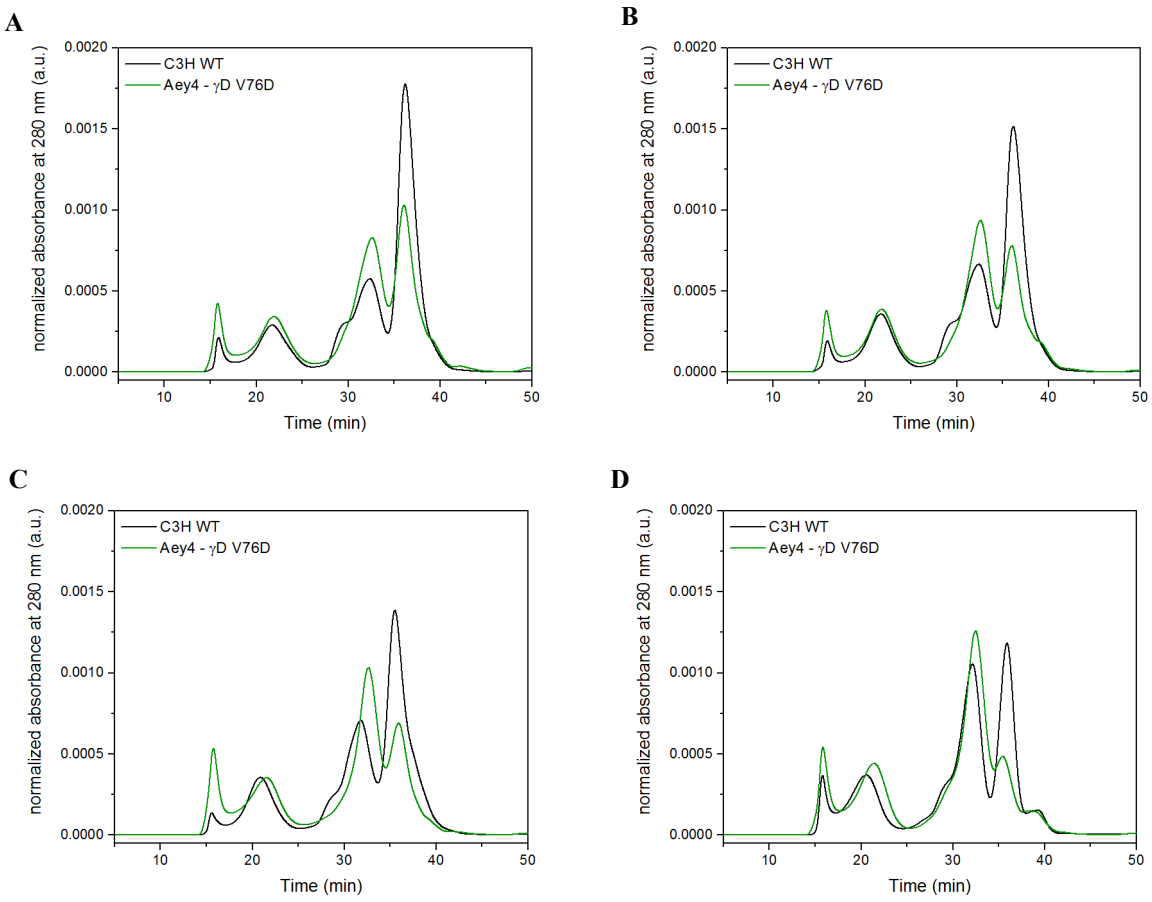

Fig. 93: Comparison of SEC-HPLC chromatograms of C3H and Aey4-lysate samples of different ages; **A:** 1 month, **B:** 2 months, **C:** 3 months, **D:** 10 months. In young animals until an age of 3 months, the HMW-peak intensity increases. The γ-crystallin peak-intensity is lower compared to WT samples from birth on, but it decreases from 3 months on additionally. The β_h-peak is not visible in all Aey4 samples.

From the 2-DE analysis of soluble and urea-soluble fractions, it is not clear why γ-crystallin-mutations influence α-crystallin during lens development. To analyze, if γD-crystallin V76D is bound by α-crystallin and thereby destabilizes the α-crystallin-complex itself, 2-DE analysis of purified αL-crystallin was performed (fig. 94). The same spots were detected as already found in purified αL-crystallin from WT lenses: αA-, αB-, and αA_{ins}, as well as βB2 in different modifications. Unfortunately, no analysis of the HMW-fraction is available so far.

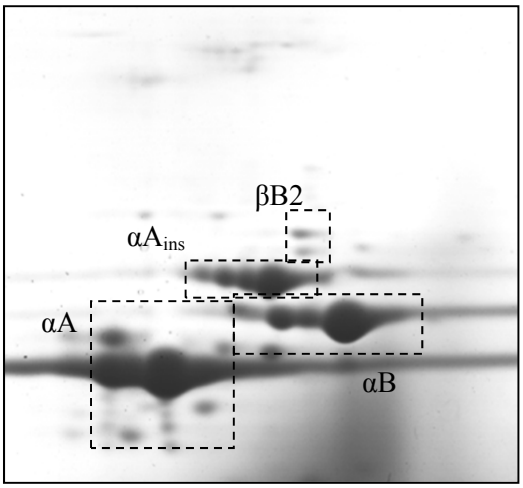

Fig. 94: 2-DE (pH 3-10) of α-crystallin from 12 months old Aey4 lenses. No γD V76D could be detected to αL-crystallin. βB2 was detected as in WT samples before.

In contrast to the expectations, the data obtained here give the impression that degradation and aggregation of α-crystallin is the reason for the observed aggregates found in the lens of Aey4 mice. It was reported that besides the light scattering aggregates, remnants of cell nuclei were observed as well as altered fiber cell morphologies (Graw et al., 2002). There are at least two possible explanations for these observations.

Maybe the γ-crystallins themselves have a major contribution to early fiber cell development and the reduced expression levels observed in new-born mice impair proper cell differentiation. Another possible explanation could be the change in α-crystallin function. It was observed that α-crystallin is found in the aggregate fraction to a higher extent in Aey4 lenses than in WT lenses. In samples of young Aey4-animals, both isoforms were truncated and post-translationally modified to a higher extent. It was shown in previous studies that these modifications lead to formation of HMW complexes accompanied by loss of function and subsequent aggregation (Liang and Akhtar, 2000). As mentioned above, this phenomenon is only observed as long as γ-crystallin mRNA is found in the lens.

4.3.3 Summary and discussion

The goal of this project was to identify substrate proteins bound to lens α-crystallin *in vivo* for characterization of substrate binding determinants to authentic substrates *in vitro*. Therefore, a setup for mouse lens analysis was established. The characteristic pattern of spots on the 2-DE gels of WT lens samples could be assigned according to literature (Ueda et al., 2002) and the obtained SEC-HPLC chromatograms showed the characteristic peak

distribution of HMW-fraction peak as well as α-, β_h-, β_L- and γ-crystallin peaks in the respective order (Kibbelaar and Bloemendal, 1975). When samples of different ages were compared, progressing modification of α-crystallin was observed. These modifications were reported to consist mainly of C-terminal truncations, deaminations and phosphorylations. While the unmodified full-length proteins were mainly found in the soluble fraction, the modified variants were mostly part of in the aggregated fraction as reported before (Schaefer et al., 2006). It became apparent that α-crystallin makes a large contribution to the light scattering aggregate fraction. This fact matches the latest published data on small molecules that have a stabilizing effect on α-crystallin and thereby prevent or even reverse cataract formation in the lens (Makley et al., 2015; Zhao et al., 2015). Numerous studies were performed (Hoehenwarter et al., 2006; Lampi et al., 1998; Sharma and Santhoshkumar, 2009; Takemoto and Sorensen, 2008; Ueda et al., 2002) on water-soluble and -insoluble fractions of lenses of different organisms and all studies resulted in similar hypotheses: In young lenses, crystallins are unmodified and soluble. With age, all types of crystallins become progressively modified and lose their conformational stability. As long as α-crystallin exhibits a chaperone capacity high enough to bind all aggregating proteins, no light scattering aggregates are found. When α-crystallin loses its chaperone activity through modifications, all crystallins will sooner or later form aggregates. This is a rather rational explanation for the development of age-related cataract. As already mentioned in section 1.5.4, there are some inconsistencies that could be confirmed in this study: α-crystallin truncations and modifications are observed at an early time point in lens development. In the case of mice, already at the age of four weeks, major changes were observed and modified α-crystallin was found in the aggregate fraction (fig. 63). At that time, when β- and γ-crystallins undergo destabilizing modifications, α-crystallin is already highly modified, which was reported to diminish its chaperone function (Ueda et al., 2002). However, also mutations in α-crystallin that lead to increased chaperone activity *in vitro*, were reported to lead to cataract formation, too (Chen et al., 2010; Huang et al., 2009). These contradictory reports convey the impression that the whole lenticular crystallin family, fiber cell stabilizing intermediate filaments as well as many other less abundant lens proteins is too complex to explain lens transparency with the ‘sponge-like’ function of α-crystallin only. The only protein bound to α-crystallin oligomers in WT lenses in detectable amounts was βB2-crystallin. This protein is only present in the lens cytosol in minor amounts at birth and is strongly upregulated in the first weeks of life. In all analyzed mutant mouse samples, larger amounts of a modified version of this β-crystallin compared to WT mice were found in the lysates as well as in the

aggregate fraction. At the same time, α-crystallin was shown to be truncated to a higher extent. These truncations were connected to a decrease in chaperone function before (Takemoto and Boyle, 1994). From this observation it seems that functional α-crystallin rather protects βB2-crystallin from modification than rescues the modified protein from aggregation. The latter was not found in 2-DE to interact with α-crystallin.

Several studies on βB2-crystallin discussed its role in the lens cytosol and in cataract formation. It was shown in an *in vitro* study that α-crystallin might presumably interact with and also stabilize an unfolding intermediate of βB2-crystallin (Evans et al., 2008). After binding to α-crystallin the solvent accessibility of βB2-crystallin is changed (Lampi et al., 2012). Deamination of βB2 was reported to decrease the thermal stability and lead to aggregation. α-crystallin could inhibit aggregation of βB2 WT, but could not rescue the aggregation of the deaminated variant completely (Michiel et al., 2010). Deamination of βB2-crystallin also alters interactions within β-crystallin hetero-oligomers. This might also influence other β-crystallins due to the fact that they not only form homo-, but also hetero-oligomers within their family (Takata et al., 2009). Contradictory studies exist on the degree of post-translational modifications of βB2 in the lens that range from an extremely low level of modifications (Zhang et al., 2001) to 'extensive truncation' (Srivastava and Srivastava, 2003). Due to their findings, Zhang et al. (2001) suggest a stabilizing effect of βB2-crystallin on other crystallins and even 'chaperone-like properties' for βB2, especially during aging. In a different study, the effect of targeted knock-out of βB2 was analyzed. It was shown, that this knock-out does not influence lens development in young individuals. With age, cataract developed in posterior and anterior cortex and lenses were significantly smaller. It was suggested that the role of βB2 is increasingly important with age and could be related to stability of other lens crystallins and stress protection (Zhang et al., 2008). This 'delayed' role of βB2 in stabilizing the crystallins in the mammalian lens could correlate to the later expression of βB2-crystallin which is the last of the crystallins to be expressed in murine lenses.

Taken together, it appears that βB2-crystallin, being present in high amounts in lenses of adult mice, exists in an equilibrium between a compact folded state and a more flexible intermediate state. This equilibrium is presumably stabilized by α-crystallin interacting with flexible regions in the intermediate form and inhibiting further modification and aggregation. This interaction might reflect a reversible type-I interaction only preventing further unfolding or modification without formation of stable complexes as suggested by Bakthisaran and described in section 1.3 (fig. 5, Bakthisaran et al. (2015)). If α-crystallin is not available or

less functional, the βB2-crystallin folding intermediate might be more prone to modifications since flexible parts in proteins are always easier accessible to modifying enzymes or small molecules. This presumably results in a shift in equilibrium between the prevalent variants of βB2-crystallin in solution with increasing amounts of modified βB2-crystallin. This observation was reported in a comparative proteomic analysis of αA-/αB-double knockout-mice (Andley et al., 2013). In single αB-knockout mice, this effect was not observed (Brady et al., 2001), indicating a more important role of αA-crystallin. In the course of the study of αA-crystallin single-knockouts unfortunately no 2-DE-analysis was performed (Brady et al., 1997).

The question rising from these results is the correlation between βB2-crystallin modifications and cataract formation in the different analyzed cataract mouse lines.

When destabilizing mutations were introduced into either member of the crystallin family, the respective crystallin was not found in larger amounts in the aggregated fraction. However, other crystallins were affected. As described above, a common observation for all analyzed mutants was the increase in signal intensity of the spot of modified βB2-crystallin accompanied by higher amounts of modified αA- and αB-crystallin. This was observed to an extraordinary high extent in the γD-crystallin mutation mouse line. The γD-mutation V76D was analyzed before (Wang et al., 2007). The conclusion drawn in this study was that the reduced solubility of γD-V76D leads to formation of light scattering aggregates and these particles diminish proper fiber cell differentiation. A close look at the 2-DE gels shown in this publication also reveals a larger amount of modified αA-crystallin in the insoluble fraction as well as a spot where modified βB2-crystallin usually can be found. Unfortunately, this spot was not assigned in the publication.

When SEC-HPLC chromatograms of the different mutant samples are compared to WT, in young animals the main differences in peak intensities affect the peaks of the crystallins bearing the mutation and the peak of higher order β-crystallins cannot be found (β_h). This is due to the lack of one or more subfamily members. However, it is striking that chromatograms of all samples of aged mice bearing a mutation in any crystallin show a loss in γ-crystallin peak intensity independent of the mutation (fig. 95).

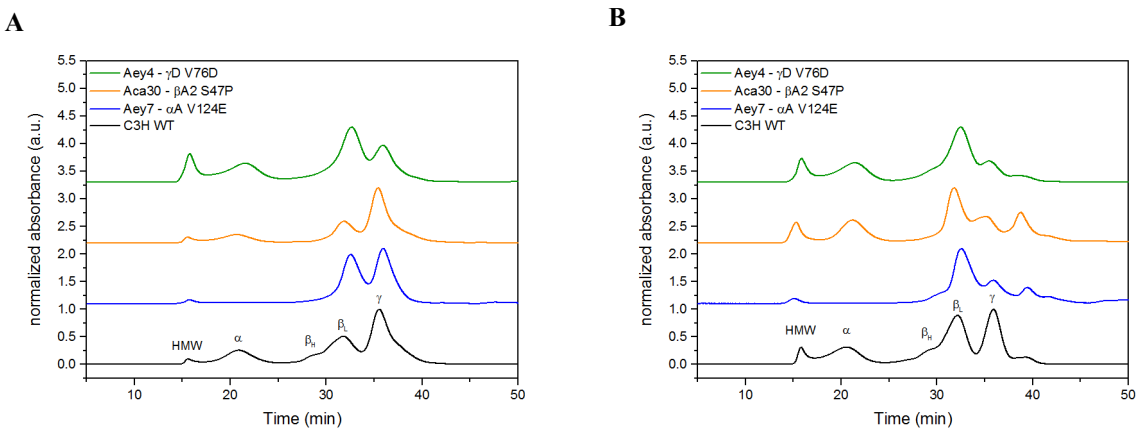

Fig. 95: Comparison of SEC-HPLC chromatograms of C3H and Aey7, Aca30 and Aey4-lysate samples of young and old animals; **A:** 3 months, **B:** 10 months.

The observed effects can be summarized as follows: Mutations in any crystallin subfamily lead to destabilization or modification of both α-crystallin isoforms accompanied by formation of a larger amount of HMW-particles and aggregation of α-crystallin accompanied by loss of its chaperone function. This, however, seems to be correlated with increased modification of at least one β-crystallin expressed later during lens development, namely βB2. However, with increasing age, γ-crystallins are affected. Their overall signal in SEC-HPLC-chromatograms decreases, but the proteins are not necessarily found in the aggregate fraction, which hints to degradation. These observations lead to the conclusion that βB2-crystallin has a favorable influence on γ-crystallins and support the hypothesis of Zhang et al. (2001) about the stabilizing function of βB2 in the lens cytosol.

Interestingly, in lenses of new-born mice, there are hardly any effects on lysates composition visible except for the lack of the mutated crystallin. Only after βB2-expression is upregulated, both α-crystallin isoforms are affected by modification.

The picture emerges that the interaction of βB2-crystallin with other crystallins is the tender spot in the crystallin family. It seems that α-crystallin does not play a major role in solubilization of damaged crystallins with age in stable substrate complexes. It rather protects e.g. βB2 from ‘loss of function-modifications’. If this is mechanism is impaired, other crystallins are affected.

From the available data the following hypothesis is derived: The fiber cell cytosol is a complex high-concentration protein solution with a proposed short-range order (Delaye and Tardieu, 1983). Proteins contributing to the system are evolutionary engineered not to interact with each other in an undefined manner. Maybe the lens fiber cell cytosol can be imagined as a ‘Lego® construction kit’ consisting of large, medium-sized and small building

blocks that are arranged in a gapless pattern. The attractive and repulsive interactions have to be in equilibrium in order to keep the system functional. If destabilizing mutations are introduced in any crystallin family member, they influence its biophysical properties like surface hydrophobicity, stability and the exact fold of the protein. This, however, will presumably lead to disturbances in the highly balanced lens-crystallin interactions, interpretable as a domino effect. An example from this work is βA2. If it is not present in the cytosol due to mutations, other β-crystallins cannot form hetero-assemblies with βA2. The lack of these interactions, however, will lead to destabilization of the proposed short-range order and in turn facilitate modifications of e.g. α-crystallin oligomers. As a consequence these proteins are susceptible to truncation. This again may lead to unfavorable interactions or modifications of the other crystallins with each other resulting in a depletion of soluble γ-crystallins.

In this study, as well as the cited publications, the major focus was on the crystallins in the lens. However, multiple functions of all crystallins besides their role as structural proteins have to be investigated to shed more light on the complex interplay during lens development and homeostasis of fiber cells.

The loss of γD-crystallin for example results in incomplete fiber cell denucleation (Graw et al., 2002). This indicates a role of γ-crystallins in that process that is not fully characterized yet. α-crystallins are known to participate in fiber cell specific beaded filaments structure. A loss of function is very likely to cause disarrangements and destabilization of the fiber cell cytoskeleton that is important for the extraordinary shape of this cell type (Nicholl and Quinlan, 1994; Quinlan et al., 1996).

The usually observed smaller size of the lenses of mutant mouse lines might also be associated with increased cell death during cataract development. This could be due to apoptosis and unfolded protein response-processes that are both reported to be influenced by α-crystallin. It was reported that α-crystallin interacts with apoptosis-inducing proteins and thereby inhibit their ability to initiate caspase-cleavage leading to apoptosis. Loss of α-crystallin function might disturb this regulation of programmed cell death. (Andley and Goldman, 2016; Morozov and Wawrousek, 2006; Pasupuleti et al., 2010; Wignes et al., 2013).

4.4 Conclusion – the interplay of α-crystallin with potential substrate proteins in the cell

The data obtained during the course of this work do not confirm the general concept of α-crystallin as a sponge-like molecule that forms stable substrate complexes with unfolding proteins to prevent the formation of aggregates. This theory was especially interesting in the context of the eye lens, since in aged fiber cells most of the contributors to proteostasis are abolished, but the formation of light scattering aggregates is very unfavorable. However, the findings of this work support a different mechanism of α-crystallin function of temporary interactions to prevent post-translational modifications, mainly of βB2-crystallin.

At the same time, light could be shed on the determinants of substrate recognition of αB-crystallin. From the peptide array experiments, it was concluded, that the NTRs of αB-crystallin act as pseudo-substrates and occupy the binding sites within the oligomer. When amino acid stretches are exposed in substrate proteins that resemble the NTRs with respect to their biophysical properties, and that are not accessible in the native fold, they are protected by α-crystallin to prevent damage to the protein. In the eye lens, this mechanism is especially important due to the highly sensitive equilibrium between all crystallins to guarantee lens transparency. Substrate interaction can take place during subunit exchange or during partial dissociation of the oligomer upon phosphorylation. These substrate interactions are presumably reversible and controlled in a concentration-dependent manner (fig. 96).

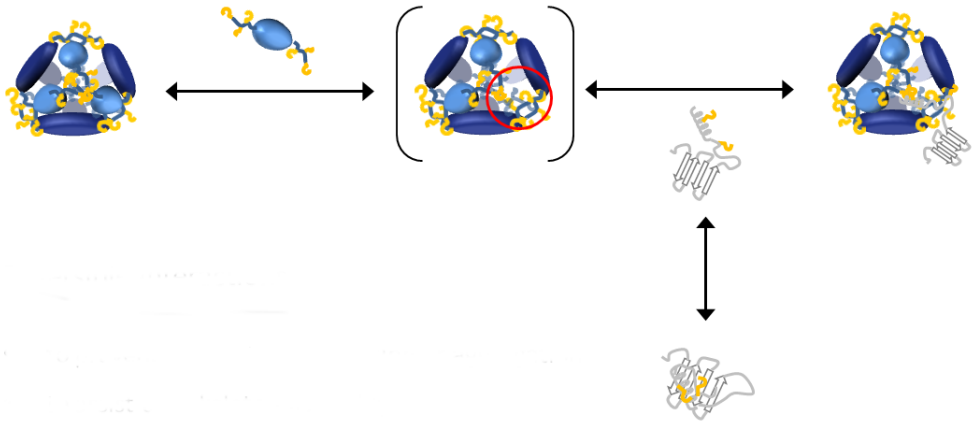

Fig. 96: Model of reversible interactions to prevent destabilizing substrate protein modifications, to assist cytoskeleton-polymerization or inhibition of apoptosis as protective function of α-crystallin in the cell, especially in lens fiber cells. The NTRs of αB-crystallin act as pseudo substrates in the oligomeric assembly and allow access of substrate proteins to the interaction sites created by several subunits in the oligomer during subunit exchange. The oligomer shown in brackets represents the intermediate state during subunit exchange. When a sequence similar to the NTR is exposed in unfolding intermediates of substrate proteins, it can replace the NTR of the exchanging subunits. Yellow hooks represent similar sequence motifs in the NTRs of the oligomer s (blue) and in substrate proteins (grey).

If too many unfolding substrate proteins are present, the equilibrium is shifted to the formation of substrate-complexes. If α-crystallin is increasingly truncated and the oligomeric structure is destabilized, it becomes a substrate itself and contributes to the shift in equilibrium. These substrate complexes currently assumed to fulfill the chaperone function of α-crystallin are highly aggregation-prone and are unfavorable for proteostasis. The cataract-preventing effect of sterol compounds (Makley et al., 2015)can therefore be explained by stabilization of α-crystallin. This could be achieved by suppressing α-crystallin modifications that lead to aggregation or by reducing the substrate binding affinity of α-crystallin that prevents co-aggregation with the bound substrates.

Within these aggregates of substrate-complexes, α-crystallin does not unfold completely. The cataract-reversing effect of sterol compounds can be explained by the disaggreation-properties of these small molecules due to their amphipathic nature. Interaction with sterols presumably leads to a decreasing affinity of α-crystallin to its substrate and therefore to dissolution of the substrate-complex aggregates. The mechanism of ‘irreversible’-interaction of α-crystallin with proteins and the possible fates for these substrate-complexes are depicted in fig. 97.

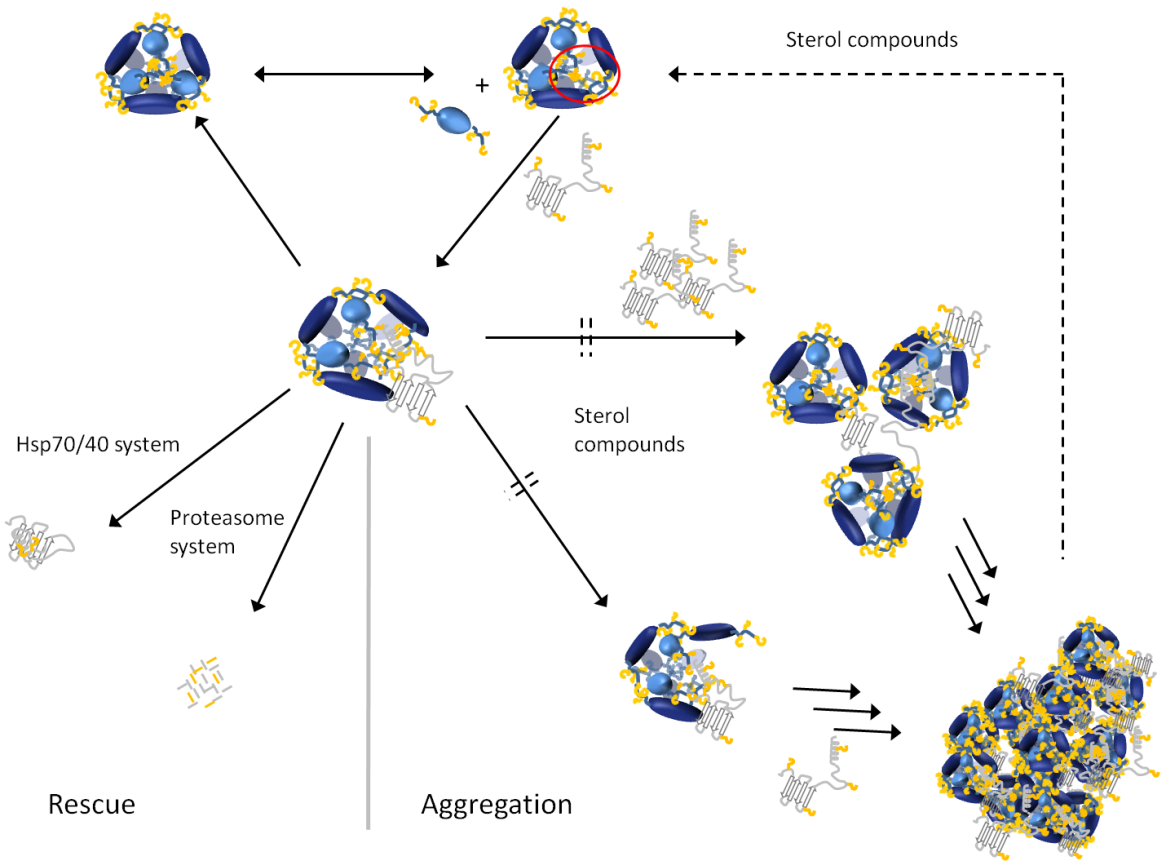

Fig. 97: Model of irreversible interactions of αB-crystallin with damaged substrate proteins. If larger amounts of substrate proteins with exposed binding sites are present under stress conditions, α-crystallin cannot stabilize the large amount of unfolding intermediates anymore. Two possibilities to rescue the system and to prevent aggregation are the refolding of the substrate by ATP-dependent foldases or the degradation by the proteasome system (left side). If the rescue options cannot be achieved sufficiently, the complexes will form unfavorable aggregates either by crosslinking of several α-crystallin oligomers through binding to different sites in the substrate proteins (upper right). This is probably dependent on the concentration of unfolding proteins. Dependent on the substrate, the oligomer assembly could also be disturbed to an extent that destabilizes α-crystallin and leads to aggregation (lower right). Both ways could be inhibited or decelerated by stabilization of α-crystallin or by reducing affinity of α-crystallin for substrate proteins by sterol compounds. These might also dissolve the already formed aggregates in the lens by disrupting interaction of substrate proteins with aggregated, but not completely unfolded α-crystallin. In this model, substrate proteins may be any destabilized protein and especially also truncated or otherwise modified α-crystallin itself. Yellow hooks represent similar sequence motifs in the NTRs of the oligomer s (blue) and in substrate proteins (grey).

In the course of this work, the substrate binding mechanism of αB-crystallin was studied extensively *in vitro*. The information acquired on interaction with other lens crystallins in the context of cataract-inducing mutations represents the foundation for further *in vivo* characterization of this highly abundant sHsp. Additional studies targeting the contribution of all crystallins to cell development and especially to cellular signaling pathways could confirm or further complement the suggested model of α-crystallin function.

References

Abdelkader, H., Alany, R.G., and Pierscionek, B. (2015). Age-related cataract and drug therapy: opportunities and challenges for topical antioxidant delivery to the lens. The Journal of pharmacy and pharmacology *67*, 537-550.

Acosta-Sampson, L., and King, J. (2010). Partially folded aggregation intermediates of human gammaD-, gammaC-, and gammaS-crystallin are recognized and bound by human alphaB-crystallin chaperone. J Mol Biol *401*, 134-152.

Acunzo, J., Katsogiannou, M., and Rocchi, P. (2012). Small heat shock proteins HSP27 (HspB1), alphaB-crystallin (HspB5) and HSP22 (HspB8) as regulators of cell death. Int J Biochem Cell Biol *44*, 1622-1631.

Ahmad, M.F., Raman, B., Ramakrishna, T., and Rao Ch, M. (2008). Effect of phosphorylation on alpha B-crystallin: differences in stability, subunit exchange and chaperone activity of homo and mixed oligomers of alpha B-crystallin and its phosphorylation-mimicking mutant. J Mol Biol *375*, 1040-1051.

Ahrman, E., Gustavsson, N., Hultschig, C., Boelens, W.C., and Emanuelsson, C.S. (2007a). Small heat shock proteins prevent aggregation of citrate synthase and bind to the N-terminal region which is absent in thermostable forms of citrate synthase. Extremophiles : life under extreme conditions *11*, 659-666.

Ahrman, E., Lambert, W., Aquilina, J.A., Robinson, C.V., and Emanuelsson, C.S. (2007b). Chemical cross-linking of the chloroplast localized small heat-shock protein, Hsp21, and the model substrate citrate synthase. Protein Sci *16*, 1464-1478.

Andley, U.P., and Goldman, J.W. (2016). Autophagy and UPR in alpha-crystallin mutant knock-in mouse models of hereditary cataracts. Biochim Biophys Acta *1860*, 234-239.

Andley, U.P., Malone, J.P., Hamilton, P.D., Ravi, N., and Townsend, R.R. (2013). Comparative proteomic analysis identifies age-dependent increases in the abundance of specific proteins after deletion of the small heat shock proteins alphaA- and alphaB-crystallin. Biochemistry *52*, 2933-2948.

Andley, U.P., Mathur, S., Griest, T.A., and Petrash, J.M. (1996). Cloning, expression, and chaperone-like activity of human alphaA-crystallin. J Biol Chem *271*, 31973-31980.

Andley, U.P., Song, Z., Wawrousek, E.F., Fleming, T.P., and Bassnett, S. (2000). Differential protective activity of alpha A- and alphaB-crystallin in lens epithelial cells. J Biol Chem *275*, 36823-36831.

Aquilina, J.A., and Watt, S.J. (2007). The N-terminal domain of alphaB-crystallin is protected from proteolysis by bound substrate. Biochem Biophys Res Commun *353*, 1115-1120.

Arai, H., and Atomi, Y. (1997). Chaperone activity of alpha B-crystallin suppresses tubulin aggregation through complex formation. Cell structure and function *22*, 539-544.

Arrigo, A.P., Paul, C., Ducasse, C., Manero, F., Kretz-Remy, C., Virot, S., Javouhey, E., Mounier, N., and Diaz-Latoud, C. (2002). Small stress proteins: novel negative modulators of

apoptosis induced independently of reactive oxygen species. Progress in molecular and subcellular biology *28*, 185-204.

Asomugha, C.O., Gupta, R., and Srivastava, O.P. (2011). Structural and functional roles of deamidation of N146 and/or truncation of NH2- or COOH-termini in human alphaB-crystallin. Molecular vision *17*, 2407-2420.

Atkins, P.W. (2004). Physikalische Chemie.

Bagneris, C., Bateman, O.A., Naylor, C.E., Cronin, N., Boelens, W.C., Keep, N.H., and Slingsby, C. (2009). Crystal structures of alpha-crystallin domain dimers of alphaB-crystallin and Hsp20. J Mol Biol *392*, 1242-1252.

Bakthisaran, R., Tangirala, R., and Rao Ch, M. (2015). Small heat shock proteins: Role in cellular functions and pathology. Biochim Biophys Acta *1854*, 291-319.

Balch, W.E., Morimoto, R.I., Dillin, A., and Kelly, J.W. (2008). Adapting proteostasis for disease intervention. Science *319*, 916-919.

Banerjee, P.R., Pande, A., Shekhtman, A., and Pande, J. (2015). Molecular mechanism of the chaperone function of mini-alpha-crystallin, a 19-residue peptide of human alpha-crystallin. Biochemistry *54*, 505-515.

Basha, E., O'Neill, H., and Vierling, E. (2012). Small heat shock proteins and alpha-crystallins: dynamic proteins with flexible functions. Trends Biochem Sci *37*, 106-117.

Bassnett, S. (2009). On the mechanism of organelle degradation in the vertebrate lens. Exp Eye Res *88*, 133-139.

Bhagyalaxmi, S.G., Srinivas, P., Barton, K.A., Kumar, K.R., Vidyavathi, M., Petrash, J.M., Bhanuprakash Reddy, G., and Padma, T. (2009). A novel mutation (F71L) in alphaA-crystallin with defective chaperone-like function associated with age-related cataract. Biochim Biophys Acta *1792*, 974-981.

Bhattacharyya, J., Padmanabha Udupa, E.G., Wang, J., and Sharma, K.K. (2006). Mini-alphaB-crystallin: a functional element of alphaB-crystallin with chaperone-like activity. Biochemistry *45*, 3069-3076.

Bloemendal, H., de Jong, W., Jaenicke, R., Lubsen, N.H., Slingsby, C., and Tardieu, A. (2004). Ageing and vision: structure, stability and function of lens crystallins. Prog Biophys Mol Biol *86*, 407-485.

Bloemendal, H., and de Jong, W.W. (1991). Lens proteins and their genes. Progress in nucleic acid research and molecular biology *41*, 259-281.

Boelens, W.C., Croes, Y., and de Jong, W.W. (2001). Interaction between alphaB-crystallin and the human 20S proteasomal subunit C8/alpha7. Biochim Biophys Acta *1544*, 311-319.

Bork, P., Holm, L., and Sander, C. (1994). The immunoglobulin fold. Structural classification, sequence patterns and common core. J Mol Biol *242*, 309-320.

Bova, M.P., Ding, L.L., Horwitz, J., and Fung, B.K. (1997). Subunit exchange of alphaA-crystallin. J Biol Chem *272*, 29511-29517.

Bova, M.P., Yaron, O., Huang, Q., Ding, L., Haley, D.A., Stewart, P.L., and Horwitz, J. (1999). Mutation R120G in B-crystallin, which is linked to a desmin-related myopathy, results in an irregular structure and defective chaperone-like function. Proceedings of the National Academy of Sciences *96*, 6137-6142.

Boyle, D.L., Takemoto, L., Brady, J.P., and Wawrousek, E.F. (2003). Morphological characterization of the AlphaA- and AlphaB-crystallin double knockout mouse lens. BMC Ophthalmology *3*, 3.

Bradford, M.M. (1976). A rapid and sensitive method for the quantitation of microgram quantities of protein utilizing the principle of protein-dye binding. Anal Biochem *72*, 248-254.

Brady, J.P., Garland, D., Duglas-Tabor, Y., Robison, W.G., Jr., Groome, A., and Wawrousek, E.F. (1997). Targeted disruption of the mouse alpha A-crystallin gene induces cataract and cytoplasmic inclusion bodies containing the small heat shock protein alpha B-crystallin. Proc Natl Acad Sci U S A *94*, 884-889.

Brady, J.P., Garland, D.L., Green, D.E., Tamm, E.R., Giblin, F.J., and Wawrousek, E.F. (2001). AlphaB-crystallin in lens development and muscle integrity: a gene knockout approach. Invest Ophthalmol Vis Sci *42*, 2924-2934.

Braun, N., Zacharias, M., Peschek, J., Kastenmuller, A., Zou, J., Hanzlik, M., Haslbeck, M., Rappsilber, J., Buchner, J., and Weinkauf, S. (2011). Multiple molecular architectures of the eye lens chaperone alphaB-crystallin elucidated by a triple hybrid approach. Proceedings of the National Academy of Sciences of the United States of America *108*, 20491-20496.

Brockwell, D.J., and Radford, S.E. (2007). Intermediates: ubiquitous species on folding energy landscapes? Current opinion in structural biology *17*, 30-37.

Brown, Z., Ponce, A., Lampi, K., Hancock, L., and Takemoto, L. (2007). Differential binding of mutant (R116C) and wildtype alphaA crystallin to actin. Curr Eye Res *32*, 1051-1054.

Buchner, J., Grallert, H., and Jakob, U. (1998). Analysis of chaperone function using citrate synthase as nonnative substrate protein. Methods in enzymology *290*, 323-338.

Carver, J.A., Aquilina, J.A., Truscott, R.J.W., and Ralston, G.B. (1999). Identification by ¹H NMR spectroscopy of flexible C-terminal extensions in bovine lens α-crystallin. FEBS Letters *311*, 143-149.

Carver, J.A., Lindner, R.A., Lyon, C., Canet, D., Hernandez, H., Dobson, C.M., and Redfield, C. (2002). The Interaction of the Molecular Chaperone α-Crystallin with Unfolding α-Lactalbumin: A Structural and Kinetic Spectroscopic Study. Journal of Molecular Biology *318*, 815-827.

Carver, J.A., Nicholls, K.A., Aquilina, J.A., and Truscott, R.J. (1996). Age-related changes in bovine alpha-crystallin and high-molecular-weight protein. Exp Eye Res *63*, 639-647.

Chen, B., Retzlaff, M., Roos, T., and Frydman, J. (2011). Cellular strategies of protein quality control. Cold Spring Harb Perspect Biol *3*, a004374.

Chen, Q., Ma, J., Yan, M., Mothobi, M.E., Liu, Y., and Zheng, F. (2009). A novel mutation in CRYAB associated with autosomal dominant congenital nuclear cataract in a Chinese family. Molecular vision *15*, 1359-1365.

Chen, Q., Yan, M., Xiang, F., Zhou, X., Liu, Y., and Zheng, F. (2010). Characterization of a mutant R11H alphaB-crystallin associated with human inherited cataract. Biol Chem *391*, 1391-1400.

Cheng, G., Basha, E., Wysocki, V.H., and Vierling, E. (2008). Insights into small heat shock protein and substrate structure during chaperone action derived from hydrogen/deuterium exchange and mass spectrometry. J Biol Chem *283*, 26634-26642.

Clark, A.R., Lubsen, N.H., and Slingsby, C. (2012). sHSP in the eye lens: crystallin mutations, cataract and proteostasis. Int J Biochem Cell Biol *44*, 1687-1697.

Clark, A.R., Naylor, C.E., Bagneris, C., Keep, N.H., and Slingsby, C. (2011). Crystal structure of R120G disease mutant of human alphaB-crystallin domain dimer shows closure of a groove. J Mol Biol *408*, 118-134.

Crooks, G.E., Hon, G., Chandonia, J.M., and Brenner, S.E. (2004). WebLogo: a sequence logo generator. Genome research *14*, 1188-1190.

de Jong, W.W., Caspers, G.J., and Leunissen, J.A. (1998). Genealogy of the alpha-crystallin--small heat-shock protein superfamily. International journal of biological macromolecules *22*, 151-162.

de Jong, W.W., Leunissen, J.A., and Voorter, C.E. (1993). Evolution of the alpha-crystallin/small heat-shock protein family. Molecular biology and evolution *10*, 103-126.

Delaye, M., and Tardieu, A. (1983). Short-range order of crystallin proteins accounts for eye lens transparency. Nature *302*, 415-417.

Delbecq, S.P., and Klevit, R.E. (2013). One size does not fit all: the oligomeric states of alphaB crystallin. FEBS Lett *587*, 1073-1080.

Derham, B.K., and Harding, J.J. (1999). Alpha-crystallin as a molecular chaperone. Progress in retinal and eye research *18*, 463-509.

Dobson, C.M. (2003). Protein folding and misfolding. Nature *426*, 884-890.

Ecroyd, H., Meehan, S., Horwitz, J., Aquilina, J.A., Benesch, J.L., Robinson, C.V., Macphee, C.E., and Carver, J.A. (2007). Mimicking phosphorylation of alphaB-crystallin affects its chaperone activity. Biochem J *401*, 129-141.

Ehrnsperger, M., Graber, S., Gaestel, M., and Buchner, J. (1997). Binding of non-native protein to Hsp25 during heat shock creates a reservoir of folding intermediates for reactivation. The EMBO journal *16*, 221-229.

Eifert, C., Burgio, M.R., Bennett, P.M., Salerno, J.C., and Koretz, J.F. (2005). N-terminal control of small heat shock protein oligomerization: changes in aggregate size and chaperone-like function. Biochim Biophys Acta *1748*, 146-156.

Ericsson, U.B., Hallberg, B.M., Detitta, G.T., Dekker, N., and Nordlund, P. (2006). Thermofluor-based high-throughput stability optimization of proteins for structural studies. Anal Biochem *357*, 289-298.

Evans, P., Slingsby, C., and Wallace, B.A. (2008). Association of partially folded lens βB2-crystallins with the α-crystallin molecular chaperone. Biochemical Journal *409*, 691-699.

Eyles, S.J., and Gierasch, L.M. (2010). Nature's molecular sponges: small heat shock proteins grow into their chaperone roles. Proc Natl Acad Sci U S A *107*, 2727-2728.

Fairbanks, G., Steck, T.L., and Wallach, D.F. (1971). Electrophoretic analysis of the major polypeptides of the human erythrocyte membrane. Biochemistry *10*, 2606-2617.

Foit, L., George, J.S., Zhang, B.W., Brooks, C.L., 3rd, and Bardwell, J.C. (2013). Chaperone activation by unfolding. Proc Natl Acad Sci U S A *110*, E1254-1262.

Fujita, Y., Ohto, E., Katayama, E., and Atomi, Y. (2004). alphaB-Crystallin-coated MAP microtubule resists nocodazole and calcium-induced disassembly. Journal of cell science *117*, 1719-1726.

Garrido, C., Paul, C., Seigneuric, R., and Kampinga, H.H. (2012). The small heat shock proteins family: the long forgotten chaperones. Int J Biochem Cell Biol *44*, 1588-1592.

GE Healthcare (2010), 2-D Electrophoresis – Principles and Methods, http://www.gelifesciences.com/file_source/GELS/Service%20and%20Support/Documents%20and%20Downloads/Handbooks/pdfs/2-D%20Electrophoresis.pdf; 07. Feb. 2016.

Ghosh, J.G., Shenoy, A.K., Jr., and Clark, J.I. (2006). N- and C-Terminal motifs in human alphaB crystallin play an important role in the recognition, selection, and solubilization of substrates. Biochemistry *45*, 13847-13854.

Graw, J. (2004). Congenital hereditary cataracts. The International journal of developmental biology *48*, 1031-1044.

Graw, J. (2009a). Genetics of crystallins: cataract and beyond. Exp Eye Res *88*, 173-189.

Graw, J. (2009b). Mouse models of cataract. Journal of genetics *88*, 469-486.

Graw, J., Loster, J., Soewarto, D., Fuchs, H., Meyer, B., Reis, A., Wolf, E., Balling, R., and Hrabe de Angelis, M. (2001). Characterization of a new, dominant V124E mutation in the mouse alphaA-crystallin-encoding gene. Invest Ophthalmol Vis Sci *42*, 2909-2915.

Graw, J., Loster, J., Soewarto, D., Fuchs, H., Reis, A., Wolf, E., Balling, R., and Hrabe de Angelis, M. (2002). V76D mutation in a conserved gD-crystallin region leads to dominant cataracts in mice. Mammalian genome : official journal of the International Mammalian Genome Society *13*, 452-455.

Gu, F., Luo, W., Li, X., Wang, Z., Lu, S., Zhang, M., Zhao, B., Zhu, S., Feng, S., Yan, Y.B., *et al.* (2008). A novel mutation in AlphaA-crystallin (CRYAA) caused autosomal dominant congenital cataract in a large Chinese family. Hum Mutat *29*, 769.

Gupta, R., and Srivastava, O.P. (2004). Deamidation affects structural and functional properties of human alphaA-crystallin and its oligomerization with alphaB-crystallin. J Biol Chem *279*, 44258-44269.

Hagemann, T.L., Boelens, W.C., Wawrousek, E.F., and Messing, A. (2009). Suppression of GFAP toxicity by alphaB-crystallin in mouse models of Alexander disease. Hum Mol Genet *18*, 1190-1199.

Hamaguchi, K. (1964). STRUCTURE OF MURAMIDASE (LYSOZYME). V. EFFECT OF N,N-DIMETHYLFORMAMIDE AND THE ROLE OF DISULFIDE BONDS IN THE STABILITY OF MURAMIDASE. Journal of biochemistry *55*, 333-339.

Hanazono, Y., Takeda, K., Oka, T., Abe, T., Tomonari, T., Akiyama, N., Aikawa, Y., Yohda, M., and Miki, K. (2013). Nonequivalence observed for the 16-meric structure of a small heat shock protein, SpHsp16.0, from Schizosaccharomyces pombe. Structure *21*, 220-228.

Hartl, F.U., and Hayer-Hartl, M. (2009). Converging concepts of protein folding in vitro and in vivo. Nat Struct Mol Biol *16*, 574-581.

Hartman, D.J., Surin, B.P., Dixon, N.E., Hoogenraad, N.J., and Hoj, P.B. (1993). Substoichiometric amounts of the molecular chaperones GroEL and GroES prevent thermal denaturation and aggregation of mammalian mitochondrial malate dehydrogenase in vitro. Proceedings of the National Academy of Sciences of the United States of America *90*, 2276-2280.

Haslbeck, M., Franzmann, T., Weinfurtner, D., and Buchner, J. (2005). Some like it hot: the structure and function of small heat-shock proteins. Nat Struct Mol Biol *12*, 842-846.

Haslbeck, M., Ignatiou, A., Saibil, H., Helmich, S., Frenzl, E., Stromer, T., and Buchner, J. (2004). A domain in the N-terminal part of Hsp26 is essential for chaperone function and oligomerization. J Mol Biol *343*, 445-455.

Haslbeck, M., Peschek, J., Buchner, J., and Weinkauf, S. (2016). Structure and function of alpha-crystallins: Traversing from in vitro to in vivo. Biochim Biophys Acta *1860*, 149-166.

Haslbeck, M., and Vierling, E. (2015). A first line of stress defense: small heat shock proteins and their function in protein homeostasis. J Mol Biol *427*, 1537-1548.

Hayes, D.B., and Stafford, W.F. (2010). SEDVIEW, real-time sedimentation analysis. Macromolecular bioscience *10*, 731-735.

Heirbraut, M. (2015). Everything but the ACD, Functional Conservation of the Non-conserved Terminal Regions in sHSPs. In The Big Book on Small Heat Shock Proteins, R.M. Tanguay, and L.E. Hightower, eds. (Cham [u.a.]: Springer International Publishing).

Hilton, G.R., Lioe, H., Stengel, F., Baldwin, A.J., and Benesch, J.L. (2012). Small Heat-Shock Proteins: Paramedics of the Cell. Topics in current chemistry.

Hoehenwarter, W., Klose, J., and Jungblut, P.R. (2006). Eye lens proteomics. Amino Acids *30*, 369-389.

Horwitz, J. (1992). Alpha-crystallin can function as a molecular chaperone. Proc Natl Acad Sci U S A *89*, 10449-10453.

Horwitz, J. (2003). Alpha-crystallin. Experimental Eye Research *76*, 145-153.

Huang, Q., Ding, L., Phan, K.B., Cheng, C., Xia, C.H., Gong, X., and Horwitz, J. (2009). Mechanism of cataract formation in alphaA-crystallin Y118D mutation. Invest Ophthalmol Vis Sci *50*, 2919-2926.

Iwaki, T., Kume-Iwaki, A., and Goldman, J.E. (1990). Cellular distribution of alpha B-crystallin in non-lenticular tissues. The journal of histochemistry and cytochemistry : official journal of the Histochemistry Society *38*, 31-39.

Jakob, U., Gaestel, M., Engel, K., and Buchner, J. (1993). Small heat shock proteins are molecular chaperones. J Biol Chem *268*, 1517-1520.

Jaya, N., Garcia, V., and Vierling, E. (2009). Substrate binding site flexibility of the small heat shock protein molecular chaperones. Proc Natl Acad Sci U S A *106*, 15604-15609.

Jehle, S., van Rossum, B., Stout, J.R., Noguchi, S.M., Falber, K., Rehbein, K., Oschkinat, H., Klevit, R.E., and Rajagopal, P. (2009). alphaB-crystallin: a hybrid solid-state/solution-state NMR investigation reveals structural aspects of the heterogeneous oligomer. J Mol Biol *385*, 1481-1497.

Jehle, S., Vollmar, B.S., Bardiaux, B., Dove, K.K., Rajagopal, P., Gonen, T., Oschkinat, H., and Klevit, R.E. (2011). N-terminal domain of alphaB-crystallin provides a conformational switch for multimerization and structural heterogeneity. Proc Natl Acad Sci U S A *108*, 6409-6414.

Ji, F., Jung, J., Koharudin, L.M., and Gronenborn, A.M. (2013). The human W42R gammaD-crystallin mutant structure provides a link between congenital and age-related cataracts. J Biol Chem *288*, 99-109.

Johnson, I. (2010). The Molecular Probes Handbook: A Guide to Fluorescent Probes and Labeling Technologies, 11th Edition (Life Technologies Corporation).

Kamradt, M.C., Chen, F., and Cryns, V.L. (2001). The small heat shock protein alpha B-crystallin negatively regulates cytochrome c- and caspase-8-dependent activation of caspase-3 by inhibiting its autoproteolytic maturation. J Biol Chem *276*, 16059-16063.

Kamradt, M.C., Lu, M., Werner, M.E., Kwan, T., Chen, F., Strohecker, A., Oshita, S., Wilkinson, J.C., Yu, C., Oliver, P.G.*, et al.* (2005). The small heat shock protein alpha B-crystallin is a novel inhibitor of TRAIL-induced apoptosis that suppresses the activation of caspase-3. J Biol Chem *280*, 11059-11066.

Kannan, R., Sreekumar, P.G., and Hinton, D.R. (2012). Novel roles for alpha-crystallins in retinal function and disease. Progress in retinal and eye research *31*, 576-604.

Kappe, G., Boelens, W.C., and de Jong, W.W. (2010). Why proteins without an alpha-crystallin domain should not be included in the human small heat shock protein family HSPB. Cell stress & chaperones *15*, 457-461.

Kayser, J., Haslbeck, M., Dempfle, L., Krause, M., Grashoff, C., Buchner, J., Herrmann, H., and Bausch, A.R. (2013). The small heat shock protein Hsp27 affects assembly dynamics and structure of keratin intermediate filament networks. Biophys J *105*, 1778-1785.

Kelley, P.B., and Abraham, E.C. (2003). Thermally induced disintegration of the oligomeric structure of alphaB-crystallin mutant F28S is associated with diminished chaperone activity. Mol Cell Biochem *252*, 273-278.

Kelly, S.M., and Price, N.C. (2000). The use of circular dichroism in the investigation of protein structure and function. Current protein & peptide science *1*, 349-384.

Khan, A.O., Abu Safieh, L., and Alkuraya, F.S. (2010). Later retinal degeneration following childhood surgical aphakia in a family with recessive CRYAB mutation (p.R56W). Ophthalmic genetics *31*, 30-36.

Kibbelaar, M., and Bloemendal, H. (1975). The topography of lens proteins based on chromatography and two-dimensional gel electrophoresis. Exp Eye Res *21*, 25-36.

Koretz, J.F., and Augusteyn, R.C. (1988). Electron microscopy of native and reconstituted alpha crystallin aggregates. Curr Eye Res *7*, 25-30.

Kramps, H.A., Stols, A.L.H., Hoenders, H.J., and De Groot, K. (1975). On the Quaternary Structure of High-Molecular-Weight Proteins from the Bovine Eye Lens. European Journal of Biochemistry *50*, 503-509.

Kriehuber, T. (2012). Strukturelle Organisation von kleinen Hitzeschockproteinen. In Fakultät für Chemie (Technische Universität München).

Kriehuber, T., Rattei, T., Weinmaier, T., Bepperling, A., Haslbeck, M., and Buchner, J. (2010). Independent evolution of the core domain and its flanking sequences in small heat shock proteins. FASEB journal : official publication of the Federation of American Societies for Experimental Biology *24*, 3633-3642.

Kundu, M., Sen, P.C., and Das, K.P. (2007). Structure, stability, and chaperone function of alphaA-crystallin: role of N-terminal region. Biopolymers *86*, 177-192.

Kyte, J., and Doolittle, R.F. (1982). A simple method for displaying the hydropathic character of a protein. J Mol Biol *157*, 105-132.

Laemmli, U.K. (1970). Cleavage of structural proteins during the assembly of the head of bacteriophage T4. Nature *227*, 680-685.

Laganowsky, A., Benesch, J.L., Landau, M., Ding, L., Sawaya, M.R., Cascio, D., Huang, Q., Robinson, C.V., Horwitz, J., and Eisenberg, D. (2010). Crystal structures of truncated alphaA and alphaB crystallins reveal structural mechanisms of polydispersity important for eye lens function. Protein Sci *19*, 1031-1043.

Laganowsky, A., and Eisenberg, D. (2010). Non-3D domain swapped crystal structure of truncated zebrafish alphaA crystallin. Protein science : a publication of the Protein Society *19*, 1978-1984.

Lampi, K.J., Fox, C.B., and David, L.L. (2012). Changes in solvent accessibility of wild-type and deamidated betaB2-crystallin following complex formation with alphaA-crystallin. Exp Eye Res *104*, 48-58.

Lampi, K.J., Ma, Z., Hanson, S.R., Azuma, M., Shih, M., Shearer, T.R., Smith, D.L., Smith, J.B., and David, L.L. (1998). Age-related changes in human lens crystallins identified by two-dimensional electrophoresis and mass spectrometry. Exp Eye Res *67*, 31-43.

Lang, G.K. (2014). Augenheilkunde, Vol 5. überarb. Aufl. (Stuttgart: Thieme).

Lanneau, D., Wettstein, G., Bonniaud, P., and Garrido, C. (2010). Heat shock proteins: cell protection through protein triage. TheScientificWorldJournal *10*, 1543-1552.

Laue, T.M., Shah, B.D., Ridgeway, T.M., and Pelletier, S.L. (1992). Computer-aided interpretation of analytical sedimentation data for proteins. In Analyticall Ultracentrifugation in Biochemistry and Polymer Science (Cambridge, UK: Royal Society of Chemistry).

Launay, N., Goudeau, B., Kato, K., Vicart, P., and Lilienbaum, A. (2006). Cell signaling pathways to alphaB-crystallin following stresses of the cytoskeleton. Exp Cell Res *312*, 3570-3584.

Laurie, K.J., Dave, A., Straga, T., Souzeau, E., Chataway, T., Sykes, M.J., Casey, T., Teo, T., Pater, J., Craig, J.E.*, et al.* (2013). Identification of a novel oligomerization disrupting mutation in CRYAlphaA associated with congenital cataract in a South Australian family. Hum Mutat *34*, 435-438.

Lee, G.J., Roseman, A.M., Saibil, H.R., and Vierling, E. (1997). A small heat shock protein stably binds heat-denatured model substrates and can maintain a substrate in a folding-competent state. The EMBO journal *16*, 659-671.

Lentze, N., and Narberhaus, F. (2004). Detection of oligomerisation and substrate recognition sites of small heat shock proteins by peptide arrays. Biochem Biophys Res Commun *325*, 401-407.

Li, H., Li, C., Lu, Q., Su, T., Ke, T., Li, D.W., Yuan, M., Liu, J., Ren, X., Zhang, Z.*, et al.* (2008). Cataract mutation P20S of alphaB-crystallin impairs chaperone activity of alphaA-crystallin and induces apoptosis of human lens epithelial cells. Biochim Biophys Acta *1782*, 303-309.

Liang, J.J., and Akhtar, N.J. (2000). Human lens high-molecular-weight alpha-crystallin aggregates. Biochem Biophys Res Commun *275*, 354-359.

Liu, H., Du, X., Wang, M., Huang, Q., Ding, L., McDonald, H.W., Yates, J.R., 3rd, Beutler, B., Horwitz, J., and Gong, X. (2005). Crystallin {gamma}B-I4F mutant protein binds to {alpha}-crystallin and affects lens transparency. The Journal of biological chemistry *280*, 25071-25078.

Liu, J.P., Schlosser, R., Ma, W.Y., Dong, Z., Feng, H., Lui, L., Huang, X.Q., Liu, Y., and Li, D.W. (2004). Human alphaA- and alphaB-crystallins prevent UVA-induced apoptosis through regulation of PKCalpha, RAF/MEK/ERK and AKT signaling pathways. Exp Eye Res *79*, 393-403.

Lund, A.L., Smith, J.B., and Smith, D.L. (1996). Modifications of the water-insoluble human lens alpha-crystallins. Exp Eye Res *63*, 661-672.

Mainz, A., Peschek, J., Stavropoulou, M., Back, K.C., Bardiaux, B., Asami, S., Prade, E., Peters, C., Weinkauf, S., Buchner, J.*, et al.* (2015). The chaperone alphaB-crystallin uses

different interfaces to capture an amorphous and an amyloid client. Nat Struct Mol Biol *22*, 898-905.

Makley, L.N., McMenimen, K.A., DeVree, B.T., Goldman, J.W., McGlasson, B.N., Rajagopal, P., Dunyak, B.M., McQuade, T.J., Thompson, A.D., Sunahara, R.*, et al.* (2015). Pharmacological chaperone for alpha-crystallin partially restores transparency in cataract models. Science *350*, 674-677.

Mao, Y.W., Liu, J.P., Xiang, H., and Li, D.W. (2004). Human alphaA- and alphaB-crystallins bind to Bax and Bcl-X(S) to sequester their translocation during staurosporine-induced apoptosis. Cell death and differentiation *11*, 512-526.

Marcinowski, M. (2011). Functional conformations of the molecular chaperone BiP In Fakultät für Chemie (Technische Universität München).

Masilamoni, J.G., Jesudason, E.P., Bharathi, S.N., and Jayakumar, R. (2005). The protective effect of alpha-crystallin against acute inflammation in mice. Biochim Biophys Acta *1740*, 411-420.

McGaughey, G.B., Gagne, M., and Rappe, A.K. (1998). pi-Stacking interactions. Alive and well in proteins. J Biol Chem *273*, 15458-15463.

McHaourab, H.S., Lin, Y.L., and Spiller, B.W. (2012). Crystal structure of an activated variant of small heat shock protein Hsp16.5. Biochemistry *51*, 5105-5112.

Meehan, S., Berry, Y., Luisi, B., Dobson, C.M., Carver, J.A., and MacPhee, C.E. (2004). Amyloid fibril formation by lens crystallin proteins and its implications for cataract formation. J Biol Chem *279*, 3413-3419.

Messina-Baas, O.M., Gonzalez-Huerta, L.M., and Cuevas-Covarrubias, S.A. (2006). Two affected siblings with nuclear cataract associated with a novel missense mutation in the CRYGD gene. Molecular vision *12*, 995-1000.

Michiel, M., Duprat, E., Skouri-Panet, F., Lampi, J.A., Tardieu, A., Lampi, K.J., and Finet, S. (2010). Aggregation of deamidated human betaB2-crystallin and incomplete rescue by alpha-crystallin chaperone. Exp Eye Res *90*, 688-698.

Miesbauer, L.R., Zhou, X., Yang, Z., Yang, Z., Sun, Y., Smith, D.L., and Smith, J.B. (1994). Post-translational modifications of water-soluble human lens crystallins from young adults. J Biol Chem *269*, 12494-12502.

Mishra, S., Stein, R.A., and McHaourab, H.S. (2012). Cataract-linked gammaD-crystallin mutants have weak affinity to lens chaperones alpha-crystallins. FEBS Lett *586*, 330-336.

Mochizuki, T., and Masai, I. (2014). The lens equator: a platform for molecular machinery that regulates the switch from cell proliferation to differentiation in the vertebrate lens. Development, growth & differentiation *56*, 387-401.

Morgan, A.A., and Rubenstein, E. (2013). Proline: the distribution, frequency, positioning, and common functional roles of proline and polyproline sequences in the human proteome. PLoS One *8*, e53785.

Morishita, H., and Mizushima, N. (2015). Autophagy in the lens. Exp Eye Res.

Morozov, V., and Wawrousek, E.F. (2006). Caspase-dependent secondary lens fiber cell disintegration in alphaA-/alphaB-crystallin double-knockout mice. Development *133*, 813-821.

Narberhaus, F. (2002). Alpha-crystallin-type heat shock proteins: socializing minichaperones in the context of a multichaperone network. Microbiology and molecular biology reviews : MMBR *66*, 64-93; table of contents.

Nicholl, I.D., and Quinlan, R.A. (1994). Chaperone activity of alpha-crystallins modulates intermediate filament assembly. The EMBO journal *13*, 945-953.

Numoto, N., Kita, A., Fujii, N., and Miki, K. (2012). A P39R mutation at the N-terminal domain of human alphaB-crystallin regulates its oligomeric state and chaperone-like activity. Biochem Biophys Res Commun *425*, 601-606.

Ousman, S.S., Tomooka, B.H., van Noort, J.M., Wawrousek, E.F., O'Connor, K.C., Hafler, D.A., Sobel, R.A., Robinson, W.H., and Steinman, L. (2007). Protective and therapeutic role for alphaB-crystallin in autoimmune demyelination. Nature *448*, 474-479.

Panda, A.K., Nandi, S.K., Chakraborty, A., Nagaraj, R.H., and Biswas, A. (2016). Differential role of arginine mutations on the structure and functions of alpha-crystallin. Biochim Biophys Acta *1860*, 199-210.

Pang, M., Su, J.T., Feng, S., Tang, Z.W., Gu, F., Zhang, M., Ma, X., and Yan, Y.B. (2010). Effects of congenital cataract mutation R116H on alphaA-crystallin structure, function and stability. Biochim Biophys Acta *1804*, 948-956.

Pasta, S.Y., Raman, B., Ramakrishna, T., and Rao Ch, M. (2003). Role of the conserved SRLFDQFFG region of alpha-crystallin, a small heat shock protein. Effect on oligomeric size, subunit exchange, and chaperone-like activity. J Biol Chem *278*, 51159-51166.

Pasupuleti, N., Matsuyama, S., Voss, O., Doseff, A.I., Song, K., Danielpour, D., and Nagaraj, R.H. (2010). The anti-apoptotic function of human alphaA-crystallin is directly related to its chaperone activity. Cell Death Dis *1*, e31.

Pattison, J.S., Osinska, H., and Robbins, J. (2011). Atg7 induces basal autophagy and rescues autophagic deficiency in CryABR120G cardiomyocytes. Circulation research *109*, 151-160.

Perkins, D.N., Pappin, D.J.C., Creasy, D.M., and Cottrell, J.S. (1999). Probability-based protein identification by searching sequence databases using mass spectrometry data. ELECTROPHORESIS *20*, 3551-3567.

Perng, M.D., Cairns, L., van den, I.P., Prescott, A., Hutcheson, A.M., and Quinlan, R.A. (1999a). Intermediate filament interactions can be altered by HSP27 and alphaB-crystallin. Journal of cell science *112 (Pt 13)*, 2099-2112.

Perng, M.D., Muchowski, P.J., van Den, I.P., Wu, G.J., Hutcheson, A.M., Clark, J.I., and Quinlan, R.A. (1999b). The cardiomyopathy and lens cataract mutation in alphaB-crystallin alters its protein structure, chaperone activity, and interaction with intermediate filaments in vitro. J Biol Chem *274*, 33235-33243.

Peschek, J. (2012). Structural and Functional Principles of the Small Heat Shock Protein alpha-Crystallin. In Fakultät für Chemie (Technische Universtät München).

Peschek, J., Braun, N., Franzmann, T.M., Georgalis, Y., Haslbeck, M., Weinkauf, S., and Buchner, J. (2009). The eye lens chaperone alpha-crystallin forms defined globular assemblies. Proc Natl Acad Sci U S A *106*, 13272-13277.

Peschek, J., Braun, N., Rohrberg, J., Back, K.C., Kriehuber, T., Kastenmuller, A., Weinkauf, S., and Buchner, J. (2013). Regulated structural transitions unleash the chaperone activity of alphaB-crystallin. Proc Natl Acad Sci U S A *110*, E3780-3789.

Philo, J.S. (2006). Improved methods for fitting sedimentation coefficient distributions derived by time-derivative techniques. Anal Biochem *354*, 238-246.

Porath, J., and Flodin, P. (1959). Gel filtration: a method for desalting and group separation. Nature *183*, 1657-1659.

Puk, O., Ahmad, N., Wagner, S., Hrabe de Angelis, M., and Graw, J. (2011). First mutation in the betaA2-crystallin encoding gene is associated with small lenses and age-related cataracts. Invest Ophthalmol Vis Sci *52*, 2571-2576.

Quinlan, R.A., Carte, J.M., Sandilands, A., and Prescott, A.R. (1996). The beaded filament of the eye lens: an unexpected key to intermediate filament structure and function. Trends in cell biology *6*, 123-126.

Radmann, P. (2013). Charakterisierung verschiedener Varianten des Augenlinsenproteins gD-Crystallin. In Fakultät für Chemie (Technische Universität München).

Raju, M., Santhoshkumar, P., and Sharma, K.K. (2011). Cataract-causing alphaAG98R-crystallin mutant dissociates into monomers having chaperone activity. Molecular vision *17*, 7-15.

Richardson, J.S. (1977). beta-Sheet topology and the relatedness of proteins. Nature *268*, 495-500.

Richter, K., Haslbeck, M., and Buchner, J. (2010). The heat shock response: life on the verge of death. Molecular cell *40*, 253-266.

Ritossa, F. (1962). A new puffing pattern induced by temperature shock and DNP in drosophila. Experientia *18*, 571-573.

Ritossa, F.M. (1964). EXPERIMENTAL ACTIVATION OF SPECIFIC LOCI IN POLYTENE CHROMOSOMES OF DROSOPHILA. Exp Cell Res *35*, 601-607.

Robinson, M.L., and Overbeek, P.A. (1996). Differential expression of alpha A- and alpha B-crystallin during murine ocular development. Invest Ophthalmol Vis Sci *37*, 2276-2284.

Roshan, M., Vijaya, P.H., Lavanya, G.R., Shama, P.K., Santhiya, S.T., Graw, J., Gopinath, P.M., and Satyamoorthy, K. (2010). A novel human CRYGD mutation in a juvenile autosomal dominant cataract. Molecular vision *16*, 887-896.

Roy, D., and Spector, A. (1976). Absence of low-molecular-weight alpha crystallin in nuclear region of old human lenses. Proceedings of the National Academy of Sciences of the United States of America *73*, 3484-3487.

Santhiya, S.T., Soker, T., Klopp, N., Illig, T., Prakash, M.V., Selvaraj, B., Gopinath, P.M., and Graw, J. (2006). Identification of a novel, putative cataract-causing allele in CRYAA (G98R) in an Indian family. Molecular vision *12*, 768-773.

Santhoshkumar, P., Murugesan, R., and Sharma, K.K. (2009). Deletion of (54)FLRAPSWF(61) residues decreases the oligomeric size and enhances the chaperone function of alphaB-crystallin. Biochemistry *48*, 5066-5073.

Santhoshkumar, P., and Sharma, K.K. (2001). Analysis of alpha-crystallin chaperone function using restriction enzymes and citrate synthase. Molecular vision *7*, 172-177.

Santhoshkumar, P., and Sharma, K.K. (2002). Identification of a region in alcohol dehydrogenase that binds to alpha-crystallin during chaperone action. Biochim Biophys Acta *1598*, 115-121.

Schaefer, H., Chamrad, D.C., Herrmann, M., Stuwe, J., Becker, G., Klose, J., Blueggel, M., Meyer, H.E., and Marcus, K. (2006). Study of posttranslational modifications in lenticular alphaA-Crystallin of mice using proteomic analysis techniques. Biochim Biophys Acta *1764*, 1948-1962.

Schuck, P. (2000). Size-distribution analysis of macromolecules by sedimentation velocity ultracentrifugation and lamm equation modeling. Biophys J *78*, 1606-1619.

Scott, D.J., and Schuck, P. (2006). Analytical ultracentrifugation. In A Brief Introduction to the Analytical Ultracentrifugation of Proteins for Beginners, D.J. Scott, S.E. Harding, and A.J. Rowe, eds. (Cambridge: RCS publishing).

Sharma, K.K., Kaur, H., and Kester, K. (1997). Functional elements in molecular chaperone alpha-crystallin: identification of binding sites in alpha B-crystallin. Biochem Biophys Res Commun *239*, 217-222.

Sharma, K.K., Kumar, R.S., Kumar, G.S., and Quinn, P.T. (2000). Synthesis and characterization of a peptide identified as a functional element in alphaA-crystallin. J Biol Chem *275*, 3767-3771.

Sharma, K.K., and Santhoshkumar, P. (2009). Lens aging: effects of crystallins. Biochim Biophys Acta *1790*, 1095-1108.

Shen, Y., Maupetit, J., Derreumaux, P., and Tuffery, P. (2014). Improved PEP-FOLD Approach for Peptide and Miniprotein Structure Prediction. Journal of chemical theory and computation *10*, 4745-4758.

Shroff, N.P., Cherian-Shaw, M., Bera, S., and Abraham, E.C. (2000). Mutation of R116C results in highly oligomerized alpha A-crystallin with modified structure and defective chaperone-like function. Biochemistry *39*, 1420-1426.

Sievers, F., Wilm, A., Dineen, D., Gibson, T.J., Karplus, K., Li, W., Lopez, R., McWilliam, H., Remmert, M., Soding, J.*, et al.* (2011). Fast, scalable generation of high-quality protein multiple sequence alignments using Clustal Omega. Molecular systems biology *7*, 539.

Siezen, R.J., and Hoenders, H.J. (1979). The Quaternary Structure of Bovine α-Crystallin. European Journal of Biochemistry *96*, 431-440.

Singh, B.N., Rao, K.S., Ramakrishna, T., Rangaraj, N., and Rao Ch, M. (2007). Association of alphaB-crystallin, a small heat shock protein, with actin: role in modulating actin filament dynamics in vivo. J Mol Biol *366*, 756-767.

Singh, D., Raman, B., Ramakrishna, T., and Rao Ch, M. (2006). The cataract-causing mutation G98R in human alphaA-crystallin leads to folding defects and loss of chaperone activity. Molecular vision *12*, 1372-1379.

Slingsby, C., and Clout, N.J. (1999). Structure of the crystallins. Eye (London, England) *13 (Pt 3b)*, 395-402.

Smith, M.A., Bateman, O.A., Jaenicke, R., and Slingsby, C. (2007). Mutation of interfaces in domain-swapped human betaB2-crystallin. Protein Sci *16*, 615-625.

Song, S., Hanson, M.J., Liu, B.-F., Chylack, L.T., and Liang, J.J.N. (2008). Protein-protein interactions between lens vimentin and αB-crystallin using FRET acceptor photobleaching. Molecular vision *14*, 1282-1287.

Srinivasan, A.N., Nagineni, C.N., and Bhat, S.P. (1992). alpha A-crystallin is expressed in non-ocular tissues. J Biol Chem *267*, 23337-23341.

Srivastava, O.P., and Srivastava, K. (2003). BetaB2-crystallin undergoes extensive truncation during aging in human lenses. Biochem Biophys Res Commun *301*, 44-49.

Stafford, W.F., 3rd (1992). Boundary analysis in sedimentation transport experiments: a procedure for obtaining sedimentation coefficient distributions using the time derivative of the concentration profile. Anal Biochem *203*, 295-301.

Stryer, L. (1965). The interaction of a naphthalene dye with apomyoglobin and apohemoglobin. A fluorescent probe of non-polar binding sites. J Mol Biol *13*, 482-495.

Su, S.P., McArthur, J.D., Truscott, R.J., and Aquilina, J.A. (2011). Truncation, cross-linking and interaction of crystallins and intermediate filament proteins in the aging human lens. Biochim Biophys Acta *1814*, 647-656.

Sugiyama, M., Kurimoto, E., Yagi, H., Mori, K., Fukunaga, T., Hirai, M., Zaccai, G., and Kato, K. (2011). Kinetic asymmetry of subunit exchange of homooligomeric protein as revealed by deuteration-assisted small-angle neutron scattering. Biophys J *101*, 2037-2042.

Takata, T., Woodbury, L.G., and Lampi, K.J. (2009). Deamidation alters interactions of β-crystallins in hetero-oligomers. Molecular vision *15*, 241-249.

Takemoto, L., and Boyle, D. (1994). Molecular chaperone properties of the high molecular weight aggregate from aged lens. Curr Eye Res *13*, 35-44.

Takemoto, L., Emmons, T., and Horwitz, J. (1993). The C-terminal region of alpha-crystallin: involvement in protection against heat-induced denaturation. Biochem J *294 (Pt 2)*, 435-438.

Takemoto, L., and Sorensen, C.M. (2008). Protein-protein interactions and lens transparency. Exp Eye Res *87*, 496-501.

Takeuchi, N., Ouchida, A., and Kamei, A. (2004). C-terminal truncation of alpha-crystallin in hereditary cataractous rat lens. Biological & pharmaceutical bulletin *27*, 308-314.

Taylor, R.P., and Benjamin, I.J. (2005). Small heat shock proteins: a new classification scheme in mammals. J Mol Cell Cardiol *38*, 433-444.

Tessier, D.J., Komalavilas, P., Panitch, A., Joshi, L., and Brophy, C.M. (2003). The small heat shock protein (HSP) 20 is dynamically associated with the actin cross-linking protein actinin. The Journal of surgical research *111*, 152-157.

Thampi, P., Hassan, A., Smith, J.B., and Abraham, E.C. (2002). Enhanced C-terminal truncation of alphaA- and alphaB-crystallins in diabetic lenses. Invest Ophthalmol Vis Sci *43*, 3265-3272.

Treweek, T.M., Rekas, A., Walker, M.J., and Carver, J.A. (2010). A quantitative NMR spectroscopic examination of the flexibility of the C-terminal extensions of the molecular chaperones, alphaA- and alphaB-crystallin. Exp Eye Res *91*, 691-699.

Truscott, R.J., and Friedrich, M.G. (2016). The etiology of human age-related cataract. Proteins don't last forever. Biochim Biophys Acta *1860*, 192-198.

Tyedmers, J., Mogk, A., and Bukau, B. (2010). Cellular strategies for controlling protein aggregation. Nature reviews Molecular cell biology *11*, 777-788.

Ueda, Y., Duncan, M.K., and David, L.L. (2002). Lens proteomics: the accumulation of crystallin modifications in the mouse lens with age. Invest Ophthalmol Vis Sci *43*, 205-215.

Validandi, V., Reddy, V.S., Srinivas, P.N., Mueller, N.H., Bhagyalaxmi, S.G., Padma, T., Petrash, J.M., and Reddy, G.B. (2011). Temperature-dependent structural and functional properties of a mutant (F71L) alphaA-crystallin: molecular basis for early onset of age-related cataract. FEBS Lett *585*, 3884-3889.

van de Klundert, F.A., Smulders, R.H., Gijsen, M.L., Lindner, R.A., Jaenicke, R., Carver, J.A., and de Jong, W.W. (1998). The mammalian small heat-shock protein Hsp20 forms dimers and is a poor chaperone. European journal of biochemistry / FEBS *258*, 1014-1021.

van Dijk, M.A., Sweers, M.A., and de Jong, W.W. (2001). The evolution of an alternatively spliced exon in the alphaA-crystallin gene. Journal of molecular evolution *52*, 510-515.

van Leen, R.W., van Roozendaal, K.E., Lubsen, N.H., and Schoenmakers, J.G. (1987). Differential expression of crystallin genes during development of the rat eye lens. Developmental biology *120*, 457-464.

Vicart, P., Caron, A., Guicheney, P., Li, Z., Prévost, M.C., Faure, A., Chateau, D., Chapon, F., Tomé, F., Dupret, J.M., *et al.* (1998). A missense mutation in the alphaB-crystallin chaperone gene causes a desmin-related myopathy. Nat Genet *20*, 92-95.

Walter, S., and Buchner, J. (2002). Molecular chaperones--cellular machines for protein folding. Angewandte Chemie (International ed in English) *41*, 1098-1113.

Wang, K., Cheng, C., Li, L., Liu, H., Huang, Q., Xia, C.H., Yao, K., Sun, P., Horwitz, J., and Gong, X. (2007). GammaD-crystallin associated protein aggregation and lens fiber cell denucleation. Invest Ophthalmol Vis Sci *48*, 3719-3728.

Wang, X., Garcia, C.M., Shui, Y.B., and Beebe, D.C. (2004). Expression and regulation of alpha-, beta-, and gamma-crystallins in mammalian lens epithelial cells. Invest Ophthalmol Vis Sci *45*, 3608-3619.

Watanabe, G., Kato, S., Nakata, H., Ishida, T., Ohuchi, N., and Ishioka, C. (2009). αB-crystallin: A novel p53-target gene required for p53-dependent apoptosis. Cancer science *100*, 2368-2375.

Wignes, J.A., Goldman, J.W., Weihl, C.C., Bartley, M.G., and Andley, U.P. (2013). p62 expression and autophagy in alphaB-crystallin R120G mutant knock-in mouse model of hereditary cataract. Exp Eye Res *115*, 263-273.

Wilkins, M.R., Gasteiger, E., Bairoch, A., Sanchez, J.C., Williams, K.L., Appel, R.D., and Hochstrasser, D.F. (1999). Protein identification and analysis tools in the ExPASy server. Methods in molecular biology (Clifton, NJ) *112*, 531-552.

Xi, J.H., Bai, F., Gross, J., Townsend, R.R., Menko, A.S., and Andley, U.P. (2008). Mechanism of small heat shock protein function in vivo: a knock-in mouse model demonstrates that the R49C mutation in alpha A-crystallin enhances protein insolubility and cell death. J Biol Chem *283*, 5801-5814.

Xia, C.H., Liu, H., Chang, B., Cheng, C., Cheung, D., Wang, M., Huang, Q., Horwitz, J., and Gong, X. (2006). Arginine 54 and Tyrosine 118 residues of {alpha}A-crystallin are crucial for lens formation and transparency. Invest Ophthalmol Vis Sci *47*, 3004-3010.

Zhang, J., Li, J., Huang, C., Xue, L., Peng, Y., Fu, Q., Gao, L., Zhang, J., and Li, W. (2008). Targeted Knockout of the Mouse βB2-crystallin Gene (Crybb2) Induces Age-Related Cataract. Investigative Ophthalmology & Visual Science *49*, 5476-5483.

Zhang, Z., David, L.L., Smith, D.L., and Smith, J.B. (2001). Resistance of human betaB2-crystallin to in vivo modification. Exp Eye Res *73*, 203-211.

Zhao, L., Chen, X.J., Zhu, J., Xi, Y.B., Yang, X., Hu, L.D., Ouyang, H., Patel, S.H., Jin, X., Lin, D.*, et al.* (2015). Lanosterol reverses protein aggregation in cataracts. Nature *523*, 607-611.

Appendix

Abbreviations

3E	αB-crystallin-3E (S19/45/59E)
aa	amino acid
ACD	α-crystallin domain
AUC	Analytical ultracentrifugation
bp	base pairs
CD	circular dichroism
CTR	Carboxy-terminal region
CS	Citrate Synthase
Da	Dalton
DNA	Deoxyribonucleic acid
EM	Electron microscopy
FRET	Fluorescence resonance energy transfer
Hsp	Heat shock protein
MDH	Malate dehydrogenase
n.d.	not determined
NMR	Nuclear magnetic resonance
$N_{2(l)}$	liquid nitrogen
ns	negative stain
NTR	amino terminal region
ox.	oxidized
PBS	Phosphate buffered saline
red.	reduced
rt	Room temperature
SDS-PAGE	sodium dodecyl sulfate-polyacrylamide gel electrophoresis
SE	Sedimentation equilibrium
SEC	Size exclusion chromatography
SU	Subunit
sHsp	Small heat shock protein
SV	Sedimentation velocity
SX	subunit exchange

TEM	Transmission electron microscopy
UV	ultra violet
(v/v)	volume per volume
(w/v)	weight per volume
X-link	cross link
αA	αA-crystallin
αB	αB-crystallin
γD	γD-crystallin

Table of amino acids

Amino acid	3-Letter Code	1-Letter Code
Alanine	Ala	A
Arginine	Arg	R
Asparagine	Asn	N
Aspartate	Asp	D
Cysteine	Cys	C
Glutamate	Glu	E
Glutamine	Gln	Q
Glycine	Gly	G
Histidine	His	H
Isoleucine	Ile	I
Leucine	Leu	L
Lysine	Lys	K
Methionine	Met	M
Phenylalanine	Phe	F
Proline	Pro	P
Serine	Ser	S
Threonine	Thr	T
Tryptophan	Trp	W
Tyrosine	Tyr	Y
Valine	Val	V

DNA and amino acid sequences of human and murine αA- and αB-crystallin

All introduced mutations or numbering of amino acids was based on the following sequences.

human αA

DNA-sequence:

atggacgtgaccatccagcacccctggttcaagcgcaccctggggcccttctaccccagccggctgtt
cgaccagtttttcggcgagggccttttgagtatgacctgctgcccttcctgtcgtccaccatcagcc
cctactaccgccagtccctcttccgcaccgtgctggactccggcatctctgaggttcgatccgaccgg
gacaagttcgtcatcttcctcgatgtgaagcacttctccccggaggacctcaccgtgaaggtgcagga
cgactttgtggagatccacggaaagcacaacgagcgccaggacgaccacggctacatttcccgtgagt
tccaccgccgctaccgcctgccgtccaacgtggaccagtcggccctctcttgctccctgtctgccgat
ggcatgctgaccttctgtggccccaagatccagactggcctggatgccacccacgccgagcgagccat
ccccgtgtcgcgggaggagaagcccacctcggctccctcgtcctaa

Amino acid-sequence:

MDVTIQHPWFKRTLGPFYPSRLFDQFFGEGLFEYDLLPFLSSTISPYYRQSLFRTVLDSGISEVRSDR
DKFVIFLDVKHFSPEDLTVKVQDDFVEIHGKHNERQDDHGYISREFHRRYRLPSNVDQSALSCSLSAD
GMLTFCGPKIQTGLDATHAERAIPVSREEKPTSAPSS

human αB

DNA-sequence:

atggacatcgccatccaccacccctggatccgccgccccttctttcctttccactcccccagccgcct
ctttgaccagttcttcggagagcacctgttggagtctgatcttttcccgacgtctacttccctgagtc
ccttctaccttcggccaccctccttcctgcgggcacccagctggtttgacactggactctcagagatg
cgcctggagaaggacaggttctctgtcaacctggatgtgaagcacttctccccagaggaactcaaagt
taaggtgttgggagatgtgattgaggtgcatggaaaacatgaagagcgccaggatgaacatggtttca
tctccagggagttccacaggaaataccggatcccagctgatgtagaccctctcaccattacttcatcc
ctgtcatctgatggggtcctcactgtgaatggaccaaggaaacaggtctctggccctgagcgcaccat
tcccatcacccgtgaagagaagcctgctgtcaccgcagcccccaagaaatag

Amino acid-sequence:

MDIAIHHPWIRRPFFPFHSPSRLFDQFFGEHLLESDLFPTSTSLSPFYLRPPSFLRAPSWFDTGLSEM
RLEKDRFSVNLDVKHFSPEELKVKVLGDVIEVHGKHEERQDEHGFISREFHRKYRIPADVDPLTITSS
LSSDGVLTVNGPRKQVSGPERTIPITREEKPAVTAAPKK

murine αA

DNA-sequence:

ATGGACGTCACCATTCAGCATCCTTGGTTCAAGCGTGCCCTGGGGCCCTTCTACCCCAGCCGACTGTT
CGACCAGTTCTTCGGCGAGGGCCTTTTTGAGTACGACCTGCTGCCCTTCCTGTCTTCCACCATCAGCC
CCTACTACCGCCAGTCCCTCTTCCGCACTGTGCTGGACTCGGGCATCTCTGAGGTCCGATCTGACCGG
GACAAGTTTGTCATCTTCTTGGACGTGAAGCACTTCTCTCCTGAGGACCTCACCGTGAAGGTACTGGA
GGATTTTGTGGAGATTCACGGCAAACACAACGAGAGGCAGGATGACCATGGCTACATTTCCCGTGAAT
TTCACCGTCGCTACCGTCTGCCTTCCAATGTGGACCAGTCCGCCCTCTCCTGCTCCCTGTCTGCGGAT
GGCATGCTGACCTTCTCTGGCCCCAAGGTCCAGTCCGGTTTGGATGCTGGCCACAGCGAGAGGGCCAT
TCCTGTGTCACGGGAGGAGAAACCCAGCTCTGCACCCTCGTCCTGA

Amino acid-sequence:

MDVTIQHPWFKRALGPFYPSRLFDQFFGEGLFEYDLLPFLSSTISPYYRQSLFRTVLDSGISEVRSDR
DKFVIFLDVKHFSPEDLTVKVLEDFVEIHGKHNERQDDHGYISREFHRRYRLPSNVDQSALSCSLSAD
GMLTFSGPKVQSGLDAGHSERAIPVSREEKPSSAPSS

murine αB

DNA-sequence:

ATGGACATCGCCATCCACCACCCCTGGATCCGGCGCCCCTTCTTCCCCTTCCACTCCCCAAGCCGCCT
CTTCGACCAGTTCTTCGGAGAGCACCTGTTGGAGTCTGACCTCTTCTCAACAGCCACTTCCCTGAGCC
CCTTCTACCTTCGGCCACCCTCCTTCCTGCGGGCACCCAGCTGGATTGACACCGGACTCTCAGAGATG
CGTTTGGAGAAGGACAGATTCTCTGTGAATCTGGACGTGAAGCACTTCTctCCGGAGGAACTCAAAGT
CAAGGTTCTGGGGGACGTGATTGAGGTCCACGGCAAGCACGAAGAACGCCAGGACGAACATGGCTTCA
TctCCAGGGAGTTCCACAGGAAGTACCGGATCCCAGCCGATGTGGATCCTCTCACCATCACTTCATCC
CTGTCATCTGATGGAGTCCTCACTGTGAATGGACCAAGGAAACAGGTGTCTGGCCCTGAGCGCACCAT
TCCCATCACCCGTGAAGAGAAGCCTGCTGTCGCCGCAGCCCCTAAGAAGTAG

Amino acid-sequence:

MDIAIHHPWIRRPFFPFHSPSRLFDQFFGEHLLESDLFSTATSLSPFYLRPPSFLRAPSWIDTGLSEM
RLEKDRFSVNLDVKHFSPEELKVKVLGDVIEVHGKHEERQDEHGFISREFHRKYRIPADVDPLTITSS
LSSDGVLTVNGPRKQVSGPERTIPITREEKPAVAAAPKK

human γD

DNA-sequence:

ATGGGTAAAATTACCCTGTATGAAGATCGTGGTTTTCAGGGTCGTCATTATGAATGTAGCAGCGATCA
TCCGAATCTGCAGCCGTATCTGAGCCGTTGTAATAGCGCACGTGTTGATAGCGGTTGTTGGATGCTGT
ATGAACAGCCGAATTATAGCGGTCTGCAGTATTTTCTGCGTCGTGGTGATTATGCAGATCATCAGCAG
TGGATGGGTCTGAGCGATAGCGTTCGTAGCTGTCGTCTGATTCCGCATAGCGGTAGCCATCGTATTCG
TCTGTATGAACGTGAAGATTATCGCGGTCAGATGATTGAATTTACCGAAGATTGTAGCTGTCTGCAGG
ATCGTTTTCGCTTTAATGAAATTCATAGCCTGAATGTTCTGGAAGGTAGCTGGGTTCTGTATGAACTG
AGCAATTATCGTGGTCGTCAGTATCTGCTGATGCTGGTGATTATCGTCGTTATCAGGATTGGGGTGCA
ACCAATGCACGTGTTGGCAGCCTGCGTCGTGTTATTGATTTTAGTTAA

Amino acid-sequence:

MGKITLYEDRGFQGRHYECSSDHPNLQPYLSRCNSARVDSGCWMLYEQPNYSGLQYFLRRGDYADHQQ
WMGLSDSVRSCRLIPHSGSHRIRLYEREDYRGQMIEFTEDCSCLQDRFRFNEIHSLNVLEGSWVLYEL
SNYRGRQYLLMPGDYRRYQDWGATNARVGSLRRVIDFS

Analyzed constructs, molecular masses and extinction coefficients

Variant	MW (g/mol)	ε (M^{-1} cm^{-1})	Origin
Murine aA	19792.1	14440	This work
maA V124E	19822.1	14440	This work
maA INS	22489.3	19940	This work
Human aA	19909.3	14440	Dr. Jirka Peschek
Murine aB	20068.8	13980	This work
Human aB	20158.9	13980	Dr. Jirka Peschek
aB Δ20	17877.2	8480	This work
aB Δ20 F27R	17886.2	8480	This work
aB Δ26	17130.4	8480	This work
aB Δ28	16765.0	8480	This work
aB Δ40	15496.6	8480	This work
aB Δ51	14247.1	6990	This work
aB ΔNTD	12513.2	1490	Dr. Jirka Peschek

aB W9C	20075.8	8480	This work
aB R11A	20073.8	13980	This work
aB R22Q	20130.8	13980	This work
aB F24A	20082.8	13980	This work
aB F24E	20140.8	13980	This work
aB F24P	20108.8	13980	This work
aB Q26A	20101.8	13980	This work
aB Q26P	20127.9	13980	This work
aB F27A	20082.8	13980	This work
aB F27E	20140.8	13980	This work
aB F27R	20167.9	13980	This work
aB F28A	20082.8	13980	This work
aB F28E	20140.8	13980	This work
aB F27,28A	20006.7	13980	This work
aB F27,28E	20122.7	13980	This work
aB E34Q	20157.9	13980	This work
aB P39Q	20189.9	13980	This work
aB W60C	20075.8	8480	This work
aB S135Q	20199.9	13980	This work
aB R163A	20073.8	13980	This work
gD WT	20606.9	42860	Dr. Jirka Peschek
gD I4F	20640.9	42860	This work
gD W43R	20576.9	37360	This work
gD I4F, W43R	20610.9	37360	This work
gD R59H	20587.8	42860	This work
gD V76D	20754.0	42860	This work

List of Sequences of the peptide arrays and arrangement on the membrane

Peptide spot arrangement on the chips.

Peptide analyzed in the peptide arrays:

no	*syn-plate*	*sequence*	*peptide name*
1	A 1	A-S-S-T-N-L-K-D-I-L-A-D-L-I-P	PDB_3ENJ peptide 1
2	A 2	T-N-L-K-D-I-L-A-D-L-I-P-K-E-Q	PDB_3ENJ peptide 2
3	A 3	K-D-I-L-A-D-L-I-P-K-E-Q-A-R-I	PDB_3ENJ peptide 3
4	A 4	L-A-D-L-I-P-K-E-Q-A-R-I-K-T-F	PDB_3ENJ peptide 4
5	A 5	L-I-P-K-E-Q-A-R-I-K-T-F-R-Q-Q	PDB_3ENJ peptide 5
6	A 6	K-E-Q-A-R-I-K-T-F-R-Q-Q-H-G-N	PDB_3ENJ peptide 6
7	A 7	A-R-I-K-T-F-R-Q-Q-H-G-N-T-V-V	PDB_3ENJ peptide 7
8	A 8	K-T-F-R-Q-Q-H-G-N-T-V-V-G-Q-I	PDB_3ENJ peptide 8
9	A 9	R-Q-Q-H-G-N-T-V-V-G-Q-I-T-V-D	PDB_3ENJ peptide 9
10	A10	H-G-N-T-V-V-G-Q-I-T-V-D-M-M-Y	PDB_3ENJ peptide 10
11	A11	T-V-V-G-Q-I-T-V-D-M-M-Y-G-G-M	PDB_3ENJ peptide 11
12	A12	G-Q-I-T-V-D-M-M-Y-G-G-M-R-G-M	PDB_3ENJ peptide 12
13	A13	T-V-D-M-M-Y-G-G-M-R-G-M-K-G-L	PDB_3ENJ peptide 13
14	A14	M-M-Y-G-G-M-R-G-M-K-G-L-V-Y-E	PDB_3ENJ peptide 14
15	A15	G-G-M-R-G-M-K-G-L-V-Y-E-T-S-V	PDB_3ENJ peptide 15
16	A16	R-G-M-K-G-L-V-Y-E-T-S-V-L-D-P	PDB_3ENJ peptide 16
17	A17	K-G-L-V-Y-E-T-S-V-L-D-P-D-E-G	PDB_3ENJ peptide 17
18	A18	V-Y-E-T-S-V-L-D-P-D-E-G-I-R-F	PDB_3ENJ peptide 18
19	A19	T-S-V-L-D-P-D-E-G-I-R-F-R-G-Y	PDB_3ENJ peptide 19
20	A20	L-D-P-D-E-G-I-R-F-R-G-Y-S-I-P	PDB_3ENJ peptide 20
21	A21	D-E-G-I-R-F-R-G-Y-S-I-P-E-C-Q	PDB_3ENJ peptide 21
22	A22	I-R-F-R-G-Y-S-I-P-E-C-Q-K-M-L	PDB_3ENJ peptide 22
23	A23	R-G-Y-S-I-P-E-C-Q-K-M-L-P-K-A	PDB_3ENJ peptide 23
24	A24	S-I-P-E-C-Q-K-M-L-P-K-A-K-G-G	PDB_3ENJ peptide 24
25	B 1	E-C-Q-K-M-L-P-K-A-K-G-G-E-E-P	PDB_3ENJ peptide 25
26	B 2	K-M-L-P-K-A-K-G-G-E-E-P-L-P-E	PDB_3ENJ peptide 26
27	B 3	P-K-A-K-G-G-E-E-P-L-P-E-G-L-F	PDB_3ENJ peptide 27
28	B 4	K-G-G-E-E-P-L-P-E-G-L-F-W-L-L	PDB_3ENJ peptide 28
29	B 5	E-E-P-L-P-E-G-L-F-W-L-L-V-T-G	PDB_3ENJ peptide 29
30	B 6	L-P-E-G-L-F-W-L-L-V-T-G-Q-I-P	PDB_3ENJ peptide 30
31	B 7	G-L-F-W-L-L-V-T-G-Q-I-P-T-E-E	PDB_3ENJ peptide 31
32	B 8	W-L-L-V-T-G-Q-I-P-T-E-E-Q-V-S	PDB_3ENJ peptide 32
33	B 9	V-T-G-Q-I-P-T-E-E-Q-V-S-W-L-S	PDB_3ENJ peptide 33

34	B10	Q-I-P-T-E-E-Q-V-S-W-L-S-K-E-W	PDB_3ENJ peptide 34
35	B11	T-E-E-Q-V-S-W-L-S-K-E-W-A-K-R	PDB_3ENJ peptide 35
36	B12	Q-V-S-W-L-S-K-E-W-A-K-R-A-A-L	PDB_3ENJ peptide 36
37	B13	W-L-S-K-E-W-A-K-R-A-A-L-P-S-H	PDB_3ENJ peptide 37
38	B14	K-E-W-A-K-R-A-A-L-P-S-H-V-V-T	PDB_3ENJ peptide 38
39	B15	A-K-R-A-A-L-P-S-H-V-V-T-M-L-D	PDB_3ENJ peptide 39
40	B16	A-A-L-P-S-H-V-V-T-M-L-D-N-F-P	PDB_3ENJ peptide 40
41	B17	P-S-H-V-V-T-M-L-D-N-F-P-T-N-L	PDB_3ENJ peptide 41
42	B18	V-V-T-M-L-D-N-F-P-T-N-L-H-P-M	PDB_3ENJ peptide 42
43	B19	M-L-D-N-F-P-T-N-L-H-P-M-S-Q-L	PDB_3ENJ peptide 43
44	B20	N-F-P-T-N-L-H-P-M-S-Q-L-S-A-A	PDB_3ENJ peptide 44
45	B21	T-N-L-H-P-M-S-Q-L-S-A-A-I-T-A	PDB_3ENJ peptide 45
46	B22	H-P-M-S-Q-L-S-A-A-I-T-A-L-N-S	PDB_3ENJ peptide 46
47	B23	S-Q-L-S-A-A-I-T-A-L-N-S-E-S-N	PDB_3ENJ peptide 47
48	B24	S-A-A-I-T-A-L-N-S-E-S-N-F-A-R	PDB_3ENJ peptide 48
49	C 1	I-T-A-L-N-S-E-S-N-F-A-R-A-Y-A	PDB_3ENJ peptide 49
50	C 2	L-N-S-E-S-N-F-A-R-A-Y-A-E-G-I	PDB_3ENJ peptide 50
51	C 3	E-S-N-F-A-R-A-Y-A-E-G-I-H-R-T	PDB_3ENJ peptide 51
52	C 4	F-A-R-A-Y-A-E-G-I-H-R-T-K-Y-W	PDB_3ENJ peptide 52
53	C 5	A-Y-A-E-G-I-H-R-T-K-Y-W-E-L-I	PDB_3ENJ peptide 53
54	C 6	E-G-I-H-R-T-K-Y-W-E-L-I-Y-E-D	PDB_3ENJ peptide 54
55	C 7	H-R-T-K-Y-W-E-L-I-Y-E-D-C-M-D	PDB_3ENJ peptide 55
56	C 8	K-Y-W-E-L-I-Y-E-D-C-M-D-L-I-A	PDB_3ENJ peptide 56
57	C 9	E-L-I-Y-E-D-C-M-D-L-I-A-K-L-P	PDB_3ENJ peptide 57
58	C10	Y-E-D-C-M-D-L-I-A-K-L-P-C-V-A	PDB_3ENJ peptide 58
59	C11	C-M-D-L-I-A-K-L-P-C-V-A-A-K-I	PDB_3ENJ peptide 59
60	C12	L-I-A-K-L-P-C-V-A-A-K-I-Y-R-N	PDB_3ENJ peptide 60
61	C13	K-L-P-C-V-A-A-K-I-Y-R-N-L-Y-R	PDB_3ENJ peptide 61
62	C14	C-V-A-A-K-I-Y-R-N-L-Y-R-E-G-S	PDB_3ENJ peptide 62
63	C15	A-K-I-Y-R-N-L-Y-R-E-G-S-S-I-G	PDB_3ENJ peptide 63
64	C16	Y-R-N-L-Y-R-E-G-S-S-I-G-A-I-D	PDB_3ENJ peptide 64
65	C17	L-Y-R-E-G-S-S-I-G-A-I-D-S-K-L	PDB_3ENJ peptide 65
66	C18	E-G-S-S-I-G-A-I-D-S-K-L-D-W-S	PDB_3ENJ peptide 66
67	C19	S-I-G-A-I-D-S-K-L-D-W-S-H-N-F	PDB_3ENJ peptide 67
68	C20	A-I-D-S-K-L-D-W-S-H-N-F-T-N-M	PDB_3ENJ peptide 68
69	C21	S-K-L-D-W-S-H-N-F-T-N-M-L-G-Y	PDB_3ENJ peptide 69
70	C22	D-W-S-H-N-F-T-N-M-L-G-Y-T-D-A	PDB_3ENJ peptide 70
71	C23	H-N-F-T-N-M-L-G-Y-T-D-A-Q-F-T	PDB_3ENJ peptide 71
72	C24	T-N-M-L-G-Y-T-D-A-Q-F-T-E-L-M	PDB_3ENJ peptide 72
73	D 1	L-G-Y-T-D-A-Q-F-T-E-L-M-R-L-Y	PDB_3ENJ peptide 73
74	D 2	T-D-A-Q-F-T-E-L-M-R-L-Y-L-T-I	PDB_3ENJ peptide 74
75	D 3	Q-F-T-E-L-M-R-L-Y-L-T-I-H-S-D	PDB_3ENJ peptide 75
76	D 4	E-L-M-R-L-Y-L-T-I-H-S-D-H-E-G	PDB_3ENJ peptide 76
77	D 5	R-L-Y-L-T-I-H-S-D-H-E-G-G-N-V	PDB_3ENJ peptide 77
78	D 6	L-T-I-H-S-D-H-E-G-G-N-V-S-A-H	PDB_3ENJ peptide 78
79	D 7	H-S-D-H-E-G-G-N-V-S-A-H-T-S-H	PDB_3ENJ peptide 79
80	D 8	H-E-G-G-N-V-S-A-H-T-S-H-L-V-G	PDB_3ENJ peptide 80
81	D 9	G-N-V-S-A-H-T-S-H-L-V-G-S-A-L	PDB_3ENJ peptide 81
82	D10	S-A-H-T-S-H-L-V-G-S-A-L-S-D-P	PDB_3ENJ peptide 82
83	D11	T-S-H-L-V-G-S-A-L-S-D-P-Y-L-S	PDB_3ENJ peptide 83
84	D12	L-V-G-S-A-L-S-D-P-Y-L-S-F-A-A	PDB_3ENJ peptide 84
85	D13	S-A-L-S-D-P-Y-L-S-F-A-A-A-M-N	PDB_3ENJ peptide 85

86	D14	S-D-P-Y-L-S-F-A-A-A-M-N-G-L-A	PDB_3ENJ peptide 86
87	D15	Y-L-S-F-A-A-A-M-N-G-L-A-G-P-L	PDB_3ENJ peptide 87
88	D16	F-A-A-A-M-N-G-L-A-G-P-L-H-G-L	PDB_3ENJ peptide 88
89	D17	A-M-N-G-L-A-G-P-L-H-G-L-A-N-Q	PDB_3ENJ peptide 89
90	D18	G-L-A-G-P-L-H-G-L-A-N-Q-E-V-L	PDB_3ENJ peptide 90
91	D19	G-P-L-H-G-L-A-N-Q-E-V-L-V-W-L	PDB_3ENJ peptide 91
92	D20	H-G-L-A-N-Q-E-V-L-V-W-L-T-Q-L	PDB_3ENJ peptide 92
93	D21	A-N-Q-E-V-L-V-W-L-T-Q-L-Q-K-E	PDB_3ENJ peptide 93
94	D22	E-V-L-V-W-L-T-Q-L-Q-K-E-V-G-K	PDB_3ENJ peptide 94
95	D23	V-W-L-T-Q-L-Q-K-E-V-G-K-D-V-S	PDB_3ENJ peptide 95
96	D24	T-Q-L-Q-K-E-V-G-K-D-V-S-D-E-K	PDB_3ENJ peptide 96
97	E 1	Q-K-E-V-G-K-D-V-S-D-E-K-L-R-D	PDB_3ENJ peptide 97
98	E 2	V-G-K-D-V-S-D-E-K-L-R-D-Y-I-W	PDB_3ENJ peptide 98
99	E 3	D-V-S-D-E-K-L-R-D-Y-I-W-N-T-L	PDB_3ENJ peptide 99
100	E 4	D-E-K-L-R-D-Y-I-W-N-T-L-N-S-G	PDB_3ENJ peptide 100
101	E 5	L-R-D-Y-I-W-N-T-L-N-S-G-R-V-V	PDB_3ENJ peptide 101
102	E 6	Y-I-W-N-T-L-N-S-G-R-V-V-P-G-Y	PDB_3ENJ peptide 102
103	E 7	N-T-L-N-S-G-R-V-V-P-G-Y-G-H-A	PDB_3ENJ peptide 103
104	E 8	N-S-G-R-V-V-P-G-Y-G-H-A-V-L-R	PDB_3ENJ peptide 104
105	E 9	R-V-V-P-G-Y-G-H-A-V-L-R-K-T-D	PDB_3ENJ peptide 105
106	E10	P-G-Y-G-H-A-V-L-R-K-T-D-P-R-Y	PDB_3ENJ peptide 106
107	E11	G-H-A-V-L-R-K-T-D-P-R-Y-T-C-Q	PDB_3ENJ peptide 107
108	E12	V-L-R-K-T-D-P-R-Y-T-C-Q-R-E-F	PDB_3ENJ peptide 108
109	E13	K-T-D-P-R-Y-T-C-Q-R-E-F-A-L-K	PDB_3ENJ peptide 109
110	E14	P-R-Y-T-C-Q-R-E-F-A-L-K-H-L-P	PDB_3ENJ peptide 110
111	E15	T-C-Q-R-E-F-A-L-K-H-L-P-H-D-P	PDB_3ENJ peptide 111
112	E16	R-E-F-A-L-K-H-L-P-H-D-P-M-F-K	PDB_3ENJ peptide 112
113	E17	A-L-K-H-L-P-H-D-P-M-F-K-L-V-A	PDB_3ENJ peptide 113
114	E18	H-L-P-H-D-P-M-F-K-L-V-A-Q-L-Y	PDB_3ENJ peptide 114
115	E19	H-D-P-M-F-K-L-V-A-Q-L-Y-K-I-V	PDB_3ENJ peptide 115
116	E20	M-F-K-L-V-A-Q-L-Y-K-I-V-P-N-V	PDB_3ENJ peptide 116
117	E21	L-V-A-Q-L-Y-K-I-V-P-N-V-L-L-E	PDB_3ENJ peptide 117
118	E22	Q-L-Y-K-I-V-P-N-V-L-L-E-Q-G-K	PDB_3ENJ peptide 118
119	E23	K-I-V-P-N-V-L-L-E-Q-G-K-A-K-N	PDB_3ENJ peptide 119
120	E24	P-N-V-L-L-E-Q-G-K-A-K-N-P-W-P	PDB_3ENJ peptide 120
121	F 1	L-L-E-Q-G-K-A-K-N-P-W-P-N-V-D	PDB_3ENJ peptide 121
122	F 2	Q-G-K-A-K-N-P-W-P-N-V-D-A-H-S	PDB_3ENJ peptide 122
123	F 3	A-K-N-P-W-P-N-V-D-A-H-S-G-V-L	PDB_3ENJ peptide 123
124	F 4	P-W-P-N-V-D-A-H-S-G-V-L-L-Q-Y	PDB_3ENJ peptide 124
125	F 5	N-V-D-A-H-S-G-V-L-L-Q-Y-Y-G-M	PDB_3ENJ peptide 125
126	F 6	A-H-S-G-V-L-L-Q-Y-Y-G-M-T-E-M	PDB_3ENJ peptide 126
127	F 7	G-V-L-L-Q-Y-Y-G-M-T-E-M-N-Y-Y	PDB_3ENJ peptide 127
128	F 8	L-Q-Y-Y-G-M-T-E-M-N-Y-Y-T-V-L	PDB_3ENJ peptide 128
129	F 9	Y-G-M-T-E-M-N-Y-Y-T-V-L-F-G-V	PDB_3ENJ peptide 129
130	F10	T-E-M-N-Y-Y-T-V-L-F-G-V-S-R-A	PDB_3ENJ peptide 130
131	F11	N-Y-Y-T-V-L-F-G-V-S-R-A-L-G-V	PDB_3ENJ peptide 131
132	F12	T-V-L-F-G-V-S-R-A-L-G-V-L-A-Q	PDB_3ENJ peptide 132
133	F13	F-G-V-S-R-A-L-G-V-L-A-Q-L-I-W	PDB_3ENJ peptide 133
134	F14	S-R-A-L-G-V-L-A-Q-L-I-W-S-R-A	PDB_3ENJ peptide 134
135	F15	L-G-V-L-A-Q-L-I-W-S-R-A-L-G-F	PDB_3ENJ peptide 135
136	F16	L-A-Q-L-I-W-S-R-A-L-G-F-P-L-E	PDB_3ENJ peptide 136
137	F17	L-I-W-S-R-A-L-G-F-P-L-E-R-P-K	PDB_3ENJ peptide 137

138	F18	S-R-A-L-G-F-P-L-E-R-P-K-S-M-S	PDB_3ENJ peptide 138
139	F19	L-G-F-P-L-E-R-P-K-S-M-S-T-D-G	PDB_3ENJ peptide 139
140	F20	P-L-E-R-P-K-S-M-S-T-D-G-L-I-K	PDB_3ENJ peptide 140
141	F21	R-P-K-S-M-S-T-D-G-L-I-K-L-V-D	PDB_3ENJ peptide 141
142	F22	K-S-M-S-T-D-G-L-I-K-L-V-D-S-K	PDB_3ENJ peptide 142
143	F23	K-V-F-G-R-C-E-L-A-A-A-M-K-R-H	PDB_193L peptide 1
144	F24	G-R-C-E-L-A-A-A-M-K-R-H-G-L-D	PDB_193L peptide 2
145	G 1	E-L-A-A-A-M-K-R-H-G-L-D-N-Y-R	PDB_193L peptide 3
146	G 2	A-A-M-K-R-H-G-L-D-N-Y-R-G-Y-S	PDB_193L peptide 4
147	G 3	K-R-H-G-L-D-N-Y-R-G-Y-S-L-G-N	PDB_193L peptide 5
148	G 4	G-L-D-N-Y-R-G-Y-S-L-G-N-W-V-C	PDB_193L peptide 6
149	G 5	N-Y-R-G-Y-S-L-G-N-W-V-C-A-A-K	PDB_193L peptide 7
150	G 6	G-Y-S-L-G-N-W-V-C-A-A-K-F-E-S	PDB_193L peptide 8
151	G 7	L-G-N-W-V-C-A-A-K-F-E-S-N-F-N	PDB_193L peptide 9
152	G 8	W-V-C-A-A-K-F-E-S-N-F-N-T-Q-A	PDB_193L peptide 10
153	G 9	A-A-K-F-E-S-N-F-N-T-Q-A-T-N-R	PDB_193L peptide 11
154	G10	F-E-S-N-F-N-T-Q-A-T-N-R-N-T-D	PDB_193L peptide 12
155	G11	N-F-N-T-Q-A-T-N-R-N-T-D-G-S-T	PDB_193L peptide 13
156	G12	T-Q-A-T-N-R-N-T-D-G-S-T-D-Y-G	PDB_193L peptide 14
157	G13	T-N-R-N-T-D-G-S-T-D-Y-G-I-L-Q	PDB_193L peptide 15
158	G14	N-T-D-G-S-T-D-Y-G-I-L-Q-I-N-S	PDB_193L peptide 16
159	G15	G-S-T-D-Y-G-I-L-Q-I-N-S-R-W-W	PDB_193L peptide 17
160	G16	D-Y-G-I-L-Q-I-N-S-R-W-W-C-N-D	PDB_193L peptide 18
161	G17	I-L-Q-I-N-S-R-W-W-C-N-D-G-R-T	PDB_193L peptide 19
162	G18	I-N-S-R-W-W-C-N-D-G-R-T-P-G-S	PDB_193L peptide 20
163	G19	R-W-W-C-N-D-G-R-T-P-G-S-R-N-L	PDB_193L peptide 21
164	G20	C-N-D-G-R-T-P-G-S-R-N-L-C-N-I	PDB_193L peptide 22
165	G21	G-R-T-P-G-S-R-N-L-C-N-I-P-C-S	PDB_193L peptide 23
166	G22	P-G-S-R-N-L-C-N-I-P-C-S-A-L-L	PDB_193L peptide 24
167	G23	R-N-L-C-N-I-P-C-S-A-L-L-S-S-D	PDB_193L peptide 25
168	G24	C-N-I-P-C-S-A-L-L-S-S-D-I-T-A	PDB_193L peptide 26
169	H 1	P-C-S-A-L-L-S-S-D-I-T-A-S-V-N	PDB_193L peptide 27
170	H 2	A-L-L-S-S-D-I-T-A-S-V-N-C-A-K	PDB_193L peptide 28
171	H 3	S-S-D-I-T-A-S-V-N-C-A-K-K-I-V	PDB_193L peptide 29
172	H 4	I-T-A-S-V-N-C-A-K-K-I-V-S-D-G	PDB_193L peptide 30
173	H 5	S-V-N-C-A-K-K-I-V-S-D-G-N-G-M	PDB_193L peptide 31
174	H 6	C-A-K-K-I-V-S-D-G-N-G-M-N-A-W	PDB_193L peptide 32
175	H 7	K-I-V-S-D-G-N-G-M-N-A-W-V-A-W	PDB_193L peptide 33
176	H 8	S-D-G-N-G-M-N-A-W-V-A-W-R-N-R	PDB_193L peptide 34
177	H 9	N-G-M-N-A-W-V-A-W-R-N-R-C-K-G	PDB_193L peptide 35
178	H10	N-A-W-V-A-W-R-N-R-C-K-G-T-D-V	PDB_193L peptide 36
179	H11	V-A-W-R-N-R-C-K-G-T-D-V-Q-A-W	PDB_193L peptide 37
180	H12	R-N-R-C-K-G-T-D-V-Q-A-W-I-R-G	PDB_193L peptide 38
181	H13	C-K-G-T-D-V-Q-A-W-I-R-G-C-R-L	PDB_193L peptide 39
182	H14	A-K-V-A-V-L-G-A-S-G-G-I-G-Q-P	PDB_1MLD peptide 1
183	H15	A-V-L-G-A-S-G-G-I-G-Q-P-L-S-L	PDB_1MLD peptide 2
184	H16	G-A-S-G-G-I-G-Q-P-L-S-L-L-L-K	PDB_1MLD peptide 3
185	H17	G-G-I-G-Q-P-L-S-L-L-L-K-N-S-P	PDB_1MLD peptide 4
186	H18	G-Q-P-L-S-L-L-L-K-N-S-P-L-V-S	PDB_1MLD peptide 5
187	H19	L-S-L-L-L-K-N-S-P-L-V-S-R-L-T	PDB_1MLD peptide 6
188	H20	L-L-K-N-S-P-L-V-S-R-L-T-L-Y-D	PDB_1MLD peptide 7
189	H21	N-S-P-L-V-S-R-L-T-L-Y-D-I-A-H	PDB_1MLD peptide 8

190	H22	L-V-S-R-L-T-L-Y-D-I-A-H-T-P-G	PDB_1MLD peptide 9
191	H23	R-L-T-L-Y-D-I-A-H-T-P-G-V-A-A	PDB_1MLD peptide 10
192	H24	L-Y-D-I-A-H-T-P-G-V-A-A-D-L-S	PDB_1MLD peptide 11
193	I 1	I-A-H-T-P-G-V-A-A-D-L-S-H-I-E	PDB_1MLD peptide 12
194	I 2	T-P-G-V-A-A-D-L-S-H-I-E-T-R-A	PDB_1MLD peptide 13
195	I 3	V-A-A-D-L-S-H-I-E-T-R-A-T-V-K	PDB_1MLD peptide 14
196	I 4	D-L-S-H-I-E-T-R-A-T-V-K-G-Y-L	PDB_1MLD peptide 15
197	I 5	H-I-E-T-R-A-T-V-K-G-Y-L-G-P-E	PDB_1MLD peptide 16
198	I 6	T-R-A-T-V-K-G-Y-L-G-P-E-Q-L-P	PDB_1MLD peptide 17
199	I 7	T-V-K-G-Y-L-G-P-E-Q-L-P-D-C-L	PDB_1MLD peptide 18
200	I 8	G-Y-L-G-P-E-Q-L-P-D-C-L-K-G-C	PDB_1MLD peptide 19
201	I 9	G-P-E-Q-L-P-D-C-L-K-G-C-D-V-V	PDB_1MLD peptide 20
202	I10	Q-L-P-D-C-L-K-G-C-D-V-V-V-I-P	PDB_1MLD peptide 21
203	I11	D-C-L-K-G-C-D-V-V-V-I-P-A-G-V	PDB_1MLD peptide 22
204	I12	K-G-C-D-V-V-V-I-P-A-G-V-P-R-K	PDB_1MLD peptide 23
205	I13	D-V-V-V-I-P-A-G-V-P-R-K-P-G-M	PDB_1MLD peptide 24
206	I14	V-I-P-A-G-V-P-R-K-P-G-M-T-R-D	PDB_1MLD peptide 25
207	I15	A-G-V-P-R-K-P-G-M-T-R-D-D-L-F	PDB_1MLD peptide 26
208	I16	P-R-K-P-G-M-T-R-D-D-L-F-N-T-N	PDB_1MLD peptide 27
209	I17	P-G-M-T-R-D-D-L-F-N-T-N-A-T-I	PDB_1MLD peptide 28
210	I18	T-R-D-D-L-F-N-T-N-A-T-I-V-A-T	PDB_1MLD peptide 29
211	I19	D-L-F-N-T-N-A-T-I-V-A-T-L-T-A	PDB_1MLD peptide 30
212	I20	N-T-N-A-T-I-V-A-T-L-T-A-A-C-A	PDB_1MLD peptide 31
213	I21	A-T-I-V-A-T-L-T-A-A-C-A-Q-H-C	PDB_1MLD peptide 32
214	I22	V-A-T-L-T-A-A-C-A-Q-H-C-P-D-A	PDB_1MLD peptide 33
215	I23	L-T-A-A-C-A-Q-H-C-P-D-A-M-I-C	PDB_1MLD peptide 34
216	I24	A-C-A-Q-H-C-P-D-A-M-I-C-I-I-S	PDB_1MLD peptide 35
217	J 1	Q-H-C-P-D-A-M-I-C-I-I-S-N-P-V	PDB_1MLD peptide 36
218	J 2	P-D-A-M-I-C-I-I-S-N-P-V-N-S-T	PDB_1MLD peptide 37
219	J 3	M-I-C-I-I-S-N-P-V-N-S-T-I-P-I	PDB_1MLD peptide 38
220	J 4	I-I-S-N-P-V-N-S-T-I-P-I-T-A-E	PDB_1MLD peptide 39
221	J 5	N-P-V-N-S-T-I-P-I-T-A-E-V-F-K	PDB_1MLD peptide 40
222	J 6	N-S-T-I-P-I-T-A-E-V-F-K-K-H-G	PDB_1MLD peptide 41
223	J 7	I-P-I-T-A-E-V-F-K-K-H-G-V-Y-N	PDB_1MLD peptide 42
224	J 8	T-A-E-V-F-K-K-H-G-V-Y-N-P-N-K	PDB_1MLD peptide 43
225	J 9	V-F-K-K-H-G-V-Y-N-P-N-K-I-F-G	PDB_1MLD peptide 44
226	J10	K-H-G-V-Y-N-P-N-K-I-F-G-V-T-T	PDB_1MLD peptide 45
227	J11	V-Y-N-P-N-K-I-F-G-V-T-T-L-D-I	PDB_1MLD peptide 46
228	J12	P-N-K-I-F-G-V-T-T-L-D-I-V-R-A	PDB_1MLD peptide 47
229	J13	I-F-G-V-T-T-L-D-I-V-R-A-N-A-F	PDB_1MLD peptide 48
230	J14	V-T-T-L-D-I-V-R-A-N-A-F-V-A-E	PDB_1MLD peptide 49
231	J15	L-D-I-V-R-A-N-A-F-V-A-E-L-K-G	PDB_1MLD peptide 50
232	J16	V-R-A-N-A-F-V-A-E-L-K-G-L-D-P	PDB_1MLD peptide 51
233	J17	N-A-F-V-A-E-L-K-G-L-D-P-A-R-V	PDB_1MLD peptide 52
234	J18	V-A-E-L-K-G-L-D-P-A-R-V-S-V-P	PDB_1MLD peptide 53
235	J19	L-K-G-L-D-P-A-R-V-S-V-P-V-I-G	PDB_1MLD peptide 54
236	J20	L-D-P-A-R-V-S-V-P-V-I-G-G-H-A	PDB_1MLD peptide 55
237	J21	A-R-V-S-V-P-V-I-G-G-H-A-G-K-T	PDB_1MLD peptide 56
238	J22	S-V-P-V-I-G-G-H-A-G-K-T-I-I-P	PDB_1MLD peptide 57
239	J23	V-I-G-G-H-A-G-K-T-I-I-P-L-I-S	PDB_1MLD peptide 58
240	J24	G-H-A-G-K-T-I-I-P-L-I-S-Q-C-T	PDB_1MLD peptide 59
241	K 1	G-K-T-I-I-P-L-I-S-Q-C-T-P-K-V	PDB_1MLD peptide 60

242	K 2	I-I-P-L-I-S-Q-C-T-P-K-V-D-F-P	PDB_1MLD peptide 61
243	K 3	L-I-S-Q-C-T-P-K-V-D-F-P-Q-D-Q	PDB_1MLD peptide 62
244	K 4	Q-C-T-P-K-V-D-F-P-Q-D-Q-L-S-T	PDB_1MLD peptide 63
245	K 5	P-K-V-D-F-P-Q-D-Q-L-S-T-L-T-G	PDB_1MLD peptide 64
246	K 6	D-F-P-Q-D-Q-L-S-T-L-T-G-R-I-Q	PDB_1MLD peptide 65
247	K 7	Q-D-Q-L-S-T-L-T-G-R-I-Q-E-A-G	PDB_1MLD peptide 66
248	K 8	L-S-T-L-T-G-R-I-Q-E-A-G-T-E-V	PDB_1MLD peptide 67
249	K 9	L-T-G-R-I-Q-E-A-G-T-E-V-V-K-A	PDB_1MLD peptide 68
250	K10	R-I-Q-E-A-G-T-E-V-V-K-A-K-A-G	PDB_1MLD peptide 69
251	K11	E-A-G-T-E-V-V-K-A-K-A-G-A-G-S	PDB_1MLD peptide 70
252	K12	T-E-V-V-K-A-K-A-G-A-G-S-A-T-L	PDB_1MLD peptide 71
253	K13	V-K-A-K-A-G-A-G-S-A-T-L-S-M-A	PDB_1MLD peptide 72
254	K14	K-A-G-A-G-S-A-T-L-S-M-A-Y-A-G	PDB_1MLD peptide 73
255	K15	A-G-S-A-T-L-S-M-A-Y-A-G-A-R-F	PDB_1MLD peptide 74
256	K16	A-T-L-S-M-A-Y-A-G-A-R-F-V-F-S	PDB_1MLD peptide 75
257	K17	S-M-A-Y-A-G-A-R-F-V-F-S-L-V-D	PDB_1MLD peptide 76
258	K18	Y-A-G-A-R-F-V-F-S-L-V-D-A-M-N	PDB_1MLD peptide 77
259	K19	A-R-F-V-F-S-L-V-D-A-M-N-G-K-E	PDB_1MLD peptide 78
260	K20	V-F-S-L-V-D-A-M-N-G-K-E-G-V-V	PDB_1MLD peptide 79
261	K21	L-V-D-A-M-N-G-K-E-G-V-V-E-C-S	PDB_1MLD peptide 80
262	K22	A-M-N-G-K-E-G-V-V-E-C-S-F-V-K	PDB_1MLD peptide 81
263	K23	G-K-E-G-V-V-E-C-S-F-V-K-S-Q-E	PDB_1MLD peptide 82
264	K24	G-V-V-E-C-S-F-V-K-S-Q-E-T-D-C	PDB_1MLD peptide 83
265	L 1	E-C-S-F-V-K-S-Q-E-T-D-C-P-Y-F	PDB_1MLD peptide 84
266	L 2	F-V-K-S-Q-E-T-D-C-P-Y-F-S-T-P	PDB_1MLD peptide 85
267	L 3	S-Q-E-T-D-C-P-Y-F-S-T-P-L-L-L	PDB_1MLD peptide 86
268	L 4	T-D-C-P-Y-F-S-T-P-L-L-L-G-K-K	PDB_1MLD peptide 87
269	L 5	P-Y-F-S-T-P-L-L-L-G-K-K-G-I-E	PDB_1MLD peptide 88
270	L 6	S-T-P-L-L-L-G-K-K-G-I-E-K-N-L	PDB_1MLD peptide 89
271	L 7	L-L-L-G-K-K-G-I-E-K-N-L-G-I-G	PDB_1MLD peptide 90
272	L 8	G-K-K-G-I-E-K-N-L-G-I-G-K-I-S	PDB_1MLD peptide 91
273	L 9	G-I-E-K-N-L-G-I-G-K-I-S-P-F-E	PDB_1MLD peptide 92
274	L10	K-N-L-G-I-G-K-I-S-P-F-E-E-K-M	PDB_1MLD peptide 93
275	L11	G-I-G-K-I-S-P-F-E-E-K-M-I-A-E	PDB_1MLD peptide 94
276	L12	K-I-S-P-F-E-E-K-M-I-A-E-A-I-P	PDB_1MLD peptide 95
277	L13	P-F-E-E-K-M-I-A-E-A-I-P-E-L-K	PDB_1MLD peptide 96
278	L14	E-K-M-I-A-E-A-I-P-E-L-K-A-S-I	PDB_1MLD peptide 97
279	L15	I-A-E-A-I-P-E-L-K-A-S-I-K-K-G	PDB_1MLD peptide 98
280	L16	A-I-P-E-L-K-A-S-I-K-K-G-E-E-F	PDB_1MLD peptide 99
281	L17	E-L-K-A-S-I-K-K-G-E-E-F-V-K-N	PDB_1MLD peptide 100
282	L18	K-A-S-I-K-K-G-E-E-F-V-K-N-M-K	PDB_1MLD peptide 101
283	L19	S-S-S-V-P-S-Q-K-T-Y-Q-G-S-Y-G	PDB_2YBG peptide 1
284	L20	V-P-S-Q-K-T-Y-Q-G-S-Y-G-F-R-L	PDB_2YBG peptide 2
285	L21	Q-K-T-Y-Q-G-S-Y-G-F-R-L-G-F-L	PDB_2YBG peptide 3
286	L22	Y-Q-G-S-Y-G-F-R-L-G-F-L-H-S-G	PDB_2YBG peptide 4
287	L23	S-Y-G-F-R-L-G-F-L-H-S-G-T-A-K	PDB_2YBG peptide 5
288	L24	F-R-L-G-F-L-H-S-G-T-A-K-S-V-T	PDB_2YBG peptide 6
289	M 1	G-F-L-H-S-G-T-A-K-S-V-T-C-T-Y	PDB_2YBG peptide 7
290	M 2	H-S-G-T-A-K-S-V-T-C-T-Y-S-P-A	PDB_2YBG peptide 8
291	M 3	T-A-K-S-V-T-C-T-Y-S-P-A-L-N-K	PDB_2YBG peptide 9
292	M 4	S-V-T-C-T-Y-S-P-A-L-N-K-M-F-C	PDB_2YBG peptide 10
293	M 5	C-T-Y-S-P-A-L-N-K-M-F-C-Q-L-A	PDB_2YBG peptide 11

294	M 6	S-P-A-L-N-K-M-F-C-Q-L-A-K-T-C	PDB_2YBG peptide 12
295	M 7	L-N-K-M-F-C-Q-L-A-K-T-C-P-V-Q	PDB_2YBG peptide 13
296	M 8	M-F-C-Q-L-A-K-T-C-P-V-Q-L-W-V	PDB_2YBG peptide 14
297	M 9	Q-L-A-K-T-C-P-V-Q-L-W-V-D-S-T	PDB_2YBG peptide 15
298	M10	K-T-C-P-V-Q-L-W-V-D-S-T-P-P-P	PDB_2YBG peptide 16
299	M11	P-V-Q-L-W-V-D-S-T-P-P-P-G-T-R	PDB_2YBG peptide 17
300	M12	L-W-V-D-S-T-P-P-P-G-T-R-V-R-A	PDB_2YBG peptide 18
301	M13	D-S-T-P-P-P-G-T-R-V-R-A-M-A-I	PDB_2YBG peptide 19
302	M14	P-P-P-G-T-R-V-R-A-M-A-I-Y-K-Q	PDB_2YBG peptide 20
303	M15	G-T-R-V-R-A-M-A-I-Y-K-Q-S-Q-H	PDB_2YBG peptide 21
304	M16	V-R-A-M-A-I-Y-K-Q-S-Q-H-M-T-E	PDB_2YBG peptide 22
305	M17	M-A-I-Y-K-Q-S-Q-H-M-T-E-V-V-R	PDB_2YBG peptide 23
306	M18	Y-K-Q-S-Q-H-M-T-E-V-V-R-R-C-P	PDB_2YBG peptide 24
307	M19	S-Q-H-M-T-E-V-V-R-R-C-P-H-H-E	PDB_2YBG peptide 25
308	M20	M-T-E-V-V-R-R-C-P-H-H-E-R-C-S	PDB_2YBG peptide 26
309	M21	V-V-R-R-C-P-H-H-E-R-C-S-D-S-D	PDB_2YBG peptide 27
310	M22	R-C-P-H-H-E-R-C-S-D-S-D-G-L-A	PDB_2YBG peptide 28
311	M23	H-H-E-R-C-S-D-S-D-G-L-A-P-P-Q	PDB_2YBG peptide 29
312	M24	R-C-S-D-S-D-G-L-A-P-P-Q-H-L-I	PDB_2YBG peptide 30
313	N 1	D-S-D-G-L-A-P-P-Q-H-L-I-R-V-E	PDB_2YBG peptide 31
314	N 2	G-L-A-P-P-Q-H-L-I-R-V-E-G-N-L	PDB_2YBG peptide 32
315	N 3	P-P-Q-H-L-I-R-V-E-G-N-L-R-V-E	PDB_2YBG peptide 33
316	N 4	H-L-I-R-V-E-G-N-L-R-V-E-Y-L-D	PDB_2YBG peptide 34
317	N 5	R-V-E-G-N-L-R-V-E-Y-L-D-D-R-N	PDB_2YBG peptide 35
318	N 6	G-N-L-R-V-E-Y-L-D-D-R-N-T-F-R	PDB_2YBG peptide 36
319	N 7	R-V-E-Y-L-D-D-R-N-T-F-R-H-S-V	PDB_2YBG peptide 37
320	N 8	Y-L-D-D-R-N-T-F-R-H-S-V-V-V-P	PDB_2YBG peptide 38
321	N 9	D-R-N-T-F-R-H-S-V-V-V-P-Y-E-P	PDB_2YBG peptide 39
322	N10	T-F-R-H-S-V-V-V-P-Y-E-P-P-E-V	PDB_2YBG peptide 40
323	N11	H-S-V-V-V-P-Y-E-P-P-E-V-G-S-D	PDB_2YBG peptide 41
324	N12	V-V-P-Y-E-P-P-E-V-G-S-D-C-T-T	PDB_2YBG peptide 42
325	N13	Y-E-P-P-E-V-G-S-D-C-T-T-I-H-Y	PDB_2YBG peptide 43
326	N14	P-E-V-G-S-D-C-T-T-I-H-Y-N-Y-M	PDB_2YBG peptide 44
327	N15	G-S-D-C-T-T-I-H-Y-N-Y-M-C-N-S	PDB_2YBG peptide 45
328	N16	C-T-T-I-H-Y-N-Y-M-C-N-S-S-C-M	PDB_2YBG peptide 46
329	N17	I-H-Y-N-Y-M-C-N-S-S-C-M-G-G-M	PDB_2YBG peptide 47
330	N18	N-Y-M-C-N-S-S-C-M-G-G-M-N-R-R	PDB_2YBG peptide 48
331	N19	C-N-S-S-C-M-G-G-M-N-R-R-P-I-L	PDB_2YBG peptide 49
332	N20	S-C-M-G-G-M-N-R-R-P-I-L-T-I-I	PDB_2YBG peptide 50
333	N21	G-G-M-N-R-R-P-I-L-T-I-I-T-L-E	PDB_2YBG peptide 51
334	N22	N-R-R-P-I-L-T-I-I-T-L-E-D-S-S	PDB_2YBG peptide 52
335	N23	P-I-L-T-I-I-T-L-E-D-S-S-G-N-L	PDB_2YBG peptide 53
336	N24	T-I-I-T-L-E-D-S-S-G-N-L-L-G-R	PDB_2YBG peptide 54
337	O 1	T-L-E-D-S-S-G-N-L-L-G-R-N-S-F	PDB_2YBG peptide 55
338	O 2	D-S-S-G-N-L-L-G-R-N-S-F-E-V-R	PDB_2YBG peptide 56
339	O 3	G-N-L-L-G-R-N-S-F-E-V-R-V-C-A	PDB_2YBG peptide 57
340	O 4	L-G-R-N-S-F-E-V-R-V-C-A-C-P-G	PDB_2YBG peptide 58
341	O 5	N-S-F-E-V-R-V-C-A-C-P-G-R-D-R	PDB_2YBG peptide 59
342	O 6	E-V-R-V-C-A-C-P-G-R-D-R-R-T-E	PDB_2YBG peptide 60
343	O 7	V-C-A-C-P-G-R-D-R-R-T-E-E-E-N	PDB_2YBG peptide 61
344	O 8	C-P-G-R-D-R-R-T-E-E-E-N-L-R-K	PDB_2YBG peptide 62
345	O 9	G-R-D-R-R-T-E-E-E-N-L-R-K-K-G	PDB_2YBG peptide 63

346	O10	G-I-V-E-Q-C-C-T-S-I-C-S-L-Y-Q	PDB_3E7J_A_peptide 1
347	O11	E-Q-C-C-T-S-I-C-S-L-Y-Q-L-E-N	PDB_3E7J_A_peptide 2
348	O12	C-T-S-I-C-S-L-Y-Q-L-E-N-Y-C-N	PDB_3E7J_A_peptide 3
349	O13	F-V-N-Q-H-L-C-G-S-H-L-V-E-A-L	PDB_3E7J_B_peptide 1
350	O14	Q-H-L-C-G-S-H-L-V-E-A-L-Y-L-V	PDB_3E7J_B_peptide 2
351	O15	C-G-S-H-L-V-E-A-L-Y-L-V-C-G-E	PDB_3E7J_B_peptide 3
352	O16	H-L-V-E-A-L-Y-L-V-C-G-E-R-G-F	PDB_3E7J_B_peptide 4
353	O17	E-A-L-Y-L-V-C-G-E-R-G-F-F-Y-T	PDB_3E7J_B_peptide 5
354	O18	L-Y-L-V-C-G-E-R-G-F-F-Y-T-P-K	PDB_3E7J_B_peptide 6
355	O19	S-I-P-E-T-Q-K-G-V-I-F-Y-E-S-H	PDB_2HCY_peptide 1
356	O20	E-T-Q-K-G-V-I-F-Y-E-S-H-G-K-L	PDB_2HCY_peptide 2
357	O21	K-G-V-I-F-Y-E-S-H-G-K-L-E-Y-K	PDB_2HCY_peptide 3
358	O22	I-F-Y-E-S-H-G-K-L-E-Y-K-D-I-P	PDB_2HCY_peptide 4
359	O23	E-S-H-G-K-L-E-Y-K-D-I-P-V-P-K	PDB_2HCY_peptide 5
360	O24	G-K-L-E-Y-K-D-I-P-V-P-K-P-K-A	PDB_2HCY_peptide 6
361	P 1	V-A-P-I-L-C-A-G-I-T-V-Y-K-A-L	PDB_2HCY_peptide 50
362	P 2	I-L-C-A-G-I-T-V-Y-K-A-L-K-S-A	PDB_2HCY_peptide 51
363	P 3	A-G-I-T-V-Y-K-A-L-K-S-A-N-L-M	PDB_2HCY_peptide 52
364	P 4	T-V-Y-K-A-L-K-S-A-N-L-M-A-G-H	PDB_2HCY_peptide 53
365	P 5	Q-V-V-K-S-I-S-I-V-G-S-Y-V-G-N	PDB_2HCY_peptide 95
366	P 6	K-S-I-S-I-V-G-S-Y-V-G-N-R-A-D	PDB_2HCY_peptide 96
367	P 7	S-I-V-G-S-Y-V-G-N-R-A-D-T-R-E	PDB_2HCY_peptide 97
368	P 8	G-S-Y-V-G-N-R-A-D-T-R-E-A-L-D	PDB_2HCY_peptide 98
369	P 9	V-G-N-R-A-D-T-R-E-A-L-D-F-F-A	PDB_2HCY_peptide 99
370	P10	R-A-D-T-R-E-A-L-D-F-F-A-R-G-L	PDB_2HCY_peptide 100
371	P11	T-R-E-A-L-D-F-F-A-R-G-L-V-K-S	PDB_2HCY_peptide 101
372	P12	A-L-D-F-F-A-R-G-L-V-K-S-P-I-K	PDB_2HCY_peptide 102
373	P13	F-F-A-R-G-L-V-K-S-P-I-K-V-V-G	PDB_2HCY_peptide 103
374	P14	R-G-L-V-K-S-P-I-K-V-V-G-L-S-T	PDB_2HCY_peptide 104
375	P15	V-K-S-P-I-K-V-V-G-L-S-T-L-P-E	PDB_2HCY_peptide 105
376	P16	P-I-K-V-V-G-L-S-T-L-P-E-I-Y-E	PDB_2HCY_peptide 106
377	P17	V-V-G-L-S-T-L-P-E-I-Y-E-K-M-E	PDB_2HCY_peptide 107
378	P18	L-S-T-L-P-E-I-Y-E-K-M-E-K-G-Q	PDB_2HCY_peptide 108
379	P19	L-P-E-I-Y-E-K-M-E-K-G-Q-I-V-G	PDB_2HCY_peptide 109
380	P20	I-Y-E-K-M-E-K-G-Q-I-V-G-R-Y-V	PDB_2HCY_peptide 110
381	P21	K-M-E-K-G-Q-I-V-G-R-Y-V-V-D-T	PDB_2HCY_peptide 111
382	P22	E-K-G-Q-I-V-G-R-Y-V-V-D-T-S-K	PDB_2HCY_peptide 112
383	P23	Ac	negative control
384	P24	Ac	negative control

Publications

Mainz, A., Peschek, J., Stavropoulou, M., Back, K.C., Bardiaux, B., Asami, S., Prade, E., Peters, C., Weinkauf, S., Buchner, J*., et al.* (**2015**). The chaperone alphaB-crystallin uses different interfaces to capture an amorphous and an amyloid client. Nat Struct Mol Biol *22*, 898-905.

Peschek, J., Braun, N., Rohrberg, J., Back, K.C., Kriehuber, T., Kastenmuller, A., Weinkauf, S., and Buchner, J. (**2013**). Regulated structural transitions unleash the chaperone activity of alphaB-crystallin. Proc Natl Acad Sci U S A *110*, E3780-3789.

Eidesstattliche Erklärung

Hiermit erkläre ich an Eides statt, dass ich die vorliegende Arbeit selbständig verfasst und keine anderen als die angegebenen Quellen und Hilfsmittel verwendet habe. Die aus fremden Quellen übernommenen Gedanken sind als solche kenntlich gemacht. Die vorliegende Arbeit wurde noch keiner anderen Prüfungsbehörde vorgelegt. Teile dieser Arbeit werden in einem wissenschaftlichen Journal veröffentlicht.

München, 08.02.2016

…….

Katrin Back

Danksagung

An erster Stelle möchte ich mich bei meinem Doktorvater Johannes Buchner bedanken für die Betreuung meiner Doktorarbeit, durch die es möglich war, vielseitige und interessante Fragestellungen zu bearbeiten. Weiterhin möchte ich mich auch für die hervorragende Infrastruktur am Lehrstuhl und die wissenschaftlichen Diskussionen bedanken sowie für die Möglichkeit, sich auf wissenschaftlichen Konferenzen mit Kollegen auszutauschen.

Bei Prof. Sevil Weinkauf möchte ich mich besonders für Möglichkeit bedanken, die Peptide Array-Experimente zur Untersuchung der Substratinteraktion durchführen zu können, ohne die ein wichtiger Teil der Arbeit nicht hätte durchgeführt werden können. Außerdem gilt ihr und ihren Mitarbeitern Dr. Carsten Peters und Dr. Christoph Kaiser ebenfalls großer Dank für die Bereicherung meines Projekts durch ihre elektronenmikroskopischen Untersuchungen.

Weiterhin möchte ich Prof. Joachim Graw für die Bereitstellung der Maus-Linsen als auch für die wissenschaftliche Unterstützung bei der Untersuchung der Linsenproteine danken. Durch dieses Kooperationsprojekt wurde eine spannende Verbindung zwischen *in vitro*-Experimenten und *in vivo*-Effekten möglich.

Großer Dank gilt auch Bettina Richter, die mir durch die 2D-Gelelektrophorese, sowie die Vorbereitung der ms-Proben und bei vielen anderen Gelegenheiten sehr geholfen hat.

Danke an Marina Daake, Helmut Krause und Gina Feind für die ms-Analytik.

Ebenfalls vielen Dank an meine Praktikanten, besonders natürlich an Philipp Schmid, der das Projekt gewissenhaft unterstützt hat und sicher auch so weiterführen wird.

Weiterhin möchte ich allen (ehemaligen) Mitarbeitern des Lehrstuhls danken, die das tägliche Leben am Laufen halten, besonders Dr. Jirka Peschek, der ‚sein Projekt' in meine Hände gelegt und mich in die Geheimnisse des Buchner-Lehrstuhls eingeführt hat.

Meinen aktuellen und ehemaligen Labor- und Bürokollegen möchte ich für die entspannte, aber doch produktive Arbeitsatmosphäre danken, besonders Marina Daake, Christine John, Patricia Schöppner, Sabine Rittinger und den weiteren ehemaligen Mitgliedern der schaumweinaffinen Damenrunde.

Den IT-Administratoren des Lehrstuhls Mathias Rosam, Daniel Rutz und Florian H. Schopf möchte ich besonders danken für den technischen Support. Durch ihren unermüdlichen Einsatz in den letzten Jahren haben sie zusammen mit Julia Eckl und Adrian Drazic das Leben am Lehrstuhl sehr viel besser gemacht.

Außerdem möchte ich natürlich meiner Familie danken für ihre stete Unterstützung!